GROWTH MECHANISM AND INTERFACE EFFECTS ON MICROSTRUCTURE OF PEROVSKITE-TYPE BARIUM TITANATE-BASED EPITAXIAL FILMS

by

JIE HE

Presented to the Faculty of the Graduate School of

The University of Texas at Arlington in Partial Fulfillment

of the Requirements

for the Degree of

DOCTOR OF PHILOSOPHY

THE UNIVERSITY OF TEXAS AT ARLINGTON

May 2012

ACKNOWLEDGEMENTS

I would like to thank all of those who have helped and supported me in any respect during the completion of this research. First of all, I would like to express my sincere gratitude to my advisor Dr. Efstathios. I. Meletis for his research advices, instructions, patience and support to my Ph.D work. I would like to give my deepest appreciation and special acknowledgement to Dr. Jiechao Jiang for guiding me into the field of materials structure characterization and electron microscopy, and providing instructions and encouragements throughout all my research. I also want to acknowledge my committee members for their time and suggestions.

I would also like to thank Dr. Chonglin Chen and Dr. Amar Balla from University of Texas at San Antonio and Dr. Chen's student: Ming Liu, Jian Liu, Chunrui Ma for research communications, collaborations and especially supplying me the research thin film samples fabricated using PLD in my studies. I would like to acknowledge my group members and friends, Dr. Hongquan Jiang, Yinsheng Fang, Liangshan Chen, Jiayin Gu, Huili Xu, Qiming Yang, Qing Feng, etc., for their countless help, encouragement, support and friendship.

I am also grateful to MSE staff, Mrs. Jennifer Standlee and Mrs. Lidia Cuauhtli, who have been always more than helpful in many aspects for completing my doctoral program.

Finally, and most importantly, I would like to thank my parents and my sister for bringing me strength and confidence everyday. Without their love, support and understanding, I could never have been able to make it this far.

This work is supported by National Science Foundation under Awards NSF/CMMI-0709293, NSF/CMS-0528873 and NSF/DMR-0821745 and State of Texas, Advanced Research Program Award.

April 11, 2012

ABSTRACT

GROWTH MECHANISM AND INTERFACE EFFECTS ON MICROSTRUCTURE OF PEROVSKITE-TYPE BARIUM TITANATE-BASED EPITAXIAL FILMS

JIE HE, PhD

The University of Texas at Arlington, 2012

Supervising Professor: Efstathios. I. Meletis

This work was motivated and focused on the growth mechanism, microstructures and interfaces of barium titanate, $BaTiO_3$ (BTO), based epitaxial thin films. Transimission electron microscopy (TEM), high resolution TEM (HRTEM), electron diffraction (ED) have been mainly employed in this study for microstructure investigations of BTO-based epitaxial thin films with the assistance of other materials characterization methods, such as X-ray diffraction (XRD), atomic force microscopy (AFM), Nanoindentation testing, etc. As a basic studying model, epitaxial BTO films were first deposited on the (001) MgO substrate using RF magnetron sputtering to provide fundamental knowledge of the film growth for BTO based thin films. The epitaxial BTO films show a tetragonal crystal structure (a = 4.02 Å and c = 4.11 Å) with epitaxial nanodomains induced from the rough film/substrate interface due to the modification of the substrate surface characteristics (steps, terraces, and kinks) during the deposition process. Two new phases of Γ_γ ($Ba_{10}Ti_8O_{26}$) and H_β ($Ba_8Ti_8O_{24}$) were formed on the MgO substrate using RF magnetron sputtering. The atomic structures of the two new phases were determined and examined. The Γ_γ phase has a monoclinic structure, ***Cm***, a=16.49 Å, b=8.94 Å, c=3.94 Å, γ=77°. The H_β phase has a monoclinic structure, ***Cm***, a = 17.88Å, b = 7.21Å, c = 3.94 Å, γ =

82°. Both Γ_γ and H_β phases have four different oriented domains. The orientation relationship between domains and MgO substrate is discussed. Initail study shows that these new phases possess novel and interesting properties.

The doped BTO films with different dopant (Sr^{2+} and Zr^{4+}) fabricated using pulsed laser deposition (PLD) have been studied for doping effects, interface effects and film growth mechanism. The (Ba,Sr)TiO_3 (BST) epitaxial films grown on 1.2° and 5.3° miscut substrates consist of lager commensurate domains, and correspondly show higher dielectric constant and dielectric tunability, and lower average modulus and hardness than those of the films grown on the 3.5° miscut substrate. The results suggest that the differences on the interfacial structure have a tremendous effect on the properties of the films. The investigation on epitaxial Ba(Zr,Ti)O_3 (BZT) and 2% Mn doped Ba(Zr,Ti)O_3 (Mn:BZT) thin films grown on MgO substrate revealed the formation of twin-coupled domains on the epilayer by sharing their {111}/{110} planes as common planes. The structure evolution from epilayer to nanopillars is accomplished by alternatively introducing {111} and {110} twin boundaries, resulting in gradual shrinking or enlarging of the lateral size of the epitaxial grains/twin coupled nanopillars. The formations of twin domains, sharing planes and structure transition mechasim have been discussed in detail.

Eventually, the microstructures and layer interfaces of [Mn:BZT//Mn:BST]$_N$ multilayer films consisting of 2% Mn doped (Ba,Sr)TiO_3 (Mn:BST) and Mn:BZT layers on MgO (001) substrates with various deposition rates, deposition period numbers N were studied to provide an integral view of the formation of multilayer films in BTO system. All the [Mn:BZT//Mn:BST]$_N$ multilayer films present epitaxial quality and induced {111}/{110} twin-coupled domains initially formed at different film thickness/layers. The film/substrate interface has an important role for the formation of twin domains and the proportion of twin domain structures in the entire films. The layer interfaces between Mn:BST and Mn:BZT with period compression and extension strains were observed and discussed. The microstructure evolution and structure-related nano-mechanical properties of the multilayer films have been systematically investigated.

TABLE OF CONTENTS

LIST OF ILLUSTRATIONS

LIST OF TABLES

CHAPTER 1

INTRODUCTION

Perovskites belong to one of the largest oxide families. The interesting physical properties and important applications have been widely investigated in this system [1-3] since the last century. Among the large perovskite family, one of the most important groups is the ferroelectric oxide, which possesses extremely high values of dielectric constant and low dielectric loss, as well as good dielectric tunability. Ferroelectricity has been known since the 1920s and ferroelectricity in perovskite $BaTiO_3$ (BTO) was first discovered in the 1940s [4,5,6]. Both ferroelectricity and ferroelectric materials have been intensively studied for over half a century and a huge amount of literature has been published on both fundamentals and applications [7-13].

Historically, ferroelectric materials have been investigated and practically applied mainly in their bulk form. However, in the last 20-25 years, more and more applications call for a continual reduction in size, and require a thin film implementation. It generally requires a film layer thinner than 1 μm, which brings a lot of new challenges in manufacture and application. Some of the challenges come from the fact that the area of surfaces and interfaces is very large compared to the volume of the thin film, while in bulk materials their importance is often negligible. Due to the restricted geometry, grain boundaries, dislocations, inclusions and all other defects have entirely different behavior compared to the bulk materials, and therefore resulting the properties of thin films are markedly different from those of their bulk counterparts. Novel and effective deposition methods for thin films have been widely investigated during last decade. However, the deposition and film growth mechanisms and the produced microstructures that dedicate the resulting properties are still not very clear. In addition, the large stresses in the film, which could result from the film growth, thermal expansion coefficient

mismatches during integration and operation, could alter the Curie temperature and change the ferroelectric phase transitions. A comprehensive understanding of the growth mechanism and interface effect for the ferroelectric thin film is therefore essential to fully make use of the unique properties of these interesting materials.

1.1 Research Motivation

Perovskite epitaxial oxide thin films possess various novel properties, such as high dielectric constant; good ferroelectric properties; low dielectric loss, and are considered as one of the most important material families to meet challenges in advanced material research and nanotechnology. In the large perovskite oxide families, BTO is one of the most attractive functional materials in the electronics industry, due to its superior dielectic, ferroelectric, piezoelectric, and electro-optical properties [14-18]. BTO thin films have been considered as promising materials for many device applications such as ferroelectric random access memories, optical modulators and switches, waveguides and micro-electromechanical systems [19-21].

Partially substituted BTO thin films have been widely investigated since the dramatic change in physical properties, caused by small amount of substitution. Substituting Ba^{2+} by Sr^{2+} in $BaTiO_3$, $(Ba,Sr)TiO_3$ (BST) thin films has been found to possess high dielectric constant, relatively low dielectric loss tangent and large electric field tunability and have attracted considerable attention for dynamic random access memories (DRAM), capacitors, detectors, and tunable microwave applications [22,23].With Ti^{4+} partially substituted by Zr^{4+} in $BaTiO_3$, $Ba(Zr,Ti)O_3$ (BZT) films exhibit high tunability and low loss, which has shown the promise for tunable filters, phase shifter, antennas, etc [24,25].

It is well known that the fabrication of highly epitaxial oxide thin films requires a good understanding of the effects of growth conditions, material parameters and the film/substrate interfacial structures on the epitaxial behavior. And also the physical properties of epitaxial thin films are strongly determined by the microstructure including crystallographic structure,

corresponding orientation, domains, and boundaries of the epitaxial films, and the interface between the film and substrate. Especially, the lattice mismatch at the interface can largely control the epitaxial behavior and film microstructure [26-29], and significantly change the physical properties, such as Curie temperature, magnetic properties, and dielectric properties [30-32]. Thus, the partial substitutions and interface structure between the film and substrate have a critical influence on the microstructure of epitaxial thin films.

Therefore, in this dissertation, the study of interface effect and doping effect on barium titanate based ferroelectric oxide thin films become essential. The fundamental investigation and development of these effects on the film growth mechanism become more important to develop an understanding of the relationship between microstructure and properties for thin films.

1.2 Research Objectives

Interfacial structure and the lattice mismatch at the interface between the film and substrate play an important role in controlling epitaxial quality, microstructure and physical properties of the films. In this work, the microstructures, interfaces and self-organized growth evolution of barium titanate based perovskite thin films deposited on (001) single crystal MgO substrate using magnetron sputtering and pulse laser deposition techniques are primarily studied.

The overall objective of the present research is to develop a fundamental understanding of the growth mechanism and interface effect on the microstructure of perovskite barium titanate based thin films. The current research work has focused on the following specific objectives:

(i) To investigate the microstructure and growth condition of BTO thin film deposited on (001) MgO substrate using RF magnetron sputtering and provide fundamental knowledge for the growth of BTO based thin films.

(ii) To study the effect of the substrate surface local structures by investigating the two dimensional interfacial structure of highly epitaxial ferroelectric $Ba_{0.6}Sr_{0.4}TiO_3$

(BST) thin films on the vicinal (001) MgO substrate with different miscut angles of 1^o, 3^o, 5^o.

(iii) To study the composition/doping effect by comparing the film microstructures and interface structures of both BST and BZT epitaxial films.

(iv) To study the microstructure and interfaces of self-organized $BaZr_{0.2}Ti_{0.8}O_3$ (BZT20) and 2%Mn doped BZT (Mn:BZT) thin films on (001) MgO substrates.

(v) To explore and develop the growth mechanisms of: (a) BST films on miscut MgO substrate; (b) BZT/MgO and Mn:BZT/MgO films; c) Multilayer films with BST and BZT alternatively changing layers on (001) MgO substrate.

1.3 Dissertation Overview

This dissertation consists of eight chapters. An outline and summary of each chapter is summarized as follows.

Chapter 1, Introduction: This chapter introduces the motivation and objectives of this research work. It also provides a brief idea about ferroelectric perovskite oxide thin films and the necessity of studying, developing and designing the barium titanate based oxide thin films.

Chapter 2, Literature Review: This chapter provides a detailed background review on perovskite structure and the structure and properties of the barium titanate and barium titanate materials. The development of thin film deposition techniques and film growth mechanisms are also included in this chapter.

Chapter 3, Thin Film Synthesis and Characterization: This chapter describes the detail deposition system set up and deposition parameters for barium titanate and barium titanate based thin films. The characterization techniques in terms of high resolution transimission electron microscopy (HRTEM), X-ray diffraction (XRD), atomic force microscopy (AFM), X-ray photoelectron spectroscopy (XPS), Raman spectroscopy, Nanoindentation tests are explained.

Chapter 4, Growth and Microstructure of Epitaxial BTO Thin Films on MgO Using RF Magnetron Sputtering: This chapter focuses on the studies of epitaxial growth of BTO thin films and film/substrate interface structure induced film nanodomain structure.

Chapter 5, Microstructure and Interfaces of Epitaxial BST Films on Miscut (001) MgO Substrate: This chapter discusses the substrate miscut angle effect on the microstructure, two-dimensional interface structure, dielectric and mechanical properties of epitaxial BST films on miscut MgO substrate.

Chapter 6, Formation and Growth Mechanism of {111} and {110} Twin-coupled Domain Structures in BZT and Mn:BZT Thin Films: This chapter provides the studies on the formation of {111}/{110} twin-coupled domain structures and structure evolution mechanism in BZT and Mn:BZT thin films.

Chapter 7, Microstructure and Interfaces Study of 2% Mn doped BZT and 2% Mn doped BST Multilayer Films ($[Mn:BZT//Mn:BST]_N$): In this chapter, The effect of the deposition rate and deposition periods on the microstructure, structure transition and mechanical properties of $[Mn:BZT//Mn:BST]_N$ multilayer films are discussed.

Chapter 8, Conclusions and future work: In this chapter, the major results and discussions, and the directions for future work are included.

CHAPTER 2

LITERATURE REVIEW

2.1 Perovskite Structure

"Perovskite" was initially the name of the mineral perovskite $CaTiO_3$; however more generally represents the large structural family of compounds having crystal structures related to perovskite $CaTiO_3$. Ideally, the crystal structure of perovskites can be described as ABX_3. X is often oxygen but also other large ions such as F^- and Cl^- are possible. The ABX_3 perovskite structure stands out by a wide margin compared with other structures, since it can produce an incredibly wide array of phases with totally different functions with various chemical manipulations, as shown in Figure 2.1.

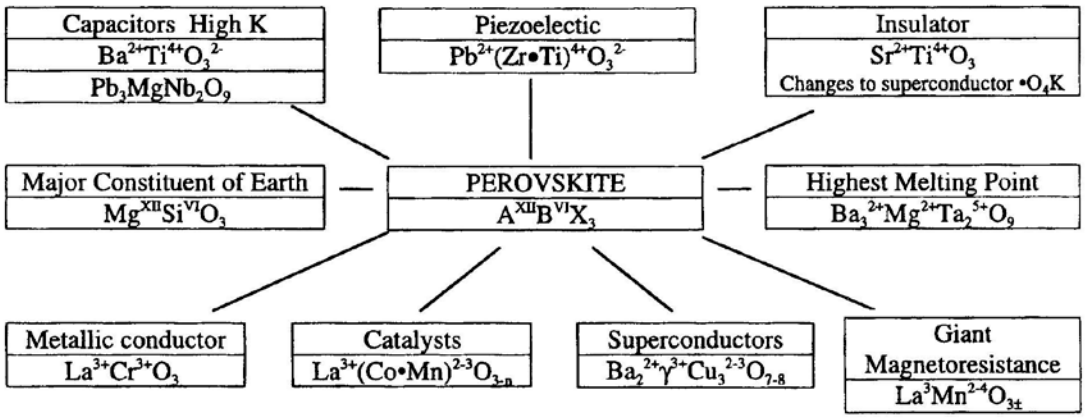

Figure 2.1 Perovskite-the maximum multifunctional structure [33].

In this family, the perovskite group of oxides with the chemical formula of ABO_3 is probably the best studied group of oxides. It can be visualized as a simple cubic unit cell with large cations A located at eight corners, smaller cations B sitting in the body center, and oxygen atoms in the face center, as shown in Figure 2.2 (a). The resulting perovskite structure can also be described as consisting of corner sharing $[BO_6]$ octahedra with the A cation occupying the

12-fold coordination site formed in the middle of the cube of eight such octahedral, as shown in Figure 2.2 (b) [34,35].

The ideal cubic perovskite structure is not very common and also the mineral perovskite itself is slightly distorted. The interest in compounds belonging to this family of crystal structures arise in the large and ever surprising variety of properties exhibited and the flexibility to accommodate almost all of the elements in the periodic system. The first structural study on perovskites we can find from literature, were conducted by Goldschmidt *et al* in the 1920s that formed the basis for further exploration of the perovskite family of oxides [36]. The distortion of the [BO_6] octahedra due to temperature changes or stress effects may cause the transition from cubic structure to tetragonal, rhombohedral or orthorhombic structures. Distorted perovskites have reduced symmetry, which is important for their magnetic and electric properties. Due to these properties, perovskites have great industrial importance and huge potential for cutting edge technology, especially the ferroelectric pseudo-cubic barium titanate, $BaTiO_3$.

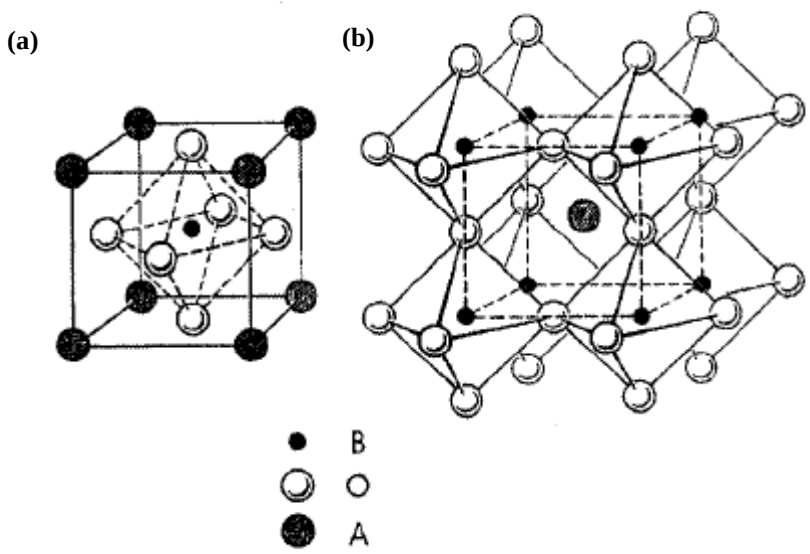

Figure 2.2 ABO_3 perovskite crystal structure [33].

In the cubic ABO_3 perovskite structure, the A atoms are in Wyckoff position 1b, ½,½,½; the B atoms in 1a, 0,0,0; and the X atoms in 3d ½,0,0; 0,½,0; 0,0,½, all special positions. If the

position of the A^{2+} ion is vacant the remaining framework is that of the ReO_3 type. Partial occupation of the A position occurs in the cubic tungsten bronzes A_xWO_3 (A = alkali metal, $0.3 \leq x \leq 0.93$). The ReO_3 structure type can be converted to a more dense packing by rotating the octahedra until a hexagonal close packing is obtained of the RhF_3 type. The void in the center has then an octahedral surrounding. If this octahedral hole is occupied, then the structure of FeTiO3 is formed. The perovskite structure is known to be very flexible and the A and B ions can be varied leading to the large number of known compounds with perovskite or related structures. Most perovskites are distorted and do not have the ideal cubic structure.

Three main factors are identified as being the possible reason for the distortion in perovskite structure: size effects of atoms, deviations from ideal composition and the Jahn-Teller effect [37]. It is hard to distinguish that a distortion of a certain perovskite oxide can be assigned to a single effect. In most cases, several factors could act together on the structure.

(1) Size Effects

In the ideal cubic case, the cell axis, *a*, is geometrically related to the ionic radii (r_A, r_B, and r_O) as described in equation (1):

$$a = \sqrt{2}(r_A + r_O) = 2(r_B + r_O) \tag{2.1}$$

The ratio of the two expressions for the cell length is called the Goldschmidt's tolerance factor *t*. Based on the ionic radii (simply ionic bonding is assumed), *t* can be used to estimate the degree of distortion. However, when the compound with a high degree of ionic bonding is considerated, another equation is addressed as equation (2):

$$t = \frac{(r_A + r_O)}{\sqrt{2}(r_B + r_O)} \tag{2.2}$$

If the A ion is smaller than the ideal value, then *t* becomes smaller than 1. As a result, the $[BO_6]$ octahedra will tilt in order to fill the space. However, in some cases the distortion of the cubic structure occurs if $0.89 < t < 1$ [38, 39]. One ideal example is cubic perovskite $SrTiO_3$, it has t=1.00, r_A=1.44 Å, r_B=0.605 Å, and r_O=1.40 Å. Lower values of *t* will reduce the symmetry

of the crystal structure. For example $GdFeO_3$ with t = 0.81 is orthorhombic (r_A = 1.107 Å and r_B = 0.78 Å) [40]. Also, the mineral perovskite, $CaTiO_3$, has the structure with t less than 0.8, and therefore, the ilmenite structure is more stable for itself [40]

On the other hand if t is larger than 1, when a large A or a small B ion is referred, then the hexagonal structure for the perovskites is more stable, *e.g.* $BaNiO_3$ type structures. The t value for $BaNiO_3$ is 1.13 (r_A = 1.61 Å and r_B = 0.48 Å). In this case the closest packing layers are stacked in a hexagonal manner in contrast to the cubic one in $SrTiO_3$ structure, leading to face sharing of the [NiO_6] octahedra. However, since perovskites are not truly ionic compounds and since the t values also depend on what values are taken for the ionic radii, the tolerance factor only can give a rough estimation for crystal structure.

(2) Composition Effects

Perovskite lattice could accommodate a great variety of metallic ions if the size and valence are compatible. The solid solution limit is significantly lower with ions of a different valence from the one replaced, presumably because of the excessive lattice vacancies that result. In Perovskites, because of the packing density, the presence of interstitial ions appears unlikely but substantial concentrations of A-site vacancies can be tolerated. There is not obvious evidence of the existence of any significant concentration of vacancies in B position of any perovskite [41, 42]. Compositions with stoichiometry that might yield a perovskite with B-site vacancies crystallize instead as a mixture of perovskite and nonperovskite phases.

An example is the family of compounds $SrFeO_x$ ($2.5 \leq x \leq 3$). The valency of the Fe ions can be changed by heating a sample in either an oxidizing or a reducing environment. As a result the oxygen content can vary in between 2.5 and 3. For the $SrFeO_{2.875}$ some Fe ions can be assigned to the oxidation state 3+ and 4+, therefore FeO_5 square pyramids are formed.

(3) Jahn-Teller Effects

The Jahn-Teller effects, sometimes also known as Jahn-Teller distortion, or the Jahn-Teller theorem. It is named after Hermann Arthur Jahn and Edward Teller, who proved that non-

linear spatially degenerate molecules cannot be stable [43]. The peculiarity of the Jahn-Teller interaction is that there must be a multiplicity of electronic states interacting with one or more normal modes of vibration, and the Jahn-Teller effect describes that for almost any set of degenerate electronic states associated with a molecular configuration, there will exist some symmetry-breaking interaction in which molecular distortion is associated with the removal of the electronic degeneracy. That is because the distortion can lower the overall energy of the complex.

In some perovskites the distortion of the structure can be assigned to Jahn – Teller active ions at the B position. For example, in $LnMnO_3$ (Ln = La, Pr or Nb) with Mn^{3+} ions the 3d4 electrons divide up into 3 t_g and 1 e_g electron. The odd number of electrons in the e_g orbital causes an elongation of the [MnO_6] octahedron.

As a result, the perovskite structure has a wide range of substitution of cations A and B, as well as the anions. The principles of substitution must maintain charge balance and keep sizes within the range for particular coordination number. Since the variation of ionic size and composition, which result in the distortion of the structure and the reduction of symmetry, have tremendous effects on the physical properties of perovskite structure materials.

2.2 Barium Titanate: Structure and Physical Properties

Barium titanate is used in a variety of electronic applications due to its excellent ferroelectric properties with high dielectric constant, low dielectric loss; and its chemical and mechanical stability. Barium titanate is one of the most investigated ferroelectric materials due to its history as the first oxide ferroelectric, simple crystallographic structure and wide spread use in the electronic, optical and communications industry. The current technology advancement imposes an ever-increasing demand of development of new ferroelectric materials and improved materials performance. Barium titanate and barium titanate based materials have become one of the most promising ferroelectric materials to meet all those practical demands.

2.2.1. Crystal Structure and Phase Transition

Barium titanate, $BaTiO_3$, the first ceramic material from which ferroelectric behavior was observed, has a typical perovskite (ABO_3) structure. It has been one of the best Pb-free ferroelectric materials for microelectronic devices applications in perovskite oxide families and also an ideal model for discussing of the ferroelectricity and spontaneous polarization from the point of view of crystal structure. The idealized cubic structure can be realized in $BaTiO_3$ above the Curie temperature. Unlike many other oxide crystals, oxygen anions in perovskite do not form a close packing structure. Barium ions (A ions), which are large in size (~158 pm), occupy the corner sites, titanate ions (B ions), which are small in size (~60 pm), locate in the centers of the cube (the oxygen octahedral) and oxygen anions are on the face-centers.

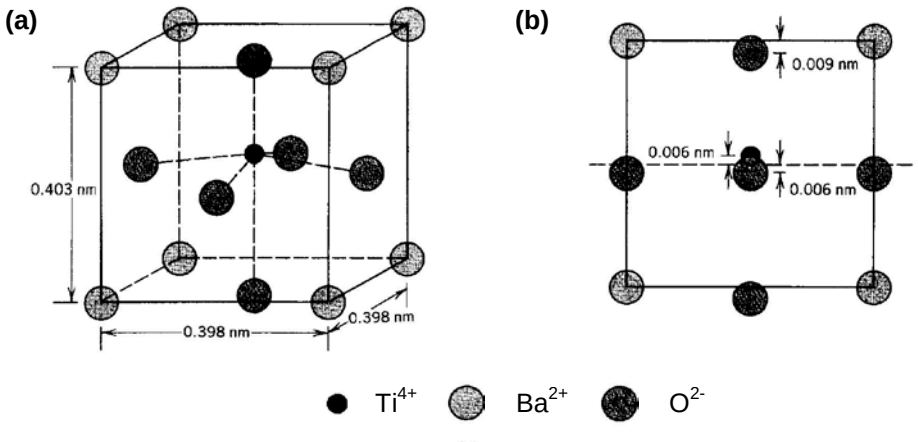

Figure 2.3 (a) A barium titanate ($BaTiO_3$) unit cell and (b) {100} projection showing the displacement of Ti^{4+} and O^{2-} ions from the center of the face [46].

At the Curie temperature, the crystal undergoes a phase transition which is also called displacement phase transition [33, 34]. Therefore, the crystal structure of $BaTiO_3$ is also temperature and stress dependent, as shown in Figure 2.3. Above the Curie temperature T_c, ~133°C, depending on the impurity content [44], the cubic structure ***Pm3m*** is stable with a=4.009 Å [45]. When cooling through the Curie temperature between 130°C and 0°C, the tetragonal structure (***P4mm***, a=3.992 Å, c=4.035 Å) is formed with octahedron distortion and

positive ion shifting off the center position, as shown in Figure 2.3(a) [46]. Associated with this distortion is a displacement of the titanium and oxygen atoms, as shown in Figure 2.3(b).The formation of the tetragonal structure makes the unit cells turn out to be permanently polarized, which leads to spontaneous polarization along the c-axis [4, 45]. Since there are six equivalent <100> axes in the cubic phase, upon cooling the polarization can arise parallel to any one of these six equivalent directions. It is the ability to reorient the spontaneous polarization with an external electric field that makes this ferroelectric material so interesting to study.

Figure 2.4 shows the distortion of the $BaTiO_3$ unit cell with temperature over a sequence of transitions [47]. The temperature of the phase transitions could be shifted a little because of the purity of barium titanate. As shown in Figure 2.4, upon further cooling below 0°C, the unit cell distorts again and the tetragonal structure changes to orthorhombic (Amm2) structure by elongating along the face-diagonal direction [45]. There are 12 equivalent <110> directions in the original cubic phase, which results in 12 possible polar directions in the orthorhombic phase. This phase is stable from approximately 0~5°C to -90°C. Below -90°C, the unit cell undergoes another distortion along the body diagonal, resulting in a rhombohedral (R3m) symmetry. There are 8 equivalent polar directions along the original cubic <111> direction in this phase. Polar axis differences due to the distortions of a perovskite crystal are summarized in Table 2.1 [48].

Table 2.1 Polar axis summary due to distortions in the perovskite structure [48].

Crystal Symmetry	Polar axis	Number of equivalent directions
Tetragonal	<100>	6
Orthorhombic	<110>	12
Rhombohedral	<111>	8

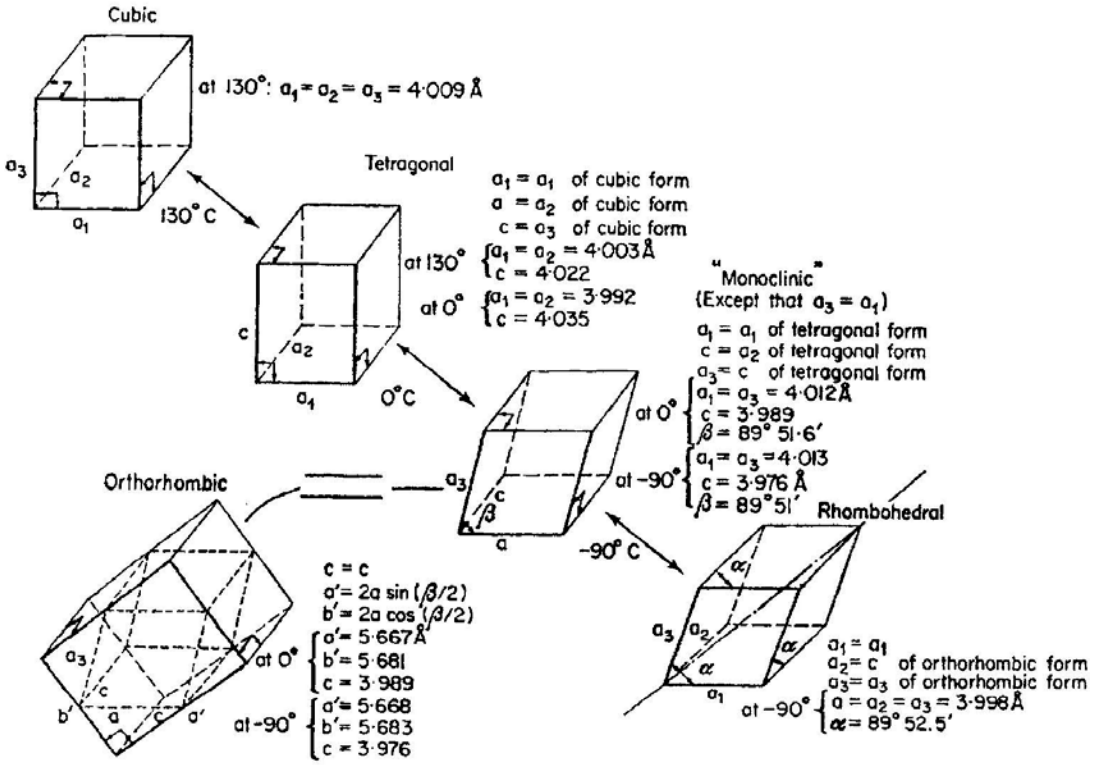

Figure 2.4 Distortion of $BaTiO_3$ unit cell showing temperature dependence [47].

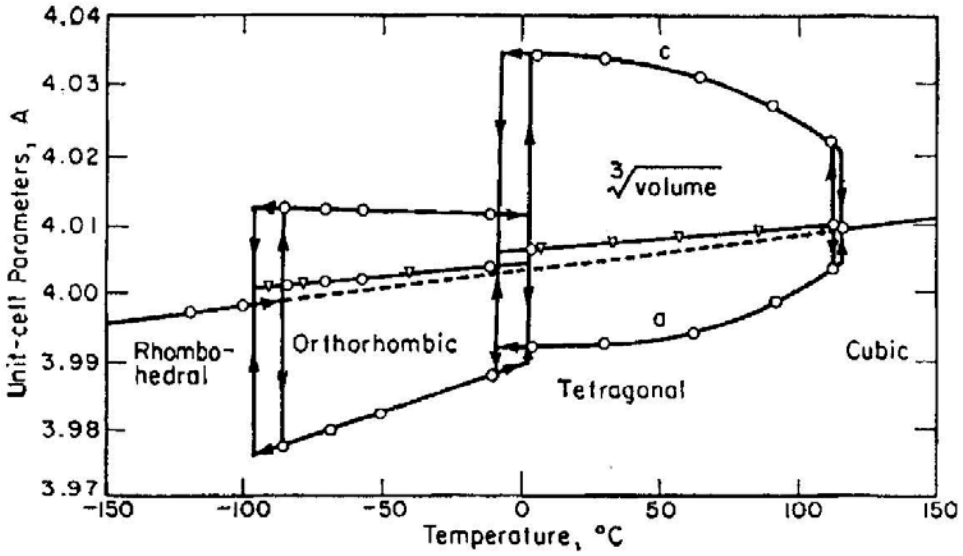

Figure 2.5 Lattice constants of $BaTiO_3$ as a function of temperature [45].

Figure 2.5 shows the variation of $BaTiO_3$ lattice parameters at different cooling temperatures. Three phase transition ranges are clearly seen in the figure. The exact transition temperatures and amount of distortion are a function of cooling rate, residual stresses, and purity of the material [48]. The size ratio of the c-axis to a-axis for pure $BaTiO_3$ is approximately 1.01 at room temperature, and therefore, the spontaneous strain for $BaTiO_3$ is approximately 1% at room temperature.

2.2.2. Ferroelectricity

Ferroelectricity is characterized by a spontaneous reorientable electric dipole in crystal. The name of ferroelectricity stems from the hysteretic nature of dielectric displacement with applied electric field, which is comparable to the magnetization hysteresis with applied magnetic field in ferromagnets. In the long history, the word of ferroelectricity has been selected and once to convince that iron is a necessary composition to the materials displaying the ferroelectric phenomenon [49].

The first report of the ferroelectric phenomenon was published in 1921 by Valasek on single crystal Rochelle salt, also called Seignette salt (sodium potassium tartrate tetrahydrate, $NaKC_4$-H_4O_6•$4H_2O$) [50]. During a decade, the Rochelle salt has been used for scientific study as the earliest ferroelectric material until the discovery of ferroelectricity in potassium dihydrogen phosphate (KH_2PO_4) by Busch and Scherrer in 1935 [51]. However, the usage of the Rochelle salt or potassium dihydrogen phosphate is limited because of their high water solubility. A new world was opened with the significant discovery of ferroelectricity in barium titanate ($BaTiO_3$), which is much more chemically stable, in 1945 and 1946, respectively, in Russia and United States. Vul and Goldman, the group in Russian, first reported a non-linear response in the permittivity with applied field and an apparent peak in permittivity at a phase transition for barium titanate [52]. They also indicated that the crystal structure of the alkaline-earth titanates was not always the cubic perovskite structure at room temperature [53]. They also found (1) an unusually large dielectric constant, (2) this high dielectric constant value was

due to ferroelectricity, and (3) the orientation of the dipoles with a process called poling [48]. In the United States, Thurnauer and Deaderick synthesized ceramics with a dielectric constant of 1100 [54]. Wainer reported the temperature dependence of permittivity and the effects of compositional modification in 1946 [55]. There were also other independent discoveries in the 1940s by Ogawa in Japan and by Coursey and Brand in England [53, 56]. A further significant step was the discovery of the poling process. Gray showed that a sufficiently high voltage can reverse the dipole moments of a ferroelectric material [57]. It was followed by single crystal investigations and then, thin film studies until the 21st century. Today, ferroelectric materials have been preferred in many application areas including high density capacitor, piezoelectric transducers, positive temperature coefficient resistors, and microwave filters with their interesting dielectric, piezoelectric, thermal, and optical properties.

There are two important criteria for ferroelectricity: one is the presence of spontaneous polarization, the other is the reversibility of this polarization with an applied electric field [58]. The polarization characteristic of ferroelectrics is described using polarization-electric field (P-E) hysteresis loop [59, 60]. This loop is the evidence showing that randomly oriented ferroelectric domains will start switching directions in response to the electric field and eventually aligned with the direction of electric field as closely as the crystal permits, when the externally applied electric field is sufficiently large. This process is called poling. The loop indicates the spontaneous polarization can be reoriented among the preferred crystallographic orientations as well. The hysteresis in the P-E relation results from the stability of the polarization along the preferred crystallographic orientations and its resistance to reorientation. Figure 2.6 shows a typical hysteresis loop for a ferroelectric ceramic. Several distinctive characteristics related to P-E loop can be described as in Figure 2.6. The saturation polarization (P_s), defined as an extrapolated value from the high field linear portion, refers to the total polarization attributable to the reversal of the spontaneous polarization. The remanent polarization (P_r) refers to the amount of polarization remaining after removal of the applied electric field. P_r can reflect the

alignment degree of the dipole moments in a ferroelectric. In an ideal single crystal, the hysteresis loop would have a rectangular central region with $P_r=P_s$. The coercive field (E_c) refers to the field value required to reverse the direction of the polarization. Nevertheless, this is not an absolute value. If a lower electric field is applied for a sufficient amount of time, the polarization will eventually switch [61]. The shape and the position of the hysteresis loop could give additional information about the material structure. For example, an off-centered loop indicates an internal field (unswitchable charge) which could be caused by space charge or aging [62]. Besides, the magnitude of the coercive field indicates the grain size or domain size (usually larger coercive field means smaller grain size). And also the loop squareness and sharpness can give general material quality and resistivity information [63].

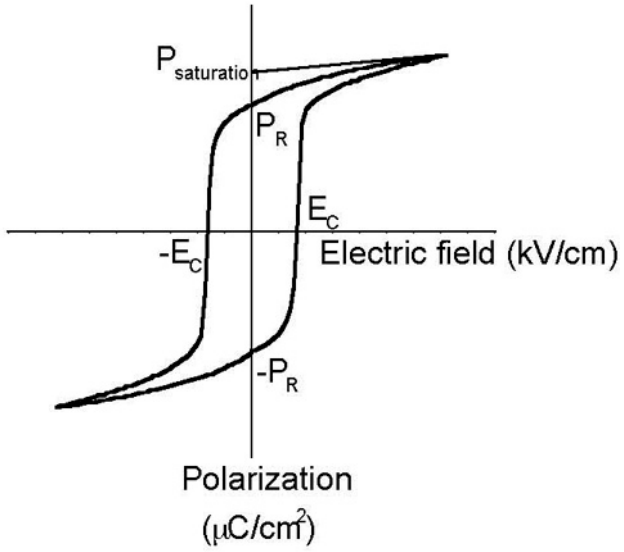

Figure 2.6 Typical ferroelectric hysteresis loop for a ferroelectric [35].

Another precondition for polarization is that the materials should have ferroelectric phase which arises from the structural transition from a high symmetry phase to a low symmetry phase. As mentioned above, the temperature at which transition occurs is known as Curie temperature. This temperature is defined by Curie-Weiss law,

$$\varepsilon_r = \varepsilon_o + \frac{C}{T - T_o} \tag{2.3}$$

Where ε_r is the relative permittivity, ε_o is the permittivity of vacuum, C is the Curie constant, and T_o is the Curie temperature. Above the transition temperature, the crystal is in the paraelectric state with no net dipole in the unit cell. Below this critical temperature, the material undergoes a phase transition into the ferroelectric state, which is a polar state having spontaneous polarization with applied electric field.

In ferroelectric crystals, the electric dipoles can only have uniform alignment in certain regions, while in other regions of the crystal spontaneous polarization exists in different direction. Such regions with uniform polarization in the crystal are called ferroelectric domains. The interface between two domains is called the domain wall [10]. Domain structures in ferroelectric materials are formed in an attempt to minimize their free energy. Without the external electric field, each domain has a random direction polarization (a net polarization), and the total orientation of all the domains will sum to zero. The polarization of the domains will be potentially reoriented and aligned uniformly by an applied electric field. Domain Walls separate domain states and have a thickness that is dependent on wall orientation and material itself. The boundary between "up" and "down" dipole orientations is called a 180^o domain wall, as shown in Figure 2.7(a). Such domain walls form intrinsically to minimize the electrostatic energy. 90^o domain wall is the wall which separates the perpendicularly oriented domains, as shown in Figure 2.7(b). Such domain walls form primarily associated with entropic and strain relief reasons. The types of domain walls in a ferroelectric crystal depend on the symmetry. The 180^o and 90^o domain walls can occur in a tetragonal perovskite, however the 180^o, 71^o, and 109^o domain walls are usually found in the rhombohedral phase [64].

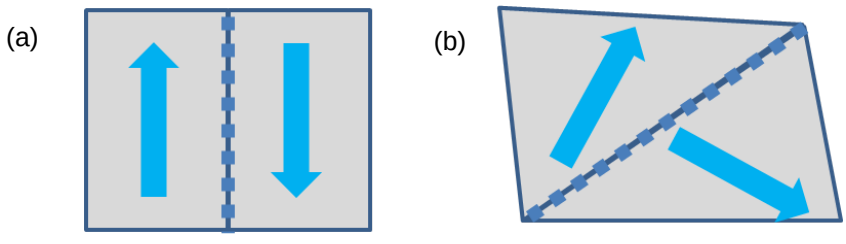

Figure 2.7 Schematic illustrations of (a) 180^o and (b) 90^o domain walls.

From all the ferroelectrics known to date, one of the most extensively studied and used is barium titanate ($BaTiO_3$). Barium titanate is a well known ferroelectric material of the perovskite family with a tetragonal crystal structure at room temperature. As $BaTiO_3$ goes through its Curie temperature, a spontaneous polarization is developed. The value of the spontaneous polarization at room temperature is 26 μV/cm as shown in Figure 2.8, which is showing the spontaneous polarization of tetragonal $BaTiO_3$ as a function of temperature [65]. The fact that $BaTiO_3$ has high ferroelectric and dielectric properties, and is easy to be fabricated into thin film form using current techniques, and stable at room temperature, makes $BaTiO_3$ a good choice for this work.

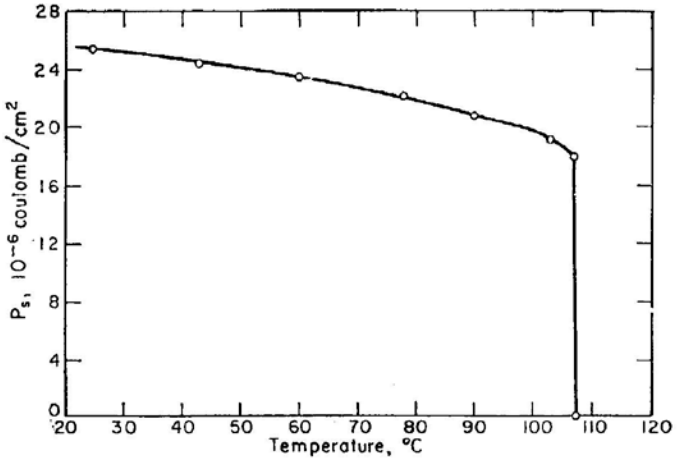

Figure 2.8 Spontaneous polarization of tetragonal $BaTiO_3$ as a function of temperature [65].

2.2.3. Dielectric Properties

When considering the dielectric properties for a ferroelectric crystal, there are several parameters need to be referred to, such as the dielectric permittivity (dielectric constant), tenability, dielectric loss, etc. The concept of these parameters will be interpreted in detail as follows.

The dielectric constant or permittivity, ε, refers to a material's ability to permit an internal electric field by becoming locally polarized. It is used to define the ability of the material

to store charge and relates to the amount of electric polarization of a material under the action of electric fields and is given as

$$\varepsilon = \varepsilon_o \varepsilon_r = \partial P / \partial E \tag{2.4}$$

where ε_o is the permittivity of free space (8.854 pF/m) and ε_r is the relative permittivity of the material. It can be observed from the equation that the permittivity value becomes maximum when there is no applied field and decreases when the applied field is increased. This behavior can be observed experimentally by measuring capacitance vs. voltage (C-V) relationship. Dielectric permittivity can be calculated from capacitance using the equation below:

$$\varepsilon_r = \frac{C}{C_o} \tag{2.5}$$

where C_o is measured under vacuum between a capacitor and the capacitance C is measured using the same capacitor and distance between its plates with a dielectric between the plates. The typical curve of the dielectric permittivity as a function of the applied field (ε_r vs. E) for a ferroelectric and a paraelectric phase is shown in Figure 2.9 [66]. It shows that below the Curie temperature, the material exhibits a “butterfly-loop” behavior characteristic of ferroelectric hysteresis. The initial increase in the permittivity with applied field is due to the increased domain wall movement which is locked-in by structural defects at the zero bias [67]. The maximum permittivity is obtained when most of the domains are switched under the applied field and the domain wall movement contribution to the polarization is maximum. After the maximum permittivity is reached, it starts to decrease with higher electron field due to two reasons. One is the number of domains and the domain walls decrease as they align with the applied field. The other is the oscillation of residual domain walls is inhibited by the higher electron field. The only contributions to the permittivity at high fields become the intrinsic polarization mechanism (e.g. ionic and electronic polarization) [68].

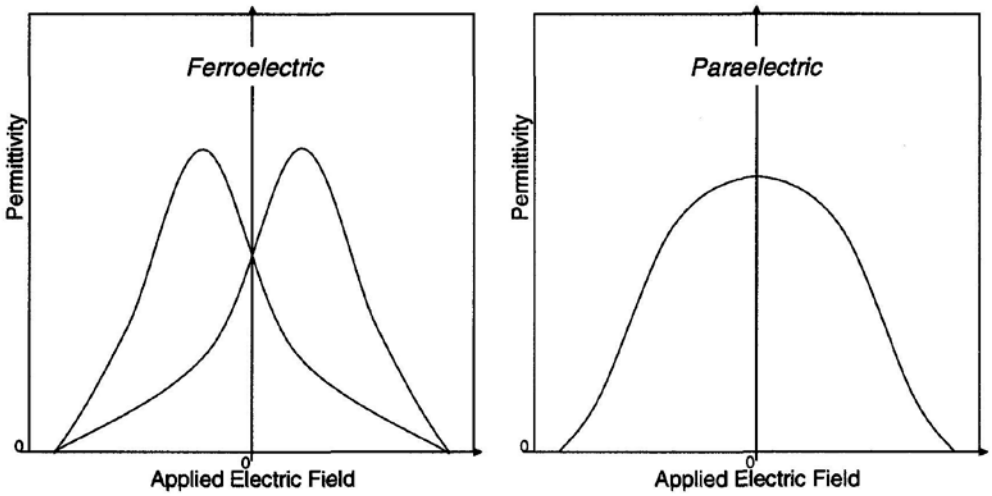

Figure 2.9 Schematic permittivity plots as a function of applied electric field for a ferroelectric material in the ferroelectric and paraelectric phases [66].

In the paraelectric state, as shown in Figure 2.9, there is not any hysteresis. A maximum permittivity is observed, even though there are no domains or domain wall contributions. At temperatures not much higher than the transition temperature, the restoring forces against the poling of the crystal are still very weak, therefore, the transient dipoles can interact with the applied field resulting in a high permittivity.

Tunability, *n* is used to define the permittivity dependence on the applied DC field and is given as:

$$n = \frac{\varepsilon_{\max}}{\varepsilon_{\min}} \tag{2.6}$$

where ε_{max} is the permittivity at zero field and ε_{min} is the permittivity at saturation fields. The relative tunability, which is the percentage change of the permittivity from its maximum value to its minimum value, is given by,

$$n_r(\%) = \frac{\varepsilon_{\max} - \varepsilon_{\min}}{\varepsilon_{\max}} \times 100\% \tag{2.7}$$

Generally, the higher permittivity gives the higher tunability [68, 69]. Tunability can be an appropriate measure to compare the level of extrinsic response to the intrinsic response of

the material and provides more information about the material quality, such as phase purity, homogeneity, microstructural properties (e.g. grain size, defects), and crystal quality. Overall, the changes in permittivity with the applied field make these ferroelectric materials very attractive for high frequency voltage-tunable devices applications, such as resonators, phase-shifters and microwave filters [69, 70-72].

Dielectric loss, ε", as shown in the equation below, is an important parameter for the usefulness of a dielectric as an insulator material. It is derived from the relative permittivity and expressed as

$$\varepsilon_r = \varepsilon' - i\varepsilon'' \tag{2.8}$$

In an ideal material, if an electric field is applied on a capacitor with an oscillating frequency, then, there is a lag of 90^o in the dielectric response of the material. However, in a real material, the response deviates from some lost energy, and results in a dielectric loss, as shown in Figure 2.10 [73]. The dielectric loss can then be expressed in another term of a phase angle between the polarizing field and the response of the material, which is called loss tangent, or dissipation factor:

$$\tan\delta = \frac{\varepsilon''}{\varepsilon'} \tag{2.9}$$

The dielectric losses in ferroelectric materials can be distinguished as extrinsic and intrinsic loss contributions. The extrinsic losses are poorly understood, as they are disorder related. One interpretation is that the main extrinsic contribution to the ferroelectric loss is the domain wall movement [64, 74]. Domain wall movement includes interactions with the surroundings which could cause internal friction for energy loss. Their origins stem from defects in the crystal, such as vacancies, interstitials, local polar regions and charged impurities [76-78]. Intrinsic losses are due to the interaction of the ac electric field and are inherent to the material. The intrinsic mechanisms were developed and many models were derived to explain the intrinsic loss origins [79-85]. Dielectric loss is a critical parameter in microwave applications

which require a low dielectric loss and high dielectric tunability. For this purpose it is desirable to reduce the dielectric constant and particularly to get a very small loss angle. Many efforts have been made to reduce the dielectric loss, and any approach at reducing the loss in a dielectric thin film is focusing on reducing the extrinsic loss.

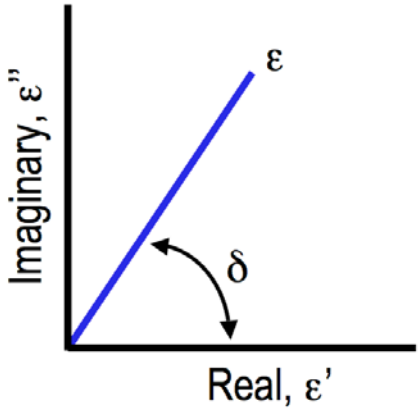

Figure 2.10 Schematic representation of permittivity separated by a phase angle [73].

For the dielectric properties of $BaTiO_3$, it is important to note that there is no absolute value for the permittivity and loss tangent, since even the slightest chemical or physical difference could have a dramatic effect on the Curie temperature and dielectric properties. Above the Curie temperature, $BaTiO_3$ is in the paraelectric state and the dielectric constant obeys the Curie-Weiss law. Below the Curie temperature, the permittivity decreases with the temperature decreasing. The permittivity dependence on the temperature for a single crystal $BaTiO_3$ is shown in Figure 2.11 [86]. At room temperature, it shows that the permittivity along the a-axis is ~4000, and along the c-axis is ~160, since the body centered Ti^{4+} has more freedom along the a-axis than c-axis. For a polycrystalline $BaTiO_3$, the permittivity value should be in between those single crystal values due to the random orientation of the grains. In the tetragonal phase, the permittivity of $BaTiO_3$ shows a frequency dependence with a drop at around 10 GHz [87]. This frequency corresponds to the piezoelectric resonance which is also accompanied by a high dielectric loss. In the cubic phase, piezoelectric resonance cannot occur, since the structure is centrosymmetric.

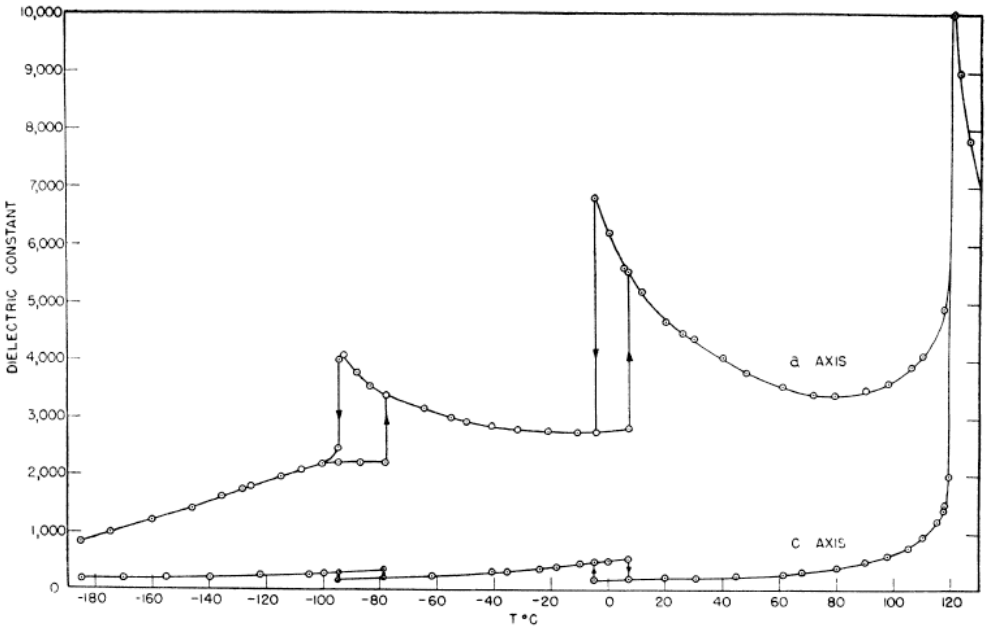

Figure 2.11 Dielectric constants ε_a and ε_c for single crystal $BaTiO_3$ [86].

2.2.4. Piezoelectricity

The piezoelectric effect is a phenomenon which relates mechanical strain to electric energy. This phenomenon was first discovered in 1880 by Jacques and Pierre Curie. They successfully observed the transitions between the mechanical strain energy and electric energy in certain materials [48]. The direct and converse piezoelectric phenomena are schematically shown in Figure 2.12 [88]. The equations [48] to describe piezoelectric response are also given below:

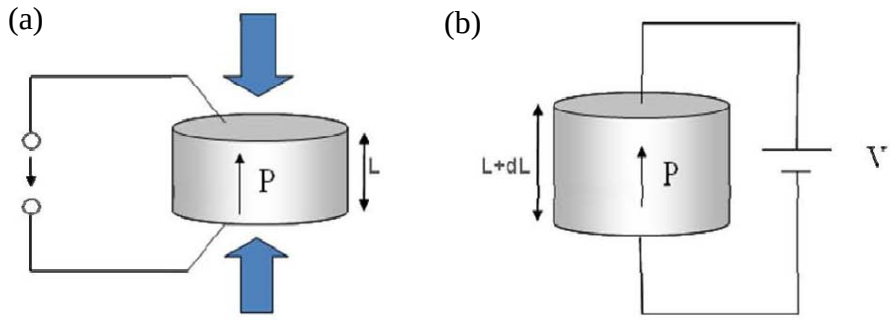

Figure 2.12 Schematic showing the (a) direct and (b) converse piezoelectric response [88].

$$\frac{\partial D_i}{\partial X_{jk}} = d_{ijk}^{E}, \frac{\partial x_{jk}}{\partial E_i} = d_{ijk}^{T} \quad (2.10)$$

where D is the dielectric displacement, X is the stress, x is the strain, E is the electric field, and d is the piezoelectric coefficient.

Almost all ferroelectric materials are also piezoelectric. Piezoelectricity in ferroelectric materials is composed of an intrinsic contribution, the distortion of the lattice due to the applied field, and an extrinsic contribution due to domain walls, particularly 90° domain wall motion [66]. The piezoelectric coefficient is therefore anisotropic and dependent on the direction of applied electric field and the measured strain. Many efforts have been made to study the piezoelectric phenomena in the past years. Du et al found the anisotropic piezoelectricity in [001] poled single crystal $BaTiO_3$ [89]. They calculated the d_{33} and coupling coefficient k_{33} for a [001] single crystal at angles from 0^o~60^o away from the poled axis and found the maxima value for d_{33} and k_{33} that were 47^o and 52^o away from [001] direction, respectively [89]. Thus, there are specific angles away from the poled direction for the tetragonal and orthorhombic crystal structures in BaTiO3 that provide optimized piezoelectric response. Some additional works were developed to enhance the piezoelectric performance by domain engineering [90]. Overall, piezoelectricity is the potential property that makes many ferroelectric perovskites, such as BTO, PZT, very useful in mechanical sensors and actuators, especially in MEMS devices [91].

2.2.5. Phase Diagram and Compositional Modification

Phase equilibria in the BaO-TiO_2 system have been of interest since the discoveries of the high dielectric constant and ferroelectricity in $BaTiO_3$ [92, 93]. After that more attention has been focused on the synthesis and phase stability of other compounds in this system for the applications with low dielectric loss and high tunability. Detailed understanding of the phase diagram is important on developing techniques for fabricating crystals with optimized properties. In 1951, the first BaO-TiO_2 phase relations in this system were established by Statton, who reported two compounds, $BaTi_2O_5$ and $BaTi_4O_9$ [94]. However, the resulting data did not

establish the phase relations in much detail and the diagram was not valid in terms of the Gibbs phase rule. Later in 1955, Rase and Roy reported a more detailed phase diagram for the entire BaO-TiO_2 system by clarifying several reactions [95]. Four compounds, $BaTiO_3$; $BaTi_2O_5$; $BaTi_3O_7$ and $BaTi_4O_9$, were identified in the region of 50 to 100 mol% TiO_2.

Subsequently, in 1974, O' Bryan and Thomson [96], and Negas et al. [97] modified the BaO-TiO_2 phase diagram with some difference on the decomposition temperatures. In 1986, Ritter further revised the phase diagram on TiO_2-rich side in the range of low temperature [98]. In 1991, Kirby and Wechsler developed a high temperature phase diagram on the TiO_2-rich side [99]. In 2000, Lu and Jin developed the thermodynamic parameters of all the stable phases in the BaO-TiO_2 system [100]. However, the solubility limits of BaO and TiO_2 in $BaTiO_3$ are not well defined.

Recently in 2007, Lee et al. published a modified phase diagram for the BaO-TiO_2 system, as shown in Figure 2.13, in which the solubility limits for the Ba and Ti rich side were estimated and nonstoichiometric $BaTiO_3$ and compounds around stoichiometric $BaTiO_3$ were revised [101]. The authors used a new approach, phase transition temperature variation, to investigate the solubility limits. They found that while the solubility limits are greater for the Ti-rich side, the solubility limits in the Ba-rich side is much larger than previously reported. It opens the possibility that both BaO and TiO_2 partial Schottky defect reactions exist.

Thus, the BaO-TiO_2 phase diagram, containing a number of phases and compounds, has been proven to be very useful for electroceramic applications. One of the most important phase, perovskite $BaTiO_3$, can be a good capacitor and positive temperature coefficient resistors [101]. The ceramics containing $Ba_2Ti_9O_{20}$ or $BaTi_4O_9$ have been used as microwave dielectric resonator filters [102, 103]. The metastable compound $BaTi_5O_{11}$ has a potential for a dielectric material [98]. The compound $BaTi_2O_5$ shows promise for lead-free high phase transition temperature ferroelectric materials [104, 105].

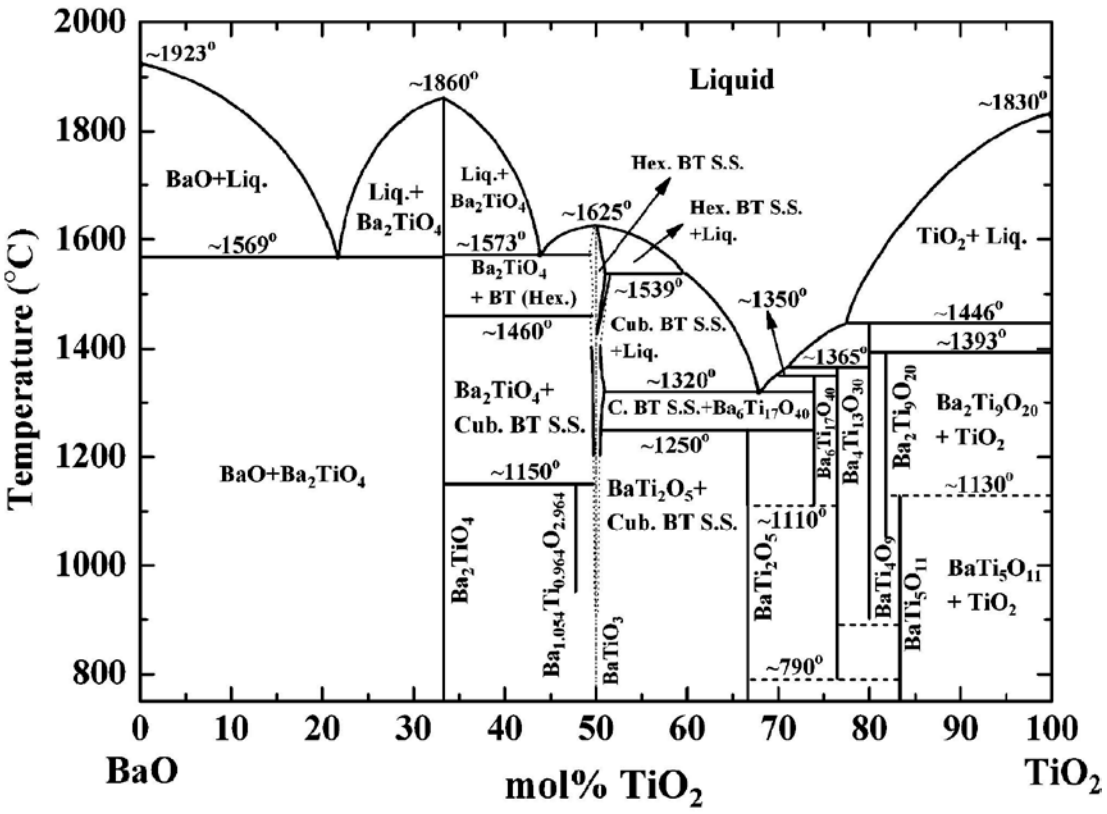

Figure 2.13 Modified phase diagram of the BaO-TiO_2 system under ambient air conditions [101].

Barium titanate, $BaTiO_3$, is one of the most widely used ferroelectrics for capacitor applications. Pure barium titanate however, strongly suffers from temperature dependent capacitance as a result from its sharp phase transitions. These sharp phase transitions and the existence of the ferroelectric phase at room temperature limits the usefulness of the pure material in practical applications. The nature, phase transition temperatures and dielectric characteristics of $BaTiO_3$ are strongly dependent on the stoichiometry and composition and therefore can be modified by partial substitution of minor amounts of foreign ions in either A-site (Ba ion) or B-site (Ti ion). The substitutions are commonly used to change Curie temperature and lower the phase transition temperatures of orthorhombic/tetragonal and rhombohedral/orthorhombic. The substitution can be isovalent in the A-site such as Sr^{+2} or Ca^{+2}, Pb^{+2} or in the B-site such as Zr^{+4}, Sn^{+4} or Hf^{+4}. A-site doping cations usually have the same

valence as Ba^{2+} and could cause the Curie temperature Tc of BTO to either decrease (Sr substitution) or increase (Pb substitution), without any significant broadening of phase transition. However, since the B-site doping is always associated with the off-center displacement of Ti^{4+} in TiO_6 octahedra, the substitution at B-site often results in a broadening of phase transition at T_c. Ions with the proper ionic size but unmatched valence can also enter the lattice in small concentrations having a strong effect on the dielectric properties. The effect of various dopants on the three phase transitions of $BaTiO_3$ is shown in Figure 2.14 [48, 106].

Since interstitial defects are not common in perovskite oxide structure, vacancies are the major defects which can be formed as the compensation of the substitutions [107]. So the change in the Curie temperature may also result from the vacancy-induced variation of lattice constants [108]. If the substitution constituent ions are randomly distributed and form micro-inhomogeneity in crystal structure, partial substitution of cations in perovskite ferroelectrics may result in broadening of the maximum peak at the Curie point [109-112]. The ferroelectric-to-paraelectric phase transition in the material will no longer occur at a single temperature. Instead, the various regions with slightly different crystal structures will undergo the phase transition in a very broad range of temperatures. Consequently, a very high dielectric constant can be obtained in a broad range of temperature [6]. Besides, several groups have studied the occupancy of rare earth ions in the $BaTiO_3$ lattice and mixed results have been obtained due to different processing parameters used during fabrication [113-116].

Barium titanate based ferroelectric compositions have attracted a great attention in searching for lead-free ferroelectric materials to meet the environmental friendly applications requirement. $BaTiO_3$ itself does not have ideal properties for some industrial applications. Chemical substitutions at Ba^{2+} or Ti^{4+} sites can tremendously change the properties to meet a variety of device and performance requirements. In the following two substituted $BaTiO_3$ solid solutions will be discussed which either can pinch or shift the Curie point of barium titanate to provide for a more desirable temperature response.

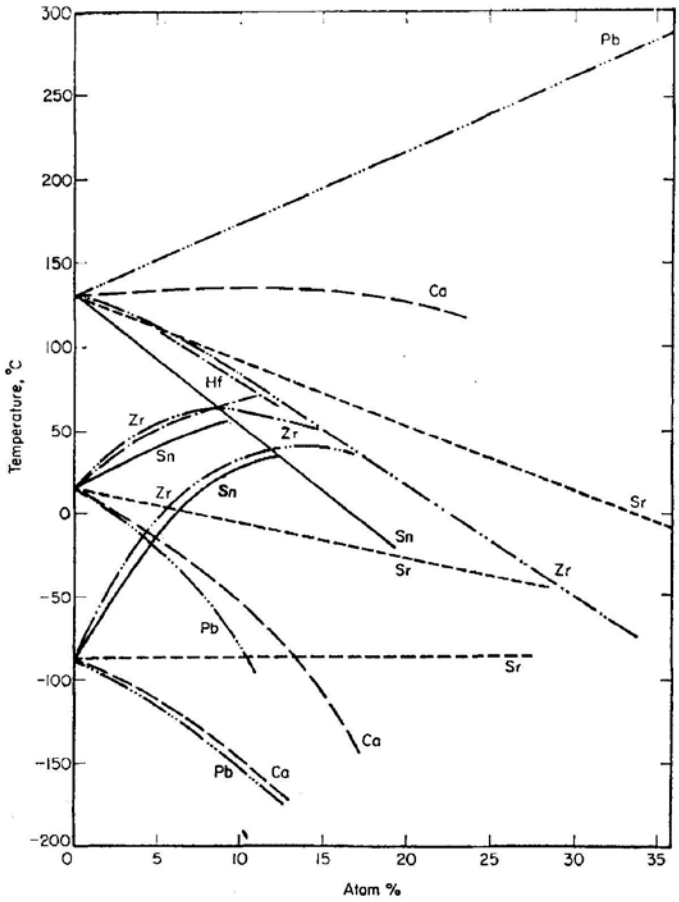

Figure 2.14 Effect of several isovalent substitutions on the transition temperature of $BaTiO_3$ [48].

Barium Strontium Titanate, ($Ba_{1-x}Sr_xTiO_3$, BST), is perhaps the most common solid solution with Sr^{2+} substitute into Ba^{2+} site in the perovskite lattice . The behavior observed with Sr^{2+} doping is normally explained as a cation size effect, since incorporating strontium into the lattice results in an overall decrease in the lattice parameter as the smaller strontium ion. Thus, the strontium substitution could stabilize the cubic structure, and then decrease the Curie point. It is interesting to note that the change in lattice parameter and phase transition temperature with strontium substitution is similar to the application of hydrostatic pressure in the unit cell and provides a connection to structure property relations in these materials.

Previous studies showed that there is a linear decrease in the Curie point with a slope of approximately 3.7^o per mole substituent. With addition strontium composition, the tetragonal-

orthorhombic phase transition temperature also decreases linearly with approximately 2^{o} per mole substituent. However, the orthorhombic-rhombohedra transition remains relatively constant [48, 117]. In the permittivity vs. temperature for BST bulk ceramics, it shows that the permittivity increases as Sr substitution level increases to approximately 30 percent and then decreases [118]. The addition of strontium into barium titanate shifts the Curie temperature, the transition temperature from ferroelectric (tetragonal) to paraelectric (cubic) phase to somewhere around room temperature, making BST a paraelectric material with a high dielectric constant for many practical applications.

There have been a lot of researches efforts on barium strontium titanate in both bulk ceramics and thin film form. Especially, dielectric BST thin films have been considered to be important materials for high density dynamic random access memories (DRAM) and tunable microwave devices such as microwave tunable phase shifters, filters, oscillators, and antennas due to their high dielectric constant, relatively low dielectric loss, and large electric field tunability [119-126]. Many efforts have been made to further enhance the dielectric properties of the BST films. However, it is not an easy endeavor since the dielectric constant (ε_r) and loss tangent ($\tan\delta$) of BST films depend strongly on the film quality and substrate materials, such as the mechanical stress [127], interface [128] and surface behavior. It has been shown that BST thin films can be grown by a variety of methods ranging from chemical solution deposition (CSD) [129], metalorganic chemical vapor deposition (MOCVD) [130], pulsed laser deposition (PLD) [120, 125, 126, 131,132], and radio frequency (RF) magnetron sputtering [133, 134]. However, the fabrication of high quality BST films with high ε_r and low $\tan\delta$ values is still a very important technical issue for pushing these materials further for practical applications.

Barium Titanate Zirconate, ($BaZr_xTi_{1-x}O_3$, BZT), is probably the second most common solid solution for dielectric applications with zirconium substitutes for titanium in barium titanate perovskite structure. This is possible because the Zr^{4+} ion has larger ionic size (0.087 nm) than the Ti^{4+} ion (0.068 nm) [135, 136]. Pontes et al. reported that this substitution result in an

expansion of the unit cell and when the Zr concentration at around 25 at.%, the BZT thin film can crystallize in the cubic structure [137]. This changes some of the properties of BZT. For example, it becomes a phase transition pincher rather than a shifter. It has been reported that with the incorporation of Zr^{4+} in $BaTiO_3$, the rhombohedral to orthorhombic (T1) and orthorhombic to tetragonal (T2) phase transition temperature corresponding to pure $BaTiO_3$ increase. However, the tetragonal to cubic (T_c) phase transition temperature decreases. Thus when Zr concentration is at about 15 at.%, the BZT system exhibits a pinched phase transition, and all three phase transition temperatures (T_1, T_2 and T_c) correspond to pure $BaTiO_3$ are merged or pinched into single phase transition [138].

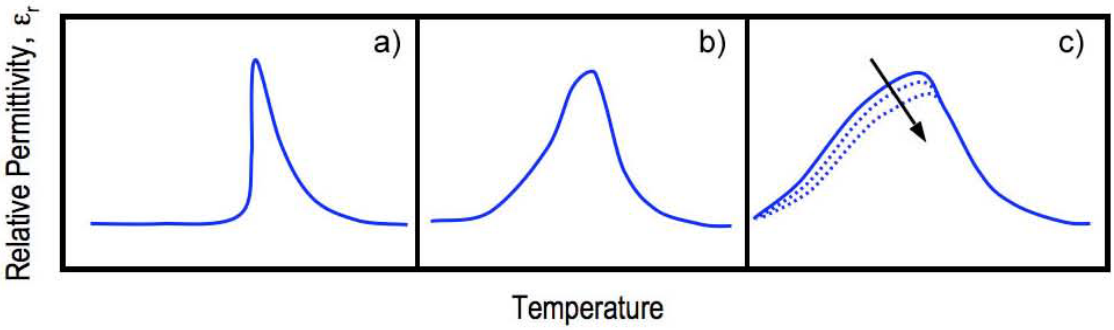

Figure 2.15 Schematic of three ferroelectric phase transitions of BZT, showing a) normal; b) diffuse; and c) relaxor [118].

There are some interesting features occurring with the amount of zirconium substituted into the barium titanate lattice. First is the pinching effect of the phase transitions, which results in a broadening of the dielectric maximum that can flatten the overall temperature response of permittivity. Between 0~15 at.% Zr, the material acts as a 'normal' ferroelectric with three phase transitions [139]. At approximately 15 at.% Zr, all phase transitions have converged to a critical point and the material can transit from cubic directly to rhomohedral at about 40^{o}C temperature [138, 140, 141]. In the compositions between 15 to 25 at.% Zr, there is a phase transition behavior that is defined as 'diffuse' where the permittivity vs. temperature plot shows a large and broad peak [118]. Above 25 at.% Zr contents, BZT system has a typical relaxor behavior showing a frequency dependence of T_{max} and a broad maximum in the permittivity [139, 142],

as shown in Figure 2.15. Although the origin of the changes in phase transition behavior is still not well understood, there has been some studies working on the mechanism and modeling [139, 143].

Although less literature exists for BZT than that of BST in the past years, $BaZr_xTi_{1-x}O_3$ (BZT) solid solution has attracted considerable attention recently in both bulk and thin film due to its potentiality for various device applications as piezoelectric transducers, DRAM, and tunable microwave devices like tunable filters, phase shifters, antennas etc [144-154]. Many multilayer capacitor applications make use of BZT based compositions for some of the highest performance devices [155-157]. A lot of attentions have been attracted on physic properties of the BZT thin films prepared by various methods. A few groups have studied the effects of zirconium on the properties of barium titanate thin film using CSD [146, 158-160], MOCVD [161, 162], RF magnetron sputtering [149] and PLD [163-166]. However, few reports are available for detailed growth mechanism and microstructure study for BZT films. In this work, more effort was put into investigating and developing the growth mechanism and interface effect in expitaxial BZT films.

2.2.6. Thin Film Behavior

It has been apparent from last two decades that many applications require materials to be employed in a thin-film form, thinner than 1 μm. Comparing with corresponding bulk materials, thin films are lower dimensional systems with various strain, and usually have more defects, and therefore their properties may be vastly different. The dielectric properties of ferroelectric thin films are usually different than that of their bulk counterparts. Figure 2.16 shows that the dielectric behavior of BST thin films as a function of temperature is entirely different from that of BST bulk material. Typically, thin films exhibit lower dielectric permittivity and higher loss tangent than the bulk ceramics with the same composition. The origins of these differences in the properties can be concluded as the following three reasons: (i) different fabrication method and processing conditions (e.g. temperature, pressure, etc), (ii) stress (or

strain) produced in thin films due to substrate constraints, domains and defects and (iii) scaling effects.

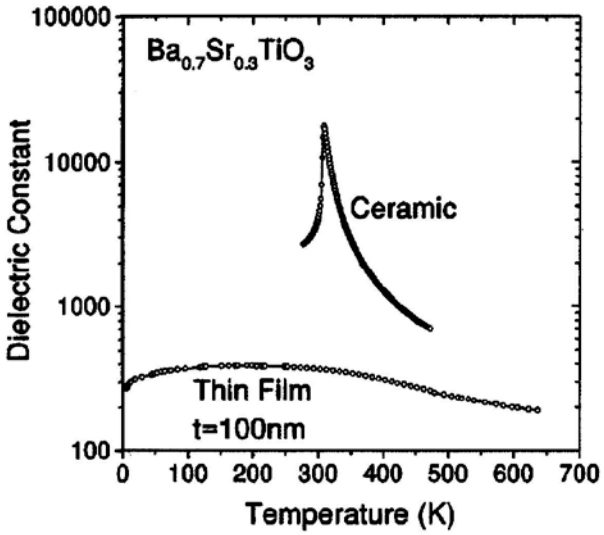

Figure 2.16 The dielectric constant of a bulk BST ceramic and a BST thin film of the same composition as a function of temperature [167].

The internal stress is generated either from different substrate materials or different film thicknesses. The thin films usually constrained at one side by a thick substrate. The substrate has significant influence on structure and properties of thin films. Grown on the surface of the substrate, the crystal structure and microstructure of a thin film is influenced by the crystal structure and surface morphology of the substrate. Experimental results revealed that the dielectric tunability of ferroelectric thin films is highly dependent upon the lattice misfit (the misfit strain). The energy of the film/substrate interface is a function of the phase, orientation and strain state of the film. Additionally, the out-of-plane thickness of the film is generally orders of magnitude thinner than the in-plane dimension. Combining these geometric factors with intrinsic growth stresses, thermal expansion coefficient mismatches between film and substrate, and possibly epitaxial misfit strains, results in a complicated stress condition. Understanding the consequences is very important for the study of ferroelectric perovskite thin films, since their behavior is highly related to stress. Stain effects on the dielectric properties of ferroelectric thin films have been widely studied both in theory and experimental over past several years. Several

studies have investigated the effect of biaxial film strain in epitaxial thin films and reported that strain can affect the order of the phase transformation, shift phase transition temperatures, and even result in new ferroelectric phases which maybe not observed in the bulk materials [168, 169].

Defects have important influences on the properties of thin films as well. Vacancies, substitutional impurities, and interstitial defects can result in electronic charge storage within the ferroelectric thin films. Interstitial defects and ions in the wrong lattice sites usually do not have significant effect on the physical properties of the films [170]. However, oxygen vacancies can form negatively charged acceptor centers, which have been recognized to significantly change the electrical properties of ferroelectric thin films [171]. In some cases, thin films are grown in an oxygen-deficient environment. As a result, the as-deposited thin films usually contain a large concentration of oxygen vacancies. Oxygen vacancies affect the nearest neighbor distance by reducing the Coulomb attractive force between cation and anion atoms, resulting in an increased lattice parameter and unit cell volume [172].Post-annealing can reduce some oxygen vacancies concentration but cannot fully remove them. Other defects, such as dislocations, grain boundaries, anti-phase boundaries have also important influences on thin film properties.

Additionally, interface and surface effects, which in bulk materials may be negligible, may have pronounced consequences for thin film [173]. This is primarily a function of the relatively large area of surfaces and interfaces compared to the limited volume of the thin film. The domain structures, epitaxial quality, and dielectric properties can be influenced by the substrate surface structures, which composed with surface terraces, steps, and many surface defects [172]. It is well known that any real surface consists of many surface defects such as adatoms, atomic clusters and islands, terraces, edges, vacancies and various atomic sites, as shown in Figure 2.17. An oxide surface is a good example of a complex crystallography with a very complicated combination of physical and chemical properties and high surface defect

concentrations, resulting in problems of obtaining a reproducible surface composition and physical properties. Therefore, appropriate substrate surface processing, which not only removes the surface contamination but also controls the surface defects density and microstructure, before film deposition is important and becomes essential to film microstructure and physical properties [172].

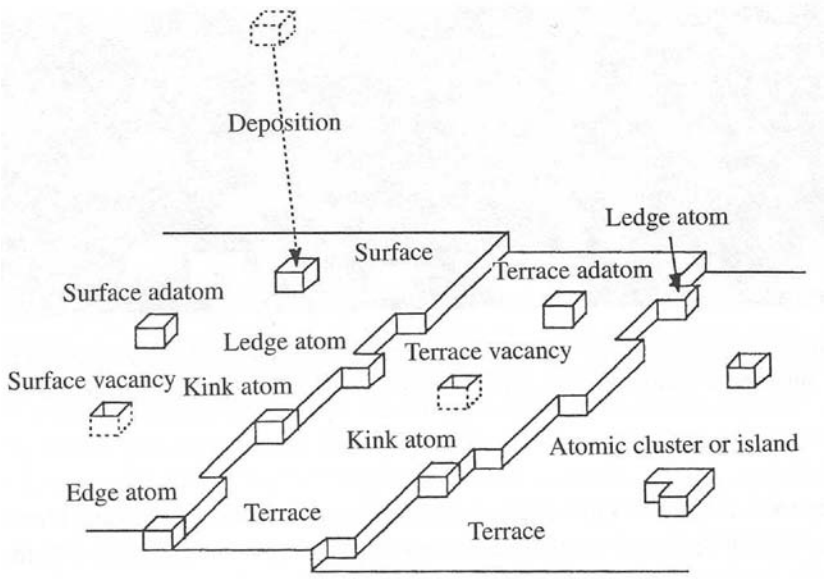

Figure 2.17 Schematic diagram showing various surface defects on a real crystal surface [172].

The film/substrate interfacial energy is a function of the phase, orientation, and strain state of the film, each of which may have a strong influence on film properties. The film can minimize the interracial energy by lattice matching across the interface when the lattice parameters of film and substrate are close. However it could result in a strong preference of certain in-plane and out-of-plane orientations with respect to the substrate and a lattice mismatch between film and substrate. The film is strained to lattice match the substrate and forms a coherent or sub-coherent interface. Even films grown under optimized conditions, the lattice mismatching and surface step-terrace structure can tremendously alter the film microstructure. Generally, the interface strain energy from lattice misfit can be released by the formation of edge dislocations at the interface if the film thickness is larger than the critical

thickness [172]. The strain arising from the lattice mismatch could be fully relaxed at the interface by forming dislocations, when the misfit value is very close to the theoretical value.

As discussed above, many factors have significant effects on the physical properties and microstructure of ferroelectric thin films. For instance, the film/substrate interfaces play an important role in the process of film growth, due to the generation of epitaxial strain from interface. The strain arising from the lattice mismatch at film/substrate interface has proved to be valuable for the fabrication of electronic or optical devices [30]. However, the stress associated with the misfit strain can also turn into a driving force for the nucleation, motion and propagation of crystalline defects, the most common being misfit dislocations, which may greatly degrade the performance of devices. Thus, once we have more knowledge base of interface effect and strain generation mechanisms, we will be able to fabricate films with better reliability and functionality can then be better able to control film properties.

2.3 Thin Film Deposition and Growth Techniques

Many processing techniques have been applied successfully in ferroelectric thin film growth and device fabrication, such as: plasma and ion-beam sputtering, PLD, CVD, MBE, MOD, CSD etc [6]. Most of these deposition methods need to satisfy the following requirement, including: (1) keeping the film with desired physical properties and chemical composition, (2) good film quality, stability and reproducibility, (3) suitable for device fabrication and practical application, (4) simple processing procedure, low cost and environmental-friendly. Among these methods, sputtering and PLD have attracted more attention due to their epitaxial film quality and practical application ability.

2.3.1. Sputtering/Plasma Sputtering [174-179]

Sputtering deposition is one of the most commonly used physical vapor deposition (PVD) techniques for the deposition of thin films. Sputtering can be defined as the ejection of surface atoms of a source/target material by energetic ion bombardment due to the kinetic energy transfer. The energetic particles, including the mixture of ions, neutral atoms,

molecules, electrons, neutrons and/or energetic photons, collide with the surface at a high energy level greater than bonding energy. The energy transfer creates a collision cascade in the target material leading to the ejection of atoms, ions, molecules, secondary electrons and photons, which thrust towards the substrate surface where they coalesce and grow as a desired thin film [180].

A typical plasma discharge will use argon as a gas source for non-reactive sputtering, which results in a mixture of argon ions, electrons, and free neutral atoms. When a surface is bombarded by energetic ions, there are numerous effects that occur [177]: emission of neutral (sputtered) particles; emission of secondary electrons; emission of positive and/or negative ions; reflection of incident particles; desorption of gases; implantation of incident particles; chemical dissociation; diffusion; crystallographic changes, etc.

When the sputtered atoms receive to substrate surface, the manner of atoms migrate, interact and nucleate on the substrate surface is impacted with many deposition process parameters; such as substrate temperature, sputtering power, sputtering gas, and background pressure. Usually the steps involved in the film growth are as followed: (1) condensation and nucleation of the atoms on the surface; (2) Nuclei growth; (3) Interface formation; (4) Film growth of nucleation and reaction with previous deposited material; (5) post-deposition modification. These interactions led to the development of Thornton Model (or called Structure Zone Model) which describes film structure as a function of temperature (T/T_M) and pressure for sputtering deposited film.

As shown in Figure 2.18, film morphology can be categorized into four growth modes which intensively dependent on the operating pressure and the ratio of substrate temperature to the melting temperature of the sputtered material. Four growth modes are named as Zone 1, Zone T, Zone 2, and Zone 3. Zone T is an intermediate growth mode found between Zone 1 and Zone 2. The mechanisms for the respective zones are: (1) Atomic shadowing during

transport; (2) surface diffusion; (3) bulk diffusion [181-183]. Zone T is unique in that is affected by a number of parameters, the most obvious of which is energetic bombardment.

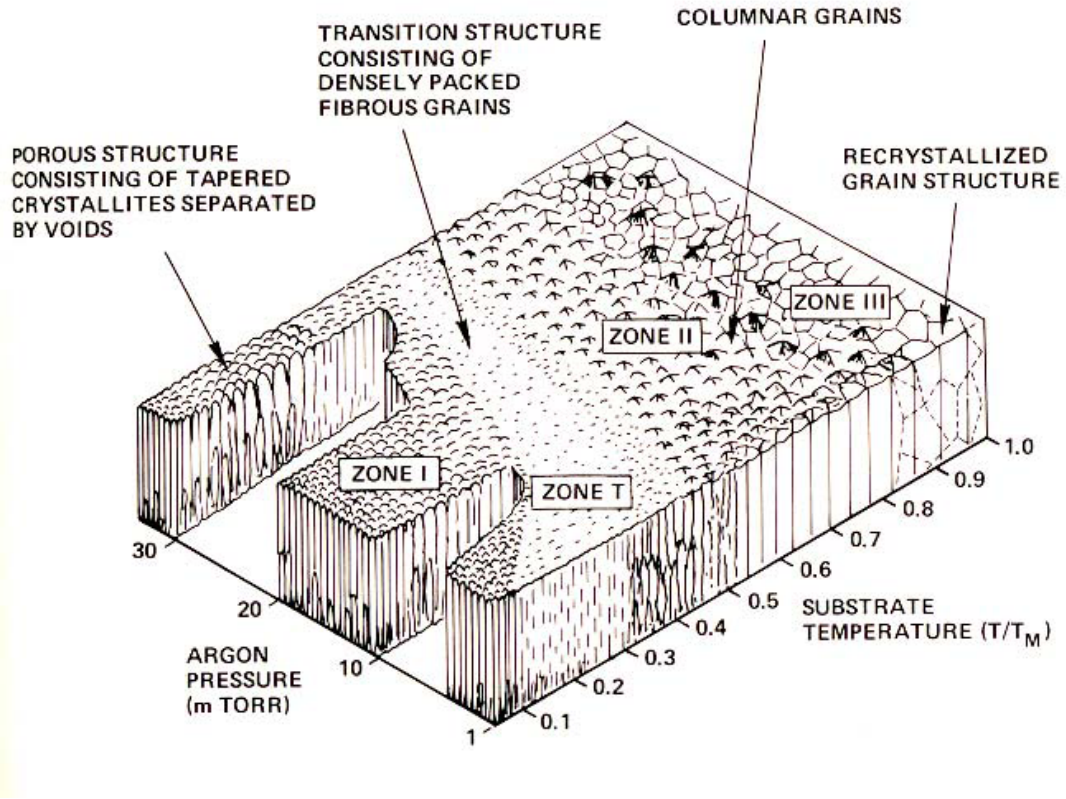

Figure 2.18 Thornton Model for sputter deposited films [175, 181, 182].

There are many methods applied to accomplish the sputtering of a target. Direct current (DC) sputtering is named because it keeps the target at a constant potential. Radio frequency (RF) sputtering uses a varying target potential and can be sputter non-conductive materials. Reactive sputtering occurs when introduced gas react with the target material and produce complex compound as the thin film. Magnetron sputtering is used with a magnet located behind target to increase target current and deposition rates. It can be performed with either a DC or RF power supply.

Among them, DC and RF-plasma sputtering are the two most common methods of sputtering. In the DC sputtering system, the sputtered particles collide with gas molecules, argon, and diffuse to the substrate due to the high gas pressure and less sputtered particles.

All kinds of metals can be deposited by DC sputtering. However, RF sputtering can be performed on all types of materials, especially to sputter an insulator target. The operating pressure needs to be reduced as low as possible since the RF electrical field in the discharge chamber increases the collision possibility between secondary electrons and gas molecules. One advantage of RF sputtering is the ability to deposit high melting point oxides at relatively low substrate temperatures.

Magnetron sputtering is a popular technique used for thin film deposition, in which a magnetic field is used by putting a magnet to the top of the cathode to trap secondary electrons near the target. It allows more collisions between secondary electrons and argon plasma at close to target region. This improves the sputtering rate by enhancing the ionization of the plasma on the surface of the target material and sustains the plasma at a lower pressure compared with normal sputtering system [184]. For these reasons, magnetron sputtering has become one of the most important sputtering technique and widely used in many industrial coating applications.

The sputtering technique has been utilized to more conveniently deposit a wide range of materials since the momentum exchange is a physical process as opposed to a chemical or thermal process. The advantage of sputtering also include low cost, high deposition growth rate, reproducibility, moderate processing temperatures, and compatibility with existing industrial semiconductor manufacturing processes [173, 185]. Besides, this simple process allows for complex chemical compositions to be deposited on a wide variety of shape, size and materials. Furthermore, sputtering has less contamination effect compared to other chemically-driven deposition techniques and often results in more reproducible characteristics of thin films.

2.3.2. Pulsed Laser Deposition [186-192]

PLD is a physical vapor deposition technique for fabricating thin films and nanostructures by utilizing a physical process called laser ablation. In the PLD method, thin

films are deposited by the ablation of one or more targets using a focused pulsed laser beam. The use of pulsed laser deposition as an energy source for film growth was first carried out by Smith and Turner in 1965 since the discovery of lasers [193]. After that, initial studies explored and involved both continuous-wave and pulsed lasers during 1960s and 1970s [172]. Then in the late 1980s, pulsed laser deposition was fast developed and attracted more attentions as a reproducible oxide film growth technique due to the successful use in growing epitaxial high temperature superconducting films [194]. Their work already showed the main characteristics of PLD setup configuration.

Since then, PLD has attracted great attentions and undergone rapid development. In the 1990s, reliable electronic Q-switched lasers became available for the generation of very short optical pulses. Thus, PLD could be used to achieve congruent evaporation of the target and to deposit stoichiometric thin films. Subsequent development led to lasers with a high efficient harmonic generator and excimer laser delivering UV radiation. From then on, non-thermal laser ablation of the target material became highly efficient. Currently, PLD technique is widely applied in laboratory research as well as in industry. Many materials that are normally difficult to deposit by other methods, especially superconducting, metallic, ferroelectric, ferromagnetic oxides and their multilayers, have been successfully deposited by PLD [191].

A PLD system usually consists three main parts: high vacuum system, deposition chamber and laser system. The principle of PLD is based on the interaction of laser and source materials. The deposition procedure of PLD is quite simple. Figure 2.19 shows a basic setup of PLD system. In the deposition, a high power pulsed laser beam is focused on the target surface inside a vacuum chamber. When the laser pulse is absorbed by the target, energy is first converted to electronic excitation and then into thermal, chemical and mechanical energy resulting in evaporation, ablation, plasma formation and even exfoliation. Consequently, the target locally absorbs the laser energy and ablates a small amount of target materials out in a form of plume like plasma containing many energetic species including

atoms, molecules, electrons, ions, clusters and others. Unlike the thermal evaporation, which produces a vapor composition dependent on the vapor pressures of elements in the target material, the laser induced expulsion generates high pressure plasma with stoichiometry similar to the target material [186]. Finally, the ablated species condense and deposit on a substrate which is short distance away from the target. Moreover, besides the basic components, a practical PLD system has many extra components and powerful software controls including optical components used to direct and focus the high power laser, various controlled-flow ports, pumps and gauges used to control and measure the inside pressure of the chamber, etc [187].

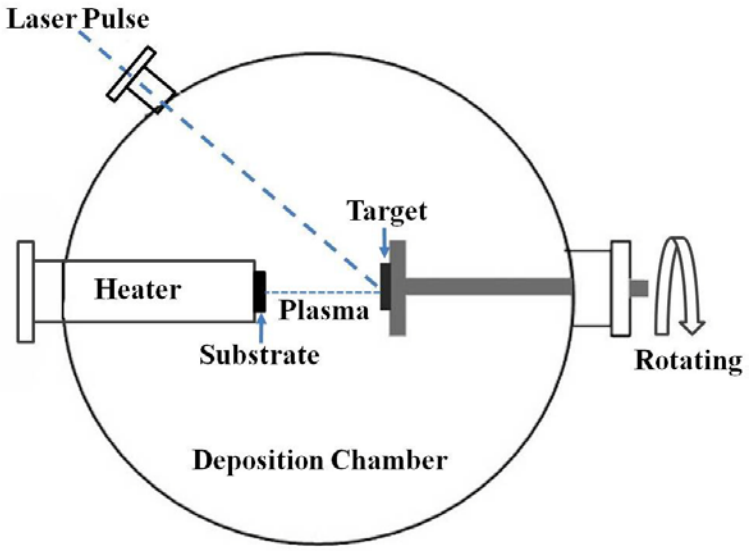

Figure 2.19 Schematic illustration of a basic setup of pulsed laser deposition (PLD) system.

Compared to the simple system setup, the thin film growth mechanism by PLD is complex. The deposition process of PLD is often described as three steps, which consists of the ablation process of the laser ablation of the target material; the development and transport of the plasma plume with high energetic species; and nucleation and crystalline growth of the film on heated substrate [187, 191]. These steps are circularly repeated in a typical deposition process and each of them is significant for the crystallinity, uniformity and stoichiometry of as grown film.

The film growth modes can be categorized into three types in thin film deposition as schematically illustrated in Figure 2.20 [189,195,196]. The first is called Frank-van der Merwe layer-by-layer growth mode, in which the adatoms attach preferentially to surface sites to form complete, atomically smooth surfaces. In this model, the dominant factor is the total surface energy of the configuration. The most electrochemically stable stacking of adatoms is the one with least surface area. Therefore, the adatoms must have a much stronger attration for the atoms in the surface than to each other for arranging over one single mono-layer at a time. The second is called Volmer-Weber 3D island mode. The film atoms are initially bound to each other and then subsequently grow into three-dimensional islands on the substrate due to a lower adhesive energy than cohesive energy. In com comparison to the Frank-van der Merwe model, many layers are needed to stack up for uniting all the separate islands over the substrate surface. The third is called Stranski-Krastanov growth mode, which involves a combination of the two modes with a transition from the layer-by-layer to island growth at a critical thickness dependent on material properties such as surface energies and lattice parameters of the film and substrate [187, 191, 197-201].

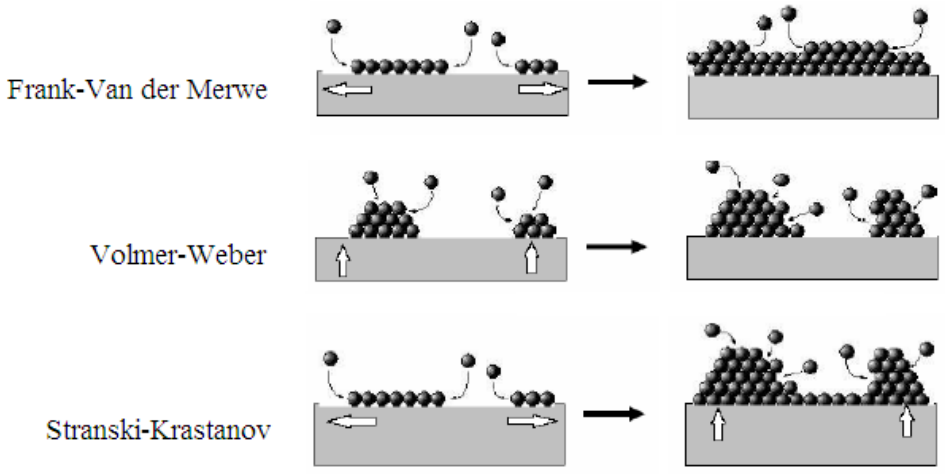

Figure 2.20 Schematic illustrations of three thin film growth modes [189].

The practical film growth is critically dependent on both thermodynamic and kinetic factors, which include the interface energy, the lattice mismatch, and the chemical interactions

between the film and the substrate [200, 201], as well as the growth conditions, including the substrate temperature, the oxygen partial pressure, the laser repetition rate, and the laser energy, etc [202].

Compared with other deposition techniques, PLD offers many advantages such as good stoichiometry, a high deposition rate, good epitaxial quality, relatively low cost, and it has become the most powerful technique to obtain epitaxial thin films of complex-composition oxide thin films. Epitaxial thin films of superconducting high Tc films, metallic, ferroelectric, ferromagnetic, dielectric oxides and their multilayers have been successfully fabricated by this method [172, 187,190, 192].

However, there are still some limitations for the application of PLD system, such as: (1) deposition of clusters, droplets or bigger particles. The presence of micro-sized particulates is harmful to the properties of as-grown films; (2) the angular distribution of the plume is strongly confined to the forward direction, which results in an inhomogeneous thickness distribution over a large area of the thin film and limits the possibility of fully application in industry; (3) Aging of the target, the original target structure changes due to the laser impact (melting) and by deposition of the vapor on the target itself; (4) The ablation process very sensitively depends on the laser used, which makes it very difficult to reproduce the same result with a slightly different laser setup[190, 192].

Many efforts have been made to compensate these disadvantages. For example, inserting a shadow mask between the substrate and the target can effectively block off the large particulates. Simultaneous rotation of the target and substrate can help to improve the uniformity. Even though there are some drawbacks, Pulsed laser deposition is still one of most important film deposition techniques as a rapid research and development tool for the fabrications of novel materials.

Overall, perovskite epitaxial oxide thin films with various novel properties, such as high dielectric constant, good ferroelectric properties and low dielectric loss have been successfully

fabricated using different films deposition techniques. They have been considered as one of the most important material families to meet challenges in advanced material research and nanotechnology. It has been well known that the physical properties of deposited thin films can be affected by many factors, including the deposition rate, film thickness, chemical composition, and film microstructures. However, the systematically studys regarding to the chemical substitution, film microstructures, interfaces, and film growth mechanism are limited. Their influences on the film properties and the relationship between the film fabrication, microstructure and properties have not been well understood. In this work, barium titanate was selected as a studying system. Barium titanate based epitaxial thin films have been successfully fabricated and studied in terms of magnetron sputtering deposition condition control, film microstructures, interfaces as well as doping effects on the film growth.

CHAPTER 3

THIN FILMS SYNTHESIS AND CHARACTERIZATION

Barium titanate thin films were fabricated on (001) MgO substrates using RF magnetron sputtering, which conducted in a lab-built hybrid plasma assisted sputtering system. The Barium titanate sputtering target was purchased from Kurt J Lesker Company with 99.9% purity. Other barium titanate based oxide thin films, such as (Ba,Sr)TiO_3 (BST), Ba(Zr,Ti)O_3 (BZT), 2%Mn doped Ba(Zr,Ti)O_3 (Mn:BZT) and Mn:BZT//Mn:BST multilayer films, were deposited on (001) MgO substrate using plused laser deposition. The details of the deposition conditions for each film are introduced in this chapter. The microstructures of the thin films were characterized in details using high-resolution transmission electron microscopy (HRTEM), X-ray diffraction (XRD), atomic force microscopy (AFM), X-ray photoelectron spectroscopy (XPS) and nanoindentation as described in the following section.

3.1 Synthesis of Barium Titanate and Barium Titanate Based Thin Films

The synthesis of barium titanate based thin films involving two deposition methods. First, a study was conducted with barium titanate thin films deposition on (001) MgO single crystal substrate using RF magnetron sputtering. The goal was to investigate the epitaxial growth mechanism of BTO films, and gain further fundamental knowledge into the epitaxial growth; interface and doping effects of BTO based thin films. Second, the BTO based epitaxial films were deposited on (001) MgO substrate using pulsed laser deposition with various deposition conditions, carried out in a lab-made PLD system.

3.1.1. RF Magnetron Sputtering

Magnetron sputtering has been one of the most effective and popular film deposition techniques during the past few years, and has been widely used both in the lab and industry for thin film research and applications. The deposition of barium titanate films was conducted in a

home-made hybrid plasma assisted sputtering system at the Surface and Nano Engineering Laboratory (SANEL). The sputtering target and deposition substrate were carefully selected. The deposition procedure and deposition conditions were discussed in detail below.

3.1.1.1 Hybrid Plasma Assisted Sputtering System

Figure 3.1 shows the home-made hybrid plasma assisted magnetron sputtering system in SaNEL. Although there has been a huge development in the sputtering technique and sputtering system design in the last decade, the principles and the basic system structure is merely the same. The stainless steel chamber has a cylindrical shape with 47 cm diameter wide and 50 cm height. The system has three 2-inch diameter magnetron guns mounted at the bottom of the chamber. The front gun has a high magnetic source, and the other two guns are equipped with low magnetic source. Each magnetron gun can be easily connected to DC or RF plasma power capabilities. The position of the magnetron gun is designed to have 30 degree inclination to the substrate holder center with a target-substrate distance about 100 mm to 150 mm. The sputtering target holder and substrate holder in the chamber have a face to face arrangement serving as electrodes, as shown in Figure 3.2. The magnetron guns can support targets with thickness of 0.125", 0.185" or 0.250". The targets can be shielded using a pneumatic shutter above the magnetron gun. The RF power can be applied in magnetron gun is up to 50 W by an AJA Seren RF generator and manual matching network. The substrate can be rotated and heated up to 900°C (setting temperature) controlled by the thermal couple located just behind substrate holder using an AJA SHQ-15 temperature control unit in both RF and DC mode. The substrate holder is a 10 cm diameter plate where the samples can be mounted and has rotation capability. The substrate can be either RF or DC biased up to 50 W and 1000 V, respectively.

Argon gas with a purity of 99.99% was introduced into the system chamber as a medium to start and maintain a glowing plasma. The gas flow was controlled using a Unit Instruments mass flow controller to meet the pressure requirement during the deposition. The deposition

chamber is connected to a mechanical pump and a cryopump from the backside of the chamber to obtain and keep high vacuum in the chamber down to 1×10^{-8} Torr. During the deposition, very precise pressure control is maintained using an automatic gate valve in conjunction with an MKS 146C PID controller. A thermalcouple gage measures the roughing line pressure and an ion gage located at the backside of the sputtering chamber measures the chamber pressure when the valve gate is open and the cryopump accessess the chamber to achieve higher vacuum. All the magnetron guns and substrate holder were cooled circularly using a Thermo Scientific NESLAB RTE 740 water chiller to avoid heating damage to all the guns and also maintain the deposition temperature stable on the substrate.

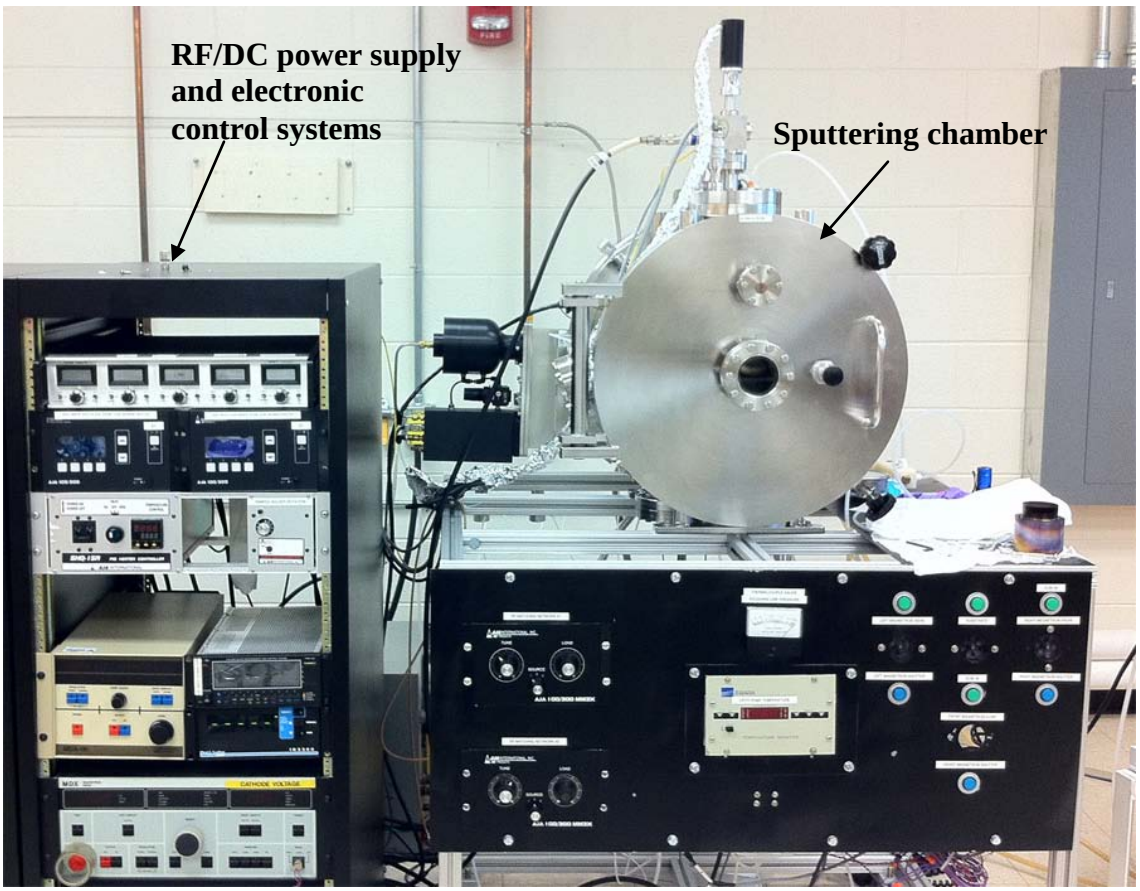

Figure 3.1 Front view of home made hybrid plasma PVD system in SANEL.

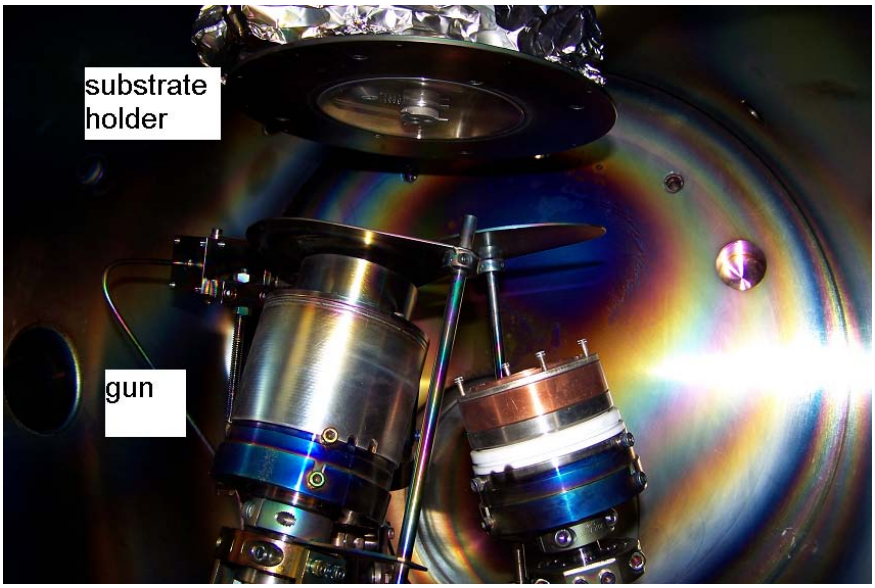

Figure 3.2 Inner view of the sputtering system showing two sputtering guns and the substrate holder.

3.1.1.2 Sputtering Target and Deposition Substrate

The barium titanate target (purity 99.9%) used was purchased from the Kurt J. Jesker company and had a size of 2" diameter and 0.25" thickness. The physical properties and crystal structure information of the most used deposition substrates and BTO bulk material are listed in Table 3.1. Magnesium Oxide (MgO) single crystal was selected to be the deposition substrate since it has relatively low lattice misfit with respect to the BTO film, and also because the MgO crystal has low dielectric loss in the microwave band, so it is an important material for high T_c superconductive microwave devices in the mobile communication as well as other industrial areas. The size of (001) MgO substrate was chosen to be 10 mm × 10 mm and was purchased from MTI corporation.

Prior to the deposition, the surface of MgO substrate was cleaned using acetone and ethanol in sequence to remove surface oil or dust. Then, the substrate was dried up with compressed air.

Table 3.1 Physical properties and crystal structure of most used substrates and BTO films.

	Substrates						Films
Chemical Formula	$LaAlO_3$	MgO	$SrTiO_3$	Si	Ni	NiO	$BaTiO_3$
Crystal Structure	Pseudo-Cubic	Cubic	Cubic	Diamond Cubic	FCC	FCC	Cubic
Melting Temperature (K)	2373	3250	2353	1683.15	1726	2228	1891
Density (g/cm^3)	6.52	3.58	5.12	2.33	8.90	6.67	6.06
Dielectric Constant	25	9.8	300	13	N/A	N/A	100~1250
Lattice Constant (Å)	3.789	4.212	3.905	5.430	3.520	4.177	4.020
Lattice misfit with BTO (%)	6.09	-4.56	2.94	-25.96	14.20	-3.76	0

3.1.1.3 Deposition Condition for BTO films on (001) MgO Substrate

BTO films were deposited on (001) MgO substrate using RF magnetron sputtering. Two kinds of as-deposited films with dramatically different stuctures have been formed at different deposition conditions. Prior to film deposition, substrate cleaning processes were carried out using Ar^+ plasma. The sputtering chamber was pumped down to 25 mTorr using the mechanical pump and then down to 10^{-7} Torr using the cryopump. The Ar flow rate was controlled at 10 sccm. The MgO substrate was cleaned by Ar^+ plasma using 30 W RF power at room temperature for 10 min to further remove the surface contaminations. The substrate was then heated up to 800 °C and stabilized for 40 min after cleaning. The detail parameters for cleaning process are shown in Table 3.2.

The BTO films were then deposited on MgO substrate by plasma sputtering a BTO target at 800°C for 4 hrs. The detailed deposition conditions for both BTO films with different structures/phases are shown in Table 3.3. After deposition, films were kept in the vacuum

chamber and cooled down to room temperature using a water cooling system. No post annealing was carried out for as-deposited films.

Table 3.2 Substrate cleaning process parameters for BTO/MgO RF sputtering.

BTO epitaxial structure		**BTO induced superstructure**	
Gas:	Ar	Gas:	Ar
Flow Rate:	10 sccm	Flow Rate:	10 sccm
Pressure:	10 mTorr	Pressure:	10 mTorr
Power:	30 W	Power:	30 W
Voltage:	218 V	Voltage:	216 V
Temperature	Room Temperature	Temperature	Room Temperature
Run Time:	10 mins	Run Time:	10 mins

Table 3.3 Deposition conditions for BTO/MgO RF sputtering.

$BaTiO_3$ epitaxial structure		**$BaTiO_3$ superstructure**	
Gun:	high magnetic power gun	Gun:	high magnetic power gun
Gun-Substrate Distance	150mm, 19.5 ^{o}	Gun-Substrate Distance	100mm, 30^{o}
Gas:	Ar	Gas:	Ar
Flow Rate:	10 sccm	Flow Rate:	10 sccm
Pressure:	20 mTorr	Pressure:	10 mTorr
Power:	50 W	Power:	50 W
Voltage:	197 V	Voltage:	78 V
Temperature	800 °C	Temperature	800 °C
Deposition Time:	4 hrs	Deposition Time:	4 hrs
Film Thickness:	120 nm	Film Thickness:	166 nm

3.1.2. Plused Laser Deposition of Barium Titanate Based Thin Films

The PLD deposition of barium titanate based epitaxial films was conducted as part of our collaboration with Prof. Chonglin Chen's group at the University of Texas at San Antonio (UTSA).

PLD is a powerful tool for depositing films of complex stoichiometry. With the rapid development of high efficient laser generator since 1990s, PLD has become one of the most popular film deposition methods widely applied in laboratory research as well as in industry application for epitaxial film growth. Many materials which are normally difficult to deposit using other deposition methods, especially multi-element oxides, have been successfully deposited by the PLD technique.

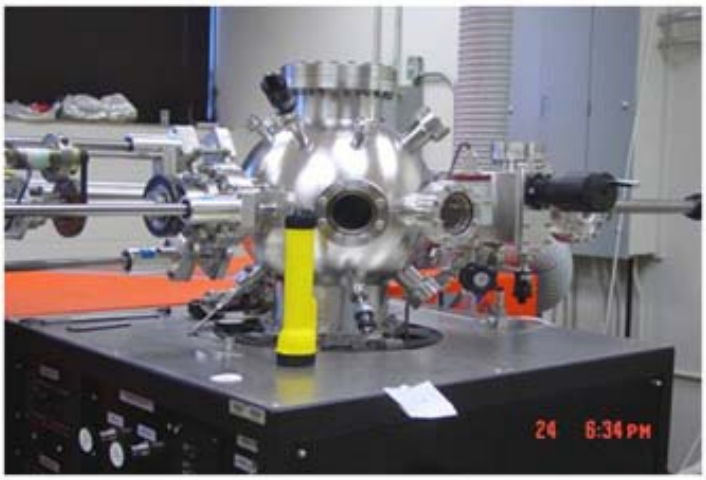

Figure 3.3 Side view of PLD system.

Figure 3.3 shows the laboratory PLD system used for the present study at UTSA.

(1) The epitaxial BST films were fabricated using a KrF excimer pulsed laser ablation at 820°C. During the deposition, a stoichiometric $Ba_{0.6}Sr_{0.4}TiO_3$ target with densitiy as high as 96% was used. The oxygen partial pressure ranged from 200 to 300 mTorr. The energy density was about 2.5 J/cm^2 and the repetition rate was 5-10 Hz. Commercially available vicinal (001) MgO substrates obtained by cutting the (001) surface with nominal angles of 1°, 3°, and 5° along the [001] direction were used as substrates. The surface roughness of the MgO substrate is less

than 1.0 nm. The accurate miscut angles were precisely determined to be 1.2°, 3.5°, and 5.3° using cross-section high resolution (HR) TEM. The single crystal (001) MgO substrate has excellent dielectric properties for microwave device applications. It has a dielectric constant $\varepsilon<9.5$ and a loss tangent, $\tan\delta=3\times10^{-7}$, better than Al_2O_3 ($\varepsilon=9.4\sim11.5$, $\tan\delta=6\times10^{-5}$) and $LaAlO_3$ ($\varepsilon=25$, $\tan\delta=6\times10^{-5}$). It is an ideal substrate to grow barium titanate based thin films. However, the calculated lattice misfits between $(Ba,Sr)TiO_3$ ($a_{Ba_{0.6}Sr_{0.4}TiO_3}$ =3.945 Å), $Ba(Zr,Ti)O_3$ ($a_{BaZr_{0.2}Ti_{0.8}O_3}$ =4.044 Å) and (001) MgO substrate (a_{MgO} =4.212 Å) are ~-6.3% and ~-4.0%, which indicates that $(Ba,Sr)TiO_3$ films could have more interfacial strains at the interface than $Ba(Zr,Ti)O_3$ films in this heterostructure system.

(2) The $Ba(Zr_{0.2}Ti_{0.8})O_3$ (BZT20) thin films and 2% Mn doped $Ba(Zr_{0.2}Ti_{0.8})O_3$ (Mn:BZT) were deposited on (001) MgO substrate using a KrF excimer PLD with a wavelength of 248 nm. For BZT20 films, a stoichiometric BZT20 target was used with density as high as 96%. The deposition was conducted at 850°C using an energy density of ~2.5 J/cm^2, laser repetition rate of 5-10 Hz and an oxygen pressure of 250 mTorr. For Mn:BZT films, the deposition temperature was 840°C with an energy density of ~2.0 J/cm^2, laser repetition rate of 4 Hz and an oxygen pressure of 250 mTorr.

(3) $[Mn:BZT//Mn:BST]_N$ multilayer films composed with 2% Mn doped $Ba(Zr_{0.2}Ti_{0.8})O_3$ and 2% Mn doped $Ba_{0.6}Sr_{0.4}TiO_3$ layers were also deposited on (001) MgO substrate using PLD. Targets with 2% Mn doped $Ba(Zr_{0.2}Ti_{0.8})O_3$ (Mn:BZT) and 2% Mn doped $(Ba_{0.6}Sr_{0.4})TiO_3$ (Mn:BST) were commercially purchased and used for the depositions of Mn:BZT//Mn:BST multilayer films.

First, two four-layered films were deposited on (001) MgO substrates with Mn:BZT as the first layer $[Mn:BST//Mn:BZT]_2$/MgO using a deposition rate of (1) ~ 2.4 Å/second (noted by ***FL-S***) and (2) ~ 6 Å/second (noted by ***FL-F***). The films were deposited using a KrF excimer PLD system with a wavelength of 248 nm. The depositions were performed at 850 ^oC using a laser repetition rate of 4 Hz and an oxygen pressure of 250 mTorr.

Second, two series Mn:BZT//Mn:BST multilayer films with the deposition sequence of $[(Mn:BZT)_3:(Mn:BST)_1]_N$ (denoted as ***ZL*** multilayer films) and $[(Mn:BZT)_1:(Mn:BST)_3]_N$ (denoted as ***SL*** multilayer films) were deposited on (001) MgO substrate, where N represents the number of deposition periods. For the $[(Mn:BZT)_3 : (Mn:BST)_1]_N$ multilayer films, the total deposition time of the whole film is the same for different N. (3:1) is the rate of deposition time for BZT:BST film layers. Similarly, $[(Mn:BZT)_1 : (Mn:BST)_3]_N$ multilayer films were deposited at the rate of (1:3) with the same total deposition time. The depositions were performed at 850 ^oC with a laser energy of 600 mJ, laser repetition rate of 4 Hz and an oxygen pressure of 250 mTorr. The total deposition time is controlled to be 40 min and the first layer deposited close to the substrate is Mn:BZT layer for all multilayer films. After deposition, the films were annealed at 825 ^oC for 30 min in an oxygen pressure of 600 Torr, and then, followed by slowly cooling down to room temperature at a rate of 3^o/min.

3.2 Thin Film Characterization Techniques

3.2.1 XRD

The structure and phase purity of the films were studied using a Siemens D500 and Bruker D8 Advance X-ray diffractometer. A Cu Kα radiation source with the wavelength of 1.54056 Å, was used at an acceleration voltage and filament current of 40 kV and 40 mA, respectively. Various scans, such as θ-2θ scan, ω scan (out of plane orientation), and φ scan (in-plane orientation) were performed.

The ω scan, also called a rocking curve measurement, provides the information on the texture and crystalline quality of the films. For a (00*l*) oriented thin film, the rocking curve scan of a Bragg reflection, is performed to determine whether atomic layers are perfectly aligned. In this scan, the detector is fixed at a 2θ position while the incident beam is rocked around a θ position. Strain around dislocations, as well as any other structural defects, can cause a broadening of the diffraction peaks in rocking curves. Therefore, the full width at half maximum (FWHM) in

high resolution rocking curves can be used as an approximate method for crystal quality characterization.

3.2.2 AFM

The surface roughness and morphology of the as-deposited films will be characterized using a Park systems' XE 70 AFM. Both contact mode and non-contact mode were used in this work. The electrical properties and piezoelectric response of the BTO films deposited using magnetron sputtering, and BZT and Mn:BZT films were also studied in this AFM system.

Electrostatic force microscope (EFM) images were obtained to investigate the polarization domains of the films under external electric fields in the same AFM system. The NSC36/Ti-Pt conductive cantilevers from Park systems were used for contact-EFM measurement. A 20nN setpoint was initially used as tip-surface contact force. A 4V AC signal was then applied between the probe and the sample at a 17.5 kHz frequency by a Model SR830 DSP lock-in amplifier, providing better image contrast. An external electric field was applied parallel to sample surface by connecting bias on both ends of the sample surface using silver paste. Then the contact-EFM images provide information of local phases/domains polarization condition corresponding to applied external electric field.

3.2.3 XPS

A Perkin-Elmer Phi 560 XPS/Auger system equipped with a standard Mg/Al source was utilized to investigate the surface composition, chemical state of elements at near surface region of the films. The composition depth profile showing the composition change from the film surface to the substrate could be achieved via Ar+ sputtering in this system. Survey scans were conducted in the 0-1200 eV range with every 0.5 eV step.

3.2.4 Raman Spectroscopy

The Raman spectra were recorded in a ThermoFisher Scientific DXR Raman microscope equipped with a DXR 532 nm excitation laser and high resolution grating for 532 nm laser.

3.2.5 TEM/High-resolution TEM

A JEOL 1200 EX transmission electron microscope (TEM) operated at 120 KV was used to record selected area electron diffraction patterns (SADP) and some low magnification bright field and dark field images. The HRTEM work was carried out in a Hitachi H-9500 electron microscope operated at 300 kV with a point resolution of 1.8Å. The dark field images can be obtained using a center dark-field method under a nearly two-beam condition. Both cross-section and plan-view TEM samples providing most of the detail information of film/substrate heterostructure microstructure were investigated in TEM/HRTEM. The cross-section TEM observation can provide important information of the interface between the substrate and the film which closely relate to the mechanism of the film crystal nucleation, growth, defect and strain, as well as the orientation relationships. However, the plan-view TEM observation could supply more information about two-dimensional interfacial structure with the effect of substrate surface on the behavior of the epitaxial films, which provides more critical structural information that is lacking from cross-section TEM.

Several imaging analysis softwares were applied to process and analyze TEM and HRTEM images. Gatan's DigitalMicrograph software installed with Hitachi H-9500 HRTEM was used for initial measurement and quantitative analysis of as-taken images, such as d-spacing and Fast Fourier Transformation (FFT). CRISP image processing software was utilized to obtain FFT and invert FFT images. EMS simulation software was used for structure simulation. Diamond 3.2-Crystal and Molecular Structure Visualization was used for structure modeling and structure modification.

3.2.6 NanoIndentation

Nano-indentation tests can provide a direct and continuous measurement of dynamic indentation hardness and modulus varying with penetration depth of the thin films. The experiments were performed in a Hysitron Ubi 1 Nanomechanical Test Instrument to investigate the mechanical properties of selected as-deposited thin films. A three-sided pyramid Berkovich

diamond tip was used in the measurements. The elastic modulus and hardness values were obtained by providing corresponding forces with the same displacement of 75 nm on each film. Sixteen indents in a 4×4 array with spot-spot distance of 3 μm within a total area of 9×9 um^2 were selected to determine the average hardness and Young's modulus of the films.

3.3 TEM Sample Preparation

3.3.1 Cross-section TEM Sample Preparation

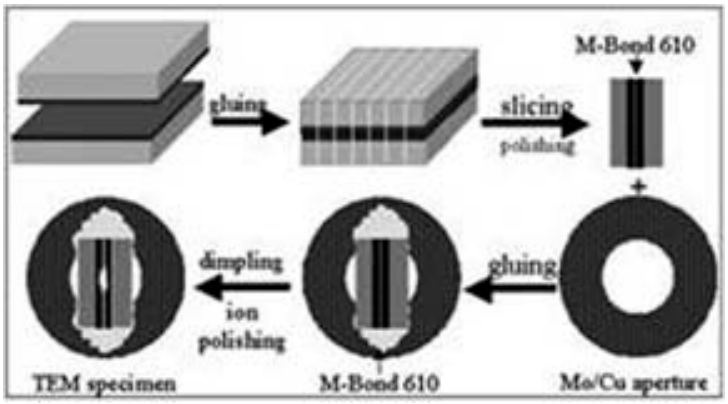

Figure 3.4 Schematic illustration showing basic steps for cross-section TEM sample preparation.

Figure 3.4 is a schematic illustration of cross-section TEM sample preparation procedure. The basic steps for preparing a cross-section TEM sample are:

1. Cut two 3×3 mm rectangular pieces from sample along a specific direction using diamond saw.

2. Glue these two as-cut slides face to face by joining the film side using M-bond 610 adhesive.

3. Polishing the sample on the cross section side sequentially conducted on diamond lapping films from 30 μm, 3 μm to 0.5 μm.

4. Mount the sample on a 3 mm copper ring and then grind using 1000 grit sand paper to gradually reduce the thickness of the sample.

5. Place the sample on a precision dimple grinder and polish the sample using copper wheel and fine diamond paste.

6. Using the Ar-ion mill system called Gatan model 691 precise ion polishing system (PIPS) to reduce the sample thickness until there is a hole produced close to the film area. The edges of the hole could be thin enough for TEM investigation.

3.3.2 Plan-view TEM Sample Preparation

The procedure of plan-view TEM sample preparation is shown in Figure 3.5. The steps involved are:

1. Cut a 2×2 mm sample piece using the diamond saw.

2. Glue the as-cut slide on a 3 mm diameter copper ring with the film side facing down using M-bond 610 adhesive.

3. Polish the sample using a 1000 grit sand paper.

4. Place the sample on a precision dimple grinder and polish the sample using copper wheel and fine diamond paste.

5. Use an Ar-ion milling PIPS to gradually reduce the sample thickness until there is a hole showing up on the sample. The thin areas close to hole edges could be good for later TEM investigation.

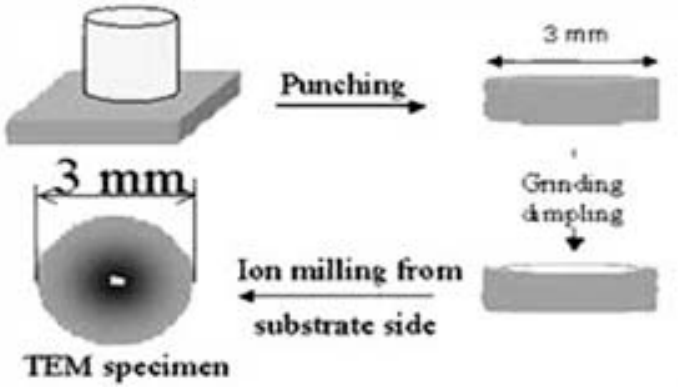

Figure 3.5 Schematic illustration showing the plan-view TEM sample preparation procedure.

CHAPTER 4

GROWTH AND MICROSTRUCTURE OF EPITAXIAL $BaTiO_3$ THIN FILMS ON MgO USING RF MAGNETRON SPUTTERING

4.1 Introduction

BTO is one of the most important ferroelectric perovskite materials due to their excellent dielectric, ferroelectric, piezoelectric and nonlinear optical properties [203-205] in capacitors, antennae, storage and electro-optical devices. The applications, such as waveguide devices require BTO to be fabricated in thin film form with long-range structural coherence, high crystal quality, preferred orientation and smooth surface, because any structural defects in the film could interrupt the wave transmission and degrade the efficiency of the devices [206, 207]. Thus, epitaxial thin films are highly desirable for the advanced device applications, especially the field where a larger film area is needed. Over the years, epitaxial BTO films have been deposited on various substrates ($LaAlO_3$ [208] and $SrTiO_3$ [209-213]) using a variety of methods including molecular beam epitaxy [209, 213, 215], PLD [216-218] and chemical vapor deposition [219, 220]. Among them, RF magnetron sputtering is becoming a very important deposition method due to its capability of depositing thin films over a large substrate area, in addition to the advantage of low cost, simplicity and reproducibility. Epitaxial $BaTiO_3$ films on MgO (001) substrates have been fabricated previously using magnetron sputtering [221-224].

Commonly, $BaTiO_3$ has a cubic perovskite structure with Ba at the cell corners, Ti in the body center, and O at the face centers at temperatures above its ferroelectric curie point (~130 °C) and a tetragonal structure (a= 3.993 Å, c= 4.034 Å) with Ti shifting of the center position resulting in permanent polarization of the structure along the c-axis. A variety of $BaTiO_3$ associated structures or compounds have been found in the BaO-TiO_2 and $BaTiO_3$-TiO_2 phase diagram since Rase and Roy published the first comprehensive phase equilibria study of the

$BaO\text{-}TiO_2$ system [95-97, 99, 101]. Some of the chemical compounds in this system have attracted great interests since they have been found to possess interesting physical properties such as ferroelectricity ($BaTiO_3$, $BaTi_2O_5$) or particular dielectric properties ($BaTiO_3$, $BaTi_4O_9$, $Ba_2Ti_9O_{20}$). For instance, ceramics containing $Ba_2Ti_9O_{20}$ or $BaTi_4O_9$ [102, 103] have been used as microwave dielectric resonator filters. The $BaTi_5O_{11}$ compound shows the potential for dielectric material [98]. The $BaTi_2O_5$ compound shows the promise for high phase transition temperature ferroelectric materials [104, 105]. The structural parameters of phases existing in $BaO\text{-}TiO_2$ system found in the literature are presented in Table 4.1 [96, 225]. It has been well known that the physical properties of deposited thin films can be affected by many factors, including structure and temperature of the substrate, rate of deposition, film thickness, chemical composition, and film microstructure. Among them, the microstructure of BTO films is crucial to the physical properties of the films and their practical applications.

Table 4.1 Structure parameters of the compounds in BaO-TiO2 system.

Phase	Symmetry	Space group	a/nm	b/nm	c/nm	α/°	β/°	γ/°	Ref.
$BaTi_2O_5$	Monoclinic	*A2/m*	0.940	0.393	1.690	90	103.5	90	[226]
$Ba_2Ti_5O_{12}$	Orthorhombic	Ammm	0.990	1.131	2.330	90	90	90	[227]
$Ba_6Ti_{17}O_{40}$	Monoclinic	*C2/c*	0.988	1.708	1.892	90	98.70	90	[228]
$Ba_4Ti_{13}O_{30}$	Orthorhombic	Cmca	1.706	0.986	1.405	90	90	90	[229]
$BaTi_4O_9$	Orthorhombic	*Pnmn*	1.453	0.379	0.629	90	90	90	[230]
$Ba_2Ti_9O_{20}$	Triclinic	*P*1	0.747	1.408	1.434	89.94	79.43	84.45	[231]
$BaTi_5O_{11}$	Monoclinic	P2/n	0.767	1.402	0.752	90	98.55	90	[232]
$BaTi_6O_{13}$	Triclinic	$P\bar{1}$	0.751	0.985	0.746	105.38	118.90	72.58	[233]
Ba_2TiO_4	Monoclinic	$P2_1/n$	0.612	0.770	1.050	90	93.8	90	[234]
$Ba_2Ti_{13}O_{22}$	Orthorhombic	*Bmab*	1.165	1.410	1.005	90	90	90	[235]

In this chapter, a home-made plasma assisted RF magnetron sputtering system has been used for depositing BTO films on MgO substrates. Epitaxial BTO films and the films composed with BTO induced new superstructures were obtained at different deposition conditions. The microstructure and the interface structure of epitaxial BTO films are discussed in detail. The structure models for the new BTO induced superstructures have been determined using HRTEM images and nano-beam electron diffraction (NBED) patterns. The accuracy of the structure models were further proved by comparing the experimental results and simulation images. The atomic structure, film microstructure and potential electric properties of the new superstructures/phases have been studied in detail.

4.2 Microstructure and Interface Structure in Epitaxial $BaTiO_3$ Thin Films on MgO Substrate

4.2.1 Epitaxial Growth of $BaTiO_3$ Thin Films on MgO Substrate

Figure 4.1 (a) shows a XPS survey spectrum of the as-deposited BTO film exhibiting mainly Ba, Ti, O and C peaks. The binding energy of this spectrum was calibrated using C 1s peaks at 284.5 eV. The binding energies of Ti $2p_{3/2}$ and $2p_{1/2}$ electrons of the investigated film are at 457.8 and 463.8 eV, respectively. The binding energy of O 1s is 530.4 eV, and that of Ba $3d_{5/2}$ and $3d_{3/2}$ are at 780.3 and 795.1 eV. The quantitative analysis shows that the as-deposited BTO film has a chemical composition of 19 at% Ba, 19 at% Ti and 62 at% O. The atomic ratio Ba : Ti : O in the film is about 1 : 1 : 3.26. The oxygen is a little higher than the stoichiometric $BaTiO_3$ bulk. The small C peak in the spectrum and residual oxygen is likely due to the surface contaminants from the environment.

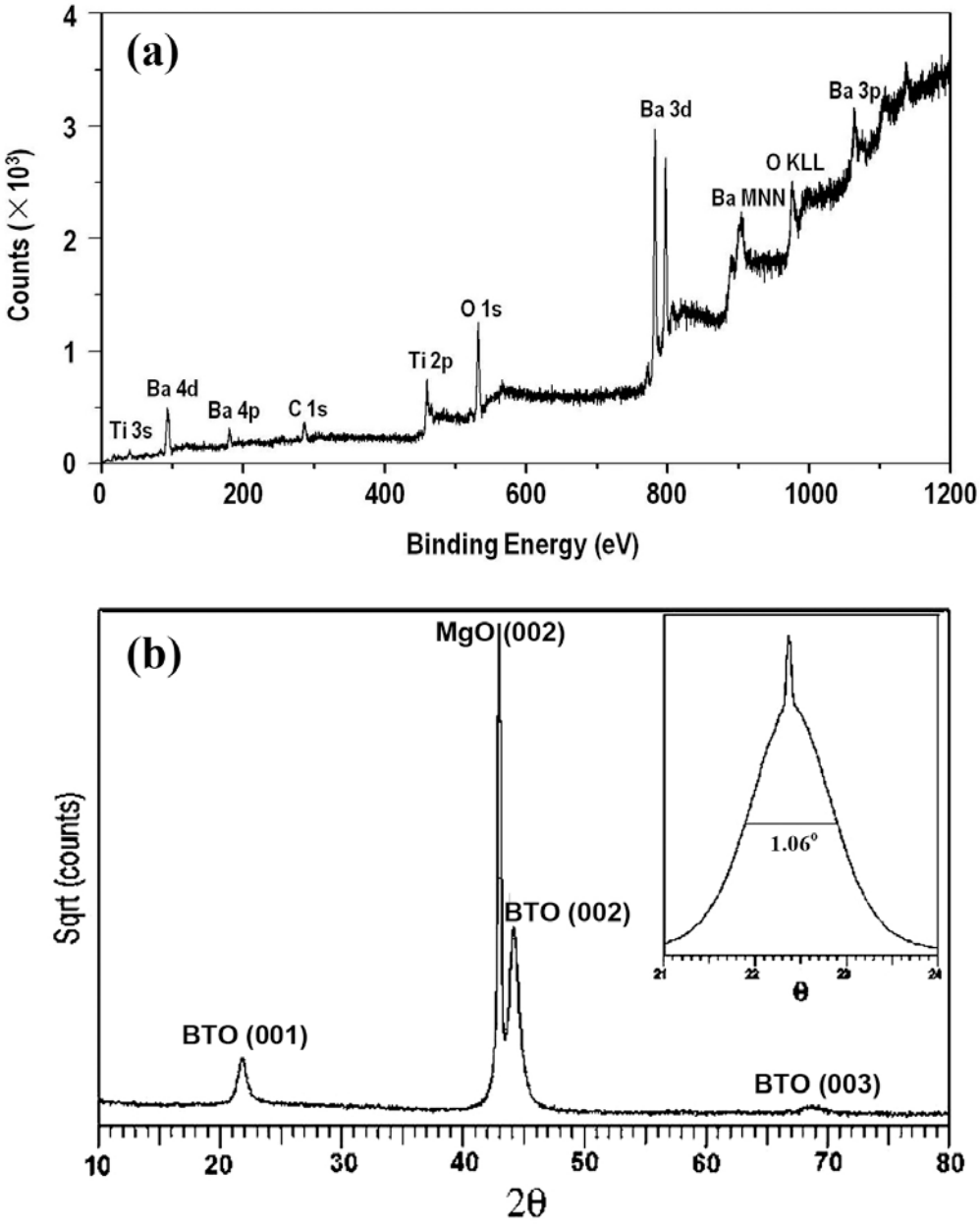

Figure 4.1 (a) XPS spectrum and (b) XRD θ–2θ scan and rocking curve (inset) of the $BaTiO_3$ thin film deposited on MgO substrate.

Figure 4.1 (b) shows a θ-2θ scan X-ray diffraction pattern and rocking curve from BTO (002) reflection (inset) of a BTO film deposited on MgO (001) substrate. Only the (00l) diffraction peaks from the film and the substrate are observed, which indicates that the film is epitaxially grown on the substrate. The rocking curve of the BTO (002) reflection of the thin film shows a

superposition of a narrow peak sitting on the top of a broad peak, as shown in the inset of Figure 4.1 (b). The FWHM of the broad peak is about 1.06^{o}, whereas the FWHM for the narrow peak can be roughly estimated to be 0.2^{o}. This result suggests that most BTO (002) planes of the thin film are parallel to the MgO substrate surface, while the rest part of the BTO (002) planes are slightly tilted away from the substrate surface. The lattice constant along the direction normal to the BTO film plane is about 4.11 Å. The out-plane lattice difference between the film and the substrate is -2.42% calculated using $(a_{BTO} - a_{MgO}) / a_{MgO}$ (a_{MgO}= 4.212 Å).

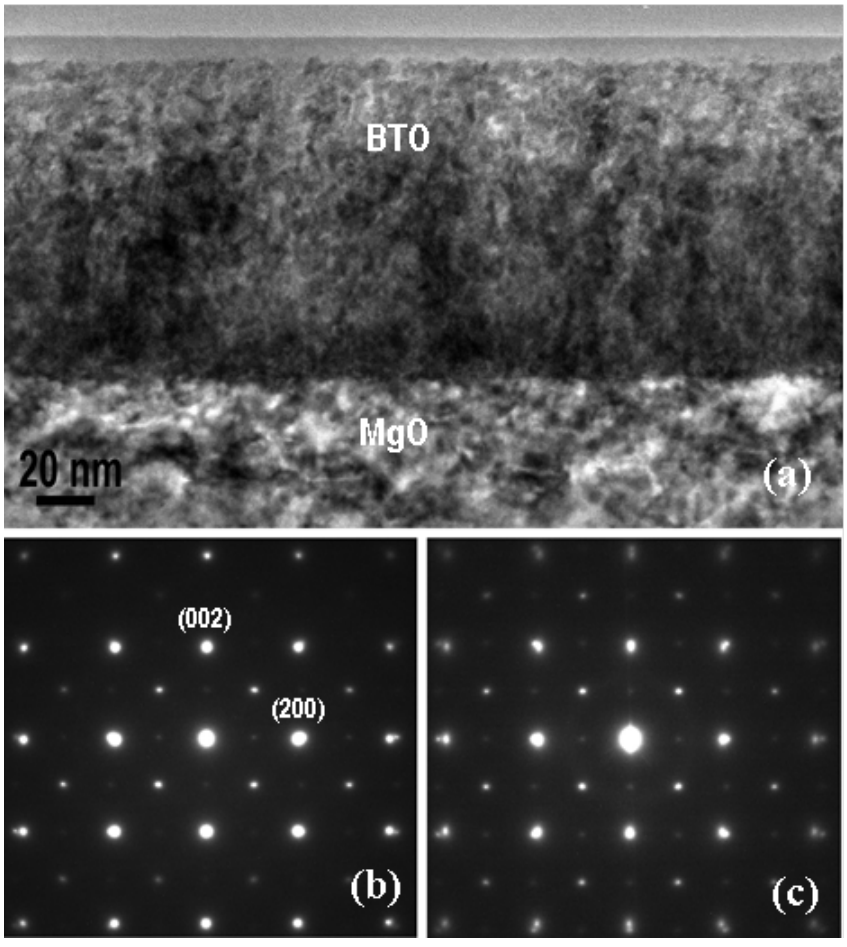

Figure 4.2 (a) Cross-section TEM image of BTO/MgO; (b) and (c) SAED pattern of the BTO film and the BTO/MgO interface.

The microstructure of as-deposited BTO films was investigated by TEM. Figure 4.2 (a) is a cross-section TEM image of the as-deposited BTO film on MgO substrate using magnetron

sputtering showing a continuous structure with a film thickness of 120 nm. The BTO film exhibits a very flat surface and a sharp interface with respect to MgO substrate. Figure 4.2 (b) is a typical SAED pattern taken from the BTO film. It shows a very clean single crystal diffraction pattern indicating that the as-deposited films have a good single crystal structure without forming any second phases or precipitates. The film was identified to have a tetragonal structure with a_{BTO} = 4.02 Å and c_{BTO} = 4.11 Å (The measurements of the lattice constants were calibrated using the MgO lattice constant, a_{MgO} =4.21 Å). The c_{BTO} / a_{BTO} ratio of the BTO tetragonal structure is ~1.02, a little larger than that of the bulk BTO (~1.01). The c-axis of the BTO film is parallel to the growth direction and the a-axis is in the film plane.

Figure 4.2 (c) is a SAED pattern taken from a cross-section BTO/MgO interface region with the electron beam parallel to $[100]_{MgO}$. It is a superposition of the electron diffraction patterns from the [100] zone MgO and the [100] zone BTO. Figure 4.2 (c) further confirms the epitaxial growth of the BTO film on MgO substrate. The orientation relationship between the film and substrate is $(001)_{BTO}//(001)_{MgO}$ and $<100>_{BTO}//<100>_{MgO}$. The lattice difference between the film and substrate along the growth direction is -2.46%, which is very close to the value obtained from the XRD measurement (-2.42%). The in-plane lattice mismatch between the film and substrate is about -4.14%.

4.2.2 Formation of Nanodomain Structure in Epitaxial $BaTiO_3$/MgO Thin Films

Figure 4.3 (a) is a plan-view HRTEM image of the BTO film exhibiting nanodomains and boundaries. The size of the nanodomains varies from 3 to 20 nm. The boundaries have a width varies from 0.5 to 1.5 nm. The electron diffraction patterns taken from a large area covering numerous domains show a very clean single crystal diffraction pattern with sharp diffraction spots (inset in Figure 4.3 (a)). The SAED pattern in Figure 4.3 (a) corresponds to the [001] zone diffraction pattern of the tetragonal BTO. It indicates that the nanodomains in the BTO thin films have the same crystallographic orientation.

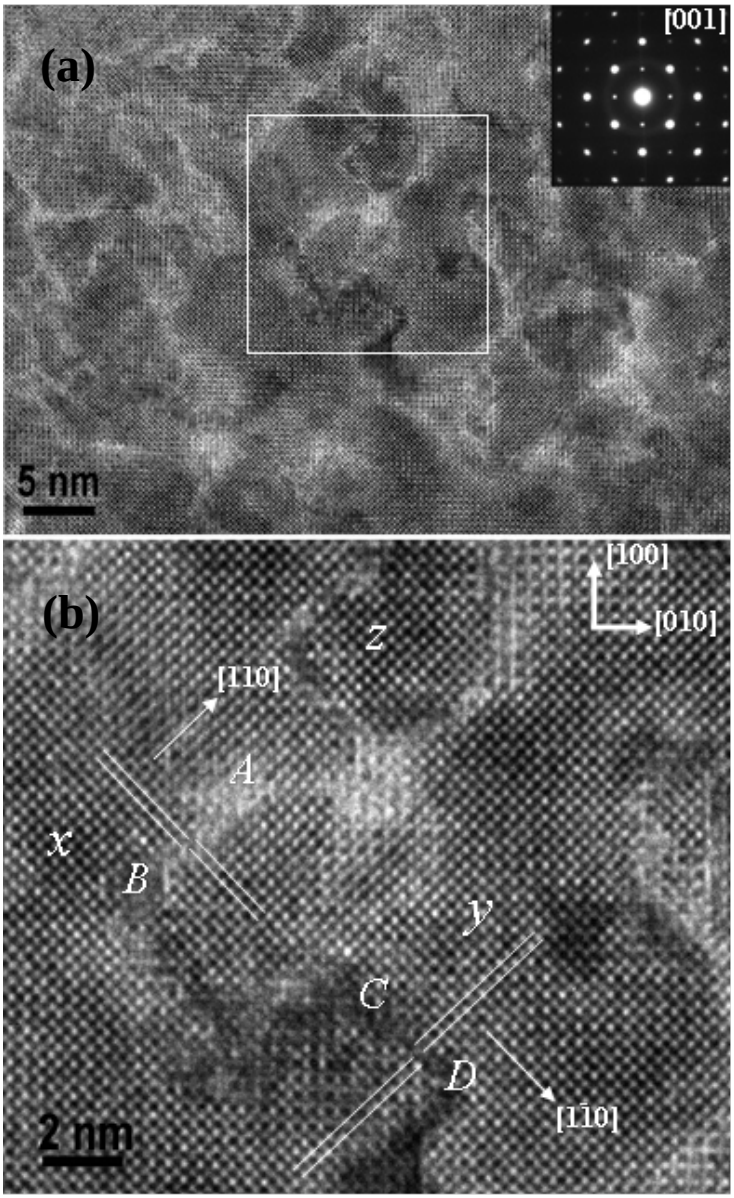

Figure 4.3 (a) HRTEM image and SAED pattern (insert) from a plan-view BTO film and (b) enlarged image of the marked area in (a).

Figure 4.3 (b) is an enlarged image of the marked area in Figure 4.3 (a) showing three nano domains (*x*, *y* and *z*) and the boundaries in between. The domain *x* is shifted with respect to the domain *y* by $\frac{1}{2}d_{(110)}$ along the [110] direction (boundary AB in Figure 4.3 (b)) and by $\frac{1}{2}d_{(1\bar{1}0)}$ along the $[1\,\bar{1}0]$ direction (boundary CD in Figure 4.3 (b)). Such displacement

relationship between the two domains can also be found between domain *x* and *z*, and between domain *y* and *z*. Previous studies showed that the defects observed in thin films, such as anti-phase boundary (APB), dislocations, are formed in association with the surface structure (steps, terraces and kinks) of the substrate [23]: (1) a film grown on a (001) MgO substrate surface that has a step with a height of $\frac{1}{2}a_{MgO}$ has a conservative anti-phase boundary between the two crystals on the adjacent terraces; (2) a film grown on a (001) MgO substrate surface that has a terrace with a width of odd number of $\frac{1}{2}a_{film}$ has a non-conservative anti-phase boundary; (3) a film grown on a (001) MgO substrate surface that has a kink and/or its associated terrace with a width of odd number of $\frac{1}{2}a_{film}$ has an APB with C-APB and NC-APB components between the two adjacent crystals.

The boundary structures observed in the BTO films fabricated using magnetron sputtering have similar characteristics to those previously observed in epitaxial (Ba,Sr)TiO3 thin films on MgO substrate [23] but with a much higher boundary density in the film. Non-conservative boundaries (with the displacement vector perpendicular to the boundary plane) were also frequently observed in the as-deposited epitaxial BTO films such as AB and CD. These results indicate that the nanodomains and boundaries are arisen from the MgO substrate surface structure. The small size of the domains and the high density of the boundaries might be arisen from a rough surface of the substrate.

Figure 4.4 (a) shows a cross-section HRTEM image of the BTO/MgO interface showing a typical interface structure between the film and the substrate. A wavy rough interface was formed at the interface. The distance between two adjacent wave peaks or valleys (such as *u* and *v*) is about 10 nm. Abruptly atomic sharp interface between the BTO film and the substrate was not observed in this heterostructure. The height between the position *u* and *z* is about 3 unit cells. Since the cross-section TEM shows only one-dimensional (1-D) information of the interface, a hill- or island- like 3-D interface structure would be expected to be formed between the film and the substrate. The hills or the islands and the valleys on the substrate surface (i.e.,

interface plane) are about several unit cells high and deep. In another words, a hill-like rough substrate surface was produced prior to the deposition of the films.

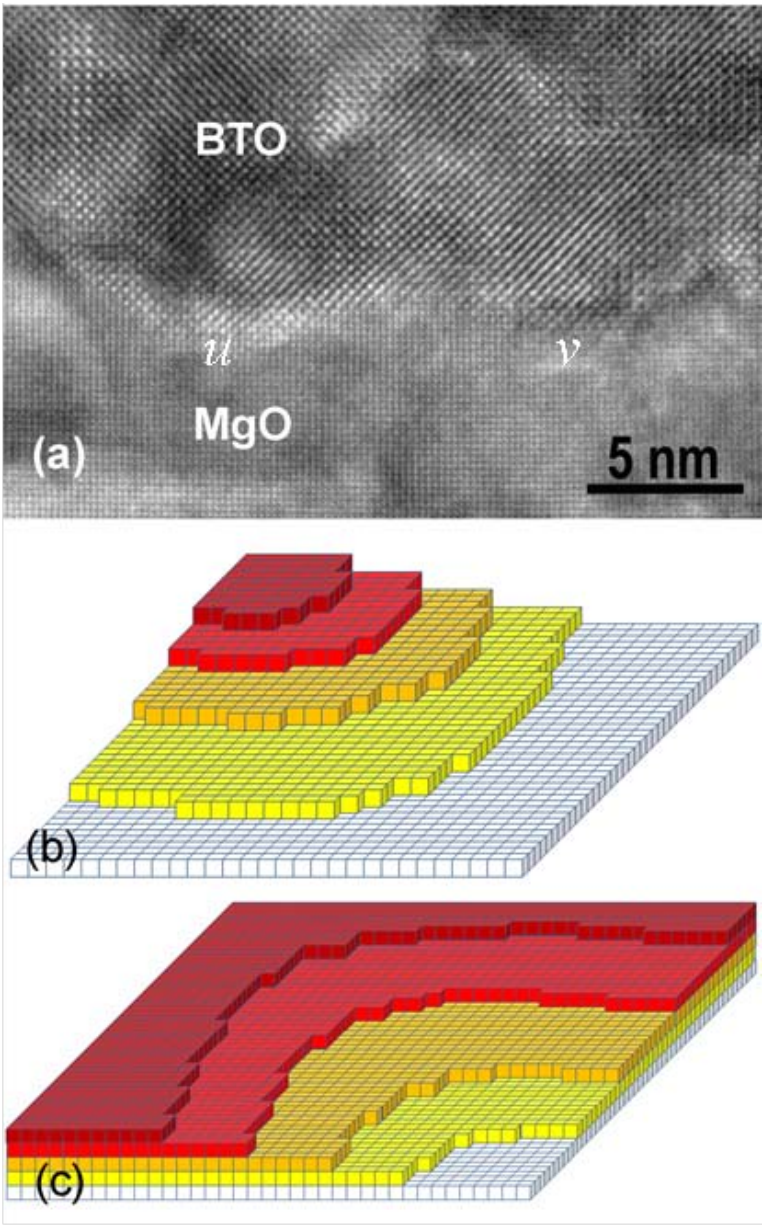

Figure 4.4 (a) Cross-section HRTEM image of the BTO/MgO interface; (b) and (c) schematic illustration of a possible 3D arrangement of the MgO unit cells on the substrate surface near the hill and valley region, respectively. One cube represents one MgO unit cell.

It is possible that such rough interface was induced during the substrate surface clean process. Before the film deposition, Ar^+ plasma was used to clean the MgO substrate surface to

reduce the surface contamination. The plasma clean could modify the MgO substrate surface structure and introduce large number of steps, terraces, and kinks on the surface which results in the nanodomain and boundaries in the BTO films. Figure 4.4 (b) and (c) schematically illustrate a possible three-dimensional arrangement of the MgO unit cells on the substrate surface near the hill and valley regions. It can be clearly seen that such surfaces roughness characteristics possess a tremendous larger number of surface steps, terraces and kinks compared to the flat surface of single crystal substrates. Such large number of step, terraces and kinks result in high density boundaries observed in plan-view TEM of the BTO film.

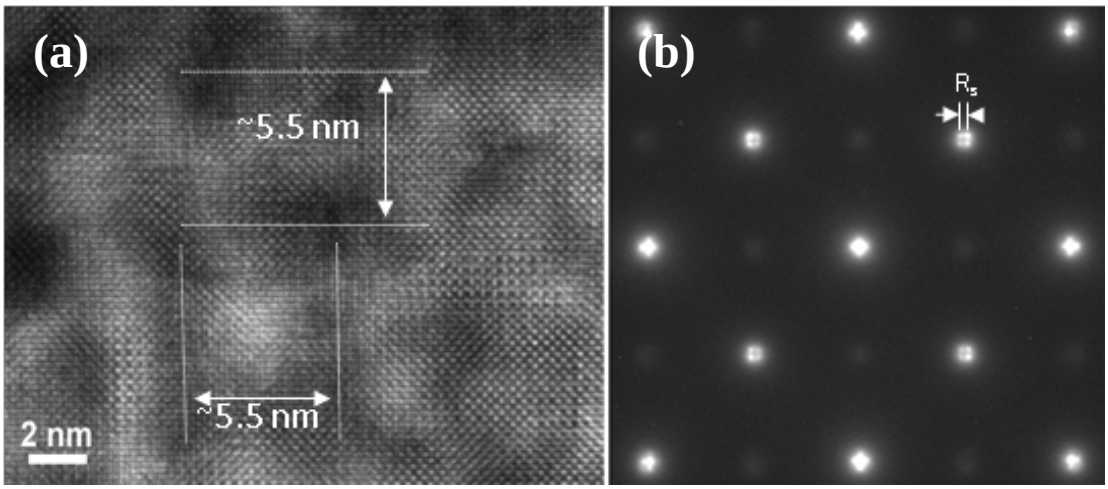

Figure 4.5 (a) Plan-view HRTEM and (b) EDP of 2-D BTO/MgO interface.

Figure 4.5 (a) and (b) show a HRTEM image and the corresponding SAED pattern of the two-dimensional BTO/MgO interface viewed in a plan-view TEM sample. Figure 4.5 (b) is different from that shown in Figure 4.2 (c) and shows more diffraction spots than a simple superposition of the EDPs of BTO [001] zone and MgO [001] zone. The extra diffraction spots in Figure 4.5 (b) were produced from the double diffraction. The lattice mismatch (Δδ) between the film and substrate is -3.68% as determined using the formula:

$$\Delta\delta = \frac{-1}{\frac{L\lambda}{R_s d_{(200)}^{MgO}} + 1} \qquad (4.1)$$

Where L is the camera length, λ is the wavelength of the electron beam, and R_s is the distance between two adjacent double diffraction spots, measured from the EDP [131, 236, 237]. The lattice mismatch obtained from the 2-D interface plane is smaller than that measured from the cross-section TEM (-4.14%). This result is different from some previous observations that the lattice mismatch between the film and the substrate obtained from the 2-D interface plane is larger than that measured from the cross-section TEM [216, 217]. The present smaller lattice mismatch obtained from the 2-D interface using plan-view TEM than that obtained using cross-section TEM could be possibly due to the rough MgO substrate surface or rough interface as observed in Figure 4.4 (a).

The bright regions in Figure 4.5 (a) correspond to the commensurate domains of the BTO film and the MgO substrate, whereas the dark regions correspond to the strained domain boundary areas where the misfit dislocations are located. It has been reported that misfit dislocations in the (Ba,Sr)TiO_3/MgO heterostructure were periodically distributed at the interface [23]. The size of the commensurate domain (d_s) between the film and the substrate at the interface, (i.e., the domain size between the adjacent misfit dislocations) is about 5.5 nm calculated using $d_s = L\lambda / R_s$. This is very close to the distance between the dark regions in Figure 4.5 (a). This means that quasi periodically distributed misfit dislocations were formed at the interface for every 26 (200) or (020) planes of MgO along the [100] or [010] direction.

The smaller lattice mismatched measured using plan-view TEM (-3.68%) than that measure using cross-sectional TEM (-4.14%) might be understood in the following. Tetragonal BTO has a lattice constant a_{BTO} = 4.02 Å and c_{BTO} = 4.11 Å. When the film grows on MgO substrate (a_{MgO} =4.21 Å) with its c-axis parallel to the growth direction, the unit cell in the film plane is smaller than the corresponding unit cell of the MgO substrate. It can be assumed that the growth of the epitaxial BTO film follows a 2-D layer-by-layer growth mode and the growth of the film initiates at the bottom layer on the valley of the surface which can be schematically illustrated in Figure 4.6.

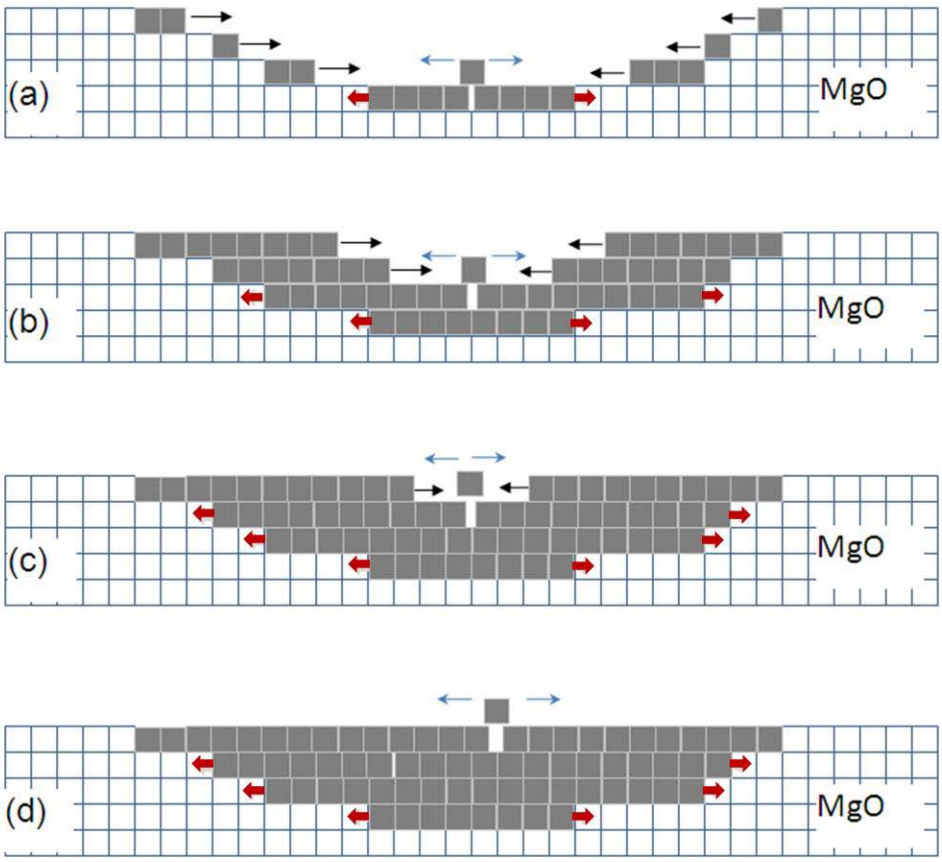

Figure 4.6 Schematic illustration of the growth process of (a) first; (b) second; (c) third and (d) fourth layer of the epitaxial BTO film.

During growth of the first monolayer on the terraces, the BTO unit cells will migrate to the step location due to the energetic preference. It can be found from Figure 4.4 (a) that the width of the bottom terraces at the valley *u* and *v* is about 8 and 6 MgO unit cells, respectively. These terraces are not wide enough to form a misfit dislocation at the interface (The terrace is required to be at least 20 unit cells wide for accommodating a misfit at the interface). After the complete growth of the first monolayer, small gap between the BTO unit cells will be formed (Figure 4.6 (a)), which provides space for the strain relaxation of the of the BTO layer. Accordingly, the BTO unit cell dimension in the a-b plane on the terrace is larger than that of the bulk BTO and results in a smaller lattice mismatch between the film and the substrate. The same growth mechanism can be applied to the growth of the second (Figure 4.6 (b)), third

(Figure 4.6 (c) and fourth (Figure 4.6 (d)) BTO layer in the valley regions. Because of the small width of the terraces, very few misfit dislocations will be formed at the interface after the complete of the first several BTO layers.

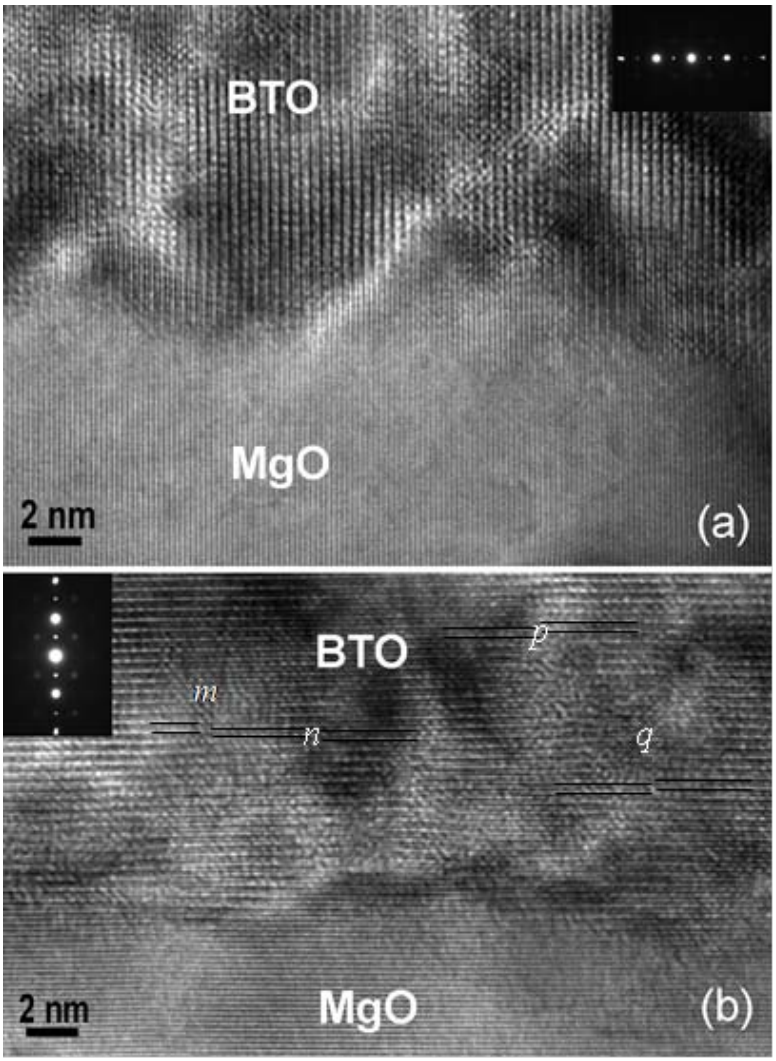

Figure 4.7 Cross-sectional HRTEM image of the BTO/MgO interface taken with the $[100]_{MgO}$ being tilted away from the incident electron beam to let only (a) the (0*k*0) and (b) the (00*l*) diffraction spots be present.

Figure 4.7 (a) and (b) shows a cross-sectional HRTEM image of the BTO/MgO interface taken with the $[100]_{MgO}$ being tilted away from the incident electron beam to let only the (0*k*0) and (00*l*) diffraction spots presented (inset). Both images clearly show rough interface structure.

Only the (0*k*0) (*k*=1 and 2) lattice fringes were presented and no misfit dislocations were observed at the interface in Figure 4.7 (a). Figure 4.7 (b) shows lattice fringes of (00*l*) planes. Boundaries such as marked by *m*, *n*, *p* and *q* were frequently observed in the BTO film (Figure 4.7 (b)). The domains beside a boundary were shifted along the growth direction by $c_{BTO}/2$. The size of the domains in Figure 4.7 (b) varies from ~4 to 10 nm, which is very close to the value measured from the plan-view TEM. These boundaries were arisen from the steps on the substrate surface [23] and the large number of the boundaries indicates high density of the steps on the MgO substrate surface. Besides, the BTO (002) lattice fringes near the interface observed in Figure 4.7 (b) are not exactly parallel to the MgO (002) fringes. The former ones are tilted away from the latter by about ±1.5^{o}. Such tilting of BTO (002) near the interface produces the broadening of the BTO (002) rocking curve, as observed in the inset of Figure 4.1 (b).

4.3 Discovery of Two New $BaTiO_3$ Induced Phases Fabricated Using RF Magetron Sputtering

4.3.1 New Stuctures/Phases Formed in As-deposited Epitaxial Thin Films on MgO Substrate

Figure 4.8 shows a XRD θ-2θ scan and rocking curve (inset) of a BTO film deposited on MgO (001) substrate using RF magnetron sputtering. It presents three diffraction peaks with the lattice spacing of 2.10 Å, 2.02 Å and 1.97 Å, respectively. The strongest peak with the lattice spacing of 2.10 Å corresponds to the MgO (002) reflection, and the weakest peak with the lattice spacing of 2.02 Å (denoted as BTO $(002)_p$) can be identified to be (002) reflection of the perovskite $BaTiO_3$. The peak with the lattice spacing of 1.97 Å (denoted by BTO $(002)_s$) cannot be identified using the known BTO related structures indicating formation of new structures or new phases in the film. The observation of only BTO $(002)_p$ and BTO $(002)_s$ diffraction peaks from the film indicates that the as-deposited thin films are epitaxially grown from MgO substrate or highly orientation preferred along normal axis of the film. The rocking curve of the BTO $(002)_s$ reflection with FWHM of about 0.8° suggests that most BTO $(002)_s$ planes of the thin film are parallel to the MgO substrate surface.

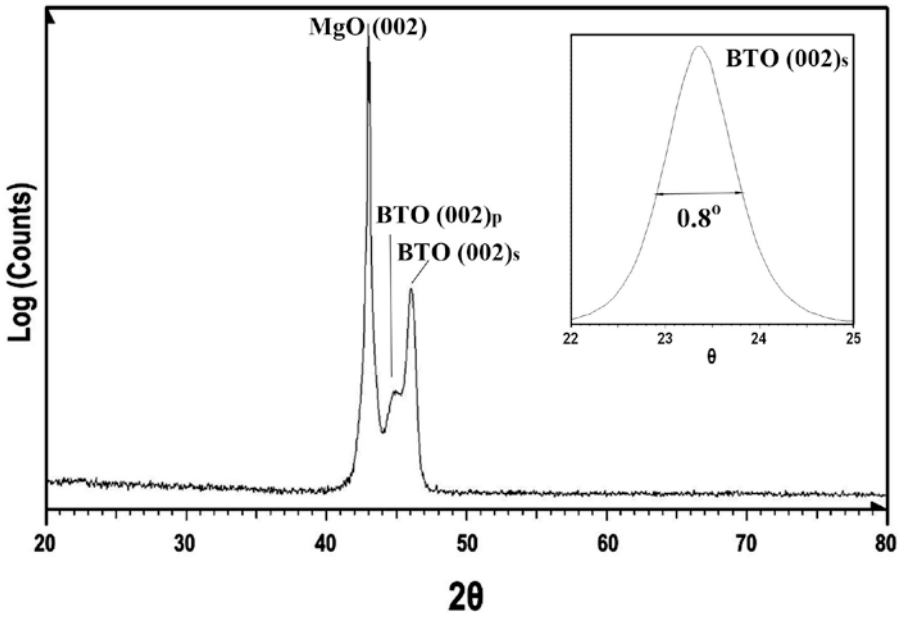

Figure 4.8 XRD θ-2θ scan and rocking curve (inset) of the BTO thin film deposited on MgO substrate.

The microstructure of as-deposited BTO films was investigated using analysis TEM. Figure 4.9 (a) is a cross-section TEM image of the as-deposited BTO film on MgO substrate showing a continuous structure with a thickness of 166 nm. The BTO film exhibits a very flat surface and a sharp interface with respect to MgO substrate. Figure 4.9 (b) is a typical SAED pattern taken from the BTO film with the incident electron beam parallel to the MgO [100] showing a single crystal clean diffraction pattern. The lattice spacing of the strong diffraction spots ξ and ω in Figure 4.9 (b) is 2.84 Å and 2.04 Å, which is very close to the (011) and (002) lattice spacing of $BaTiO_3$ perovskite structure (a= 3.993 Å, c= 4.034 Å), respectively. Thus, the strong diffraction spots in Figure 4.9 (b) present one set electron diffraction pattern similar to the [100] zone EDP of perovskite $BaTiO_3$. However, the presence of weak spots, e.g. ζ, in Figure 4.9 (b) cannot match the diffraction from perovskite $BaTiO_3$, therefore could be a new crystal structure derived from the perovskite $BaTiO_3$. Figure 4.9 (c) is a SAED pattern taken from the interface of BTO/MgO with electron beam parallel to $[100]_{MgO}$. It shows a superposition of the EDP from the $[100]_{MgO}$ zone and Figure 4.9 (b). It also indicates the epitaxial growth of the new

structure with respect to MgO substrate as the orientation relationship shown in Figure 4.9 (c). Figure 4.9 (d) and (e) exhibit two dark-field TEM images obtained using the diffraction spot ζ and ξ in Figure 4.9 (b), respectively. The bright area (marked as **B**) and dark area (marked as **D**) in Figure 4.9 (d) appear as dark and bright areas in Figure 4.9 (e). The reversal contrast in Figure 4.9 (d) and (e) confirms that the diffraction spots ζ and ξ are scattered from different domain structures in the thin films.

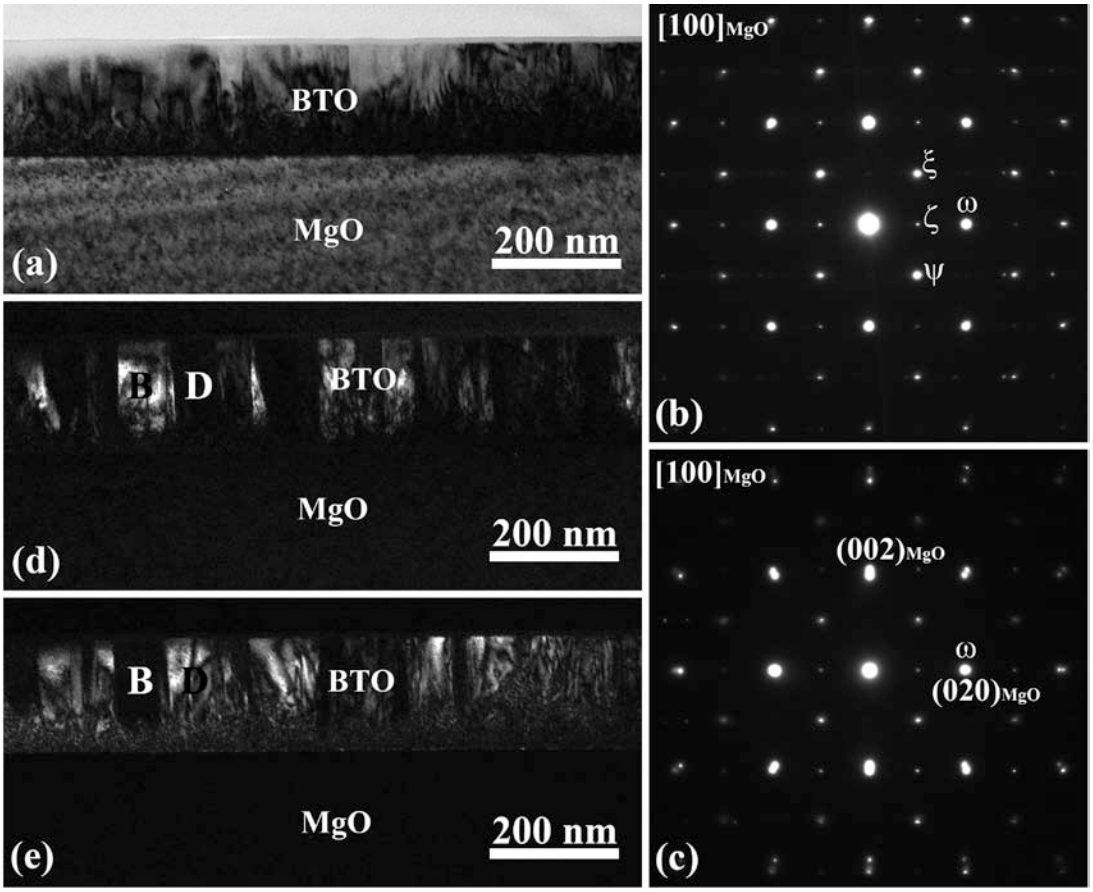

Figure 4.9 (a) Cross-section TEM image of BTO/MgO; (b) and (c) SAED pattern of the BTO film and the BTO/MgO interface; (d) and (e) dark-field image taken from ζ and ξ diffraction spots in (b), respectively.

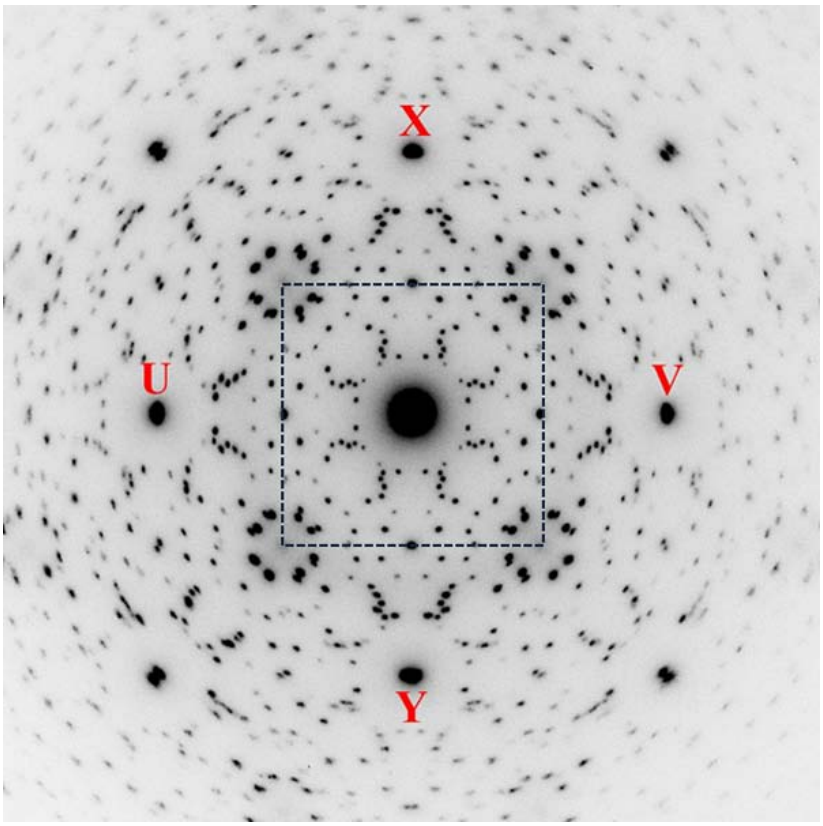

Figure 4.10 Inverse SAED pattern taken from a plan-view TEM specimen with electron beam parallel to $[001]_{MgO}$.

Figure 4.10 is an inverse SAED pattern taken from a large film area of a plan-view TEM foil with the incident electron beam parallel to the MgO [001] direction. It exhibits a very complicated pattern with many more diffraction spots than the EDP of the [001] zone of the perovskite $BaTiO_3$. However, regardless of the complexity, all of the diffraction spots are orderly distributed over the entire diffraction pattern and exhibit a four-fold symmetry. The strong diffraction spots ***U***, ***V***, ***X*** and ***Y*** have a lattice spacing of 2.0 Å, which is very close to the lattice spacing of the {200} planes of the perovskite BTO structure. All the weak spots indicate more complicated structures than perovskite-type BTO were formed in the as-deposited films. This SAED pattern has been carefully studied and finally found that it is constructed with ED patterns from two superstructures, and each superstructure has four orientations, respectively. In other word, Figure 4.10 is a superposition of eight EDPs.

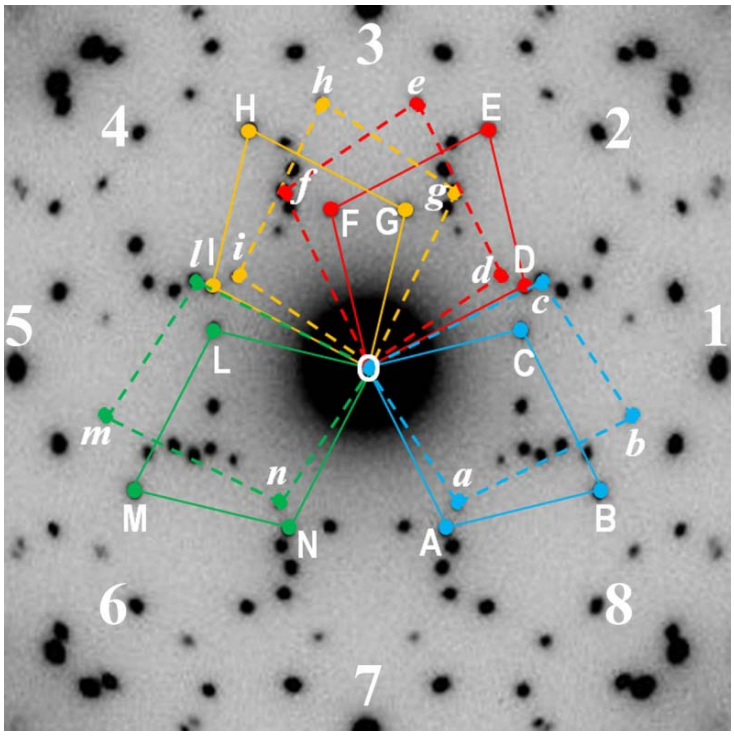

Figure 4.11 Enlarged pattern of marked area in Figure 4.10 and schematic illustration of 8 reciprocal unit cells.

Figure 4.11 shows an enlarged pattern of the marked area in Figure 4.10 and the schematic illustration of the corresponding eight reciprocal unit cells. The eight diffraction patterns can be classified into two groups corresponding to two structures: (1) group Γ_γ, which consists of ***OABC***, ***ODEF***, ***OGHI*** and ***OLMN***, and (2) group H_β, which consists of ***Oabc***, ***Odef***, ***Oghi*** and ***Olmn***. The unit cells ***OABC***, ***ODEF***, ***OGHI*** and ***OLMN*** in group Γ_γ are identical and have the same structure, but with different orientations. Each unit cell in Γ_γ has certain orientation relationship related to others and can be obtained by certain symmetry operations: The unit cell ***ODEF*** and ***OLMN*** can be obtained via rotating ***OABC*** and ***OGHI*** by 90° around the normal of the diffraction pattern, respectively. The unit cell ***OGHI*** and ***OLMN*** can be obtained from ***ODEF*** and ***OABC*** through a mirror (vertical plane passing through spots 3 and 7) symmetry operation, respectively.

Similarly, the unit cells ***Oabc***, ***Odef***, ***Oghi*** and ***Olmn*** in group H_β are also identical but with different orientations. The orientation relationships between the unit cells in group H_β are similar to those in group Γ_γ. The unit cell ***Odef*** and ***Olmn*** can be obtained via rotating ***Oabc*** and ***Oghi*** by 90° around the normal of the diffraction pattern, respectively. The unit cell ***Oghi*** and ***Olmn*** can be obtained from ***Odef*** and ***Oabc*** through a mirror (vertical plane passing through spots 3 and 7) symmetry operation, respectively. The above results indicate that there are two different phases formed corresponding to group Γ_γ and group H_β. The reciprocal unit cell parameter measured from Figure 4.11 for phase Γ_γ is a^*_Γ **= *OA*** = 8.05 Å and b^*_Γ **= *OC*** = 8.71Å with the angle between ***OA*** and ***OC*** (γ_Γ) is 77°. The reciprocal unit cell parameter for phase H_β is a^*_H **= *Oa*** = 8.86 Å and b^*_H **= *Oc*** = 7.15 Å with the angle between ***Oa*** and ***Oc*** (γ_H) is 82°.

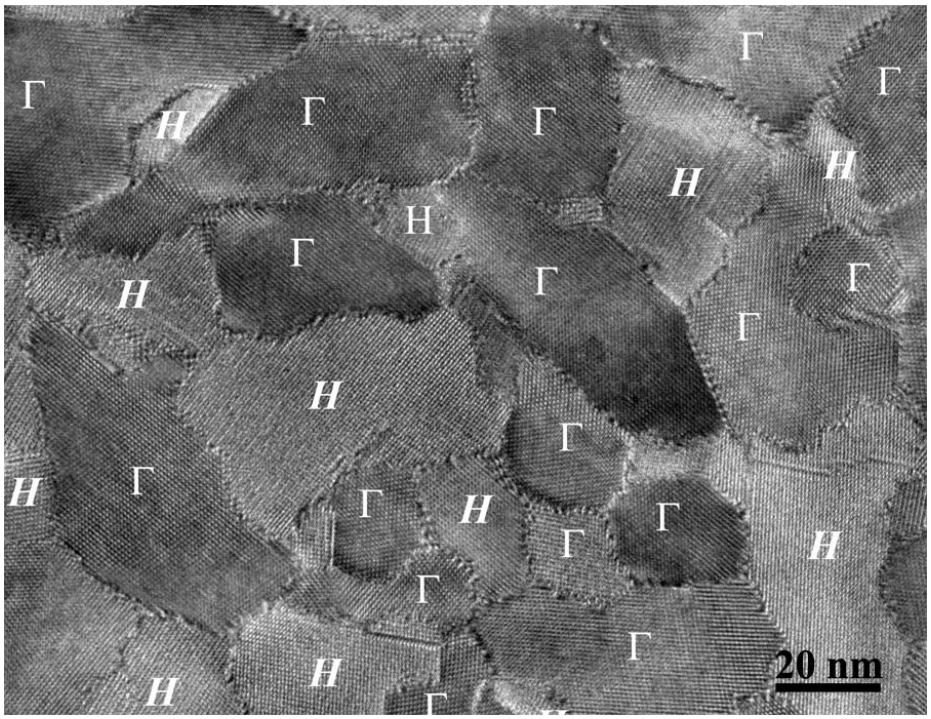

Figure 4.12 Plan-view TEM image of as-deposited BTO film showing two phases Γ_γ and H_β.

Figure 4.12 is a plan-view TEM image showing a grainy structure on the top surface of as-deposited film. The grain size is varied a lot from 5 nm to 80 nm. Each grain can be considered as a single domain with different structure orientations similar as one of the four

domains of either Γ_γ or H_β phase. Thus, the grains can be classified into two phases Γ_γ and H_β, and marked as Γ and H, respectively. More Γ_γ phase can be observed in Figure 4.12 than H_β phase, which is consistent with the SAED pattern shown in Figure 4.10 showing the stronger intensities of the diffraction spots from phase Γ_γ than those from phase H_β.

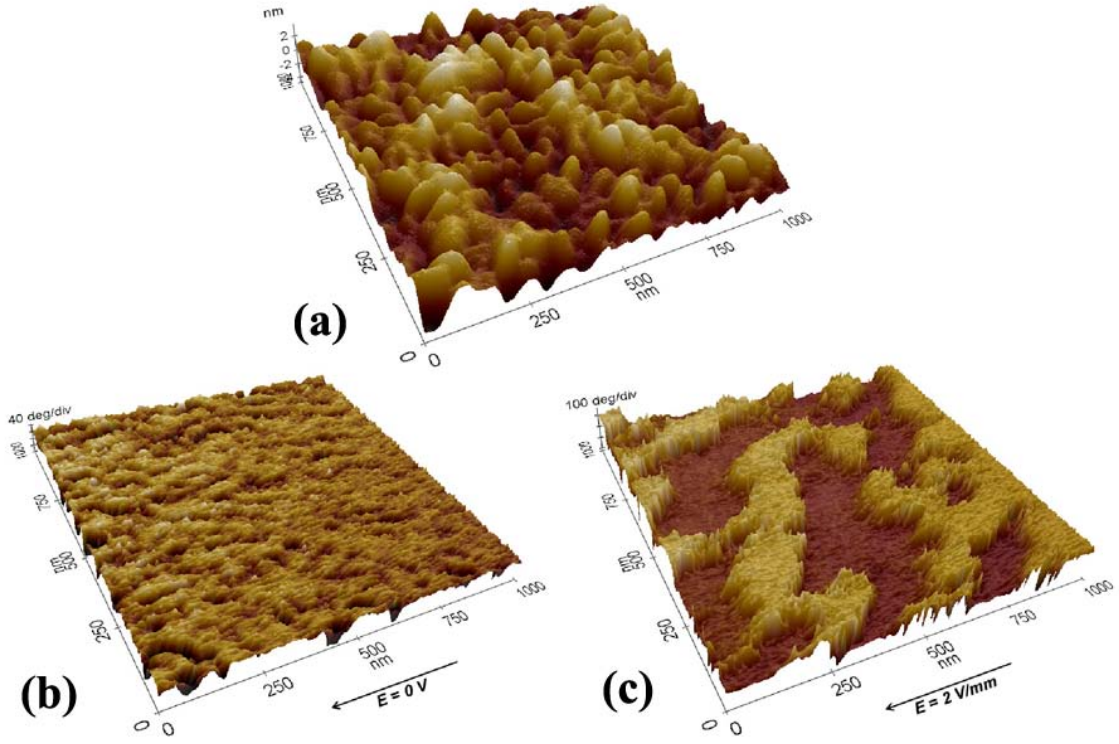

Figure 4.13 (a) Contact AFM of the as-deposited BTO film; (b) and (c) corresponding enhanced EFM image taken in an external electrical field 0 and 2 V/mm, respectively.

Figure 4.13 (a) is a 3D AFM image of the BTO film obtained using contact mode within a scan area of 1 × 1 μm^2 showing a granular structure. The grain size varies from 41 to 90 nm with the majority grain having an average size of ~40 nm, which is consistent with the data obtained from plan-view TEM. The average roughness of the film is about 1.03 nm, indicating a flat surface. Contact electrostatic force microscopy (EFM) measurements were performed to investigate the local polarization from different orientation domains/phases of as-deposited films under external electric fields in the same AFM system. An external electric field was applied parallel to sample surface by connecting bias on both ends of the sample surface using silver

paste. Then the contact-EFM images provide information of local phases/domains polarization condition corresponding to applied external electric field. Figure 4.13 (b) and (c) are enhanced contact-EFM images of the same area as shown in Figure 4.13 (a), obtained with an applied external electric field of 0 and 2 V/mm, respectively. Without applying any external electric field (V=0 V/mm), Figure 4.13 (b) shows nearly a homogenous contrast indicating a uniform polarization over the surface. After applied an electric field of 2 V/mm, the polarization of some areas was switched upside down. The dark regions in Figure 4.13 (c) represent their polarization direction is opposite to that in the bright regions. If the polarization vector in bright regions in Figure 4.13 (b) and (c) is assumed to point up, then the polarization vectors in dark regions in Figure 4.13 (c) point down. The total area of the dark regions in Figure 4.13 (c) is larger than that of the bright area. Since the as-deposited film has two phases Γ_γ and H_β. They are both c-axis oriented. Based on the plan-view TEM observation, the films exhibit more Γ_γ phase than H_β phase, it can be assumed that the dark regions in Figure 4.13 (c) are corresponding to Γ_γ phase, whose polarization vector is easily switched under an external electrical field compared to H_β phase.

4.3.2 Structure Determination of $\Gamma\gamma$ phase

Figure 4.14 (a) shows a nano-beam electron diffraction pattern (NBED) taken from a Γ_γ phase grain in the plan-view TEM foil with the electron beam parallel to [001] direction of film. It shows 2-fold symmetry. The strong spots marked with ***u, v, x*** and ***y*** have a d-spacing of 2 Å which is very close to the {200} reflections of the perovskite $BaTiO_3$ structure. The diffraction spots are found to be orderly arranged along **OC** and **OA** directions, which are referred to [010] and [100] direction of the Γ_γ phase. The d-spacing for diffraction spots **C** and **A** is about 8.71 Å and 8.05 Å, respectively. The angle between **OC** and **OA** is about 77°.

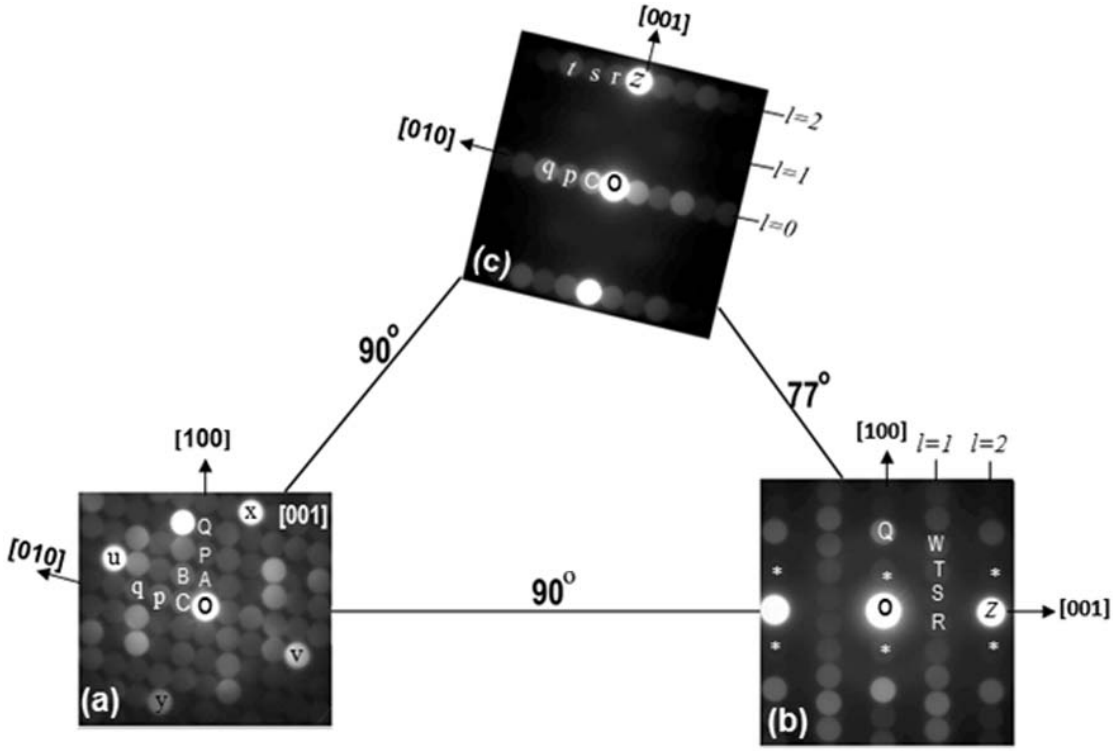

Figure 4.14 NBDPs of $\Gamma\gamma$ phase (a) [001] zone; (b) [010] and (c) [100] zone and their orientation relationship.

Tilting the Γ_γ phase along the [100] direction from Figure 4.14 (a) by 90°, a NBED as shown in Figure 4.14 (b) can be obtained from a cross-section TEM sample. The diffraction spot ***Z*** is corresponding to (002) while the (001) spot is absent in Figure 4.14 (b). The diffraction spot **Q** in Figure 4.14 (b) is consistent with the **Q** spot in Figure 4.14 (a) with the same d-spacing. Accordingly, the spot **Q**, **R**, **S**, **T** and **W** can be indexed as (600), ($\bar{1}$01), (101), (301) and (501), respectively. Thus, the diffraction spots (*h 0 l*) of the Γ_γ phase with $h + l = 2n+1$ (n=integers) are invisible in the NBED pattern along [010] direction of Γ_γ phase. The extra spot marked as "*" in Figure 4.14 (b) are coming from the other grains due to the difficulty of getting single domain from such small grain size investigated. The diffraction spot **A** and **P** in Figure 4.14 (a) can be indexed as (200) and (400), respectively. The NBED pattern shown in Figure 4.14 (c) can be obtained by tilting the Γ_γ phase in Figure (a) 90° along the [010] direction. The diffraction spot **C**, **p** and **q** in Figure 4.14 (a) and (c) can be indexed as (0$\bar{1}$0), (0$\bar{2}$0) and (0$\bar{3}$0), respectively.

And the spot **r**, **s**, and **t** in Figure 4.14 (b) can be indexed as $(0\bar{1}2)$, $(0\bar{2}2)$ and $(0\bar{3}2)$, respectively. Thus, the diffraction spots *(0 k l)* of the Γ_γ phase with *l = 2n+1* (n=integers) are invisible in NBED pattern along [100] direction of Γ_γ phase. The indices of the market diffraction spots in Figure 4.14 are listed in Table 4.2.

Table 4.2 Indices of the major diffraction spots of the Γ_γ.

Γ_γ ***phase***					
Label	*Index*	*Label*	*Index*	*Label*	*Index*
A	(200)	**R**	$(\bar{1}01)$	**λ**	(230)
B	$(2\bar{1}0)$	**S**	(101)	**δ**	$(\bar{4}10)$
C	$(0\bar{1}0)$	**T**	(301)	**χ**	$(\bar{6}10)$
P	(400)	**W**	(501)	**κ**	(430)
Q	(600)	**Z**	(002)	**u**	$(2\bar{4}0)$
p	$(0\bar{2}0)$	**r**	$(0\bar{1}2)$	**v**	$(\bar{2}40)$
q	$(0\bar{3}0)$	**s**	$(0\bar{2}2)$	**x**	$(\bar{8}20)$
		t	$(0\bar{3}2)$	**y**	$(\bar{8}\bar{2}0)$

Figure 4.15 (a) shows a plan-view HRTEM image of Γ_γ phasem grain. It exhibits very different characteristics from the perovskite $BaTiO_3$ structure. Rhombic repeating units with the dimensions of 8.94 Å and 8.25 Å and the angle of 77° were clearly seen in the image. Figure 4.15 (b) is a HRTEM image taken from a cross-section TEM foil with the electron beam parallel to the [010] axis of the Γ_γ phase. Face centered unit with the dimensions of 16.50 Å and 3.94 Å can be clearly seen in the image. The unit cell dimension along the ***a***-axis in Figure 4.15 (b) is twice of the repeating unit cell size (½***a***) in Figure 4.15 (a). Figure 4.15 (c) is a HRTEM image taken from another cross-section TEM foil with the electron beam parallel to the [100] axis of the Γ_γ phase. The unit cell has the dimensions of 8.94 Å (***b***- axis) and 3.94 Å (***c***-axis). The repeating unit dimension along the ***c***-axis in Figure 4.15 (c) is half of that observed in Figure 4.15 (b). From above results, it is can be concluded that the Γ_γ phase have a monoclinic structure with the lattice parameters of a=16.49 Å, b=8.94 Å, c=3.94 Å and α=β=90°, γ=77°.

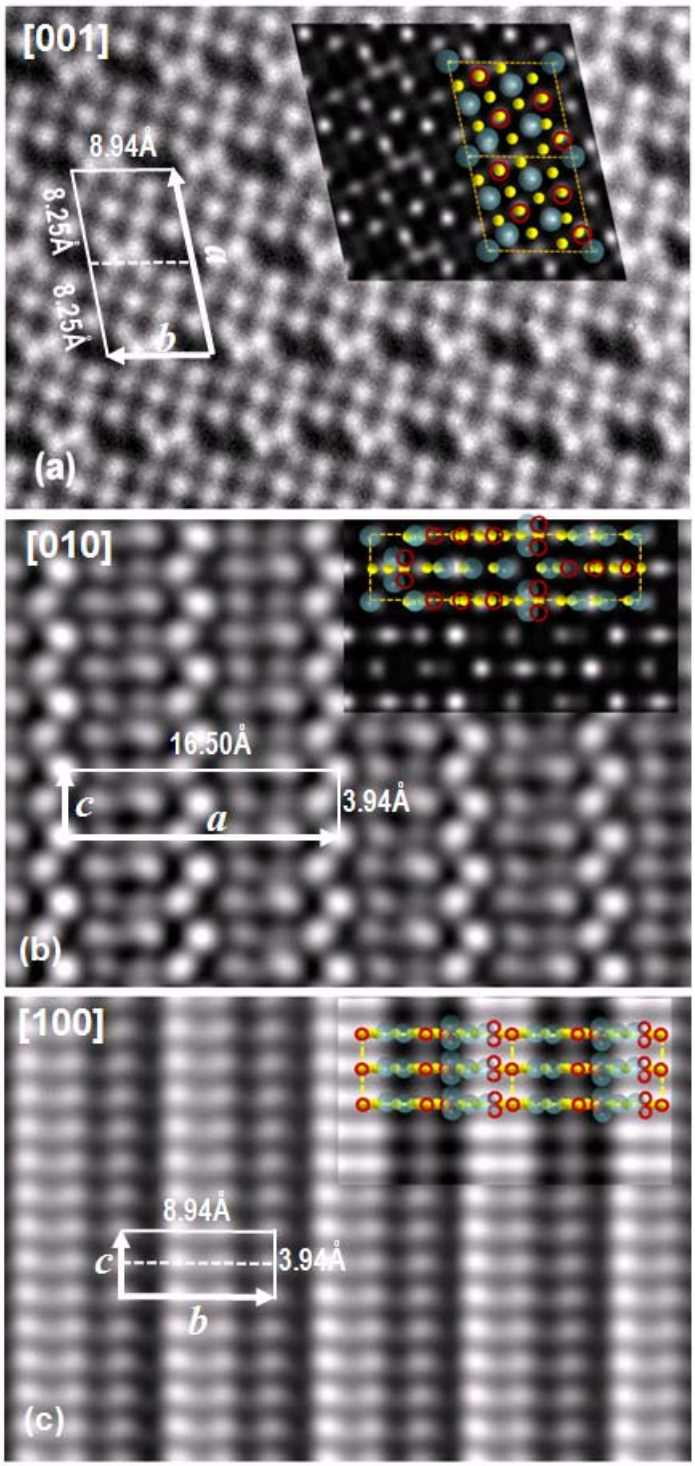

Figure 4.15 HRTEM image of phase Γ_γ viewed along the (a) [001] in plan-view sample; (b) [010] and (c) [100] in cross-section samples. Inset: relevant projection of the structural model and the corresponding simulated HRTEM of the Γ_γ phase.

A structure model of the Γ_γ phase can been obtained by using electron diffraction patterns and HRTEM images. The atomic positions have been carefully investigated in HRTEM images from all three [100], [010], [001] directions of Γ_γ phase. Finally, it can be determined to be $(Ba_5Ti_4O_{13})_2$ with a monoclinic structure and space group of ***Cm*** (No. 8, c-unique axis). The lattice parameters for $(Ba_5Ti_4O_{13})_2$ is designated to be a=16.49 Å, b=8.94 Å, c=3.94 Å and γ=77°. The atomic positions of the atoms are listed in Table 4.3.

Table 4.3 Atomic position of the atoms in $(Ba_5Ti_4O_{13})_2$

Atom	x/a	y/b	z/c	Atom	x/a	y/b	z/c
Ba1	0	0	0.5	**Ti3**	0.2777	0.3940	0
O1	0.0100	0.5000	0	**O7**	0.2650	0.3888	0.5
Ti1	0.0555	0.2777	0	**O8**	0.3000	0.8300	0.5
O2	0.0650	0.7800	0	**O9**	0.3200	0.1666	0
O3	0.1111	0.0555	0	**Ba4**	0.3333	0.6666	0
Ba2	0.1200	0.5555	0.5	**O10**	0.3900	0.4800	0.5
O4	0.1666	0.3333	0	**Ti4**	0.3888	0.9444	0.5
Ti2	0.1750	0.8333	0	**Ba5**	0.4150	0.2000	0.5
O5	0.1666	0.8333	0.5	**O11**	0.4500	0.7250	0.5
Ba3	0.2222	0.1111	0.5	**O12**	0.0555	0.2777	0.5
O6	0.2000	0.6000	0	**O13**	0.3730	0.9100	0

Figure 4.16 schematically illustrates the structure of the Γ_γ phase viewed along the [001] direction. Light and dark blue balls represent Ba atoms at z=0 and z=½; yellow and red balls represent O atoms at z=0 and z=½, and white and dark grey balls represent Ti atoms at z=0 and z=½, respectively. The bond lengths of Ba-O, Ti-O, O-O, and the closest Ba-Ba distance in this structure model are summarized in Table 4.3. The mean Ba-O distance is 2.6876 Å with the individual bond lengths varying from 2.4035 to 3.2338 Å. The bond of Ti4-O9 has a largest length of 2.8470 Å. Except it, the mean distance of the rest Ti-O bonds is 2.0293 Å with the individual values varying from 1.9609 to 2.0340 Å. The mean O-O bond length is 2.3139 Å with the individual distance varying from 2.0268 to 2.4960 Å. The closest bond length for Ba-Ba is 2.8138 Å. The density of the Γ_γ phase is calculated to be about 6.4 g/cm^{-3}, which is

higher than that of perovskite $BaTiO_3$ structure (6.02 g/cm^3), indicating a more condense structure are formed in the as-deposited film.

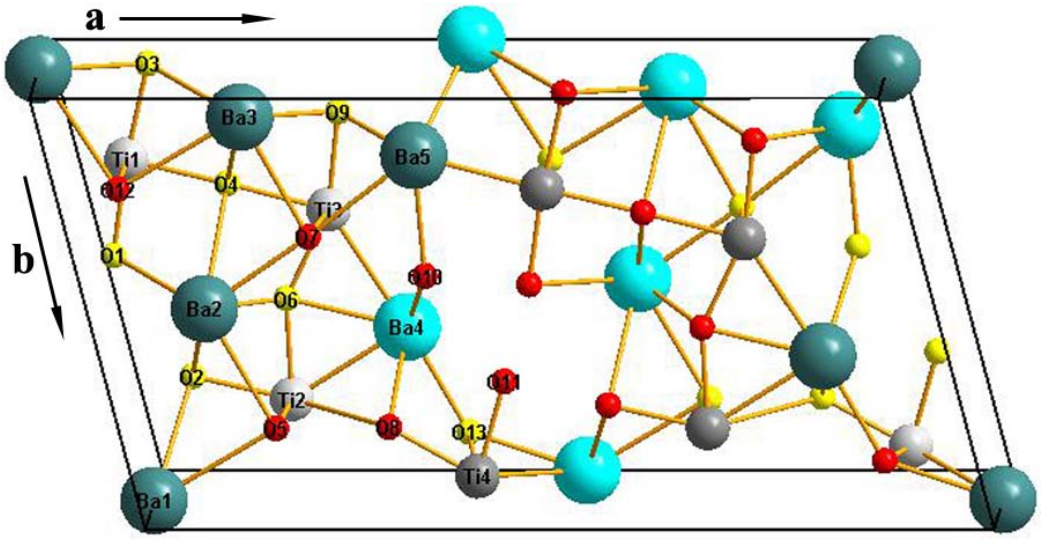

Figure 4.16 Schematic illustration of the structural model of phase Γ_γ. Large balls represent Ba atoms (light blue: z=0, dark blue: z=½); small balls represent O atoms (yellow ball: z=0, red balls: z=½) and the middle size balls represent Ti atoms (white: z=0, dark grey: z= ½).

Table 4.4 Atomic distance between two adjacent atoms in $(Ba_5Ti_4O_{13})_2$

$(Ba_5Ti_4O_{13})_2$								
Atom 1	**Atom 2**	**d $_{1,2}$**	**Atom 1**	**Atom 2**	**d $_{1,2}$**	**Atom 1**	**Atom 2**	**d $_{1,2}$**
Ba1	Ba5	2.8138	Ba5	O9	2.5758	**Ti4**	O8	1.9662
	O2	2.8021		O10	2.4448		O9	2.8470
	O3	2.8096		O12	3.2338		O11	1.9946
	O5	2.8159		O7	2.6630		O13	2.0198
	O11	3.3946	**Ti1**	O1	1.9609	**O1**	O10	2.0268
	O13	2.4069		O3	1.9926		O11	2.033
Ba2	O1	2.7970		O4	2.0036	**O2**	O6	2.4364
	O2	2.8135		O12	1.9700		O11	2.0637
	O4	2.7810	**Ti2**	O2	1.9767	**O5**	O8	2.1936
	O6	2.4528		O3	2.0293	**O7**	O10	2.3815
Ba3	O3	2.8099		O5	1.9749	**O8**	O11	2.4406
	O4	2.8020		O6	2.034		O13	2.4960
	O9	2.6627	**Ti3**	O4	2.0258	**O9**	O13	2.2652
	O8	2.5526		O6	1.9941			
Ba4	O6	2.4035		O7	1.9829			
	O8	2.4407		O9	1.9956			
	O10	2.6151						
	O13	2.4102						

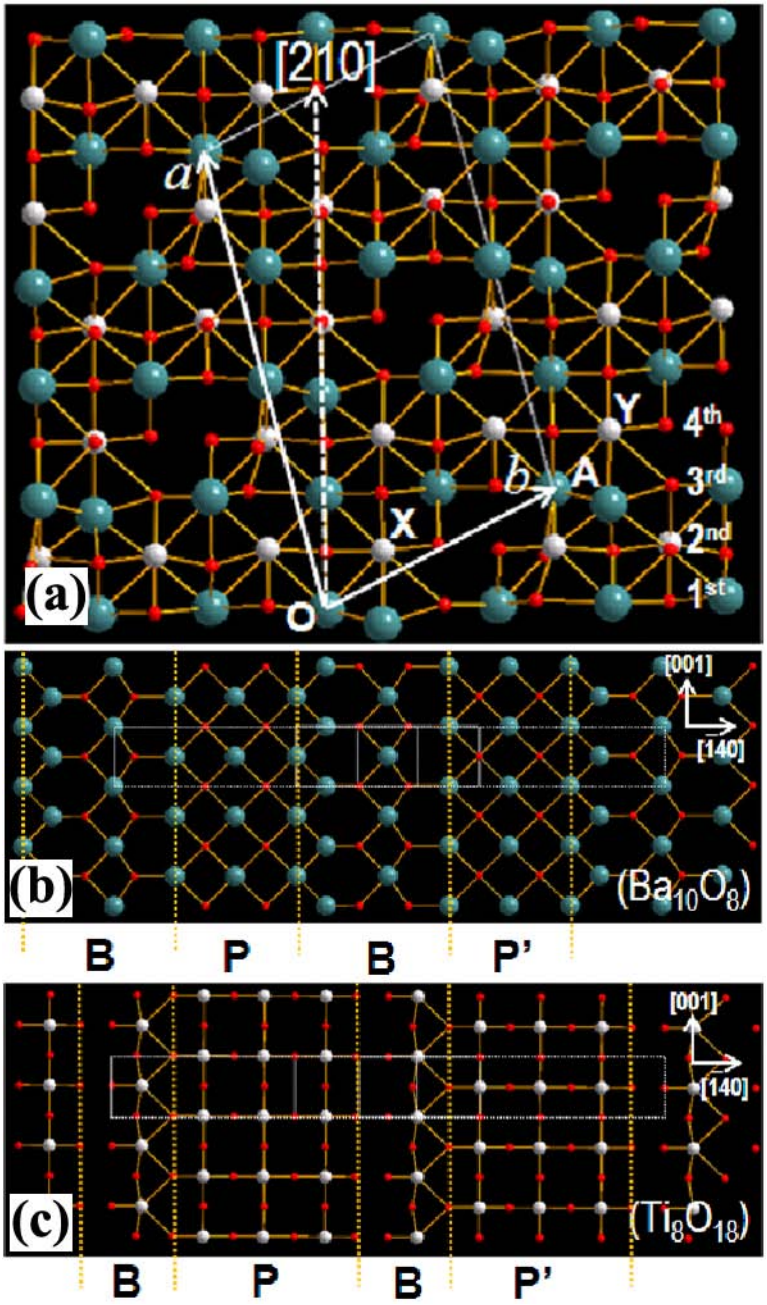

Figure 4.17 (a) [001] projection of the (Ba5Ti4O13)2 structural model; (b) and (c) illustration of the atomic arrangement in BaO and TiO layer, respectively.

Figure 4.17 (a) is the [001] projection of $(Ba_5Ti_4O_{13})_2$ structural model. It can be found that the $(Ba_5Ti_4O_{13})_2$ structure can be constructed by alternatively stacking (Ba,O) and (Ti,O) layers along the [210] direction. The adjacent period (Ba,O) and (Ti,O) layers are shifted by an

b vector (8.94 Å along [010] direction) with respect to each other. For example, the Ba atom at the position **O** in the first layer is shifted to the position **A** in the third layer by a ***b*** vector, and the Ti atom at the position **X** in the second layer is shifted to the position **Y** in fourth layer after one period. Figure 4.17 (b) and (c) show the atomic arrangement of Ba, Ti and O in (Ba,O) and (Ti,O) layers, respectively. Both layers can be obtained by a period rectangular unit, which is marked using dashed lines in the figures. The period unit in (Ba,O) layer contains 10 Ba and 8 O atoms, and 8 Ti and 18 O atoms in (Ti,O) layer. By carefully investigated, It can be found that there are two different characteristic regions shown in (Ba,O) layer and denoted as **P** and **B**. In the region **P**, atomic position of Ba and O is the same as BaO layer in the perovskite $BaTiO_3$ structure. Region **P'** is same as **P** region however shifted with half unit cell dimension along the [001] direction (***c****/2*). The atomic arrangement in region **B** is different from that in **P** and **P'**. Thus, **B** region can be called as a boundary region. Similar boundary region and perovskite regions can also be seen in (Ti,O) layer as shown in Figure 4.17 (c). The **P** region in (Ti,O) layer is the same as TiO_2 layer in the perovskite $BaTiO_3$ structure. Therefore, the entire $(Ba_5Ti_4O_{13})_2$ phase can be considered to be constructed by periodically introducing the boundaries (**B** region) between BaO and TiO_2 layers.

The accuracy of the structure model in Figure 4.16 was examined by comparing the simulated electron diffraction patterns with the experimental results. Figure 4.18 (a), (b) and (c) are NBED patterns along the [001], [010] and [100] directions obtained from as-deposited film. Figure 4.18 (d), (e) and (f) are simulated electron diffraction patterns calculated from the $(Ba_5Ti_4O_{13})_2$ structural model along the [001], [010] and [100] direction. The positions and intensities of the reflections in the calculated diffraction patterns are very well matched to those of the experimental results. For example, ***u, v, x*** and ***y*** diffraction spots show the strongest intensity, and the diffraction spot κ and χ is stronger than λ and δ, in both experimental and simulated [001] zone diffraction patterns, as shown in Figure (a) and (d). Besides, the same diffraction pattern characteristics of (*h 0 l*) diffraction spots with $h + l = 2n+1$ (n=integers) in [010]

zone and (*0 k l*) spots with *l = 2n+1 in* [100] zone are not observed in both experimental and calculated diffraction patterns. The very good agreement between the calculated and experimental electron diffraction patterns provides strong evidence of the correction of the $(Ba_5Ti_4O_{13})_2$ structural model for Γ_γ phase.

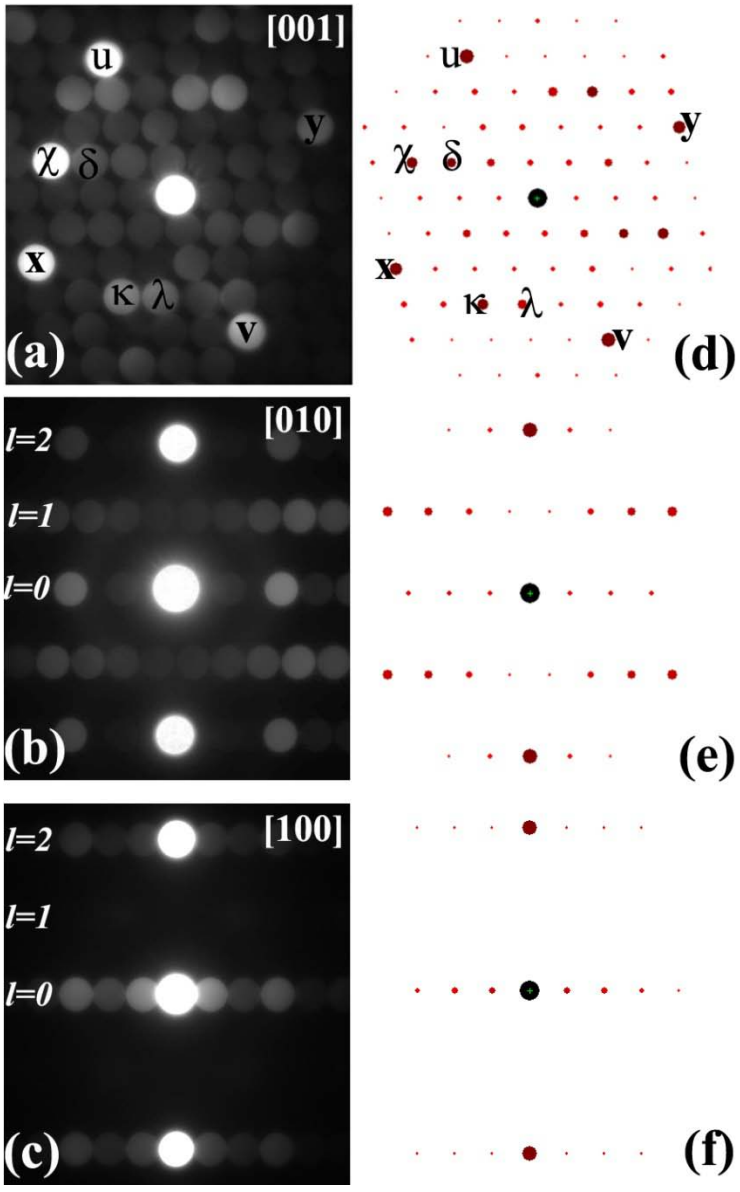

Figure 4.18 NBDPs of BTO Γ_γ phase (a) [001] zone, (b) [010] and (c) [100] zone; (d), (e) and (f) calculated EDPs of the structural model along the [001], [010] and [100] direction, respectively.

The precision of the structure model was further confirmed by comparing the simulation HRTEM images with the experimental results. Figure 4.15 (a), (b) and (c) show HRTEM images with an inset of relevant projection of the structural model and the corresponding simulated images along [001], [010] and [100] direction, respectively. The excellent matches between the experimental images and simulated images can further support the conclusion that Γ_γ phase has a structure of $(Ba_5Ti_4O_{13})_2$.

4.3.3 Structure Determination of H_β phase

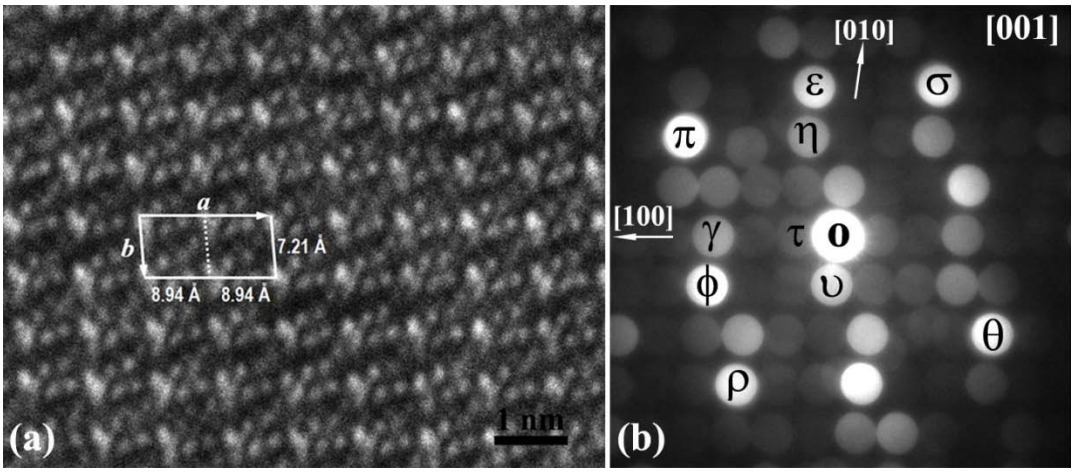

Figure 4.19 (a) HRTEM image of the H_β phase viewed along the [001] in plan-view sample and (b) corresponding NBDP.

Figure 4.19 (a) is a typical plan-view HRTEM image of phase H_β. Rhombic repeating units with the dimensions of 8.94 Å and 7.21 Å and the angle of 82° can be seen. It is totally different from the characteristics of Γ_γ phase shown in Figure 4.15 (a). Figure 4.19 (b) is a NBED pattern taken from a H_β phase grain in the plan-view TEM foil along [001] direction. The d-spacing of strong spots π, θ, ρ and σ is 2 Å, similar to the **u**, **v**, **x** and **y** diffraction spots in Figure 4.14 (a). The diffraction spots are periodically arranged along $O\tau$ and $O\upsilon$ directions, which are referred as [100] and [010] directions, respectively. The lattice spacing of the diffraction spot τ and υ measured from NBED is about 8.86 Å and 7.15 Å, respectively. The angle between the $O\tau$ and $O\upsilon$ is about 82°.

Similarly, a structure model of the H_β phase has been constructed using the knowledge obtained from both electron diffraction patterns and HRTEM images. The H_β phase are identified to have $(BaTiO_3)_8$ structure with a monoclinic structure and a space group of ***Cm*** (No. 8, *c*-unique axis). The lattice parameters for $(BaTiO_3)_8$ structure is: a = 17.88Å, b = 7.21Å, c = 3.94 Å and α=β=90°, γ = 82°. The atomic positions of the atoms are listed in Table 4.5.

Table 4.5 Atomic position of the atoms in $(BaTiO_3)_8$

Atom	x/a	y/b	z/c	Atom	x/a	y/b	z/c
Ba1	0	0	0	**Ba2**	0.2500	0.0800	0
O1	0.0313	0.3750	0.5	**Ti3**	0.2813	0.3750	0.5
O2	0.0700	0.7200	0.5	**O8**	0.2520	0.4100	0
Ti1	0.0938	0.1250	0.5	**Ba3**	0.3150	0.7800	0.5
O3	0.1100	0.2000	0	**O9**	0.3400	0.1000	0.5
O4	0.1150	0.5330	0	**O10**	0.3700	0.5300	0
Ti2	0.1563	0.8750	0.5	**O11**	0.4063	0.8750	0
O5	0.1450	0.8500	0	**Ba4**	0.4330	0.3100	0.5
O6	0.1875	0.2500	0.5	**Ti4**	0.4688	0.6250	0
O7	0.2000	0.6000	0.5	**O12**	0.4688	0.6250	0.5

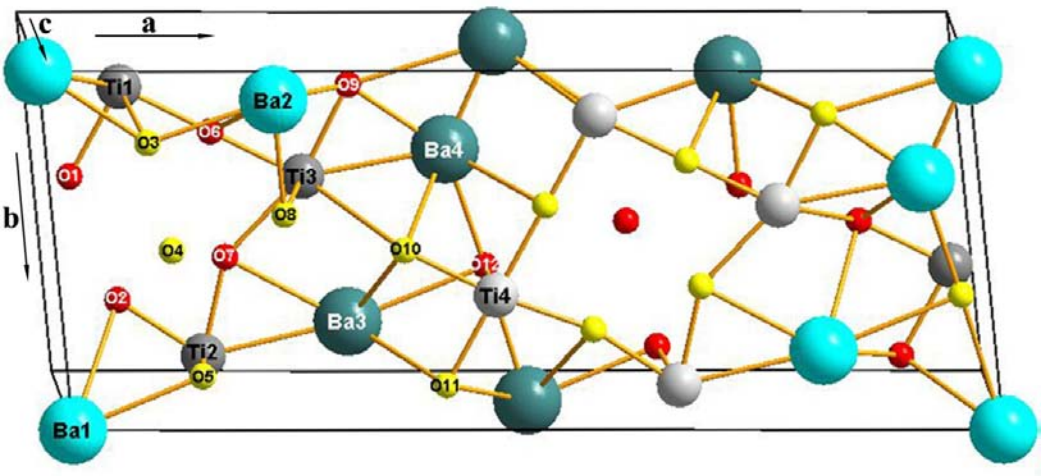

Figure 4.20 Schematic illustration of the $(BaTiO_3)_8$ structural model (large balls represent Ba atoms (light blue: z=0, dark blue: z=½), small balls represent O atoms (yellow ball: z=0, red balls: z=½) and the middle size balls represent Ti atoms (white: z=0, dark grey: z= ½))

Figure 4.20 shows the 3D structure model of the H_β phase. Llight and dark blue balls represent Ba atoms with z=0 and z=½; yellow and red balls represent O atoms with z=0 and

z=½, and white and dark grey balls represent Ti atoms with z=0 and z=½, respectively. The bond lengths of Ba-O, Ti-O, O-O, and the closest Ba-Ba in the structural model are summarized in Table 4.6. The mean Ba-O distance is 2.645 Å with the individual bond lengths varying from 2.3845 to 2.9942 Å. The mean distance of the rest Ti-O bonds is 2.1563Å with the individual values varying from 1.97 to 2.8439 Å. The mean O-O distance is 2.5627 Å with the individual bond lengths varying from 2.3775 to 2.8271 Å. The closest bond length Ba-Ba is 2.4014 Å. The density of the H_β phase is about 6.13 g/cm^{-3}, higher than that of perovskite $BaTiO_3$ structure (6.02 g/cm^3). Thus, $\Gamma_\gamma$phase and H_β phase are both more condense structure than perovskite $BaTiO_3$.

Table 4.6 Atomic distance between two adjacent atoms in $(BaTiO_3)_8$

$(BaTiO_3)_8$								
Atom 1	**Atom 2**	**d $_{1,2}$**	**Atom 1**	**Atom 2**	**d $_{1,2}$**	**Atom 1**	**Atom 2**	**d $_{1,2}$**
Ba1	Ba4	2.4014	**Ba4**	O1	2.7186	**Ti4**	O1	1.9995
	O2	2.9826		O9	2.3837		O2	2.0135
	O3	2.5790		O10	2.6875		O10	1.9715
	O5	2.6825		O12	2.4345		O11	1.9995
	O9	2.8622	**Ti1**	Ti2	1.9995		O12	1.9700
	O11	2.8067		O1	1.9995	**O1**	O2	2.6636
	O12	2.8279		O3	2.0728		O3	2.6485
Ba2	O3	2.5451		O5	2.8638		O4	2.8007
	O5	2.6546		O6	1.9992		O6	2.8271
	O6	2.5084	**Ti2**	O2	2.0136		O12	2.8070
	O8	2.3840		O5	1.9907	**O2**	O4	2.4652
	O9	2.5591		O6	2.8279		O7	2.3775
	O11	2.9942		O7	2.0392	**O3**	O4	2.4136
Ba3	O7	2.5640	**Ti3**	O6	1.9992		O6	2.4607
	O9	2.4039		O7	2.039	**O4**	O5	2.4116
	O11	2.6999		O8	2.0458		O8	2.4996
	O10	2.7672		O9	2.1256	**O8**	O10	2.3776
	O12	2.8362		O10	2.8439			

Figure 4.21 (a) is the [001] projection of the $(BaTiO_3)_8$ structure model. Similar as $\Gamma_\gamma$phase, the structure can be obtained by alternatively stacking the (Ba,O) and (Ti,O) layers along the [340] direction. The adjacent period (Ba,O) and (Ti,O) layers are shifted by ***b*** vector

with respect to each other. For example, the Ba atom at position **O** in the first layer is shifted to position α in the third layer, and the Ti atom at position ξ in the second layer is shifted to position ψ in fourth layer both by a ***b*** vector.

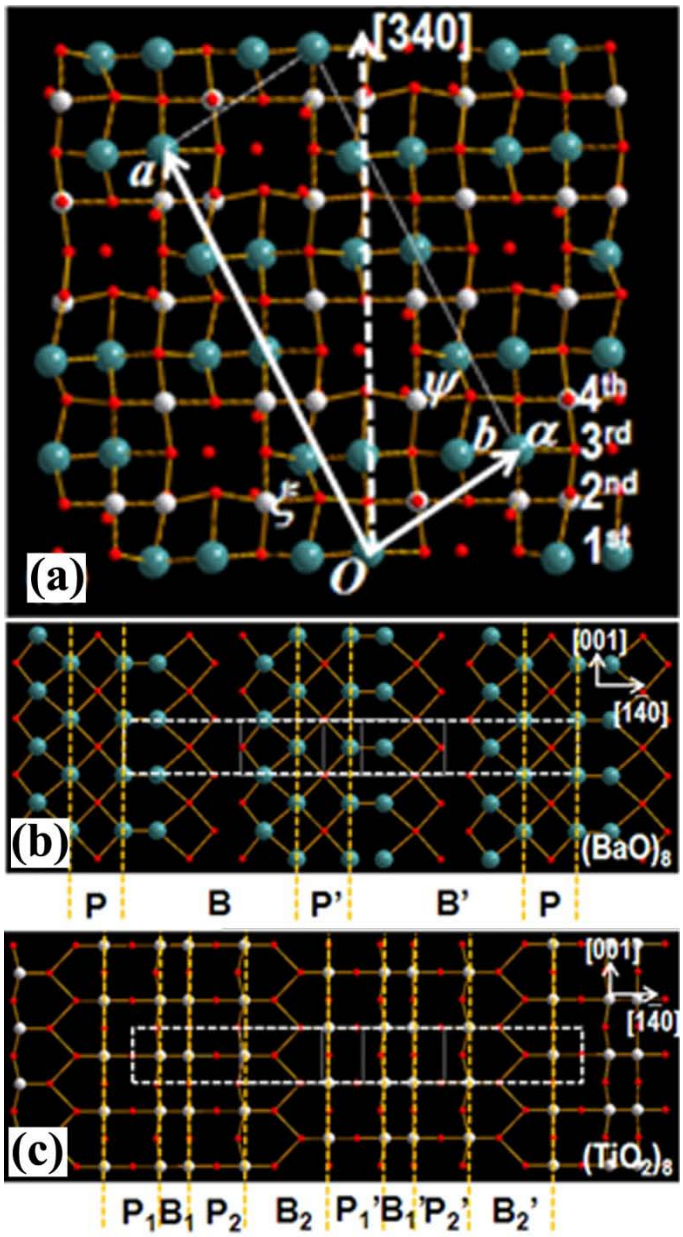

Figure 4.21 (a) [001] projection of the $(BaTiO_3)_8$; (b) and (c) illustrations of the atomic arrangement in BaO and TiO layer, respectively.

Figure 4.21 (b) and (c) show the atomic arrangement of Ba, Ti and O in the (Ba,O) and (Ti,O) layers, respectively. Both layers can be constructed by a repeating rectangular unit, as marked with dashed lines. The unit in (Ba,O) layer contains 8 Ba and 8 O atoms, and there are 8 Ti and 16 O atoms in the unit of (Ti,O) layer. The (Ba,O) layer can be identified with two regions: **P** (or **P'**) and **B** (or **B'**). In the region **P**, atomic arrangement of Ba and O is the same as BaO in the perovskite $BaTiO_3$ structure. Region **P'** has the same characteristics with **P** region but shifted by half unit cell dimension along the [001] direction (***c****/2*). *R*egion **B**, named as boundary region, is located between **P** and **P'** regions. Similar regions as **P** and **B** regions in (Ba,O) layer have also been found in (Ti,O) layer. The atomic arrangement of Ti and O is the same as TiO_2 in perovskite $BaTiO_3$ structure. Thus, the $(BaTiO_3)_8$ structure can also considered as to be obtained by periodically introducing the boundary region in $(BaO)_8$ and $(TiO_2)_8$ layers.

The simulated HRTEM image of the $(BaTiO_3)_8$ structural model along [001] direction and the corresponding structural projection is shown in the inset of Figure 4.22 (a). Good agreement can be clearly seen between the simulation and experimental HRTEM image. Figure 4.22 (c) shows simulated diffraction pattern using the $(BaTiO_3)_8$ structural model along the [001] direction. The positions and intensities of the diffraction spots match those of the experimental diffraction pattern shown in Figure 4.22 (b) very well. For example, π, θ, ρ and σ diffraction spots have the strongest intensity, and the diffraction spot ε and ϕ is stronger than their adjacent spot η and γ in both experimental and simulated diffraction patterns, as shown Figure 4.22 (b) and (c). The marked diffraction spots are indexed and listed in Table 4.7. Figure 4.22 (d) and (e) are the [140] zone NBED and simulated EDP of the H_β phase, respectively. They are also matched with each other in both images in terms of diffraction intensities and positions, which further confirms that the H_β phase has a structure of $(BaTiO_3)_8$.

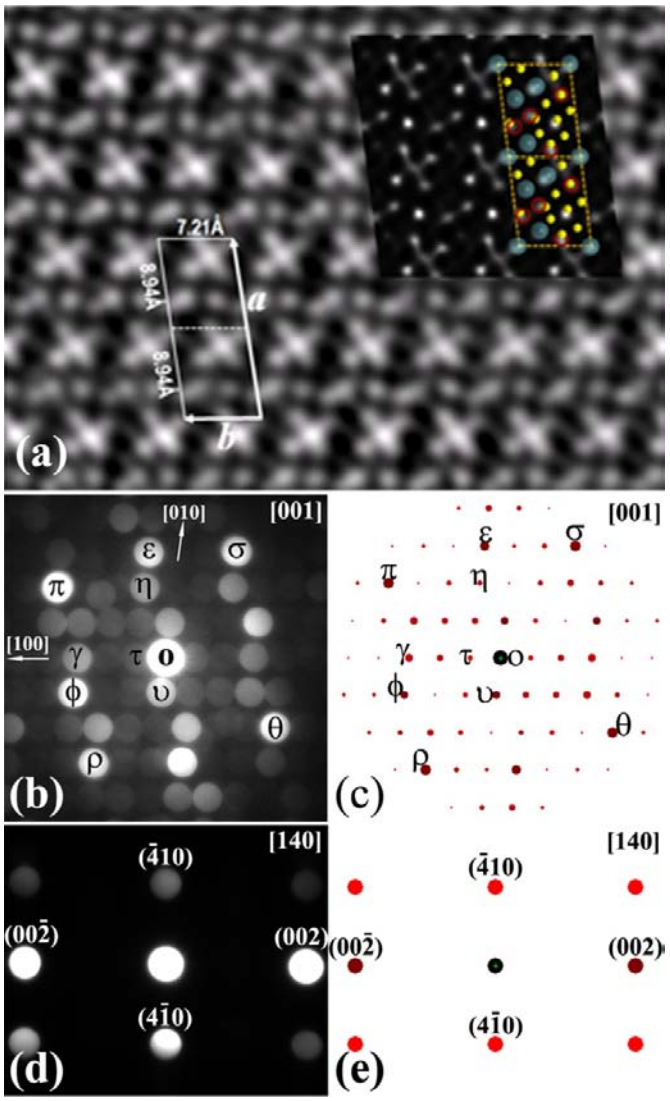

Figure 4.22 (a) HRTEM image of the H_β phase with simulated image and corresponding projection along the [001] direction; (b) and (c) NBDP along [001] zone and [140] zone, respectively; (c) and (e) corresponding simulated EDPs from structure model.

Table 4.7 Indices of the major diffraction spots of the H_β.

H_β phase			
Label	*Index*	*Label*	*Index*
τ	(200)	π	(820)
γ	(600)	θ	($\bar{8}\bar{2}$0)
ν	(0$\bar{1}$0)	ρ	(4$\bar{3}$0)
ϕ	(6$\bar{1}$0)	σ	($\bar{4}$30)
ε	(230)	η	(220)

In the as-deposited films, both Γ_γ and H_β phases have four domains with different orientations as shown in Figure 4.11. Figure 4.10 is a superposition of the eight [001] zone EDPs from four different oriented Γ_γ domains and four different oriented H_β domains. The four domains of each phase are related to each other by either a 90° rotation operation around the [001] axis or a (220) mirror plane operation. In Figure 4.10, each strong diffraction spot **U**, **V**, **X** or **Y** with a lattice spacing of 2.0 Å is a superposition of the strongest diffraction spots from eight domains. For instant, diffraction spot ***U*** is a superposition of (820), ($\bar{8}\bar{2}0$)**,** (2$\bar{4}$0) and ($\bar{2}$40) diffraction of the four different oriented Γ_γ domains as well as (820), ($\bar{8}\bar{2}0$)**,** (4$\bar{3}$0) and ($\bar{4}$30) diffraction of the four different oriented H_β domains. In another words, regardless of the orientation difference, the lattice planes with a lattice spacing of 2.0 Å in different Γ_γ and H_β domains are nearly parallel to each other.

Thus, the extra weak diffraction spots in Figure 4.9 (b) can be well understood. It is a superposition of two diffraction patterns from two oriented Γ_γ domains with the incident electron beam parallel to [1$\bar{4}$0] of one domain and [210] of the other domain. The diffraction spot **ω** in Figure 4.9 (b) is a superposition of (820) and (2$\bar{4}$0) diffraction spots of the two domain, while the diffraction spot ζ can be indexed as (410) being from one domain and the diffraction spot ξ can be indexed as (1$\bar{2}$1) from the other domain. From interface EDP in Figure 4.9 (c), it shows that the diffraction spot **ω** overlaps with the (020) of MgO. This indicates that the Γ_γ domains have a particular orientation relationship with MgO substrate. The orientation relationship of the four Γ_γ domains with MgO can be given in the following:

(1) $(001)_{\Gamma_\gamma} // (001)_{MgO}$, $[820]_{\Gamma_\gamma} // [100]_{MgO}$ and $[2\bar{4}0]_{\Gamma_\gamma} // [010]_{MgO}$,

(2) $(001)_{\Gamma_\gamma} // (001)_{MgO}$, $[\bar{2}40]_{\Gamma_\gamma} // [100]_{MgO}$ and $[820]_{\Gamma_\gamma} // [010]_{MgO}$,

(3) $(001)_{\Gamma_\gamma} // (001)_{MgO}$, $[820]_{\Gamma_\gamma} // [100]_{MgO}$ and $[\bar{2}40]_{\Gamma_\gamma} // [010]_{MgO}$,

(4) $(001)_{\Gamma_\gamma} // (001)_{MgO}$, $[2\bar{4}0]_{\Gamma_\gamma} // [100]_{MgO}$ and $[820]_{\Gamma_\gamma} // [010]_{MgO}$,

Similarly, the four H_β domains have the following orientation relationships with MgO substrate:

(1) $(001)_{H_\beta}$ // $(001)_{MgO}$, $[820]_{H_\beta}$ // $[100]_{MgO}$ and $[\bar{4}30]_{H_\beta}$ // $[010]_{MgO}$,

(2) $(001)_{H_\beta}$ // $(001)_{MgO}$, $[4\bar{3}0]_{H_\beta}$ // $[100]_{MgO}$ and $[820]_{H_\beta}$ // $[010]_{MgO}$,

(3) $(001)_{H_\beta}$ // $(001)_{MgO}$, $[820]_{H_\beta}$ // $[100]_{MgO}$ and $[4\bar{3}0]_{H_\beta}$ // $[010]_{MgO}$,

(4) $(001)_{H_\beta}$ // $(001)_{MgO}$, $[\bar{4}30]_{H_\beta}$ // $[100]_{MgO}$ and $[820]_{H_\beta}$// $[010]_{MgO}$,

4.4 Summary

4.4.1 Microstructure and Interface Study of Epitaxial $BaTiO_3$ Films

In this study, epitaxial $BaTiO_3$ thin films have been successfully fabricated on MgO substrate using RF magnetron sputtering. The BTO thin film has a ~200nm thickness with a very smooth surface and high epitaxial quality and rough interface with respect of MgO substrate. The BTO film has a tetragonal structure (a_{BTO} = 4.02Å, c_{BTO} = 4.11 Å) and an orientation relationship of $(001)_{BTO}//(001)_{MgO}$ and $<100>_{BTO}//<100>_{MgO}$ with respect to the substrate. The *c/a* of the BTO tetragonal structure in the film is ~1.02, a little larger than that of the bulk BTO (~1.01). The epitaxial BTO films fabricated using RF magnetron sputtering consists of nanodomain structures with a size ranging from 3 to 20 nm. Cross-section TEM and 2-D interface studies show that the regions in the film away from the interface have larger lattice mismatch than the regions near the interface. Such lattice mismatch difference in the different regions in the BTO film, and the formation of the nano domains are due to the surface characteristics (steps, terraces and kinks) of MgO substrate produced by the surface treatment during the process.

4.4.2 Structure Investigation of Two New BaTiO3 Induced Phases Fabricated Using RF Magnetron Sputtering

As-deposited epitaxial thin films which consist of two new phases Γ_γ ($Ba_{10}Ti_8O_{26}$) and H_β ($Ba_8Ti_8O_{24}$) have been frabricated on MgO substrate using RF magnetron sputtering. Enhanced contact-EFM measurements show that both phases are ferroelectric and the polarization vector of the Γ_γ phase can be easily switched over under an external electrical field of 2 V/mm, compared with the H_β phase. The atomic structures of the two new phases were

determined using electron diffraction pattern analysis and HRTEM images. The precision of the determined structures for two new phases were further confirmed by comparing the experimental results and simulations. The Γ_γ phase ($Ba_{10}Ti_8O_{26}$ or $(Ba_5Ti_4O_{13})_2$) has a monoclinic structure with a space group of ***Cm*** (No. 8, *c*-unique axis) and lattice parameters of a=16.49 Å, b=8.94 Å, c=3.94 Å and γ =77°. The H_β phase ($Ba_8Ti_8O_{24}$ or $(BaTiO_3)_8$) has a monoclinic structure with a space group of ***Cm*** (No. 8, *c*-unique axis) and lattice parameters of a = 17.88Å, b = 7.21Å, c = 3.94 Å and γ = 82°. Both Γ_γ and H_β phases have four domains with different orientations. In the as-deposited films, eight domains with four different oriented Γ_γ domains and four different oriented H_β domains are coexisted. The four domains of each phase are related to each other by either a 90° rotation operation around the [001] axis or a mirror plane operation. Both new structures are epitaxially grown on the MgO substrate with the following primary orientation relationship:

(1) $(001)_{\Gamma_\gamma}$ // $(001)_{MgO}$, $(820)_{\Gamma_\gamma}$ // $[100]_{MgO}$ and $[2\bar{4}0]_{\Gamma_\gamma}$ // $[010]_{MgO}$, for Γ_γ.

(2) $(001)_{H_\beta}$ // $(001)_{MgO}$, $[820]_{H_\beta}$ // $[100]_{MgO}$ and $[\bar{4}30]_{H_\beta}$ // $[010]_{MgO}$, for H_β.

CHAPTER 5

MICROSTRUCTURE AND INTERFACES OF EPITAXIAL (Ba,Sr)TiO_3 FILMS ON MICUT (001) MgO SUBSTRATE

5.1 Introduction

Ferroelectric (Ba,Sr)TiO_3 (BST) thin films have been widely investigated as potential materials for applications in microelectronic devices such as dynamic random access memories, capacitors, infrared detectors, and microwave devices due to their high dielectric constant, relatively low dielectric loss tangent, and large electric-field tunability [120, 238–240]. Many studies have found that in addition to the film composition, the selection of substrate, the microstructure of film, the mechanical stresses within the films as well as the film/substrate interface all show tremendous influence on the physical properties of BST thin films [22, 241, 242]. Thus, to optimize the performance in tunable microwave device applications, high quality BST thin films with epitaxial structure, atomically sharp interfaces and smooth surface are required. The lattice mismatch at the interface between the film and substrate can be used to control epitaxial behavior and film microstructure [27-29], and to alter the physical properties [243-246]. Furthermore, the interfacial structure plays a key role in understanding and eventually manipulating the growth mechanism of the epitaxial films.

The single-crystal (001) MgO substrate possesses excellent dielectric properties for microwave device applications compared to other oxide substrates, such Al_2O_3 and $LaAlO_3$. However, the lattice misfit between BST ($a_{Ba_{0.6}Sr_{0.4}TiO_3}$ =0.3945 nm) and MgO (a_{MgO} =0.4212 nm) is about ~6.4% which is relatively too high to obtain epitaxial and high performance thin films on BST/MgO system. Many efforts have been made previously and Chen et al. have successfully grown epitaxial BST thin films on (001) MgO substrates using PLD and have achieved improved performance [22]. It should be noted that at the atomic level, single crystal substrate surfaces

consist of local structures involving steps, kinks and terraces.The surface engineering and interface control of MgO substrate play an important role for the growth of epitaxial BST film. Some previous studies show that the surface features can induce film defects such as conservative and non-conservative anti-phase domain boundaries [23]. The influence of such local structures on the film structures and interfaces is not very well understood. More information is needed in order to fully understand the influence of the substrate surface characteristics and interfacial structure on the behavior of the epitaxial films. In this chapter, the commercially available vicinal (001) MgO obtained by cutting the (001) surface with a nominal angle of 1º, 3º, and 5º along the [001] direction were used as substrates. The effect of the substrate surface local structures obtained via substrate miscut on the 2-D interfacial structure of highly epitaxial ferroelectric $Ba_{0.6}Sr_{0.4}TiO_3$ (BST) thin films on the miscut (001) MgO substrates has been systematically studied.

5.2 Epitaxial Growth of BST Films on Miscut (001) MgO Substrates

The surface morphology and roughness of BST films grown on MgO substrates with different miscut angles were investigated using AFM in the contact mode with a scanning size of $2\times2\ \mu m^2$. Figure 5.1 (a) is a 3D AFM image of BST film grown on 1^o miscut MgO substrate, exhibiting a coarser granular structure compared to the BST films grown on 3^o and 5^o miscut MgO, which show a relative flat surface with distributed of extrusive columnar structures, as shown in Figure 5.1 (b) and (c). The extrusive columns in Figure 5.1 (c) are narrower and sharper than those in Figure 5.1 (b), in which the small columnar structure have a size varying from 70 nm to 100 nm, while the coarse columnar structure have a larger size varying from 150 nm to 250 nm. The average roughness of the BST films grown on 1º; 3º and 5º miscut MgO substrate is ~6.55 nm, 4.62 nm and 1.52 nm, respectively. It indicates that BST film grown on 5º miscut MgO substrate has a flatter surface compared to the films grown on 1º and 3º miscut MgO.

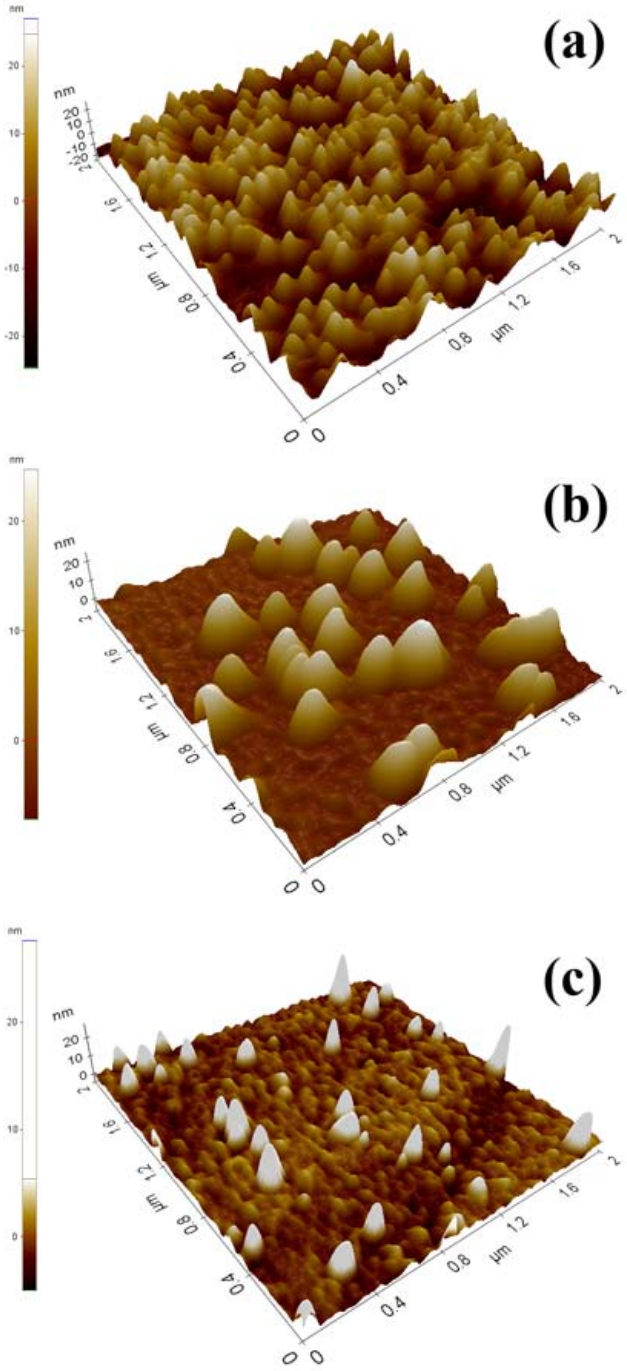

Figure 5.1 Contact Mode AFM 3D images of as-deposited BST films grown on (a) 1º; (b) 3º; (c)5º miscut MgO substrate.

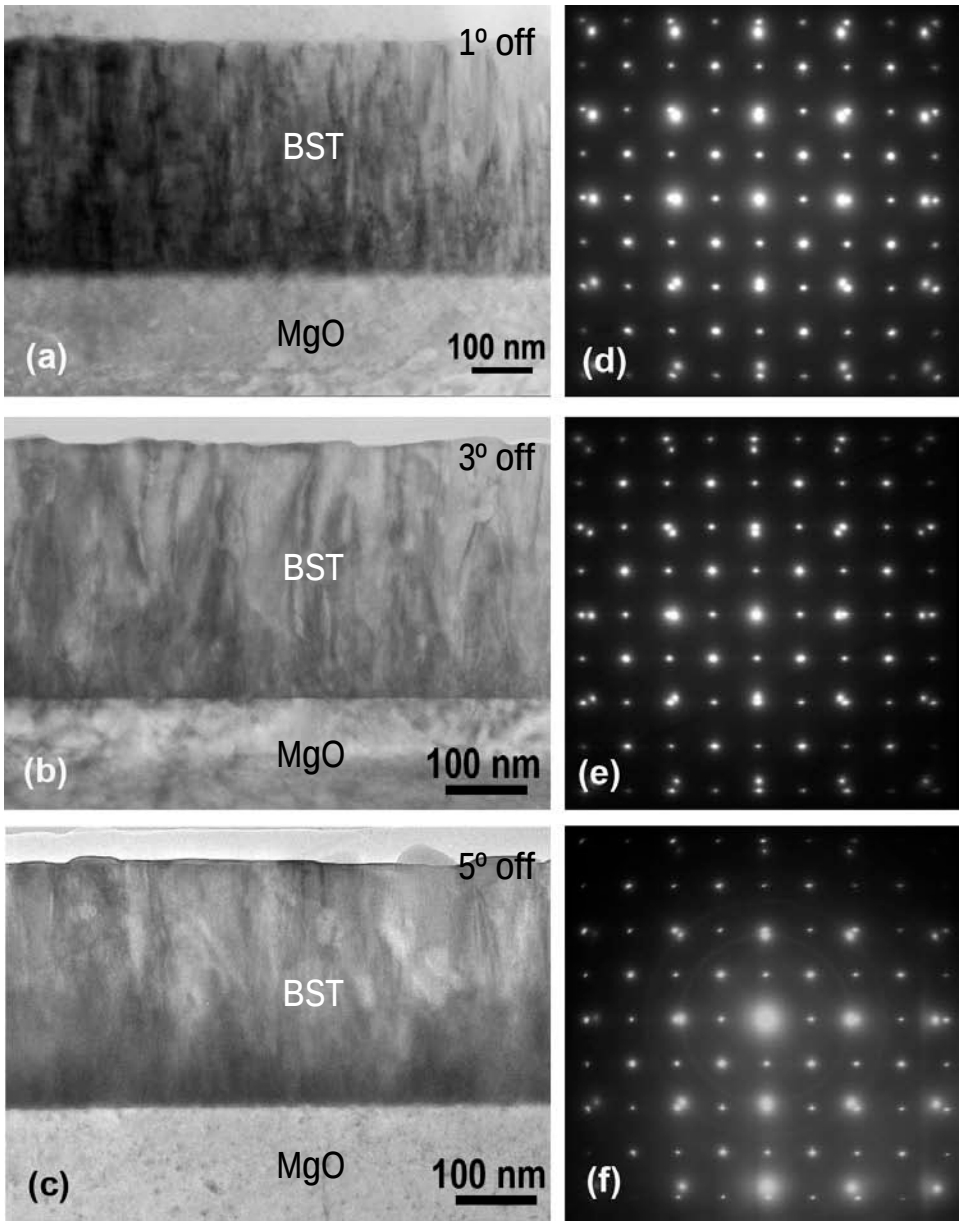

Figure 5.2 Cross-section TEM images and EDPs of BST/MgO deposited on the substrate with miscut angles of (a,d) 1.2º; (b,e) 3.5º and (c,f) 5.3º.

Figures 5.2 (a) – (c) are cross-section TEM images and (d) - (f) are EDPs of the interfaces of BST thin films grown on (001) MgO substrates with a miscut angle of 1.2º, 3.5º and 5.3º, respectively. The 1.2º, 3.5º and 5.3º miscut angles, which are slightly different from the labeled angle on commercially purchased MgO miscut substrates, are measured and calibrated from film/substrate interface using cross-section HRTEM. The films deposited on the 1.2º, 3.5º

and 5.3º miscut substrate have a thickness of about 400 nm, 340 nm and 300 nm, respectively. All three films exhibit excellent epitaxial quality, smooth surfaces and sharp interfaces with respect to the substrate, and show a single cubic crystal structure with an orientation relationship of $(001)_{BST}$ // $(001)_{MgO}$ and $<100>_{BST}$ // $<100>_{MgO}$ with respect to the substrate. The lattice mismatch, $(a_{BST}-a_{MgO})/a_{MgO}$, between the BST film and the miscut 1.2º, 3.5º and 5.3º (001) MgO is about -5.4%, -5.7% and -5.5%, respectively, as obtained from the EDPs of the interface.

5.3 Interface Structures of BST Films Grown on Miscut (001) MgO Substrates

Figure 5.3 (a) - (c) are EDPs of the plan-view BST/MgO interface for films grown on 1.2º, 3.5º and 5.3º miscut (001) MgO, respectively. The EDPs were taken with the electron beam entering the BST film and exiting from the MgO side and under the same condition with their camera length calibrated using the MgO EDP as a standard. The EDPs in Figures 5.3 (a) - (c) exhibit quite different characteristics from those shown in Figures 5.2 (d) - (f). The EDPs of the plan-view BST/MgO interface (Figures 5.3 (a) - (c)) show many more diffraction spots compared to those of the cross-section interface (Figures 5.2 (d) - (f)). The extra diffraction spots in Figures 5.3 (a) - (c) are produced from the double diffraction of the [001] BST and [001] MgO [236]. Figure 5.3 (d) shows a schematic of the diffraction spots in a quarter of the EDPs in Figures 5.3 (a) - (c). Open circles, white and grey spots represent the diffraction spots from MgO, BST and double diffractions, respectively. Double diffraction of the plan-view interface can be used to study the interface structure over a large area. The lattice mismatch ($\Delta\delta$) between the film and the substrate can be precisely evaluated with the distance Rs between two adjacent double diffraction spots measured from the EDP using the equqtion (4.1).

The lattice mismatch is directly related to R_s value. A larger R_s corresponds to a larger lattice mismatch, whereas a smaller R_s corresponds to a smaller mismatch. The $\Delta\delta$ obtained from Figure 5.3 (a), (b) and (c) using formula (1) are -5.6, -6.0% and -5.7%, respectively. These values are larger than those obtained from the cross-section TEM analysis.

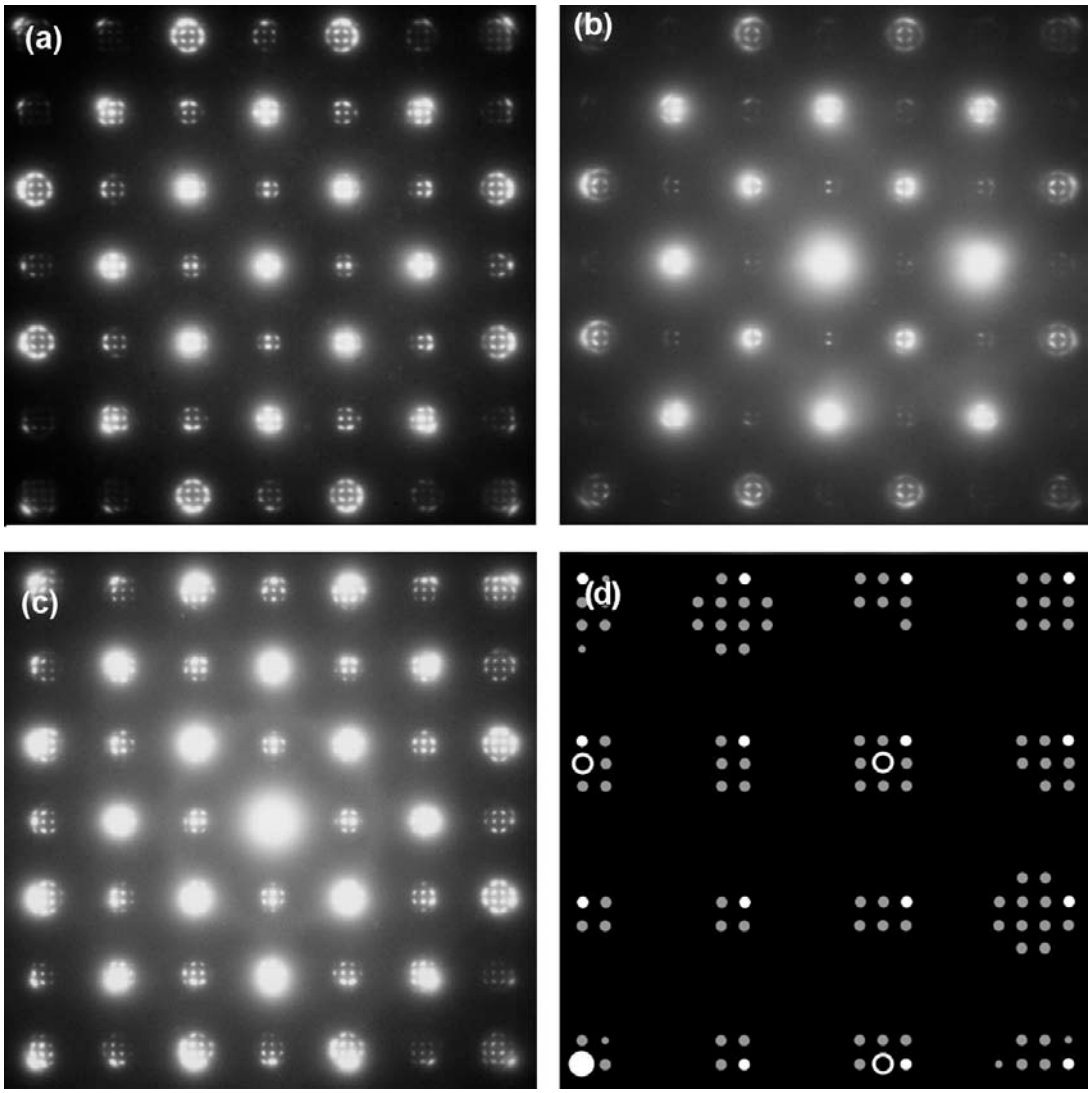

Figure 5.3 Plan-view SAED pattern of the BST/MgO interface deposited on the MgO substrate with miscut angles of (a)1.2°; (b) 3.5° and (c) 5.3°; and (d) is a schematic illustration of the diffraction spots of the EDPs.

Figures 5.3 (b) and (c) show the smaller and larger number of double diffraction spots, respectively. Previous studies showed that sharpness of the double diffraction spots can be used to evaluate the degree of commensuration between the film and the substrate [236]. Sharp double diffraction spots correspond to good commensuration between the film and the substrate over a long range or large area. Diffused double diffraction spots correspond to commensuration over a limited range. The sharp diffraction spots in Figure 5.3 (a) and (c)

indicate that the BST films grown on the 1.2º and 5.3º miscut (001) MgO commensurate well with the substrate over a relative large area. On the contrary, the diffused double diffraction spots in Figure 5.3 (b) show that the BST film grown on the 3.5º miscut commensurates with the substrate over a relative small area.

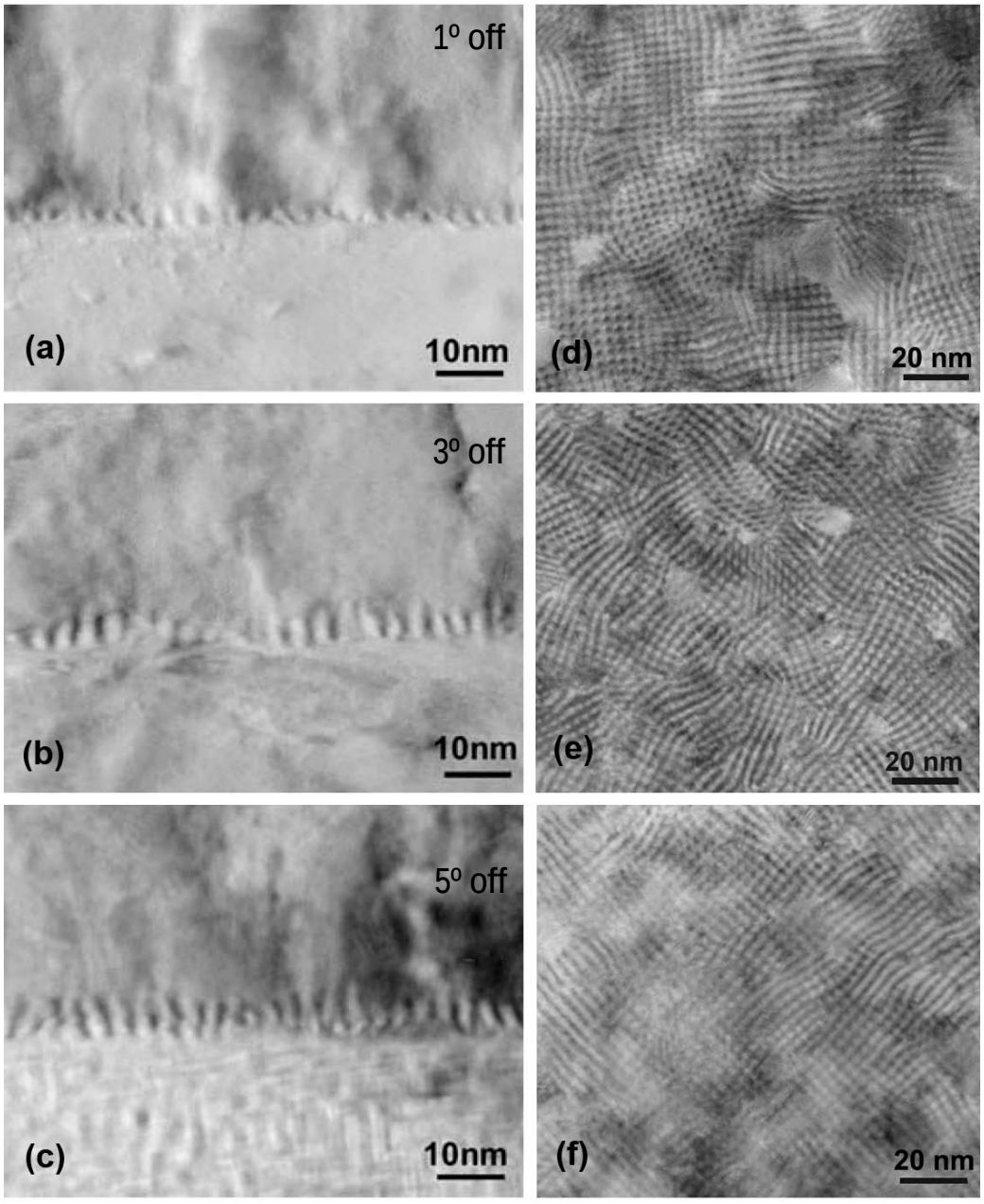

Figure 5.4 Cross-section and plan-view TEM images of the BST/MgO interface deposited on the substrate with miscut angles of (a,d) 1.2°; (b,e) 3.5° and (c,f) 5.3°.

Figures 5.4 (a) - (c) show HRTEM images of cross-sectional BST/MgO interfaces for the films grown on the 1.2º, 3.5º and 5.3º miscut substrate, respectively. Quasi-periodically distributed edge dislocations are observed at the interfaces. The average distance of the edge dislocations at the three interfaces has nearly the same value that is approximately 3.2 nm. No distinct differences can be found among the three interfaces.

Figures 5.4 (d) - (f) show HRTEM images of plan-view BST/MgO interfaces for the films grown on the 1.2º, 3.5º and 5.3º miscut substrate, respectively. The coarse lattice fringes in the images represent moiré fringes formed by the overlapping of BST and MgO. Commensurate domains in which the moiré fringes have a uniform orientation can be observed indicating good commensuration between the film and substrate. The size of the commensurate domains for the BST films grown on the 1.2º and 5.3º miscut substrates is between 30 to 40 nm, Figures 5.4 (d) and (f). The domain size for the film grown on the 3.5º miscut substrate is between 10 to 20 nm. Such domain size difference results in the variation of the number and sharpness of the double diffraction spots are shown in Figures 5.3 (a) - (c).

The surface of the (001) MgO substrate consists of steps, terraces and kinks, whose characteristics have strong influence on the microstructure as well as defects of the thin films [23]. It has been observed that (i) when BST films grow on a (001) MgO substrate that has a step with a height of $\frac{1}{2}a_{MgO}$, a conservative anti-phase boundary (C-APB) is formed between the two crystals on the adjacent terraces; (ii) when a BST film grows on a (001) MgO substrate that has a terrace with a width of odd number of $\frac{1}{2}a_{BST}$, a non-conservative anti-phase boundary (NC-APB) is formed between the two crystals on the adjacent terraces; (iii) when a BST film grows on a (001) MgO substrate that has a kink and/or its associated terrace with a width of odd number of $\frac{1}{2}a_{BST}$, an APB with C-APB and NC-APB components form between the two crystals on the adjacent terraces

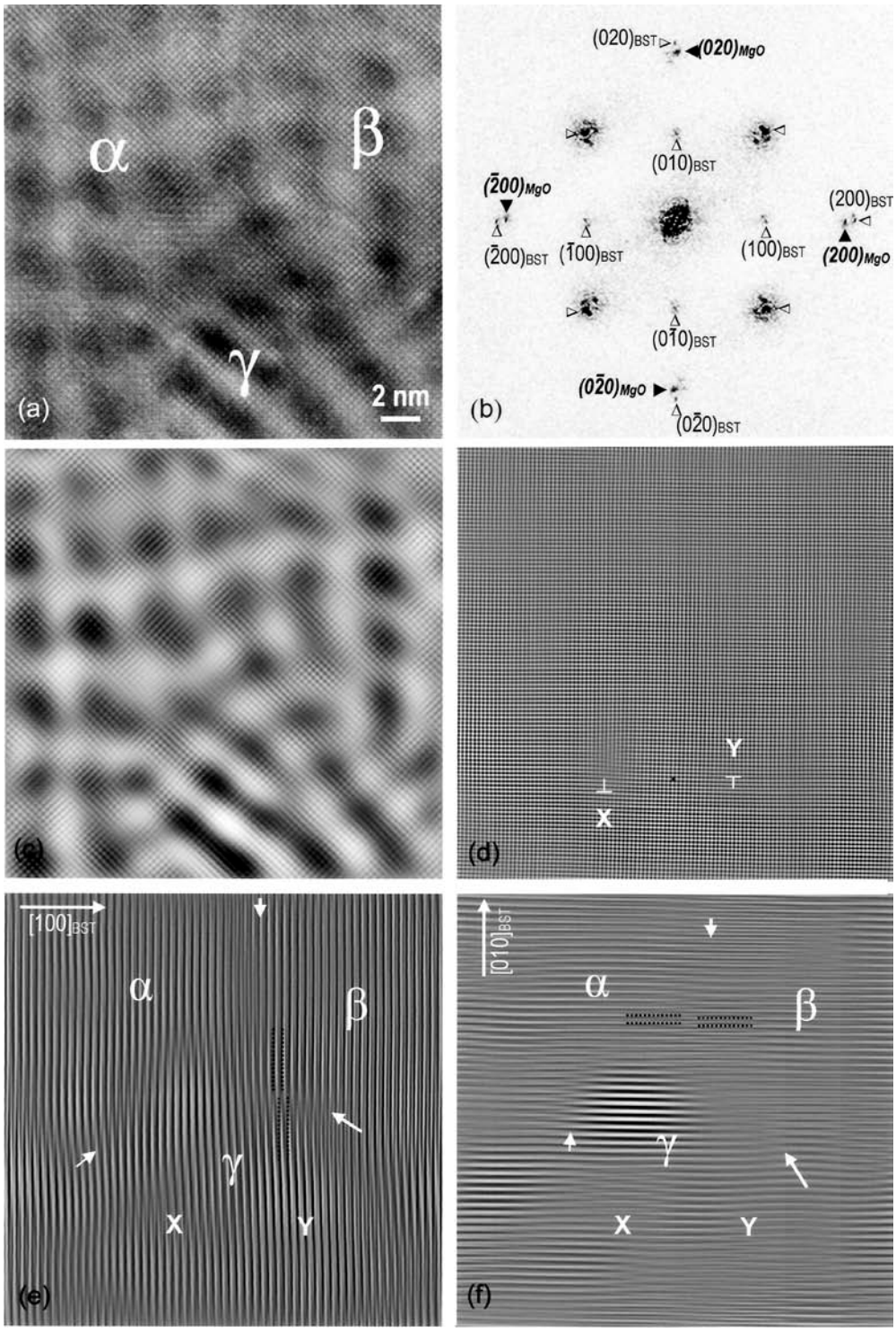

Figure 5.5 (a) HRTEM image of plan-view BST/MgO interface for the film deposited on a 3.5º miscut substrate; (b) FT of (a); (c) and (d) inverse FT of double diffraction and MgO spots, respectively; (e) and (f) inverse FT of the BST (*h*00) and (0*k*0) spots, respectively.

. Figure 5.5 (a) is a HRTEM image of the plan-view BST/MgO interface for the film grown on the 3.5º miscut substrate showing three commensurate domains α, β and γ. Figure 5.5 (b) is the Fourier transformation (FT) of the HRTEM image shown in Figure 5.5 (a), which is composed of the diffraction spots from MgO (marked by "▲"), BST (marked by "∆") and double diffraction (unmarked spots). Figure 5.5 (c) is an inverse FT of the double diffraction spots showing the presence of moiré fringes, similar to the characteristics in Figure 5.5 (a) but with lower resolution. Figure 5.5 (d) is an inverse FT obtained using the MgO diffraction spots exhibiting nearly perfect crystal lattice fringes except the two edge dislocations (**X** and **Y**). Fig. 5.5 (e) is an inverse FT obtained using the (100) and (200) diffraction spots of BST; while Figure 5.5 (f) is an inverse FT obtained using the (010) and (020) diffraction spots of BST. Anti-phase domain boundaries are observed in the boundary regions between domains α, β and γ. The domains beside the boundary are displaced by ~2 Å, i.e., $\frac{1}{2}a_{BST}$ along the $[100]_{BST}$ in Figure 5.5 (e). Similarly, the domains beside the boundary in Figure 5.5 (f) are also displaced by $\frac{1}{2}a_{BST}$ along the $[010]_{BST}$ direction. The APBs observed are composed of conservative (with the displacement vector parallel to the boundary plane) and non-conservative components (with the displacement vector perpendicular to the boundary plane). Such APBs are arisen from the structure of the terraces and the kinks on the substrate surface during the epitaxial growth process. The formation of such APBs was discussed in detail in a previous report [23].

It is clear from the results shown in Figure 5.5 that the formation of the commensurate domains and boundaries at the BST/MgO interface is directly related to the APBs produced in the film. It can be presumed that a different miscut of the substrate will produce a different surface structure. Namely, the characteristics of the steps, terraces and kinks on the substrate will vary with miscut and consequently influence the formation of APBs. Since the formation of APBs is strongly dependent upon the structure of the steps, terraces and kinks, it can be expected that the interface structure, i.e., the commensurate domains of the interface, for the film epitaxially grown on the 1.2º, 3.5º and 5.3º miscut substrate will be different.

Table 5.1 Lists step height and terrace width of the miscut MgO substrates, BST unit cell arrangements and local lattice mismatches on the terraces.

Miscut angle (α)	$Tan^{-1}(\alpha)$	Step height = 1 MgO unit cell				
		W_T	P_T	N_{BST}	N_A	δ_T
1.2˚	47.74	95	0.25	101.43	101	-5.94%
		96	0.25	102.49	102	-5.88%
3.5˚	16.35	32	0.15	34.16	34	-5.88%
		33	0.35	35.23	35	-5.71%
5.3˚	10.78	21	0.3	22.42	22	-4.54%
		22	0.2	23.48	23	-4.34%
Miscut angle (α)	**$Tan^{-1}(\alpha)$**	**Step height = 2 MgO unit cells**				
		W_T	**P_T**	**N_{BST}**	**N_A**	**δ_T**
1.2˚	47.74	191	0.5	203.92	204	-6.37%
3.5˚	16.35	65	0.2	69.4	69	-5.79%
		66	0.3	70.46	70	-5.71%
5.3˚	10.78	43	0.45	45.91	46	-6.52%
		44	0.05	46.98	47	-6.38%

W_T: Terrace width (number of half MgO unit cell); **P_T**: Probability for the formation of the terrace;
N_{BST}: Number of half BST unit cells on terrace; **δ_T**: Lattice mismatch on the terrace;
N_A: Accommodated number of half BST unit cells on terrace

Modifying the surface structure of the substrate using miscut will alter the characteristics of the steps, terraces and kinks. Atomic force microscopy studies of the MgO substrate surface showed that the height of the steps is about one or two unit cells (0.42 - 0.84 nm) [236]. On the 1.2º miscut MgO substrate, terraces associated with a step of a_{MgO} high have an average width of $95 \times \frac{1}{2}a_{MgO}$ or $96 \times \frac{1}{2}a_{MgO}$, while the terraces associated with a step of $2a_{MgO}$ high have an average width of $191 \times \frac{1}{2}a_{MgO}$ (as shown in Table 5.1). The former terraces can accommodate $101.43 \times \frac{1}{2}a_{BST}$ or $102.49 \times \frac{1}{2}a_{BST}$, while the latter can accommodate $203.92 \times \frac{1}{2}a_{BST}$. It has been acknowledged that during the epitaxial growth, the start and the end of each terrace always correspond to the atomic plane of the film and subsequently only integral

number of half BST unit cells can be accommodated on each terrace. Therefore, 101 × ½a_{BST} or 102 × ½a_{BST} are most likely queued on the terraces that are associated with a step of a_{MgO} high. The local lattice mismatch between the BST and MgO on the terraces with a width of 95 × ½a_{MgO} and 96 × ½a_{MgO} is equal to -5.94% and -5.88%, respectively. The terraces that are associated with a step of 2a_{MgO} high can accommodate 204 half BST unit cells with a local lattice mismatch of -6.37%. Presuming the probability for forming the terraces with a width of 95 × ½a_{MgO}, 96 × ½a_{MgO} and 191 × ½a_{MgO} being 0.25, 0.25 and 0.5, the average lattice mismatch estimated from this assumption could be calculated using the formula given below:

$$\delta = \sum P_T^i \delta_T^i \tag{5.1}$$

Where P_T^i is the probability to form the terrace i, and δ_T^i is the local lattice mismatch on the terrace i. The average lattice mismatch calculated using the above formula is about -6.14%. Since a NC-APB is formed in the film when BST grown on a terrace with a width of odd number of $\frac{1}{2}a_{BST}$, the average NC-APB density (d) in the BST film could be calculated using the following formula:

$$d = \sum P_T^{i_{odd}} \Big/ \sum P_T^i N_A^i \tag{5.2}$$

Where $P_T^{i_{odd}}$ is the probability to form a terrace that can accommodate odd number of half BST unit cells, and N_A^i is the accommodate number of half BST unit cells on terrace i. The average NC-APB density (d) grown on the 1.2º miscut substrate is about 1/(407 × ½a_{BST}). It should be noted that the average lattice mismatch and NC-APB density varies with the probability of the formation of the terraces. For example, if the terraces dominating the substrate surface structure associate with a step of a_{MgO} high, the average lattice mismatch and NC-APB density could be estimated to be about -5.91% and 1/(203 × ½a_{BST}) ≈ 1/40 (nm^{-1}) (corresponding commensurate domain size at the interface is about 40 nm), respectively, which is very close to the experimental observations.

On the 3.5º miscut MgO substrate, terraces associated with a step of a_{MgO} high have an average width of 32 × ½a_{MgO} or 33 × ½a_{MgO}, while those associated a step of 2a_{MgO} high have an average width of 65 × ½a_{MgO} or 66 × ½a_{MgO}. The former terraces can accommodate 34.16 or 35.23 half BST unit cells, while the latter ones can accommodate 69.4 or 70.46 half BST unit cells. Therefore, 34 or 35 half BST unit cells can be queued on the former terraces with a corresponding local lattice mismatch of -5.88% and -5.71%, respectively. On the latter terraces, 65 or 66 half BST unit cells can be queued with a local lattice mismatch of -5.79% and -5.71%, respectively. Presuming the probability for forming the terraces with a width of 32 × ½aMgO, 33 × ½aMgO, 65 × ½aMgO and 66 × ½aMgO being 0.15, 0.35, 0.2 and 0.3, the average lattice mismatch and average NC-APB density could be estimated to be -5.74% and 1/19 (nm^{-1}) (corresponding commensurate domain size at the interface is about 19 nm), which agrees with the experimental observations.

Similarly, on the 5.3º miscut MgO substrate, terraces associated with a step of a_{MgO} high have an average width of 21 × ½a_{MgO} or 22 × ½a_{MgO}, while terraces associated a step of 2a_{MgO} high have an average width of 43 × ½a_{MgO} or 44 × ½a_{MgO}. The former terraces can accommodate 22.42 or 23.48 half BST unit cells, while the latter ones can accommodate 45.91 or 46.98 half BST unit cells. Therefore, 22 or 23 half BST unit cells can be queued on the former terraces with a corresponding local lattice mismatch of -4.54% and -4.34%, respectively. On the latter terraces, 46 or 47 half BST unit cells can be queued with a local lattice mismatch of -6.52% and -6.38%, respectively. Presuming that probability for forming the terraces with a width of 21 × ½a_{MgO}, 22 × ½a_{MgO}, 43 × ½a_{MgO} and 44 × ½a_{MgO} is 0.24, 0.16, 0.54 and 0.06, the average lattice mismatch and average NC-APB density could be estimated to be -5.69% and 1/33.3 (nm^{-1}) (corresponding commensurate domain size at the interface is about 33.3 nm), which agrees well with the experimental observations. The step height and terrace width of the miscut MgO surface, BST unit cell arrangements and the local lattice mismatch on the terraces are summarized in Table 5.1.

5.4 Dielectric and Mechanical properties of BST Films Grown on Miscut (001) MgO Substrates

Such differences in the interface structure influence film microstructure and thus, are expected to result in differences in the physical properties. For example, preliminary dielectric property measurements show that the dielectric constant and dielectric tunability of the BST films grown on the 1.2º, 3.5º and 5.3º miscut substrate show dramatic differences, as summarized in Table 5.2. The films grown on 1.2º and 5.3º miscut substrates show significantly higher dielectric constant and dielectric tunability, which are about 30% more than those for the film grown on 3.5º miscut substrate. The variations in dielectric property are attributed to misfit strain difference and the resulting variations in the microstructure of the films. What is surprising here is that the misfit strain difference between the 1.2° and 5.3° mistcut and the 3.5° miscut film is only about 5% (local misfit at the interface from plan-view TEM measurements) or 3.6% (overall film strain from cross-section TEM measurements). At a first consideration, it is hard to correlate such a small difference in misfit strain to a 30% change in dielectric properties. It seems that the observed differences in properties are arising from the difference in domain structures for these films that are resulting from the variation in misfit strain. Enhanced properties were observed for films with larger domain interface structures, 30~40 nm (1.2° and 5.3° mistcut films), compared to the films with small interface domain structure, 10~20 nm (3.5º mistcut films).

Table 5.2 Dielectric properties of BST thin films on (001) MgO measured at 300 K and 2 GHz.

Sample Types	**BST Films on (001) MgO**		
	ε_r (0V)	**ε_r (40V)**	**ε_r (Tuning %)**
(001)-1.0º off	1028	682	34%
(001)-3.0º off	790	598	24%
(001)-5.0º off	1202	790	34%

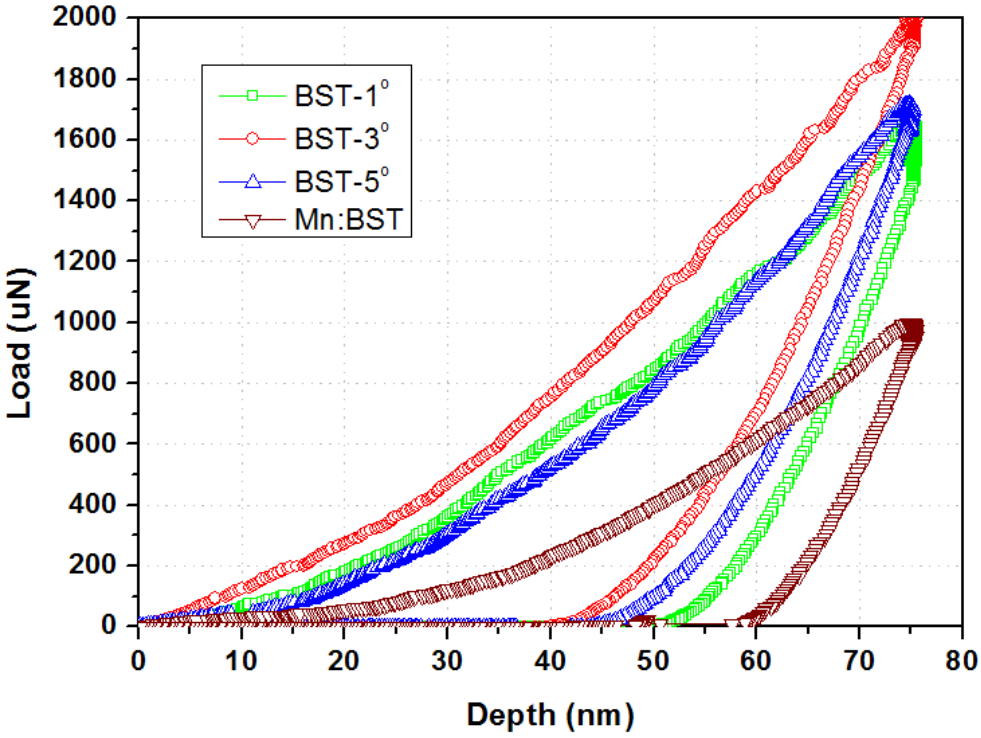

Figure 5.6 Typical load-displacement curves of BST-1^{o} off (green); BST-3^{o} off (red) and BST-5^{o} off (blue) films compared with Mn:BST (brown) films.

Figure 5.6 shows typical nano-indentation load-displacement curves for BST films on 1^{o}, 3^{o} and 5^{o} miscut MgO substrates compared to 2%Mn doped BST film grown on (001) MgO substrate. The average hardness and modulus values were determined by performing 16 array indents with the same displacement of 75 nm for each film. The mean hardness for each film is 8.06 GPa (BST-1^{o} off); 11.31 GPa (BST-3^{o} off); 9.14 GPa (BST-5^{o} off) and 4.33 GPa (Mn:BST), respectively. The mean modulus for 207.49 GPa (BST-1^{o} off); 213.19 GPa (BST-3^{o} off); 201.15 GPa (BST-5^{o} off) and 172.23 GPa (Mn:BST), respectively. Comparing the load-displacement curves of BST films grown on miscut MgO substrates and Mn:BST film deposited on (001) MgO substrate without miscut, a large difference of the maximum load at maximum displacement of 75 nm and residual penetration at zero load in the unloading segment depths were clearly observed. Mn:BST film shows a lowest modulus and hardness value due to the larger lattice mismatch (~6.4%) between film and MgO substrate compared to those of BST films grown on

miscut MgO substrates, indicating the lattice misfit at the film/substrate interface plays an important influence on the mechanical properties of epitaxial thin film. Furthermore, BST film grown on 3^o miscut MgO substrate has a highest average hardness and modulus value among BST miscut films. The higher hardness and modulus of BST 3^o miscut film can be considered to be resulted its smaller commensuration domain size at close to interface.

A further question could be raise up is if these domain structures dominate in the entire thickness of the films. Unfortunately, it is merely impossible to make such observation in the bulk of the films since this requires removing the substrate in order to obtain an electron transparent thin foil and thus, the removal of the substrate/film interface that is the source of the misfit. Nevertheless, the above results clearly indicate the importance of the domain size in determining film properties. Thus, manipulation of the interface structure can provide a potential powerful tool to obtain highly desirable properties. Obviously, additional detailed studies are needed to closer define these relationships.

5.5 Summary

In summary, the detailed microstructure and interface characterization of BST film grown on miscut MgO substrates with different miscut angles were performed using cross-section and plan-view TEM. Cross-section TEM studies reveal that the BST films grown on the substrate with a miscut angle of 1.2º, 3.5º, and 5.3º have a lattice mismatch of -5.4%, -5.7% and -5.5% with respect to the substrate, respectively, and no significant structural difference can be observed in the one dimensional (1-D) interface space. Plan-view TEM studies of the BST film/MgO interface exhibit significant structural difference in the two dimensional (2-D) interface space: (i) the BST films grown on the substrate with a miscut angle of 1.2º, 3.5º, and 5.3º have a lattice mismatch of -5.6%, -6.0% and -5.7% with respect to the substrate, respectively, larger than the value obtained using cross-section TEM; (ii) the size of the commensurate domains at the interface is about 30 to 40 nm for the films grown on the 1.2º and 5.3º miscut substrates, larger than that for the film grown on the 3.5º miscut, which is about 10 to 20 nm. The films

grown on 1.2º and 5.3º miscut substrates show about 30% higher dielectric constant and dielectric tunability than those for the film grown on 3.5º miscut substrate. However, the BST film grown on 3.5º miscut substrate possesses the highest average modulus and hardness value than those of the films grown on 1.2º and 5.3º miscut substrates. Such influence of the substrate miscut on the 2-D BST film/MgO substrate interface structure and physical properties provides direct evidence that variation of the substrate miscut results in differences in the surface steps, terraces and kinks that accordingly produce different commensuration domain structures in the 2-D interface plane. Thus, substrate miscut can serve as a nanofabrication tool to produce epitaxial films with desirable properties.

CHAPTER 6

FORMATION AND GROWTH MECHANISM OF {111} AND {110} TWIN-COUPLED DOMAIN STRUCTURES IN $Ba(Zr,Ti)O_3$ AND 2% Mn DOPED $Ba(Zr,Ti)O_3$ THIN FILMS

6.1 Introduction

Ferroelectric $Ba(Zr_xTi1_{-x})O_3$ (BZT) exhibits field-controlled nonlinear dielectric constant and even more chemically stable properties than $Ba_{1-x}Sr_xTiO_3$. BZT has been recently considered as one of the most important and promising materials for microwave devices e.g., tunable filters, phase shifter, antennas, etc. [248-252]. The most difficult task for such applications is to reduce the dielectric losses which in general increase with the frequency. The most common source of the loss normally is associated with the domains, twinning, grain boundaries and defects at the nanostructure level in the samples. Therefore, high quality epitaxial BZT thin films with a single crystalline structure, smooth surface and atomically sharp interface of this composition are highly desirable for the design of microwave components operating at very low voltages. Many efforts on improving the dielectric properties of BZT films has been recently made by changing the concentration ratio between Zr and Ti [249, 253, 254], using conductive oxide electrodes, such as $LaNiO_3$ [249, 253] and $CaRuO_3$ [255], or introducing small amount of acceptor dopants into the films. Doping of Ce, Yb or Mn into the BZT thin films are found to significantly improve the dielectric properties with enhanced dielectric tunability and lower dielectric loss [256, 257]. However, the mechanisms for such property enhancement by doping are not yet well understood. The properties of thin films are dramatically determined by the epitaxial quality, microstructure as well as film/substrate interface structure. As a consequence, understanding the microstructure, surfaces, interfaces, growth mechanism and doping effect on the microstructures in the BZT and Mn doped BZT thin films is considered necessary.

Furthermore, substitution of Ti^{4+} by Zr^{4+} results in many interesting phenomena. For example, it brings the three phase transition temperatures (T_1: rhombohedral to orthorhombic; T_2: orthorhombic to tetragonal and T_3: tetragonal to cubic) of the pure $BaTiO_3$ closer to each other, and eventually to one phase transition temperature (T_c: rhombohedral to cubic, rhombohedral phase for $T<T_c$ and cubic phase for $T>T_c$) at a concentration of ~15% Zr [258, 259]. Based on the phase diagram for the $BaTiO_3$-$BaZrO_3$ system constructed by Verbitskaia et al. in late 1950s [140], at room temperature $Ba(ZrxTi_{1-x})O_3$ solid solutions exist as rhombohedral structures (space group ***R3m***) for x from 6.5% to 20%, and as cubic (space group *Pm3m*) for x from 20% to 30%, as shown in Figure 6.1. The lattice parameters of the rhombohedral and cubic structures of $Ba(ZrxTi_{1-x})O_3$ vary with composition x. For example, $Ba(Zr_{0.195}Ti_{0.805})O_3$ (x=19.5%) has a rhombohedral structure with a_{Rh}= 4.044(0) Å and 89°57'<α_{Rh}<90°00', while $Ba(Zr0_{.21}Ti_{0.79})O_3$ (x=21%) has a cubic structure with a= 4.044(7) Å. Since the as-deposited BZT and Mn:BZT films in this work have 20% Zr composition, the microstructure of both films can be considered as a pseudo-cubic rhombohedral structure.

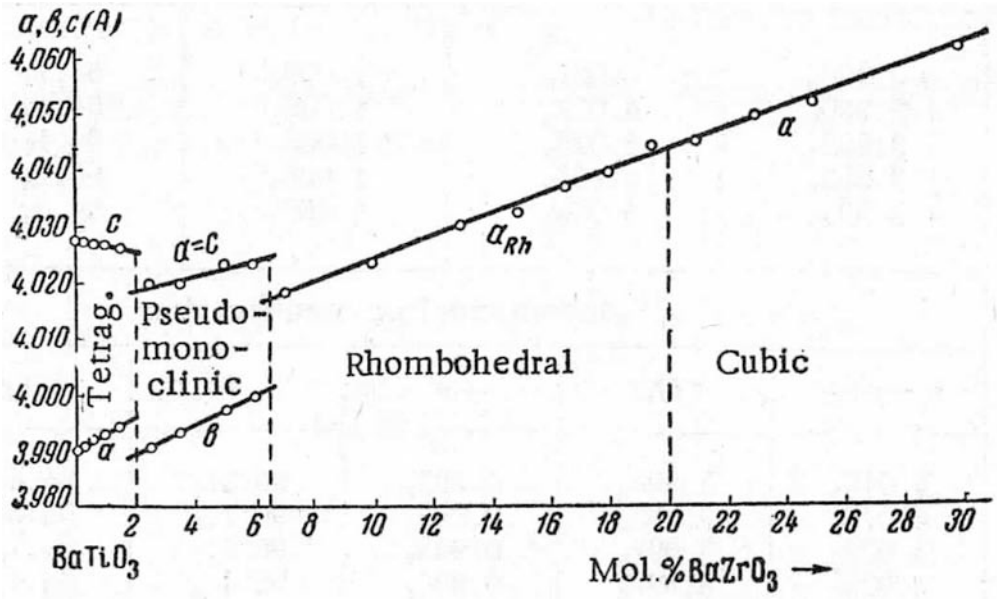

Figure 6.1 The dependence of the lattice constants on composition for the different modifications of the solid solutions in $BaTiO_3$-$BaZrO_3$ system [140].

Besides, the selected-area EDPs of the BZT films obtained from various crystallographic orientations exhibit characteristics of the cubic perovskite structure. Since the structural difference between the rhombohedral and cubic structure at close to 20% Zr composition is too small to be detected using the selected-area electron diffraction (SAED) technique, BZT and Mn:BZT films can be referred as a pseudo-cubic rhombohedral perovskite structure.

In this chapter, the microstructure and growth mechanism of $Ba(Zr_{0.2}Ti_{0.8})O_3$ (BZT) and 2% Mn doped $Ba(Zr_{0.2}Ti_{0.8})O_3$ (Mn:BZT) films deposited using PLD were investigated. Both BZT and Mn:BZT films have been found to exhibit a structure composed with an epitaxial layer near the interface followed by the formation of twin-coupled nano-pillars on the top surface. The epitaxial structure and multi-oriented twin domains are joined together by sharing their {111} or {110} plane as a common plane. The detailed microstructure, orientation relationship of epitaxial layer; twin domains and substrate, film/substrate interface, atomic structure on the sharing planes, and structure transition have been systematically discussed as follows.

6.2 Twin-coupled Domian Structures in $Ba(Zr,Ti)O_3$ Thin Films on (001) MgO Substrate

Figure 6.2 (a) is a cross-sectional BZT/MgO image with electron beam parallel to MgO [100] direction. The BZT film has a thickness of 650 nm. Two layers can be observed in the BZT film: (i) a continuous layer adjacent to the substrate with a thickness of about 150 nm and (ii) a column-featured structure layer on the top of the film with a thickness of about 500 nm. A sharp interface can be seen between the film and the MgO substrate. Figure 6.2 (b) and (c) show the selected-area EDPs (SAED) taken from BZT film with an area covering many columns and continuous layer, and the interface between BZT and MgO substrate, respectively, with the electron beam parallel to the [100] axis of MgO. Figure 6.2 (b) shows a pseudo-cubic and epitaxial single crystal structure in BZT film. Figure 6.2 (c) shows the diffraction pattern exhibiting a simple superposition of the MgO substrate and a clean single cubic crystal structure of the BZT. The BZT20 continuous epilayer is epitaxially grown on (001) MgO with an

orientation relationship of $(001)_{BZT}//(001)_{MgO}$, $[100]_{BZT}//[100]_{MgO}$, $[010]_{BZT}//[010]_{MgO}$. The lattice mismatch between the BZT continuous epilayer and MgO substrate is -4.3% calculated using $(a_{BZT}-a_{MgO})/a_{MgO}$, whereas was measured from the EDP. Correspondingly, the lattice constant of this pseudo-cubic rhombohedral structure is 4.03 Å as determined from the EDPs which were calibrated using MgO (a_{MgO} = 4.212 Å) as a standard.

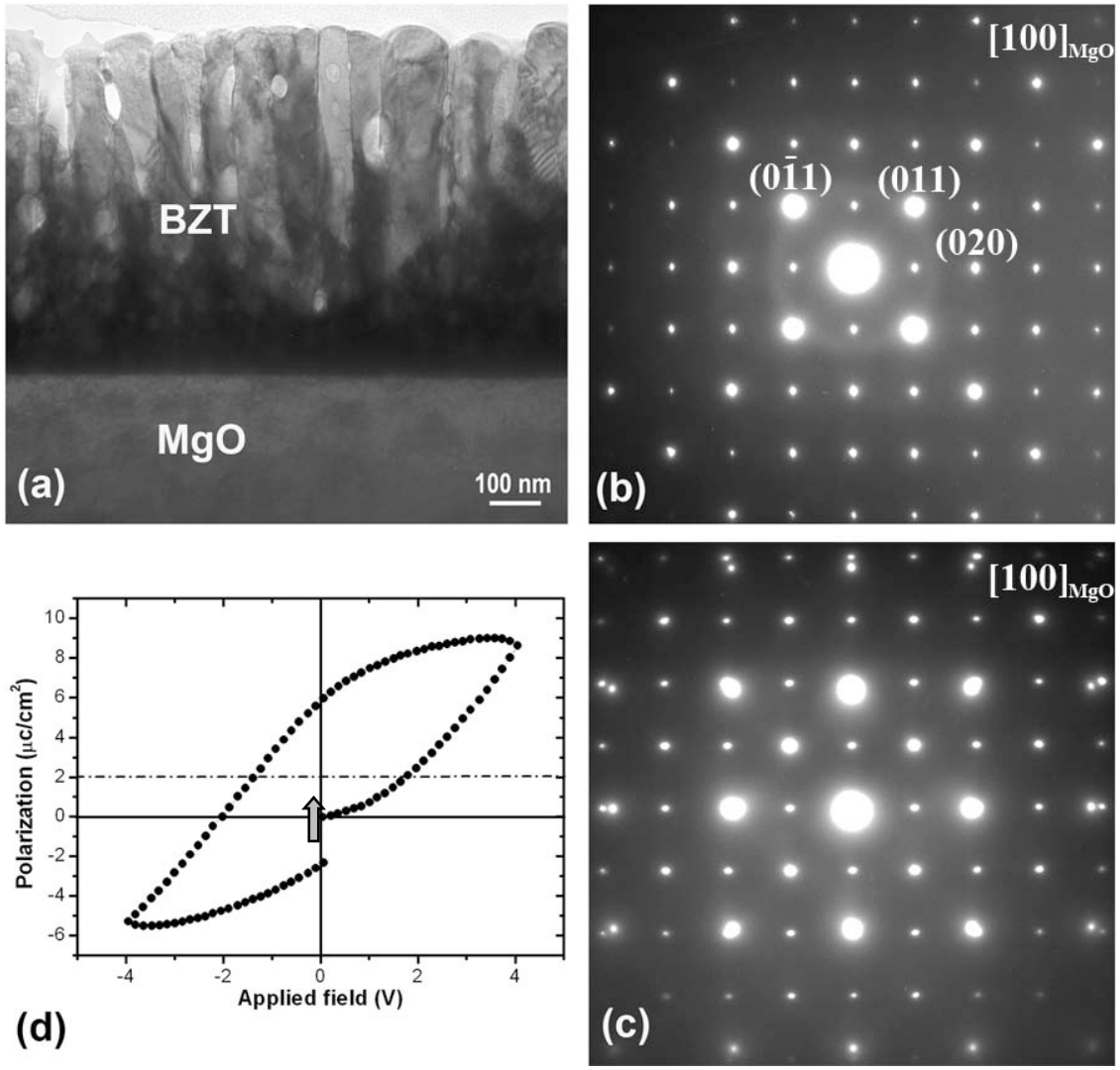

Figure 6.2 Cross-section TEM with electron beam along $[100]_{MgO}$: (a) low magnification image of BZT/MgO; SAED from (b) BZT film and (c) film/substrate interface; and (d) polarization-applied field hysteresis loop performed at room temperature.

Figure 6.2 (d) shows hysteresis loop measurements of BZT thin films obtained at room temperature indicating the ferroelectricity of the as-grown films with $SrRuO_3$ bottom electrodes and gold top electrodes. It is surprisingly to find that the as-grown pseudo-cubic films have a very large spontaneous polarization value of 9 μC/cm^2, which is much larger than that of the BZT bulk material, indicating that the BZT films have good dielectric properties. However, the center of the P-V hysteresis loop is shifted by 2 μC/cm^2 from the origin to the positive direction, as seen in Figure 6.2 (d), suggesting existence of various polarizations switching in the BZT films. This could be resulting from the different polarized domain structures or different polarized orientation in the domains and the graded coupling effects in the composite structure of the films.

One possible type of domains formed in the epitaxial films of a pseudo-cubic structure is a twin-related domain. Considering the growth of an epitaxial BZT film (called "epilayer"), twin structures are introduced by sharing their {111} planes with the epilayer structure (Figure 6.3 (a)). For example, if a corner of the cubic structure of the epilayer is cut off along the (111) plane and joined with another counterpart, of which one corner is also cut off along the {111} plane, a twin coupled structure is formed (**Twin-1** in Figure 6.3 (a)). The orientation relationship between the epilayer and the **Twin-1** can be described as: $(111)_{epilayer}//(111)_{Twin-1}$; $[\bar{1}10]_{epilayer}//[\bar{1}10]_{Twin-1}$; $[0\bar{1}1]_{epilayer}//[0\bar{1}1]_{Twin-1}$ and $[\bar{1}01]_{epilayer}//[\bar{1}01]_{Twin-1}$. Since the (111), $(\bar{1}11)$, $(\bar{1}\bar{1}1)$ and $(1\bar{1}1)$ planes of the cubic structure in the epilayer possess an equal opportunity to form twin structures, four possible oriented twin-coupled domains, namely **Twin-1**, **Twin-2**, **Twin-3** and **Twin-4** (Figure 6.3 (a)) can coexist.

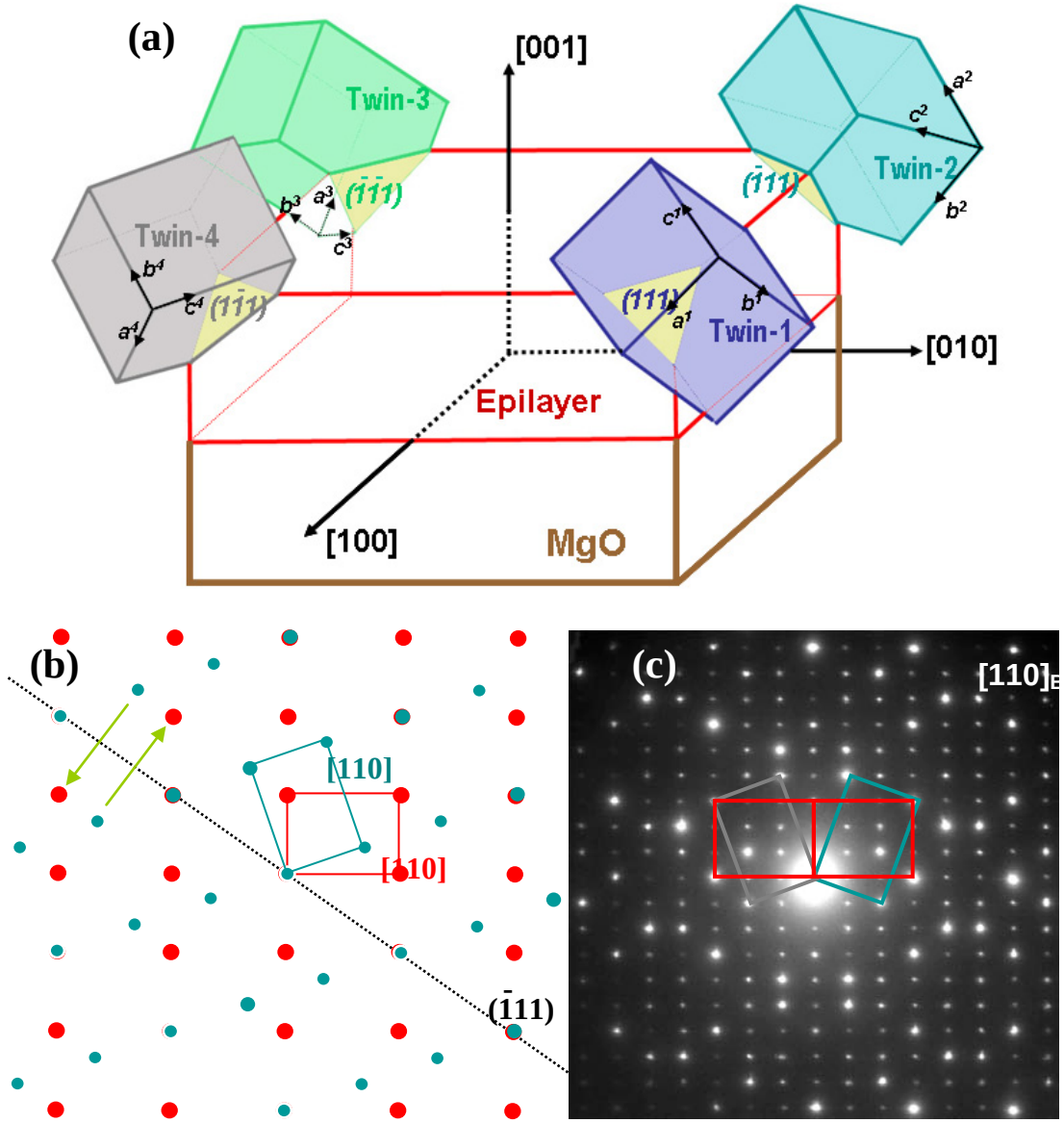

Figure 6.3 Schematic illustrations of (a) epilayer structure and four possible oriented twin domains; (b) EDP simulation of epilayer and **Twin 2** observed from $[110]_{epi}$ and (c) experimental observation of EDP from [110] direction of BZT epilayer structure, showing three Twins in BZT film: epilayer, **Twin 2** and **Twin 4**.

These Twins have symmetry along {111} with respect to epilayer structure. This symmetry also can be schematically proved by the simulation of EDP from $[110]_{epilayer}$ in Figure 6.3 (b). In Figure 6.3 (b), red spots represent [110] zone EDP from film epilayer, and blue spots represent [110] zone EDP from **Twin 2**. It presents that all the diffraction spots showing

complete symmetry along $(\bar{1}11)$. Therefore, EDPs from four twins with (111), $(\bar{1}11)$, $(\bar{1}\bar{1}1)$ and $(1\bar{1}1)$ sharing planes should be shown in [110] direction of epilayer, if {111} twin structures are formed in BZT film. Since [100] direction of epilayer is not parallel to any zone axis in four twins, the EDPs from twin structures cannot be shown $[100]_{epi}$ but only that from film epilayer, as shown in Figure 6.2 (b) and (c). Besides, only $(\bar{1}11)$ of **Twin 2** and $(1\bar{1}1)$ of **Twin 4** is parallel to $[110]_{epi}$ in all four-oriented twins, and therefore can be observed from $[110]_{epi}$ direction. As proposed, three twins with film epilayer, **Twin 2** and **Twin 4** are successfully experimental observed in $[110]_{epi}$ zone EDP of BZT film, as shown in Figure 6.3 (c). All the explanations agree well to the TEM results in Figure 6.2 and Figure 6.3. Thus, it is can be concluded that {111} multi-oriented twin domains structure has been formed in BZT films.

The epilayer and Twin domain structures can be separated observed using bright-field and dark-field TEM technique, as shown in Figure 6.4. Figure 6.4 (a) is a bright field TEM image of a cross-sectional BZT/MgO sample with electron beam parallel to [100] axis of MgO substrate. Similarly as shown in Figure 6.2 (a), two layers composed with a continuous layer at bottom close to MgO substrate and a columnar layer on the top can be clearing seen by contrast in Figure 6.4 (a). Figure 6.4 (b) is a dark-field image obtained by using the (020) reflection for BZT in Figure 6.2 (b) clearly showing the substrate and the continuous BZT epilayer (bright contrast). The observation of both substrate and the film is due to the fact that (020) reflection of BZT and MgO are nearly at the same position and both contribute to the dark-field image. It also further confirms the good epitaxial relationship between BZT epilayer and MgO substrate. Figure 6.4 (c) and (d) are dark-field images obtained using the $(0\bar{1}1)$ and (011) reflection in Figure 6.2 (b), respectively. The dark regions in Figure 6.4 (c) appear bright in Figure 6.4 (d) and vice versa. Such contrast difference between Figure 6.4 (c) and (d) suggests different corresponding domains: Twin (1, 2) and Twin (3, 4), respectively. The twin domains (bright contrast in Figure 6.4 (c) and (d)) dominate the top column layer, while epilayer structure

concentrates at the continuous layer (bright contrast in Figure 6.4 (b)). The overlap of the bright area in Figure 6.4 (b), (c) and (d) can match the entire film in Figure 6.4 (a), indicating no other domains with the orientation relationship except {111} twin domains are formed in BZT films.

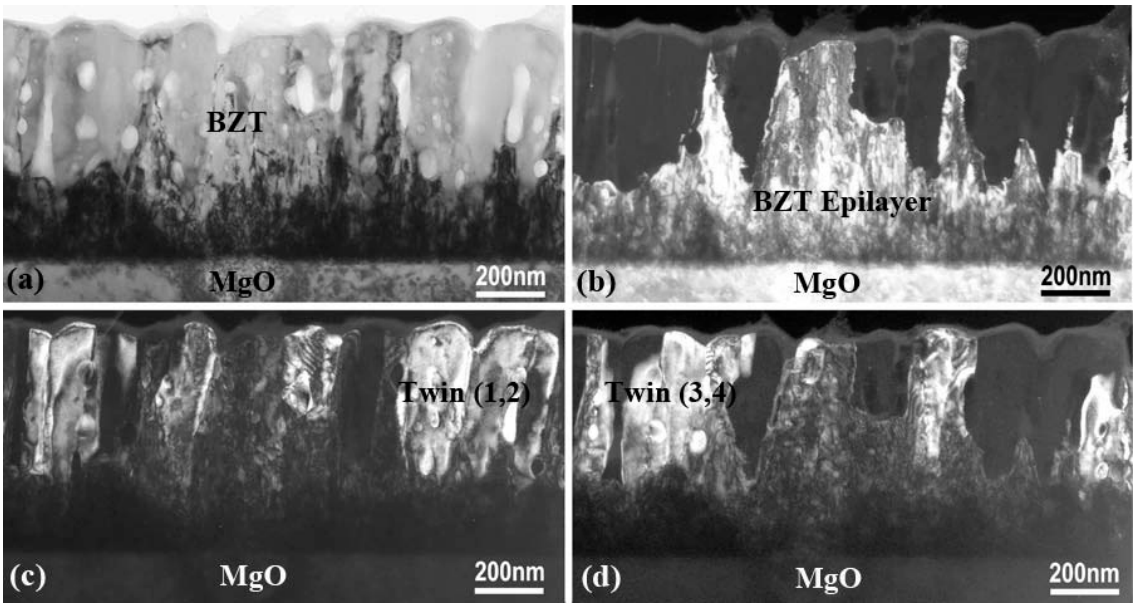

Figure 6.4 Cross-section TEM with electron beam along $[100]_{MgO}$ direction (a) bright-field image of BZT/MgO and (b); (c) and (d) center dark-field image obtained using (020); $(0\bar{1}1)$ and (011) reflection in Figure 6.2 (b), respectively.

Figure 6.5 shows EDPs of the epilayer, **Twin 2** and **Twin 4**, and their orientation relationships. In a cubic system, the angle between [001] and [111] axes is 54.7°, and the angle between [111] and [110] axes is 35.5°. These relationships are also shown in Figure 6.5. From structure model in Figure 6.3 (a), film epilayer and **Twin 2** are sharing the same $(\bar{1}11)$ plane, and similarly Epilayer and **Twin 4** have the same common plane of $(1\bar{1}1)$. The angle difference between [001] direction of matrix and [110] direction of **Twin 2** is 19.4°. And the angle difference between [001] direction of matrix and $[\bar{1}\bar{1}\bar{1}]$ direction of **Twin 4** is 15.9°. And therefore the angle difference between [110] direction of **Twin 2** and $[\bar{1}\bar{1}\bar{1}]$ direction of **Twin 4** is only 3.5°, indicating the possibility of observation both two twins within just tilting a very small angle of 3.5°.

Table 6.1 Orientation relationships between the epilayer and the multi-oriented twins.

Twin-1	***Twin-2***	***Twin-3***	***Twin-4***
$(111)_{epilayer}$ // $(111)_{Twin-1}$	$(\bar{1}11)_{epilayer}$ // $(\bar{1}11)_{Twin-2}$	$(\bar{1}\bar{1}1)_{epilayer}$ // $(\bar{1}\bar{1}1)_{Twin-3}$	$(1\bar{1}1)_{epilayer}$ // $(1\bar{1}1)_{Twin-4}$
$[\bar{1}10]_{epilayer}$ // $[\bar{1}10]_{Twin-1}$	$[110]_{epilayer}$ // $[110]_{Twin-2}$	$[1\bar{1}0]_{epilayer}$ // $[1\bar{1}0]_{Twin-3}$	$[110]_{epilayer}$ // $[110]_{Twin-4}$
$[\bar{1}01]_{epilayer}$ // $[\bar{1}01]_{Twin-1}$	$[101]_{epilayer}$ // $[101]_{Twin-2}$	$[101]_{epilayer}$ // $[101]_{Twin-3}$	$[\bar{1}01]_{epilayer}$ // $[\bar{1}01]_{Twin-4}$
$[0\bar{1}1]_{epilayer}$ // $[0\bar{1}1]_{Twin-1}$	$[0\bar{1}1]_{epilayer}$ // $[0\bar{1}1]_{Twin-2}$	$[011]_{epilayer}$ // $[011]_{Twin-3}$	$[011]_{epilayer}$ // $[011]_{Twin-4}$

Table 6.2 Orientation relationships between the multi-oriented twin domains.

	Twin-1	***Twin-2***	***Twin-3***
Twin-4	$(\bar{1}01)_{Twin-1}$ // $(\bar{1}01)_{Twin-4}$ $[212]_{Twin-1}$ // $[\bar{2}1\bar{2}]_{Twin-4}$ $[\bar{1}4\bar{1}]_{Twin-1}$ // $[1\bar{4}1]_{Twin-4}$	$(110)_{Twin-2}$ // $(110)_{Twin-4}$ $[\bar{2}21]_{Twin-2}$ // $[2\bar{2}1]_{Twin-4}$ $[1\bar{1}4]_{Twin-2}$ // $[1\bar{1}\bar{4}]_{Twin-4}$	$(011)_{Twin-3}$ // $(011)_{Twin-4}$ $[1\bar{2}2]_{Twin-3}$ // $[12\bar{2}]_{Twin-4}$ $[41\bar{1}]_{Twin-3}$ // $[\bar{4}1\bar{1}]_{Twin-4}$
Twin-3	$(1\bar{1}0)_{Twin-1}$ // $(1\bar{1}0)_{Twin-3}$ $[221]_{Twin-1}$ // $[\bar{2}\bar{2}1]_{Twin-3}$ $[\bar{1}\bar{1}4]_{Twin-1}$ // $[11\bar{4}]_{Twin-3}$	$[101]_{Twin-2}$ // $[101]_{Twin-3}$ $[21\bar{2}]_{Twin-2}$ // $[\bar{2}12]_{Twin-3}$ $[\bar{1}41]_{Twin-2}$ // $[\bar{1}\bar{4}1]_{Twin-3}$	
Twin-2	$(0\bar{1}1)_{Twin-1}$ // $(0\bar{1}1)_{Twin-2}$ $[122]_{Twin-1}$ // $[1\bar{2}\bar{2}]_{Twin-2}$ $[\bar{4}11]_{Twin-1}$ // $[4\bar{1}\bar{1}]_{Twin-2}$		

The orientation relationship between the twin-coupled domains and the epilayer is summarized in Table 6.1. In addition to their common {111} plane, the epilayer and each single twin domain share three different oriented {110} planes, such as (110), (011) and (101). Besides, any two oriented twin domains have a common {110} plane with a specific orientation relationship. For example, the orientation relationship between **Twin-2** and **Twin-4** domains can be described as: $(110)_{Twin-2}$ // $(110)_{Twin-4}$; $[\bar{2}21]_{Twin-2}$ // $[2\bar{2}1]_{Twin-4}$ and $[1\bar{1}4]_{Twin-2}$ // $[1\bar{1}\bar{4}]_{Twin-4}$. The orientation relationships among the rest twin domains are summarized in Table 6.2.

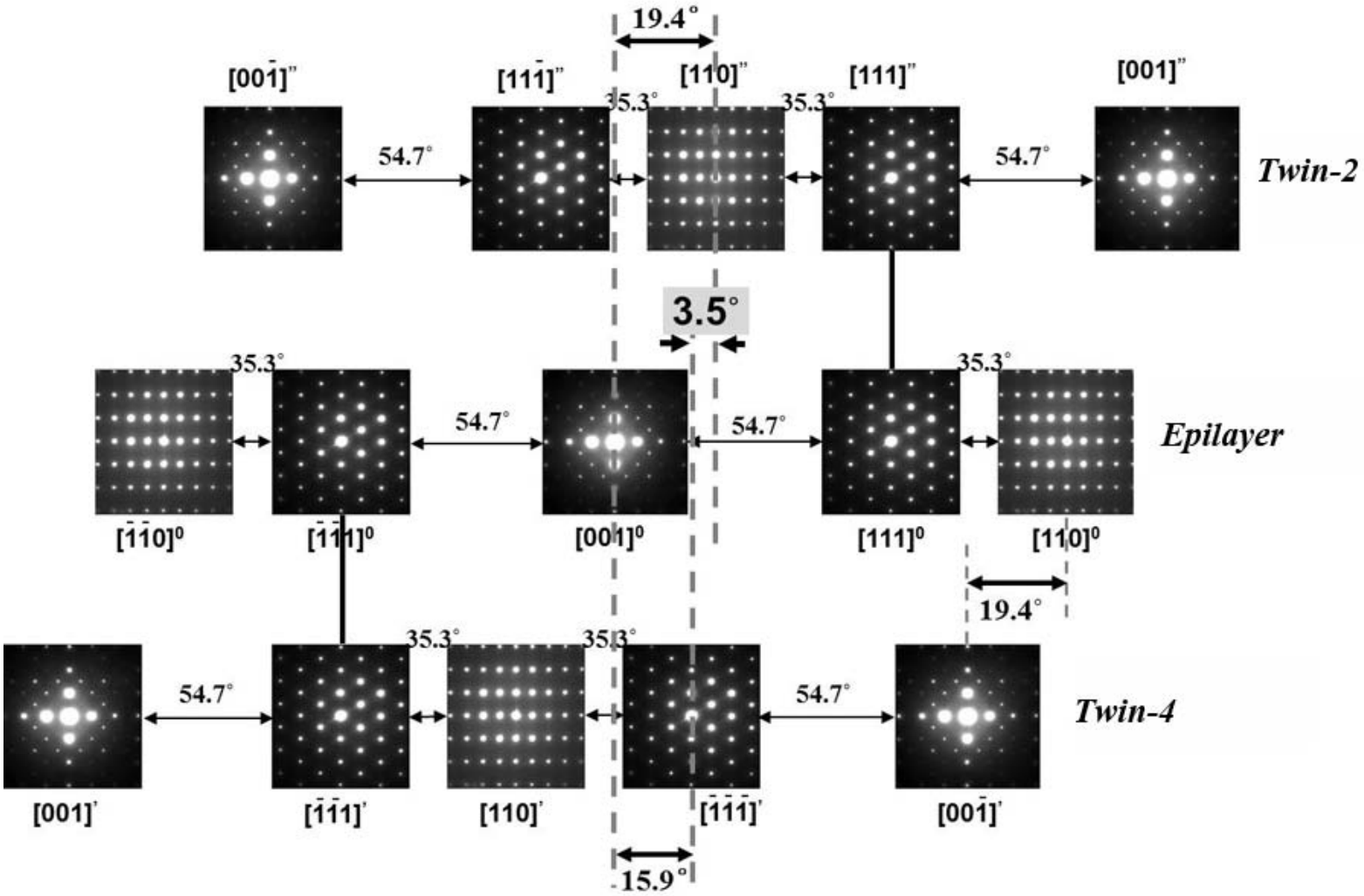

Figure 6.5 EDPs of the epilayer, **Twin-2** and **Twin-4**, and their orientation relationships.

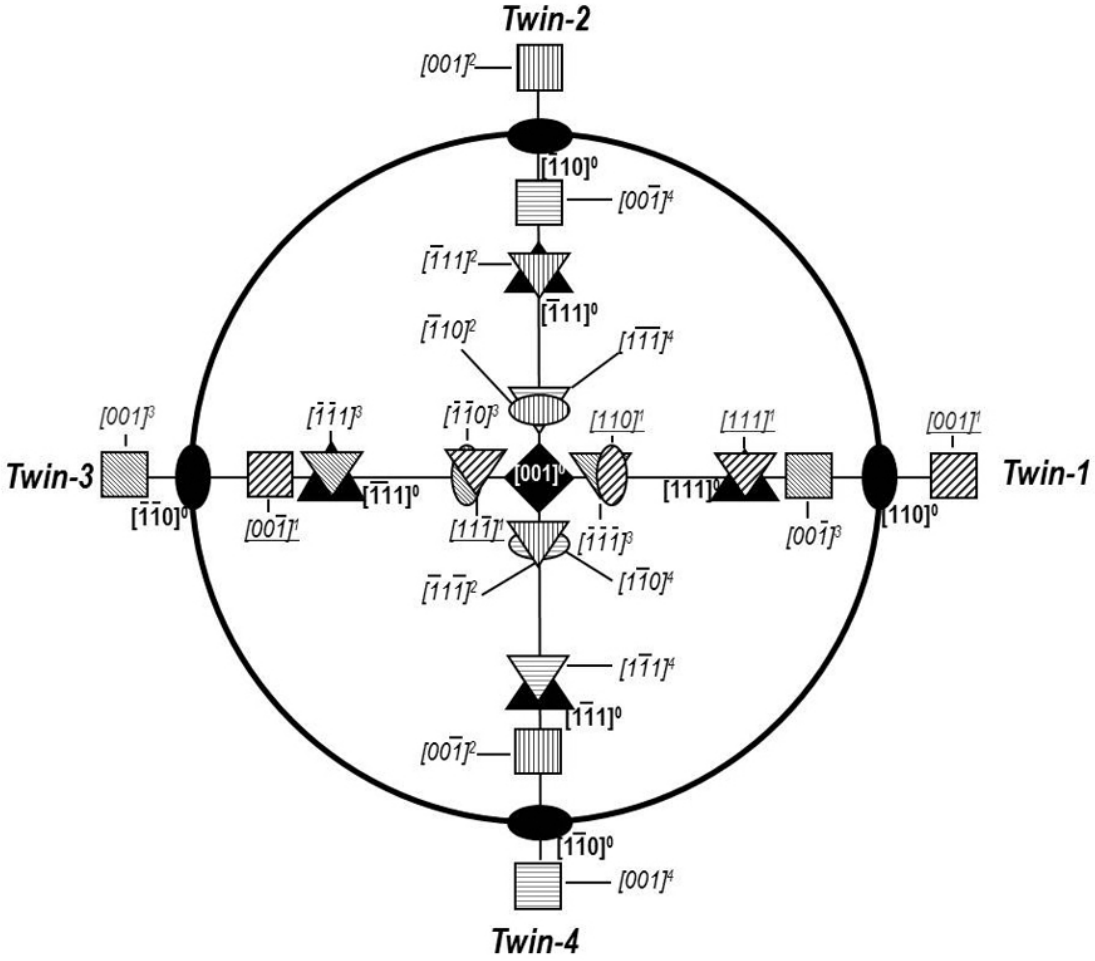

Figure 6.6 Schematic illustration of the crystallographic orientation relationships between the epilayer and the four twin domains. Solid symbols (squares, triangles and ellipses) represent the zone axes of the epilayer, while hatched symbols (coarse slope, horizontal line, fine slope and vertical line) represent the zone axes of **Twin-1**, **Twin-2**, **Twin-3** and **Twin-4**, respectively.

The orientation relationship between the twins and the epilayer in the reciprocal space is schematically illustrated in Figure 6.6. The black square, triangles and ellipses in Figure 6.6 represent the $[001]^0$, $<111>^0$ and $<110>^0$ zones of the cubic structure of the epilayer, respectively. The angle between the $<111>^0$ and its adjacent $[001]^0$ and $[110]^0$ is equal to 54.7° and 35.3°, respectively. Since the twin domains share their {111} plane with the epilayer, one of the <111> zones is coincident with one <111> of the film epilayer. For example, **Twin-2** shares its $(\bar{1}11)$ plane with the epilayer, its $[\bar{1}11]^2$ zone (upper triangle filled with vertical lines) is

coincident with the $[\bar{1}11]^0$ of the epilayer (black triangle). The $[\bar{1}10]^2$ (ellipse filled with vertical lines) and $[\bar{1}1\bar{1}]^2$ (lower triangle filled with vertical lines) of **Twin-2** have an angle of 19.4˚ and 15.9˚ with respect to the $[001]^0$ of the epilayer, respectively. The angular orientation relationships of **Twin-1**, **Twin-3**, and **Twin-4** with respect to the epilayer can be obtained in a similar manner and are illustrated in Figure 6.5. The angle between $[\bar{1}10]^2$ of **Twin-2** and $[1\bar{1}\bar{1}]^4$ of **Twin-4** is equal to (19.4˚ - 15.9˚) = 3.5˚. Similarly, the angle between $[110]^1$ of **Twin-1** and $[\bar{1}\bar{1}\bar{1}]^3$ of **Twin-3** is equal to = 3.5˚.

Figure 6.7 shows plan-view TEM images presenting the microstructure of the top layer of the BZT on the film plane. Grainy structures and nano pores were observed in the film plane (Figure 6.7 (a)). Selected-area EDPs taken from an area covering many grains show a single crystal electron diffraction pattern, as presented in the inset in Figure 6.7 (a). It should be noticed that when the electron beam parallel to the [001] direction of the BZT epilayer, only the $(\bar{1}10)$ planes of **Twin-1** ($(\bar{1}10)_{Twin-1}$) and **Twin-3** ($(\bar{1}10)_{Twin-1}$), and the (110) planes of **Twin-2** ($(110)_{Twin-2}$) and **Twin-4** type ($(110)_{Twin-4}$) parallel to the electron beam. The $(\bar{1}10)$ diffraction spot in the inset EDP in Figure 6.7 (a) is resulted from the epilayer, the **Twin-1** and **Twin-3** domains, while the (110) diffraction spot in the inset EDP of Figure 6.7 (a) is resulted from the epilayer, the **Twin-2** and **Twin-4** domains.

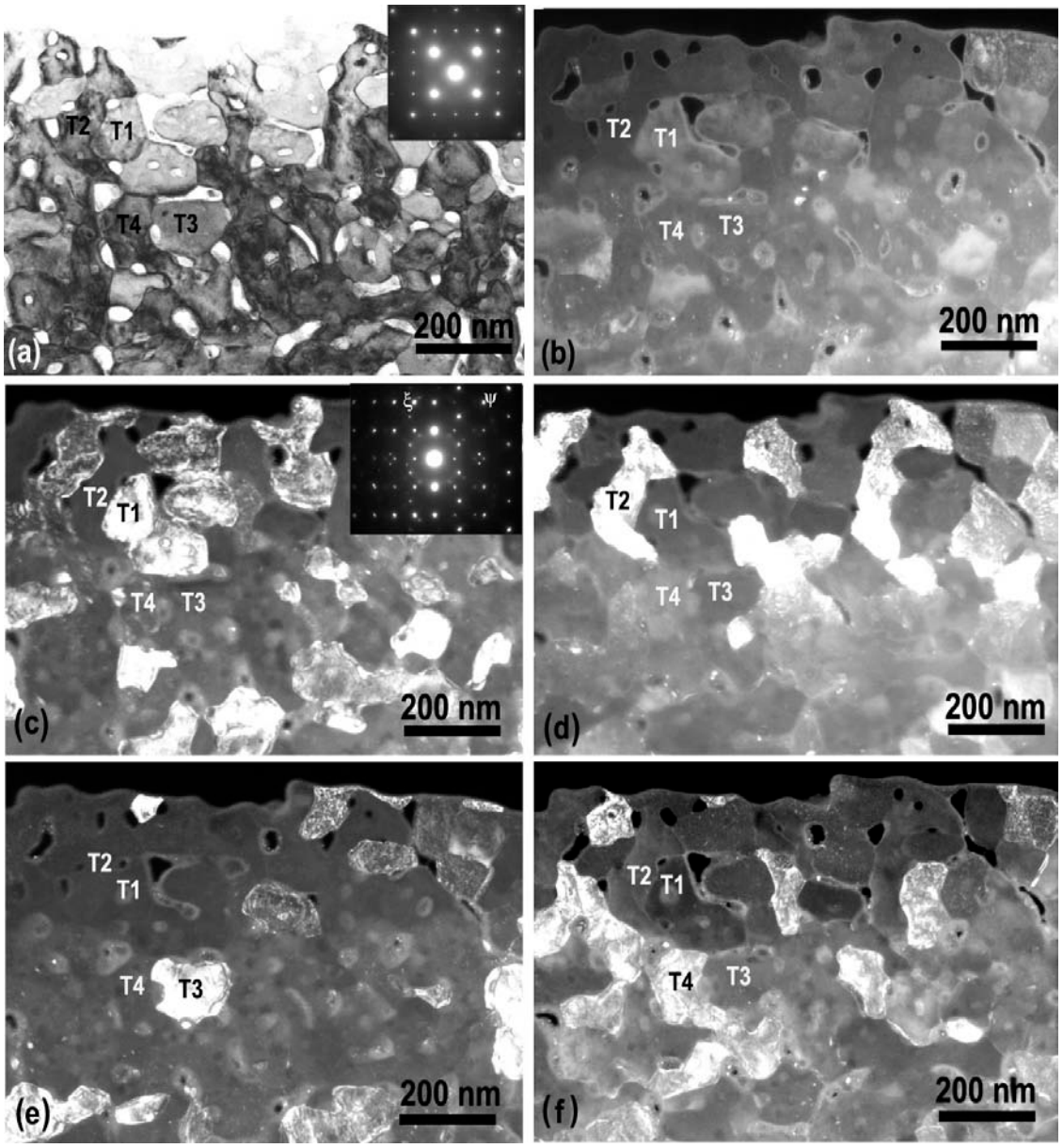

Figure 6.7 Plan-view TEM (a) bright-field image of BZT20 film near the surface and an inset EDP; (b) Center dark-field image obtained using the weak (200) reflection in the inset EDP in (a); (c); (d); (e) and (f) Dark field images showing presence of twin domain **Twin-1** (T1), **Twin-2** (T2), **Twin-3** (T3), and **Twin-4** (T4), respectively. Inset EDP in (c) is an overlap of the [110] and [111] EDPs.

Figure 6.7 (b) is a dark-field TEM image obtained using one of the weak diffraction spots in the inset EDP of Figure 6.7 (a), showing very weak contrast. Tilting the plan-view TEM film from the [001] zone axis by about 17 along the $[\bar{1}10]$ direction of the BZT epilayer, an EDP

consisting of an overlap of the $[110]^1$ zone of **Twin-1** and $[\bar{1}\bar{1}\bar{1}]^3$ zone of **Twin-3** can be obtained as shown in the inset of Figure 6.7 (c). Fig. 6.7 (c) shows a dark-field TEM image obtained using the ξ reflection (belongs to the $[110]^1$ zone EDP of **Twin-1**) in inset EDP of Figure 6.7 (c). The bright areas in Figure 6.7 (c) correspond to the domains of the **Twin-1** type. Figure 6.7 (e) is a dark-field TEM image obtained using the ψ reflection (belongs to the $[\bar{1}\bar{1}\bar{1}]^3$ zone of **Twin-3**) in inset EDP of Figure 6.7 (c). The bright areas in Figure 6.7 (e) correspond to the domains of the **Twin-3** type. Since the $(\bar{1}10)$ diffraction spot in the inset EDP of Figure 6.7 (a) is diffracted from, in addition to the epilayer, both type **Twin-1** and **Twin-3** domains, dark-field image of the $(\bar{1}10)$ reflection in the inset EDP of Figure 6.7(a) exhibit bright regions which are the superposed bright areas shown in Figure 6.7 (c) and Figure 6.7 (e). Similarly, tilting the plan-view TEM film from the [001] zone axis by about 17° along the [110] direction of the BZT epilayer, an EDP consisting of an overlap of the $[\bar{1}10]^2$ zone of **Twin-2** and $[1\bar{1}\bar{1}]^4$ zone of **Twin-4** can be obtained. This EDP is the same as that shown in the inset in Figure 6.7 (c).

Figure 6.7 (d) is a dark-field TEM image obtained using a reflection in the $[\bar{1}10]^2$ zone EDP of **Twin-2** domain with the bright areas presenting the domains of the **Twin-2** type. Figure 6.7 (f) is a dark-field TEM image obtained using a reflection in the $[1\bar{1}\bar{1}]^4$ zone of **Twin-4** domain with the bright areas presenting the domains of the **Twin-4** type. The dark-field image of the common (1 1 0) reflection for both **Twin-2** and **Twin-4** type domains show bright regions that can be obtained by superposing those in Figure 6.7 (d) and Figure 6.7 (f). The superposition of the bright regions shown in Figure 6.7 (c); (d); (e) and (f) fill almost the entire area shown in Figure 6.7 (a) indicating that the top layer of the BZT film is dominated by the four types of twin domains. This conclusion is confirmed by the very weak contrast in dark-field image of the epilayer (Figure 6.7 (b)) indicating presence of very little epilayer material. When

the electron beam is parallel to the [001] direction of the BZT epilayer, the zone axes of the other four type domains are off the electron beam direction. Since the {110} planes of the twin domains are coincident with the {110} planes of the epilayer, the twin domains will contribute to those diffraction spots that are located on the [110] and $[1\bar{1}0]$ direction of the [001] zone EDP of the epilayer. This produces much stronger diffraction spots compared with those reflections off the two directions.

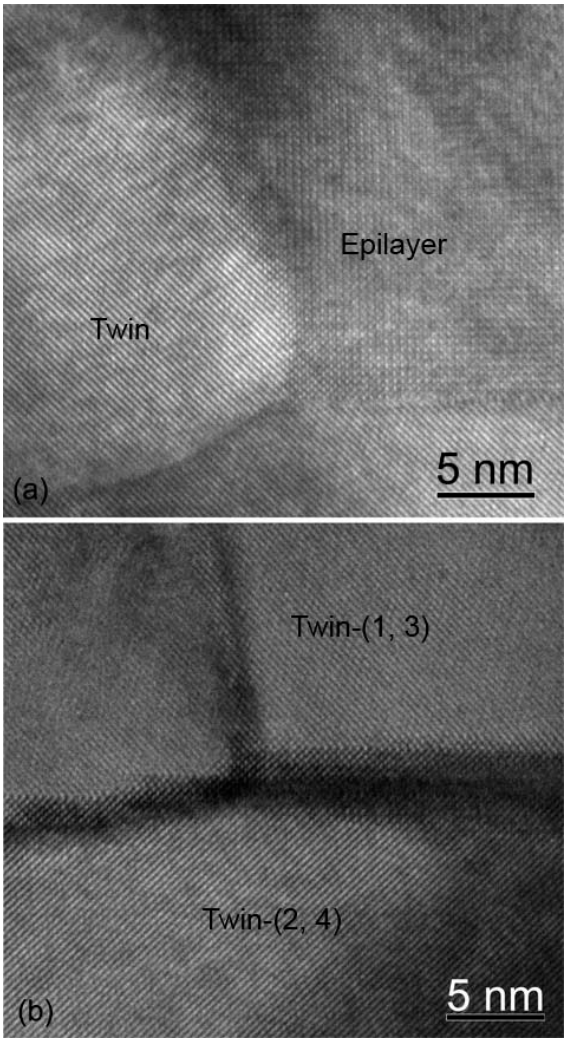

Figure 6.8 HRTEM images of a plan-view TEM sample showing coexistence of (a) epilayer and twin; (b) twins with their {110} planes perpendicular to each other, e.g., Twin-(1,3) and Twin-(2,4).

Figures 6.8 (a) and (b) show HRTEM images taken from a plan-view TEM foil with the electron beam parallel to the [001] axis of the epilayer. Figure 6.8 (a) exhibits presence of the epilayer and the twin domains. It is very clear that the lattice image of the (110) planes extended from the twin domains to the epilayer region. Also, the boundaries between the twin domains are clearly seen, beside which the twin domains are shifted half lattice spacing of the {110} planes along the [110] direction. Fig. 6.8 (b) exhibits presence of three twin domains, the lattice image of the (110) planes in one domain is perpendicular to the other two domains. The domains with different oriented (110) plane can be associated to either Twin-(1,3) or Twin-(2,4) type.

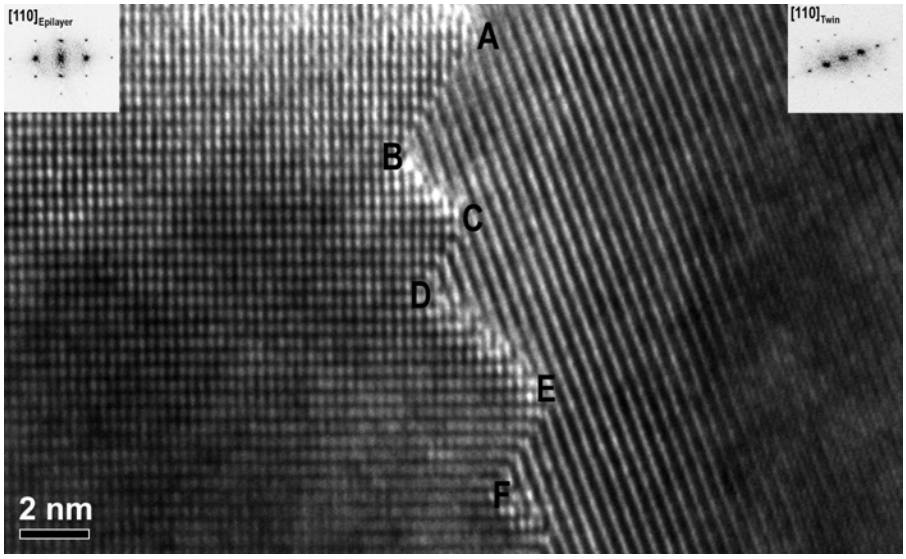

Figure 6.9 HRTEM image of a cross-section BZT/MgO viewed along the [110] direction of MgO.

Figure 6.9 shows a HRTEM image taken from a cross-section BZT/MgO sample with the electron beam parallel to the [110] of the substrate exhibiting coexistence of the epilayer (left) and a twin-coupled domain (right). The insets on the top-left and top-right corner present the fourier transformations (FTs) calculated from the left epilayer and the right twin-coupled domain, respectively. Each individual fourier transformation exhibits a pattern similar to the [110] EDP of the BZT. A zig-zag boundary composed of straight line segments along the $(1\bar{1}1)$ (AB, CD and EF) or $(\bar{1}11)$ (BC and DE) plane of the BZT were clearly seen in Figure 6.9. This

result further provides direct evidence that twin structures were introduced by sharing their {111} planes with the epilayer structure.

6.3 Structure Evolution of Nanopillars in $Ba(Zr,Ti)O_3$ and 2% Mn-doped $Ba(Zr,Ti)O_3$ Thin Films Driven by {110} Twin Boundaries

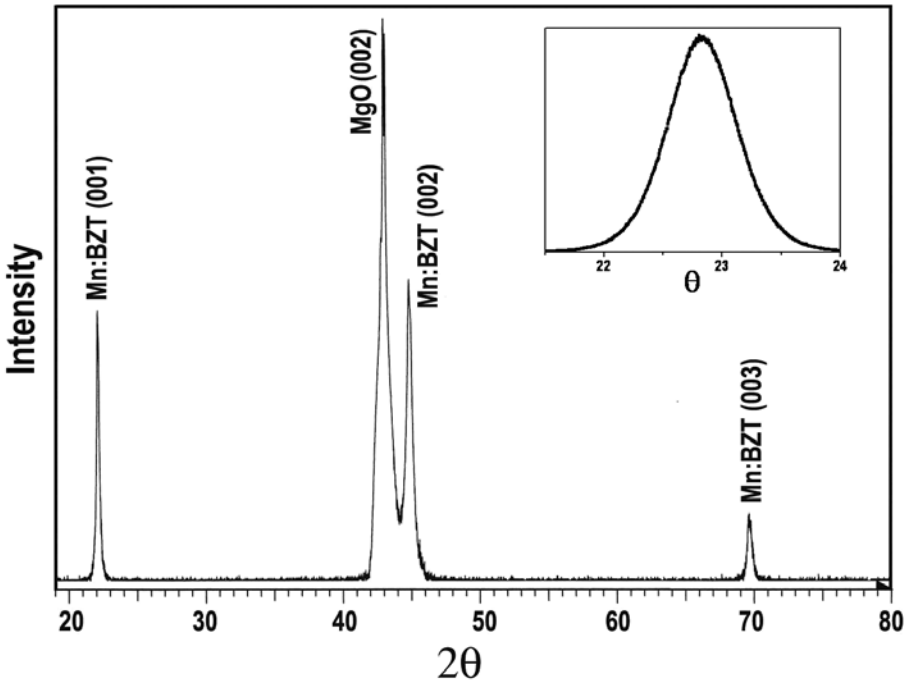

Figure 6.10 θ-2θ scan X-ray diffraction pattern of an as-grown Mn:BZT film on MgO (001) substrate and the rocking curve of Mn:BZT (002) reflection (inset).

Figure 6.10 shows a XRD θ-2θ scan of the as-grown Mn:BZT film deposited on MgO (001) substrate and the rocking curve of Mn:BZT (002) reflection. Only (00l) peaks for Mn:BZT and MgO substrate are observed in the θ-2θ scan diffraction pattern, indicating that the film is highly c-axis oriented (c = 4.04 Å). The full width at half maximum (FWHM) of the rocking curve is about 0.68 degree. Such small angle differences in rocking curve indicate a good epitaxial quality of the Mn:BZT film deposited on MgO substrate. The lattice mismatch between the film and the substrate is about -3.8%.

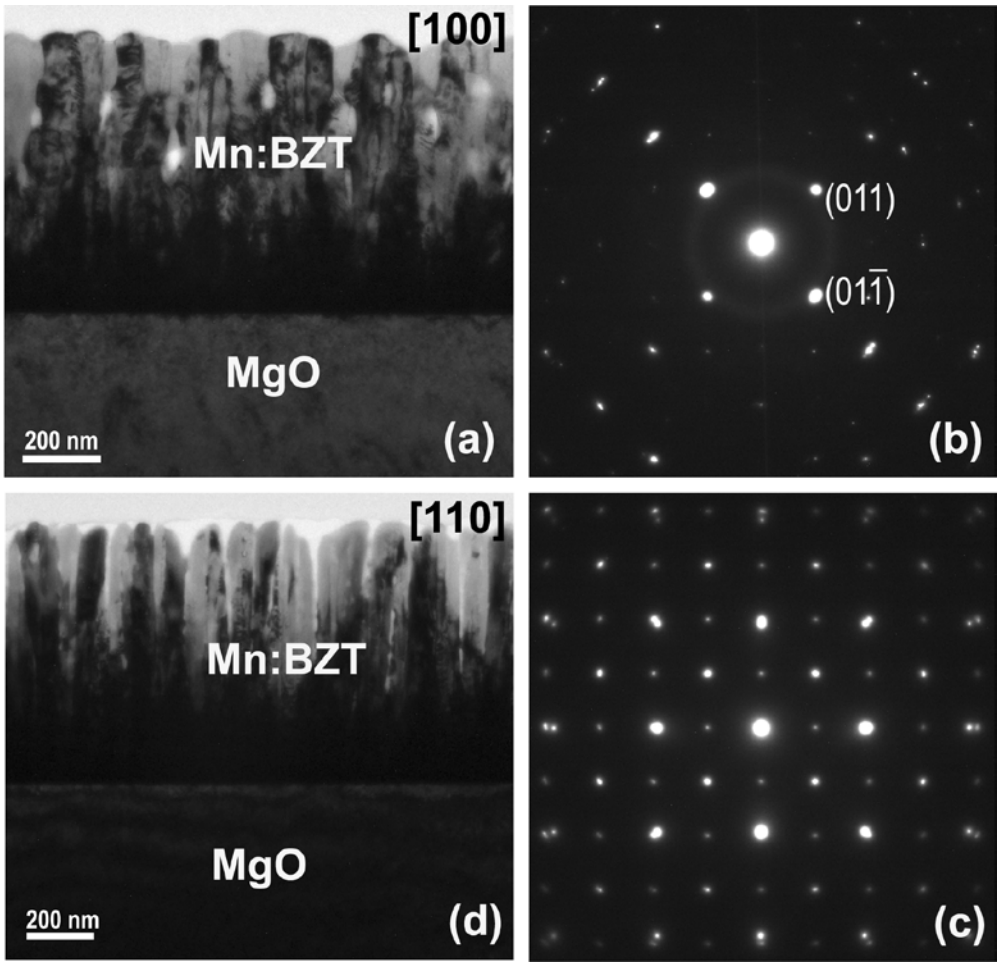

Figure 6.11 (a) Cross-sectional TEM image of Mn:BZT/MgO sample viewed along [100]MgO; (b) and (c) SAED from the top layer of the film and the interfacial area, respectively; (d) Cross-sectional TEM image of Mn:BZT/MgO viewed along [110]MgO.

Figure 6.11(a) shows a cross-sectional TEM image of a Mn:BZT/MgO sample viewed with the electron beam parallel to the $[100]_{MgO}$ direction. The Mn:BZT film has a thickness of 670 nm and is found to consist of two layers: a continuous layer (~ 150 nm thick) next to the substrate followed by a column-featured structure layer. Figure 6.11 (b) and (c) are SAED patterns taken respectively, from the top layer and from a near interfacial area which covers the continuous layer and the MgO substrate. Figure 6.11 (c) exhibits a superposition of the EDPs of the $[100]_{MgO}$ zone and of the $[100]_{Mn:BZT}$ zone of a single crystal pseudo-cubic structure. This indicates that the Mn:BZT continuous layer is epitaxially grown on the (001) MgO substrate with

a lattice mismatch (δ) of about -3.8%. The lattice constant for Mn:BZT is 4.05Å calculated using $\delta = (a_{BZT} - a_{MgO}) / a_{MgO}$. The orientation relationship between the continuous epilayer and the substrate can be described as $(001)_{Mn:BZT} \parallel (001)_{MgO}$, $<100>_{Mn:BZT} \parallel <100>_{MgO}$. Figure 6.11 (b) shows a clean pattern presenting only the $(0hh)$ and $(0h\bar{h})$ (h = ····-2, -1, 1, 2,···) diffraction spots, indicating that the top layer of the Mn:BZT thin films consists of mainly the four-types of twin-coupled domain structures reported in our previous work [164]. Figure 6.11 (d) is a cross-sectional TEM image of a Mn:BZT/MgO viewed along the $[110]_{MgO}$ direction, in which nanopillars and boundaries within the top layer can be clearly seen. The boundaries are usually straight and parallel to the growth direction indicating that the boundaries may have preferred orientation parallel to the $[110]_{MgO}$ direction. The nanopillars have a lateral size varying from 25nm to 80nm. No reflections from the twin-coupled nanopillars are detected in the θ-2θ XRD diffraction pattern (Figure 6.10) due to the particular orientation relationship between the twin-coupled domain structures and the substrate which results in no crystallographic planes parallel to the (001) MgO substrate surface.

Figure 6.12 (a) is a plan-view TEM image showing the microstructure of the top surface nanopillar layer and the corresponding SAED (inset). Regardless of the grainy structures observed in the films, the inset SAED taken from an area covering many grains shows a very clean diffraction pattern exhibiting only the $(hh0)$ and $(h\bar{h}0)$ (h = ····-2, -1, 1, 2,···) diffraction spots indicating that the top layer consists only of the four-type twin-coupled domain structures. Figures 6.12 (b) and (c) are dark filed images obtained by selecting the (110) and $(1\bar{1}0)$ diffraction spot, respectively. The bright areas in Figure 6.12 (b) correspond to the dark regions in Figure 6.12 (c) and vice versa. Assuming that the (110) spot is reflected from the two twin domains that were formed on the (111) or $(\bar{1}\bar{1}1)$ planes of the epitaxial perovskite structure, then the $(1\bar{1}0)$ diffraction spot is contributed by the other two twin domains that were formed on

the $(\bar{1}11)$ or $(1\bar{1}1)$ planes of the epitaxial structure. The superposition of the bright areas in Figures 6.12 (b) and (c) can cover the whole area in Figure 6.12 (a) indicating that the top surface nanopillar layer is constructed mainly by the four-type twin-coupled domains.

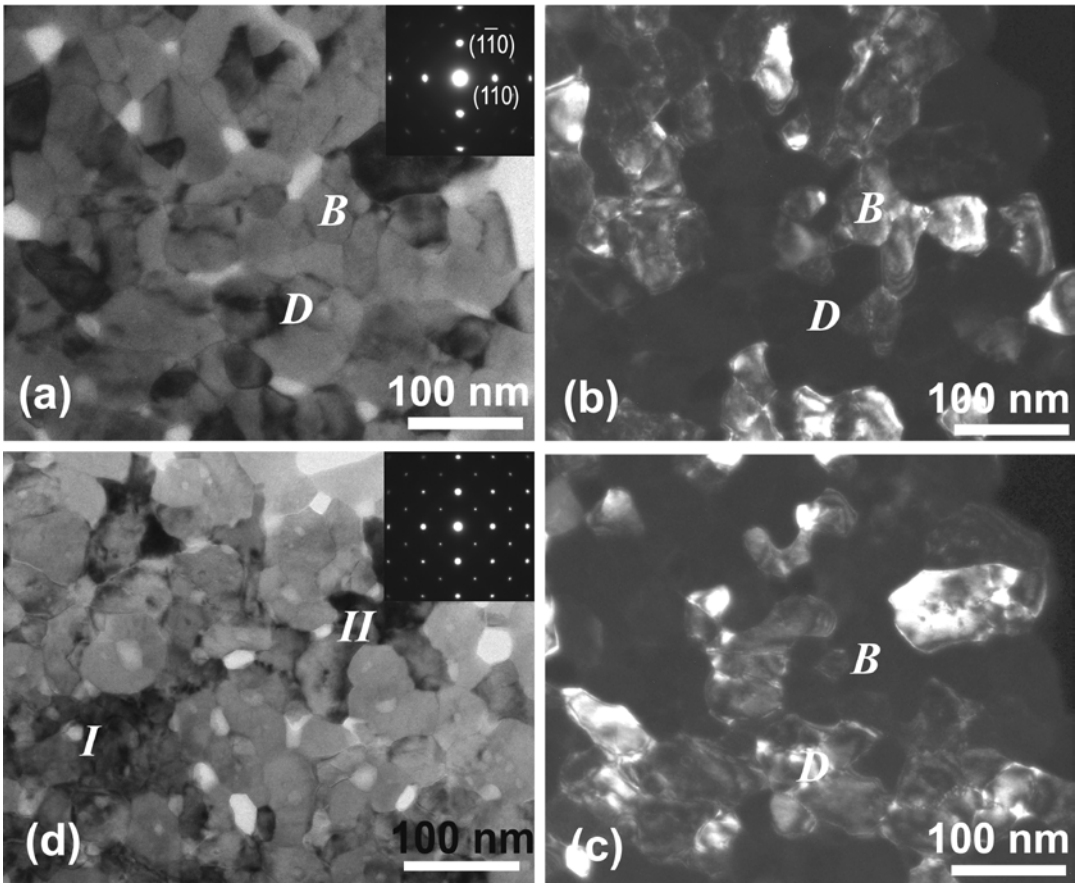

Figure 6.12 (a) Plan-view TEM image of the nanopillar layer at the top surface and the corresponding SAED (inset); (b) and (c) dark filed image of the (110) and $(1\bar{1}0)$ diffraction spot, respectively; (d) plan-view TEM image of the bottom layer of the Mn:BZT film near the interface.

Figure 6.12 (d) is a plan-view TEM image of the bottom layer close to the interface with the columnar structured Mn:BZT film. This sample was obtained by removing the top columnar layer using ion-milling. Figure 6.12 (d) still shows grainy structures as Figure 6.12 (a), but the former shows smaller grain size. The inset SAED in Figure 6.12 (d) was taken from the Mn:BZT layer near the interface showing the [001] zone EDP of the epilayer, in addition to the $(hh0)$ and $(h\bar{h}0)$ (h = ····-2, -1, 1, 2,···) diffraction spots resulting from the four twin-coupled domains. The

epitaxial grains in Figure 6.12 (d) (dark contrast such as marked by ***I*** and ***II*** in the image) have significantly larger size than the twin-coupled domains.

The aforementioned results show that the layer close to the interface has an epitaxial nature of a single pseudo-cubic structure. The growth of Mn:BZT films consists of two stages: formation of the epilayer grown from the interface followed by the formation of the four type twin-coupled domain structures by sharing their {111} with the epilayer and aligning their <110> directions parallel to the <110> axes of the epilayer.

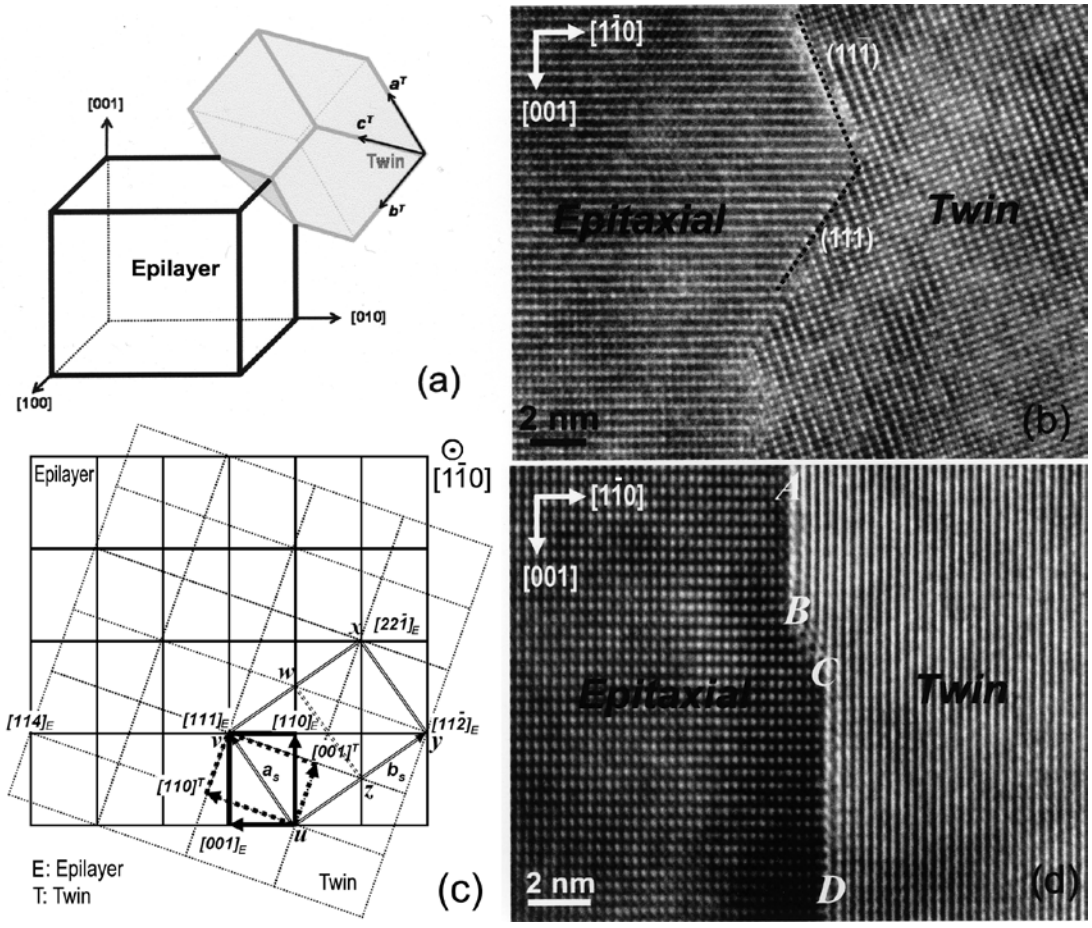

Figure 6.13 (a) Illustration of the epilayer joining a twin domain by sharing $(\bar{1}11)$ plane; (b) HRTEM image of a cross-section Mn:BZT/MgO along $[110]_{MgO}$ showing an epitaxial grain and a twin-coupled domain joined on {111} planes; (c) Illustration of another way that the epilayer joins a twin domain by sharing (110) as a common plane; (d) HRTEM image of a cross-section Mn:BZT/MgO showing an epitaxial grain and a twin-coupled domain joined on (110) and (111) planes.

Figure 6.13 (a) schematically illustrates the crystallographic orientation relationship between the epilayer and one twin by sharing a common plane of $(\bar{1}11)$ and a common zone axis of [110]. Such an orientation relationship can be described as $(\bar{1}11)_{epilayer}$ // $(\bar{1}11)_{twin}$, $[110]_{epilayer}$ // $[110]_{twin}$, $[101]_{epilayer}$ // $[101]_{twin}$, $[0\bar{1}1]_{epilayer}$ // $[0\bar{1}1]_{twin}$. This orientation relationship between the epilayer and the twin is observed in the electron diffraction pattern and HRTEM. For example, Figure 6.13 (b) is a HRTEM image taken from a cross section Mn:BZT/MgO TEM sample with the electron beam parallel to the $[110]_{epilayer}$ axis showing the presence of the epilayer (left) and a twin-coupled domain (right). The epitaxial grain and the twin-coupled domain are connected by a zigzag boundary that is composed of segments parallel to $(1\bar{1}1)$ or $(\bar{1}11)$ planes.

The epitaxial grain and the twin-couple domain can also coexist by sharing their $(1\bar{1}0)$ plane as a common plane as is schematically shown in Figure 6.13 (c). Their orientation relationship can then be described as: $(1\bar{1}0)_{epilayer}$ // $(1\bar{1}0)_{twin}$, $[22\bar{1}]_{epilayer}$ // $[001]_{twin}$, $[114]_{epilayer}$ // $[110]_{twin}$. As shown in Figure 6.13 (c), the two twin-coupled domains share a common super structure (uvxy) in the $(1\bar{1}0)$ boundary plane. One axis of the super structure unit cell (uv) equals to the [111] of both the epilayer and the twin domain (uv = as = $\sqrt{3}a_{BZT}$ = 7.02Å), whereas the other perpendicular axis (uy) is equal to the $[11\bar{2}]_{epilayer}$ or $[\bar{1}\bar{1}2]_{twin}$ (uy = bs = $\sqrt{6}a_{BZT}$ = 9.92 Å). However, it should be pointed that in the projection viewed along the $[1\bar{1}0]$ direction, the repeating unit in Figure 6.13 (c) is uvwz with a dimension uv = 7.02 Å and uz = bs /2 = 4.96 Å. For such a case, when a HRTEM image is taken with the electron beam parallel to the $[110]_{epilayer}$ axis, only the $(1\bar{1}0)_{twin}$ planes will be observed in the image, as shown in Figure 6.13 (d). The HRTEM image in the twin region (right side in Figure 6.13 (d)) exhibits only the

lattice fringes of the (110) planes. An atomically sharp boundary that is composed of three straight line segments AB, BC and CD was observed between the epitaxial grain and the twin domain. The boundary portion BC is parallel to $(\bar{1}11)$, whereas AB and CD portions are parallel to $(1\,\bar{1}0)$ plane. The bottom part of the epitaxial grain (left side in Figure 6.13 (d)) is wider than the top part, whereas the bottom part of the twin domain (right in Figure 6.13 (d)) is narrower than the top part, indicating that formation of a $(\bar{1}11)$ twin boundary (BC) reduces the lateral size of the epitaxial grain and increases the twin domain size. Such kinds of boundaries were frequently observed in the HRTEM images viewed with the electron beam parallel to the $[110]_{epilayer}$ axis.

Figure 6.14 (a) shows a SAED taken from two twin-coupled domains which are overlapped along the incident electron beam direction showing a superposition of two EDPs of the [110] zone of the epitaxial grain and the twin domain. In addition to the diffraction spots belonging to the two [110] EDPs that are located on the grids, additional spots that were located off the reciprocal lattice grid were observed. Such additional spots may possibly be arisen from the double diffraction because of the overlapping of the two twin domains. It should be noticed that all diffraction spots including those from the two twin domains and the additional spots construct a well-defined rectangular reciprocal lattice with a unit cell dimension of a_s^* and b_s^* (Figure 6.14 (a)) indicating formation of a commensurate superstructure due to the overlapping of the twin domains. Figure 6.14 (b) shows a HRTEM image taken with the electron beam parallel to the $[110]_{epilayer}$ axis showing presence of the epitaxial grain (left), the twin domain (right) and the overlapping region (middle). A commensurate superlattice structure (a_s =7.02 Å, b_s=4.96 Å) was observed in the overlapping area. The commensurate superstructure observed in HRTEM image (Figure 6.14 (b)) is consistent with the formation of the superlattice reflections in Figure 6.14 (a). The unit cell dimension of the commensurate super structure is equivalent to

the repeating unit cell dimension in the projection of the twin-coupled domains along the $[1\bar{1}0]$ direction (Figure 6.13 (c)).

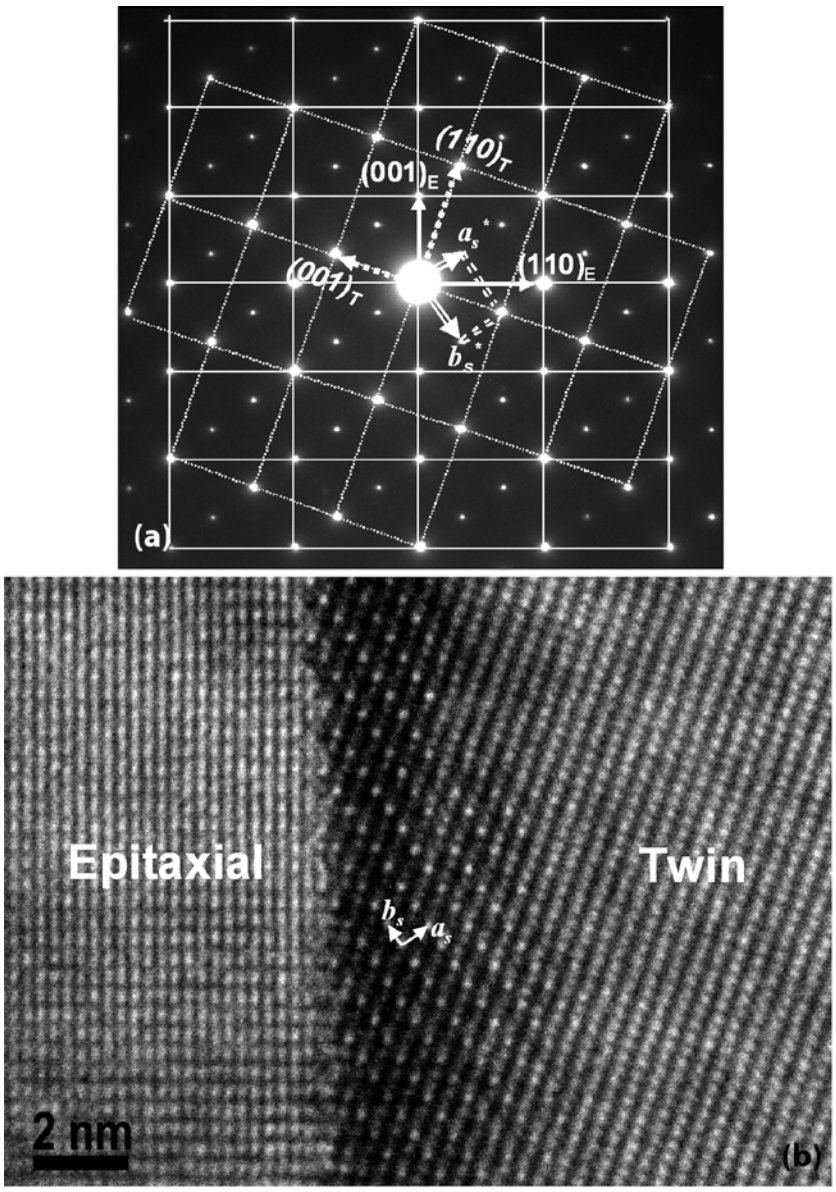

Figure 6.14 (a) SAED of two overlapped twin-coupled domains and (b) HRTEM image of two twin-coupled domains and the overlapping region, taken with electron beam parallel to the $[110]_{epilayer}$.

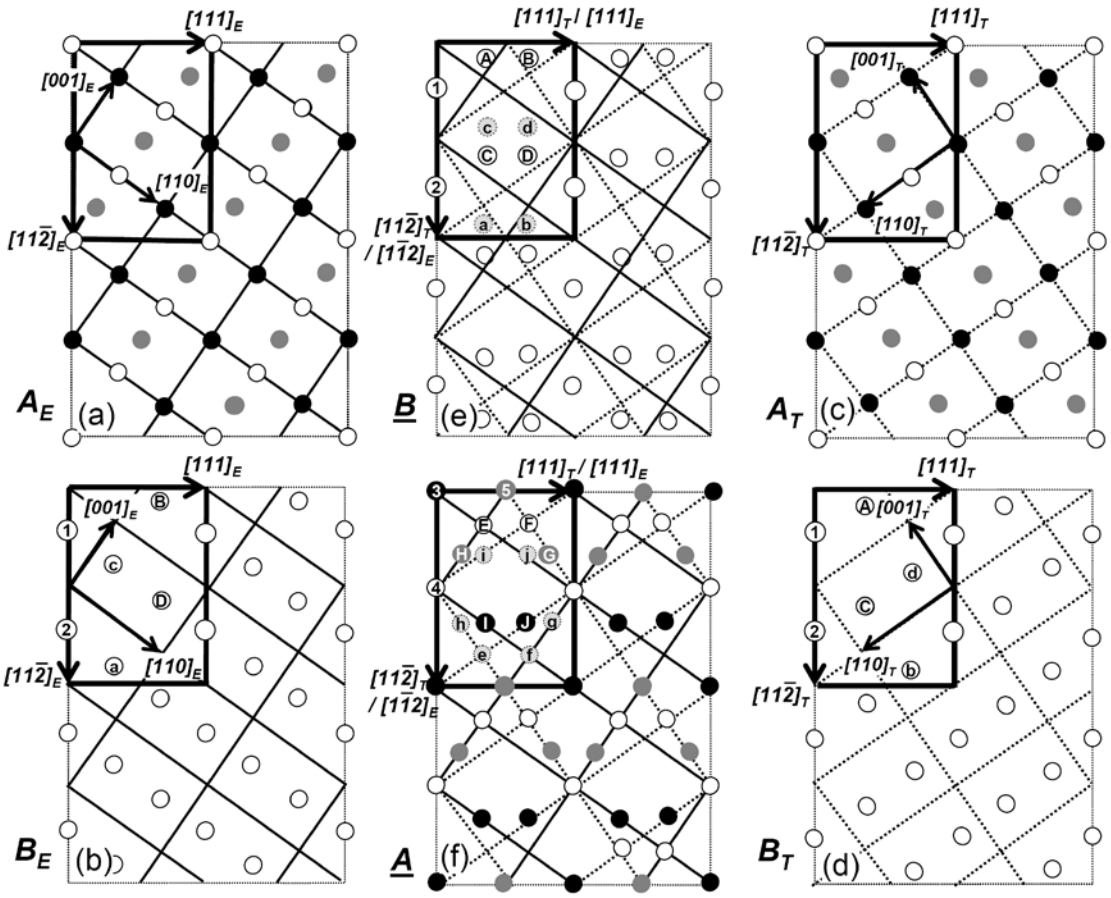

Figure 6.15 (a) and (c) Atomic structure of the BZT (110) plane layer that consists of Ba, (Zr,Ti) and O atoms for epitaxial structure (layer AE) and twin domain (layer AT), respectively; (b) and (d) Atomic structure of the BZT (220) plane layer for epitaxial structure (layer BE) and twin domain (layer BT), respectively; (e) and (f) Atomic structure of B and A boundary layer, respectively. Black circles represent Ba atoms, open circles represent O atoms and grey circles represent (Ti, Zr) atoms.

Understanding of the twin-coupled domains being joined on a {110} plane is not as straightforward as the twin-coupled domain structures being joined on a {111} plane. The atomic structure of the {110} plane twin boundary is not well understood. Figure 6.15 schematically illustrates the possible atomic structures of the (110) twin boundary plane. The $Ba(Zr,Ti)O_3$ perovskite structure can be considered as an alternatively packing the (110) plane atomic layer which is composed of Ba at (000), (Zr,Ti) at (-½ ½ ½) and O at (-½ ½ 0) atoms (denoted by A, Figure 6.15 (a)), and the (220) plane atomic layer which consists of O atoms at (0 ½ ½) and (½ 0 ½) (denoted by B, Figure 6.15 (b)) along the [110] direction. The $Ba(Zr,Ti)O_3$ perovskite

structure can be constructed by a sequent packing of ABA'BABA'B…, where the layer A' implies the same layer as A but with its coordinate being shifted by $\sqrt{2}a/2$ along the $[1\bar{1}0]$ direction. Figures 6.15 (a) and (b) schematically show the atomic structure of the A and B layers of the BZT epilayer (denoted by A_E and B_E), respectively. The atomic structure of the corresponding A and B layers of the twin domain structure (denoted by A_T and B_T) is shown in Figures 6.15 (c) and (d), respectively. The corresponding unit cell of the super structure at the boundary plane is schematically marked on each atomic layer (Figures 6.15 (a) to (d)). The atomic structure of layer A_T can be obtained from that of the layer A_E using a mirror operation via the $(111)_E$ (or $(111)_T$) plane, and vice versa. The same operation is applied to the relationship between the layer B_E and B_T. It should be noted that the layer A_E and B_E also has a mirror operation symmetry via the $(11\bar{2})_E$ (or $(11\bar{2})_T$) plane with respect to A_T and B_T, respectively. When the BZT epilayer and twin domain join on the (110) plane, the twin boundary could take place at either A (A') or B layer to form a twin structure of …AE'BEAEBEABTATBTAT'… or …BEAE'BEAEBATBTAT'BT…. Figures 6.15 (e) and (d) show the atomic structure of the boundary plane at the B and A layer, respectively. In layer B (Figure 6.15 (e)), the superstructure unit cell has six O atoms (1, 2, A, B, C and D), which is the same as that in layer B_E (Figure 6.15 (b)) and B_T (Figure 6.15 (d)). The O atoms 1, 2, B and D in layer B have the same atomic position as the corresponding atoms in layer B_E (Figure 6.15 (b)), whereas the O atoms 1, 2, A and C have the same atomic position as the corresponding atoms in layer B_T (Figure 6.15 (d)). The closest atomic distance between two O atoms (for example A and B) in layer B is about 2.3 Å. In layer B, A and C atoms have a (111) mirror symmetry with respect to B and D atoms, respectively. If the B and D atoms are relocated to the position b and d through the $(11\bar{2})_E$ (or $(11\bar{2})_T$) mirror symmetry operation, the layer B will become identical to the layer B_T. Similarly, if the A and C atoms are relocated to the position a and c through the $(11\bar{2})_E$ (or $(11\bar{2})_T$) mirror symmetry operation, the layer B will become identical to the layer B_E.

The superstructure unit cell of the layer A (Figure 6.15 (f)) consists of three Ba (3, I and J), three (Ti, Zr) (5, G and H) and three O (4, E and F) atoms, which has the same number of atoms as the corresponding unit cell in layer $A_{E'}$ and $A_{T'}$ (not shown). The closest atomic distance (L) between the Ba, (Ti, Zr) and O atoms is about $L_{Ba\text{-}O}$=2.83 Å, $L_{Ti\text{-}O}$=2 Å, $L_{Ba\text{-}Ti}$=3.46 Å calculated using a lattice constant 4 Å of $Ba(Zr,Ti)O_3$. Inside the superstructure unit cell of layer A, atoms E (O), H (Ti, Zr) and I (Ba) have a (111) mirror symmetry with respect to atoms F (O), G (Ti, Zr) and J (Ba), respectively. If atoms F, G and J atoms are relocated to the position f, g, and j through the $(11\bar{2})_E$ (or $(11\bar{2})_T$) mirror symmetry operation, the layer A will become identical to the layer $A_{E'}$. Similarly, if atoms E, H and I atoms are relocated to the position e, h, and i through the $(11\bar{2})_E$ (or $(11\bar{2})_T$) mirror symmetry operation, the layer A will become identical to the layer $A_{T'}$.

It can be seen from the aforementioned discussions that the proposed atomic structure model for the twin boundary layer A and B might be feasible. However, from current results, it is difficult to identify if there is any preference for the twin boundary to form at the layer A or B.

Figure 6.16 (a) is a plan-view HRTEM image of the bottom layer (close to the interface) of the Mn:BZT film obtained by removing the top layer using ion-milling. The image was taken with the electron beam parallel to $[001]_{epilayer}$ and exhibits typical boundaries between the epitaxial grain (***E***) and the twin domains (such as ***X*** and ***Y***). The boundaries between the epitaxial grain and the twin domains are parallel <110> or <100> direction. The boundary segment between the epitaxial grain and twin **X** is parallel to the $[\bar{1}10]$ direction and is atomically abrupt sharp. Such a boundary can be considered as the projection of the AB boundary in Figure 6.13 (d) along the $[001]_{epilayer}$ direction. However, the boundary segment between the epitaxial grain and twin **Y** that is parallel to the $[110]$ direction is a strip or band with a thickness equal to several lattice spacing of (110) planes. The side edges of the strip/band correspond to a (110) plane. The characteristics of such a boundary look like a

projection of the AB, BC and CD boundaries in Figure 6.13 (d) along the $[001]_{epilayer}$ direction. Specifically, the two sharp side edges (A'B' and C'D') of the boundary strip correspond to the projection of AB and CD, while the strip corresponds to the projection of BC region along the $[001]_{epilayer}$ direction. The strip/band boundary is actually an overlap of the projections of the epitaxial grain and a twin domain along the $[001]_{epilayer}$ direction.

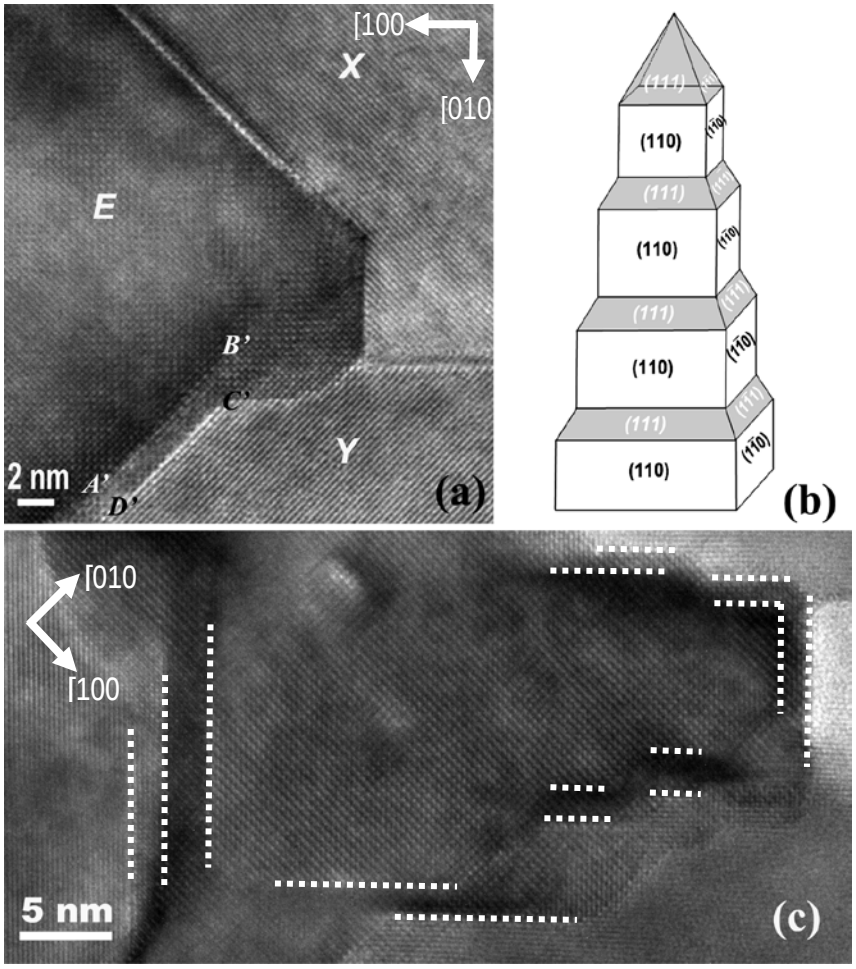

Figure 6.16 (a) Plan-view HRTEM image of the bottom layer (close to the interface) of the Mn:BZT film showing an epitaxial grain (**E**) and the twin domains **X** and **Y**; (b) Schematic illustration showing reduction of the epitaxial grain size by forming alternating twin boundaries along the (110) and (111); (c) Plan-view HRTEM image of the Mn:BZT film showing an epitaxial grain enclosed by {110} sharp boundaries and associated {111} overpasses.

Based on the above results, it can be speculated that when the film grows epitaxially to a certain thickness (~150 nm), the epitaxial layer starts to break into epitaxial grains by introducing twin boundaries and associated twin-coupled domains. The boundaries shown in Figure 6.16 (a) are typical features observed in the plan-view HRTEM of the film. This means that the epitaxial grains and their associated twin-coupled domains share their {110} planes as the common twin planes. While the {111} planes usually form overpasses connecting the adjacent {110} twin planes. Such a way forming twin-coupled domains and boundaries enclosing the epitaxial grains results in reduction of the lateral size of the epitaxial grains as the film grows. And accordingly, the twin-coupled domain size gradually increases as the film grows. This is consistent with the results that the Mn:BZT film is a two-layered structure consisting of a continuous epitaxial layer at the bottom of the film and a nanopillar layer of twin-coupled domains at the top of the film. In other words, the epitaxial layer gradually turns into twin-coupled nanopillar structures by the development of the twin boundaries. Such phenomena are also revealed by the fact that the grain size of twin domains at the bottom of the film is smaller than that at the top of the film. The development of the epitaxial grains and associated twin domains and boundaries is schematically illustrated in Figure 6.16 (b). Continuous epitaxial layer will initially grow on the substrate. As the film grows, the effect of the substrate on the film microstructure gradually fades away and the twin-coupled domains and boundaries will be introduced. Alternative formation of the twin boundaries along the (110) and (111) results in the lateral size decreasing of the epitaxial grains. At a certain thickness, the epitaxial grains completely turn into the twin-coupled domains. In the Mn doped BZT, it is possible that the Zr atoms occupy certain positions to form Zr or Mn- rich (110) and (111) planes. Since the Zr^{4+} and Mn^{2+} ions have a larger ionic size than Ti^{4+}, the Zr and Mn- rich (110) and (111) planes are expected to expand, which are energetically favorable for forming twin boundaries. Figure 6.16 (c) is plan-view HRTEM image of the Mn:BZT film showing an example of an epitaxial grain enclosed by {110} sharp boundaries (such as dotted lines in the image) and associated {111}

overpasses (such as regions between two dotted lines), which provides further evidence that the epitaxial grains are gradually slimmed down by alternative forming {111} and {110} twin boundaries.

6.4 Refining of Nanopillars induced by Mn doping in $Ba(Zr,Ti)O_3$ Thin Films

Figure 6.17 shows XRD θ-2θ scans of the as-grown BZT (top) and Mn:BZT (bottom) films deposited on MgO (001) substrate. Only the (00*l*) peaks of BZT, Mn:BZT and MgO substrate were observed, which indicates that the BZT and Mn:BZT films are epitaxially grown on the MgO substrates with their (001) planes parallel to the MgO (001) substrate surface. No significant difference between the XRD of BZT and Mn:BZT films can be observed. The lattice mismatch between the films and the substrate is -4.5% for BZT/MgO and -4.2% for Mn:BZT/MgO with respect to MgO substrate.

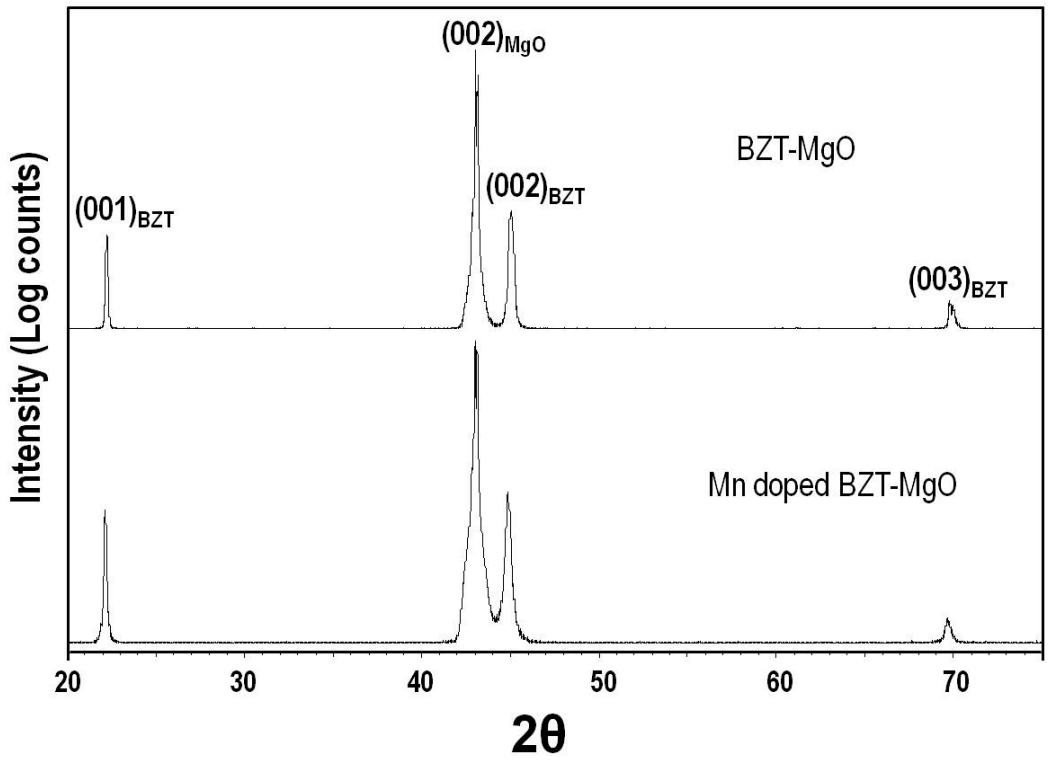

Figure 6.17 θ-2θ scan X-ray diffraction pattern of an as-grown BZT (top) and Mn:BZT (bottom) films on MgO (001) substrate.

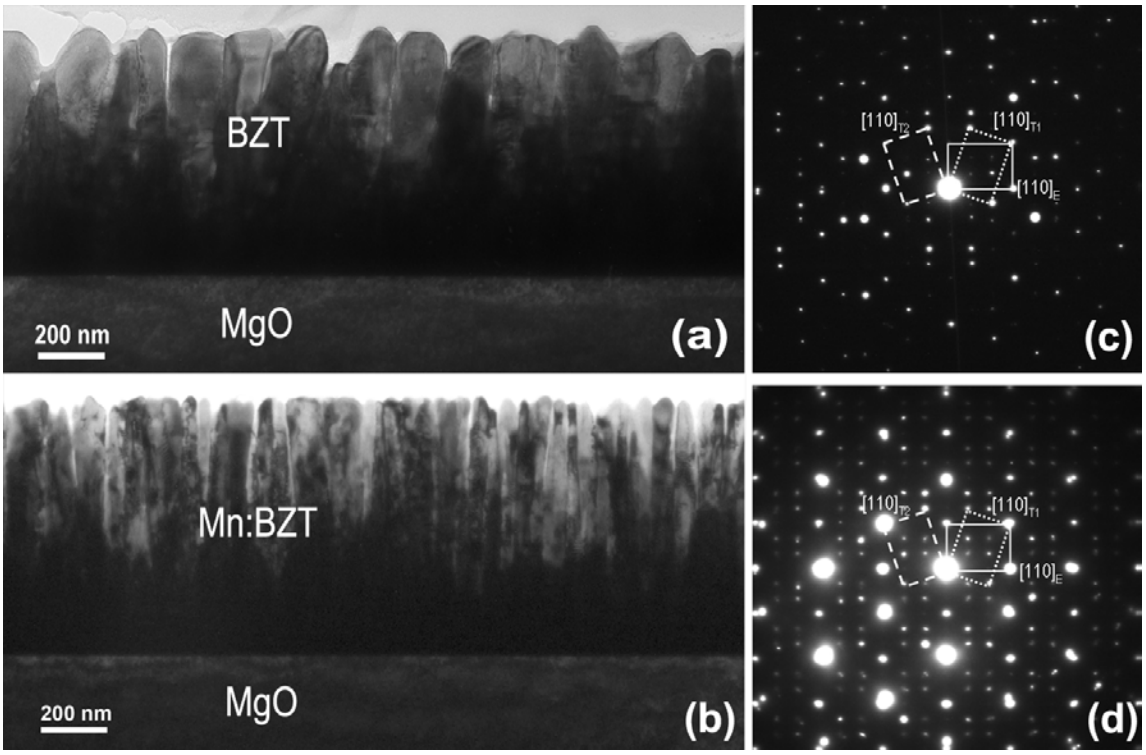

Figure 6.18 Cross-sectional TEM image of (a) BZT/MgO and (b) Mn:BZT/MgO sample viewed along $[110]_{MgO}$; (c) and (d) SAED taken from the top layer of the film and the interfacial area of the BZT/MgO sample.

Figures 6.18 (a) and (b) are cross-sectional TEM images of a BZT/MgO and a Mn:BZT/MgO sample, respectively, viewed with the electron beam parallel to the $[110]_{MgO}$ direction. The BZT and Mn:BZT film has a thickness of 740 nm and 770 nm, respectively. Both films are found to consist of a two-layered structure: (1) a continuous layer near the film/substrate interfaces and (2) a nanopillar-featured structure layer on the top of the films. Sharp interfaces between the films and the MgO substrate were observed. The average lateral dimension of the nanopillars in the BZT and Mn:BZT films is about 130 nm and 35 nm, respectively. Selected-area electron diffraction patterns taken from both BZT/MgO and Mn:BZT/MgO show nearly the same characteristics. Figure 6.18 (c) shows a typical SAED pattern taken from the top layer of the BZT film. This electron diffraction pattern can be formed by superposing three [110] zone EDPs of the BZT film: the $[110]_E$ EDP of the epitaxial BZT structure, the$[110]_{T1}$ and $[110]_{T2}$ EDPs of the twin-related BZT domain structures which were

introduced by sharing the $(1\bar{1}1)$ and $(\bar{1}11)$ plane with respect to the epitaxial structure, respectively. Figure 6.18 (d) is a SAED pattern taken from the BZT/MgO interfacial area which covers the film continuous layer and the substrate showing a superposition of three [110] zone EDPs of the BZT film and the [110] EDP of MgO substrate. In Figure 6.18 (c) the diffraction spots of the $[110]_{T1}$ and $[110]_{T2}$ EDPs of the twin domains show much stronger intensities than that of the $[110]_E$ EDP of the epitaxial BZT structure indicating that the twin-related structures are dominant in the nanopillar structures on the top of the film. Whereas in Figure 6.18 (d), the diffraction spots of the $[110]_E$ EDP of the epitaxial BZT and the [110] EDP of MgO show much stronger intensities than that of the EDPs of the twin-related domain structures, which indicates that the epitaxial BZT structure are dominant in continuous layer near the interface.

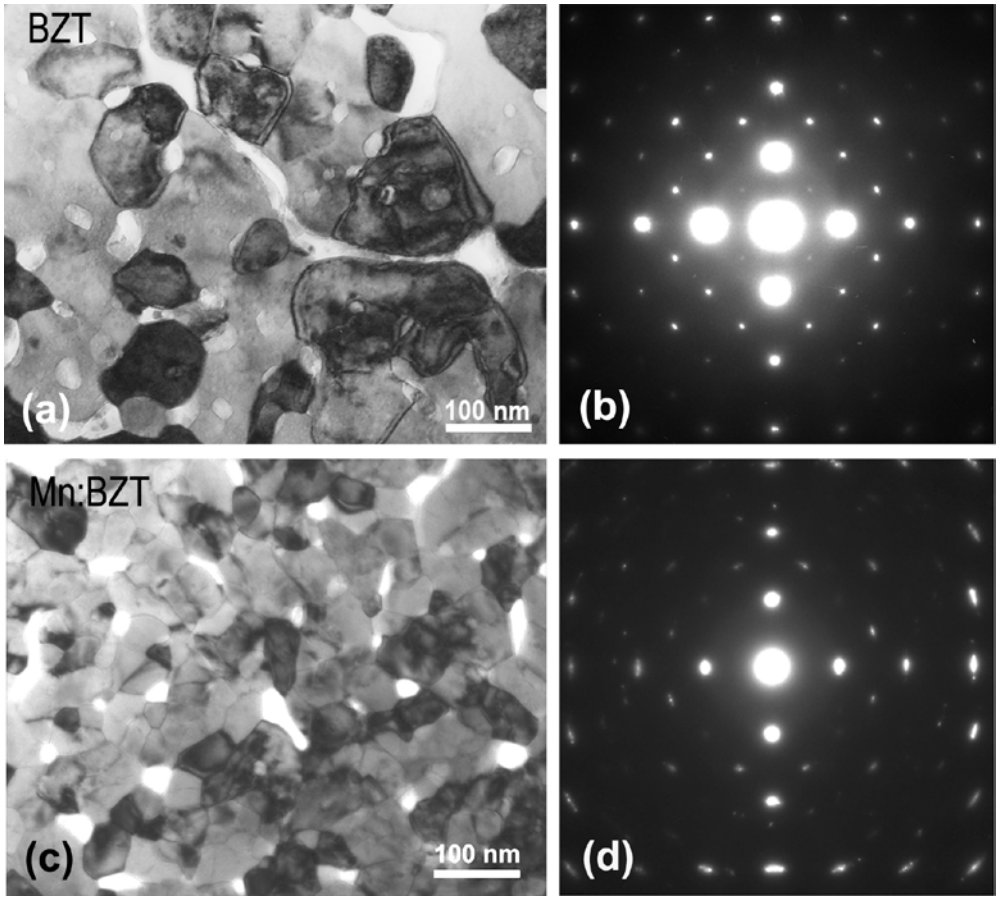

Figure 6.19 Plan-view TEM image of the nanopillar layer of (a) BZT and (c) Mn:BZT film; and SAED pattern of the Plan-view TEM foil of (b) BZT and (d) Mn:BZT film, respectively.

Figure 6.19 (a) is a plan-view TEM image of a BZT film showing the microstructure of the top surface nanopillar layer. Grainy structures and nano pores were observed. The size of the grains varies from 70 nm to 250 nm. Figure 6.19 (b) is a SAED pattern taken from an area covering many grains. A very clean single crystal electron diffraction pattern was observed regardless of the grainy structures in the films. The intensities of the $(hh0)$ and $(h\bar{h}0)$ (h = ···-2, -1, 1, 2,···) diffraction spots in Figure 6.19 (b) are significantly stronger than that of the rest diffraction spots which are scattered from the epitaxial structure, indicating that the top layer of the BZT film is dominated by the twin domain structures. Figure 6.19 (c) is a plan-view TEM image of a Mn:BZT film showing similar grainy structure to that in BZT films. The size of the majority nanopillars in Mn:BZT film varies from 20 nm to 60 nm. Figure 6.19 (d) is a SAED pattern taken from an area covering many Mn:BZT nanopillars also showing a very clean electron diffraction pattern, in which only the $(hh0)$ and $(h\bar{h}0)$ diffraction spots are visible and the rest of the spots contributed from the epitaxial structure are nearly invisible. This indicates that the top nanopillar layer of the Mn:BZT film nearly consists of only twin domain structures.

Formation of the twin-related domain structures can be induced by either sharing the $(\bar{1}11)$ or (110) plane as a common plane with respect to the epitaxial structure as schematically illustrated in Figure 6.20 (a) and (b). The crystallographic orientation relationship between the twin and the epilayer formed by sharing the $(\bar{1}11)$ as the common plane and the [110] as a common zone axis is illustrated in Figure 6.20 (a) and can be described as $(\bar{1}11)_{epilayer}$ // $(\bar{1}11)_{twin}$, $[110]_{epilayer}$ // $[110]_{twin}$, $[101]_{epilayer}$ // $[101]_{twin}$, $[0\bar{1}1]_{epilayer}$ // $[0\bar{1}1]_{twin}$. Such orientation relationship is observed in the EDP (Figure 6.18 (c)). The orientation relationship between the twin and the epilayer formed by sharing the $(1\bar{1}0)$ as the common plane is schematically shown in Figure 6.20 (b) and can be described as $(1\bar{1}0)_{epilayer}$ // $(1\bar{1}0)_{twin}$, $[22\bar{1}]_{epilayer}$ // $[001]_{twin}$, $[114]_{epilayer}$ // $[110]_{twin}$. In this case, when a HRTEM image is taken with the

electron beam parallel to the $[110]_{epilayer}$ axis, only the $(1\bar{1}0)_{twin}$ planes will be observed in the image.

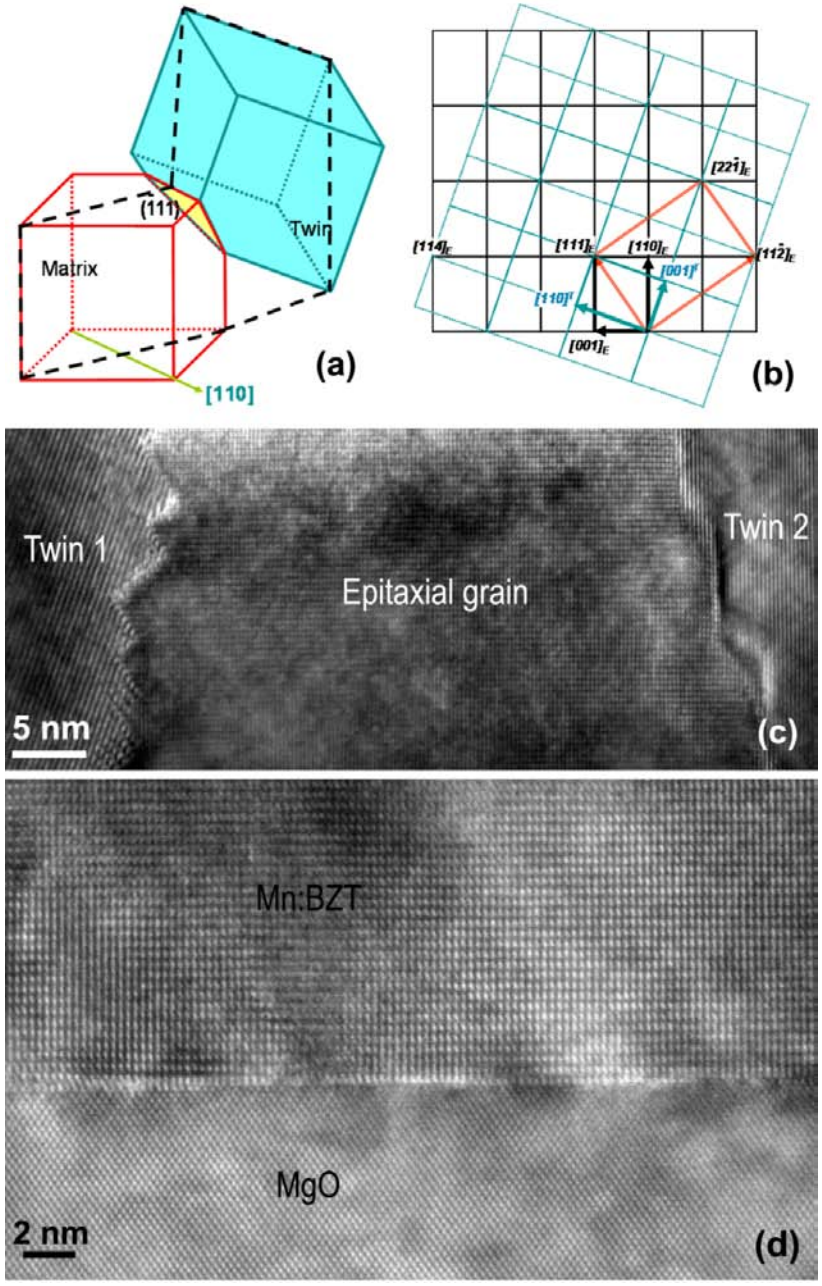

Figure 6.20 (a) and (b) schematic illustration of a twin domain joining the epilayer by sharing the $(\bar{1}11)$ and (110) plane, respectively; (c) HRTEM image of a cross-section Mn:BZT/MgO along $[110]_{MgO}$ showing an epitaxial grain joined with two twin-coupled domains on {111} and (110) planes; (d) HRTEM image of the Mn:BZT/MgO interface viewed along $[110]_{MgO}$.

Figure 6.20 (c) is a cross section HRTEM image of Mn:BZT/MgO taken with the electron beam parallel to the $[110]_{epilayer}$ axis showing the presence of the epilayer (middle) and two twin-coupled domains (left and right). The left twin-coupled domain and the epitaxial grain are connected by a zigzag boundary that is composed of segments parallel to $(1\bar{1}1)$ or $(\bar{1}11)$ planes. The HRTEM image in the right twin region exhibits only the lattice fringes of the (110) planes. The right twin-coupled domain structure and the epitaxial grain are connected by a boundary that is composed of segments parallel to $(\bar{1}11)$ and $(1\bar{1}0)$ planes. It is clearly seen that the bottom part of the epitaxial grain is wider than the top part. It can be found that the alternative formation of $(\bar{1}11)$ and $(1\bar{1}0)$ twin boundary significantly reduces the lateral size of the epitaxial grain and increases the twin-coupled domain size. Such kinds of boundaries were frequently observed in the HRTEM images of both BZT and Mn:BZT thin films viewed with the electron beam parallel to the $[110]_{epilayer}$ axis. Figure 6.20 (d) is a cross section HRTEM image of the interface between the Mn:BZT continuous layer and the MgO substrate viewed along the $[110]_{MgO}$. It provides further evidence for the epitaxial growth of the continuous Mn:BZT layer. An atomically sharp interface was formed between the film and the substrate.

Figure 6.21 (a) shows a HRTEM image of a plan-view BZT/MgO interface. The coarse lattice fringes in the image represent moiré fringes formed by the overlapping of BZT and MgO. The orientation of the moiré fringes varies from area to area indicating the formation of the domains within which the BZT commensurate with MgO substrate. The size of such commensurate domain is about 40 nm. Figure 6.21 (b) shows a corresponding EDP of a plan-view BZT/MgO interface shown in Figure 6.21 (a). The lattice mismatch $\Delta\delta$ is about -7.6% obtained from Figure 6.21 (b) using the equation (4.1) [225,226].

Figure 6.21 (c) shows a HRTEM image of a plan-view Mn:BZT/MgO interface. The size of the commensurate domain is about 20 nm. Figure 6.21 (d) shows a corresponding EDP of a plan-view Mn:BZT/MgO interface shown in Figure 6.21 (c). The lattice mismatch $\Delta\delta$ is about -

6.6% obtained from Figure 6.21 (d). The diffraction spots in Figure 6.21 (d) are more diffused or blurred compared to those in Figure 6.21 (b), which is in agreement with the smaller commensurate domain size in Figure 6.21 (c).

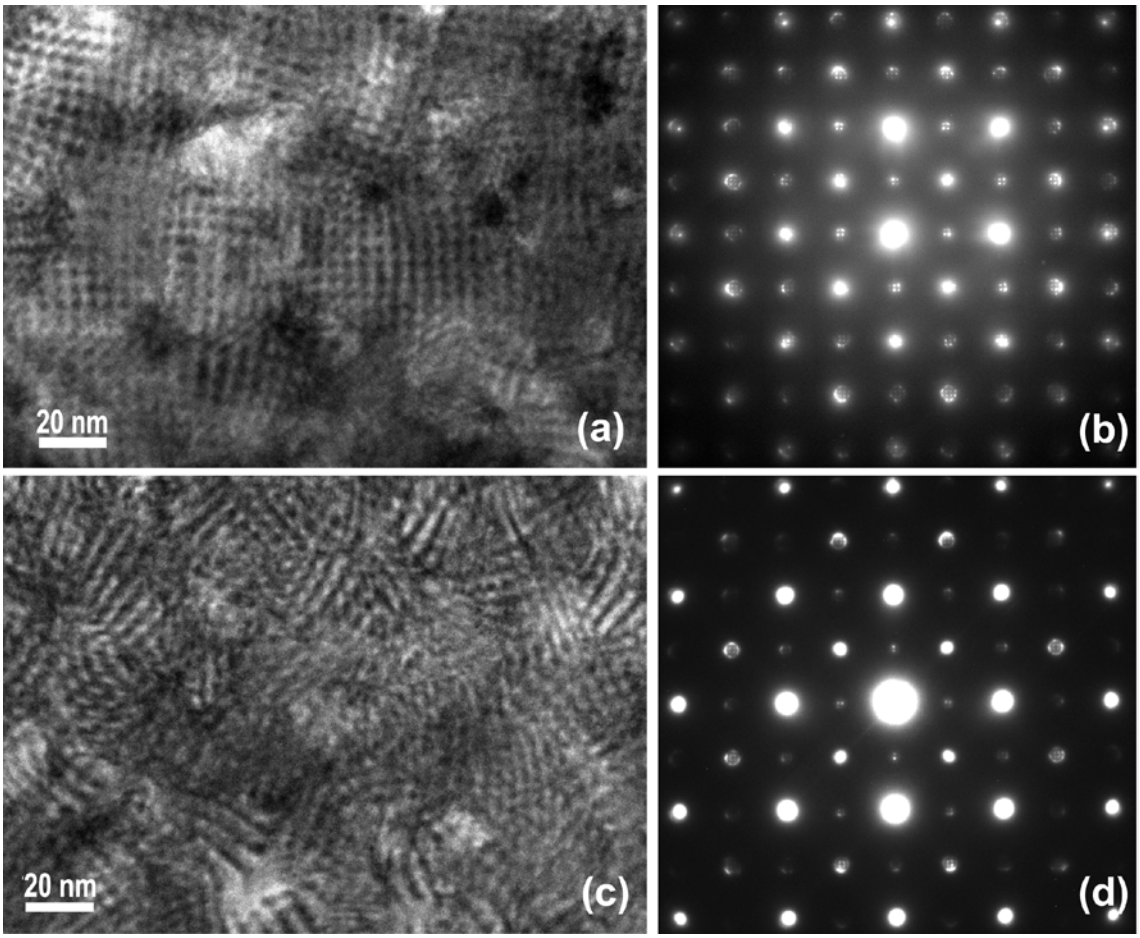

Figure 6.21 (a) plan-view HRTEM and (b) EDP of BZT/MgO interface; (c) plan-view HRTEM and (d) EDP of Mn:BZT/MgO interface.

The Raman spectra of the BZT and Mn:BZT films on MgO (001) substrate were shown in Figure 6.22. The A_1(TO) phonon mode was clearly seen at 188 cm^{-1} , 295 cm^{-1} and 517 cm^{-1} for BZT film, and at 178 cm^{-1} , 289 cm^{-1} and 514 cm^{-1} for Mn:BZT film. The A_1(LO) mode indicating the presence of the tetragonal structure was observed at 720 cm^{-1} for BZT film and at 671 cm^{-1} for Mn:BZT film. By doping Mn into the BZT films, the peaks of the A_1(TO) and A_1(LO) become wider and less defined with their intensity reduced and position shifted to a lower

wavenumber. The sharp weak peaks at the position of 60, 75, 83, 92, 107 and 482 cm^{-1}, which are nearly the same for both BZT and Mn:BZT films are resulting from the MgO substrate.

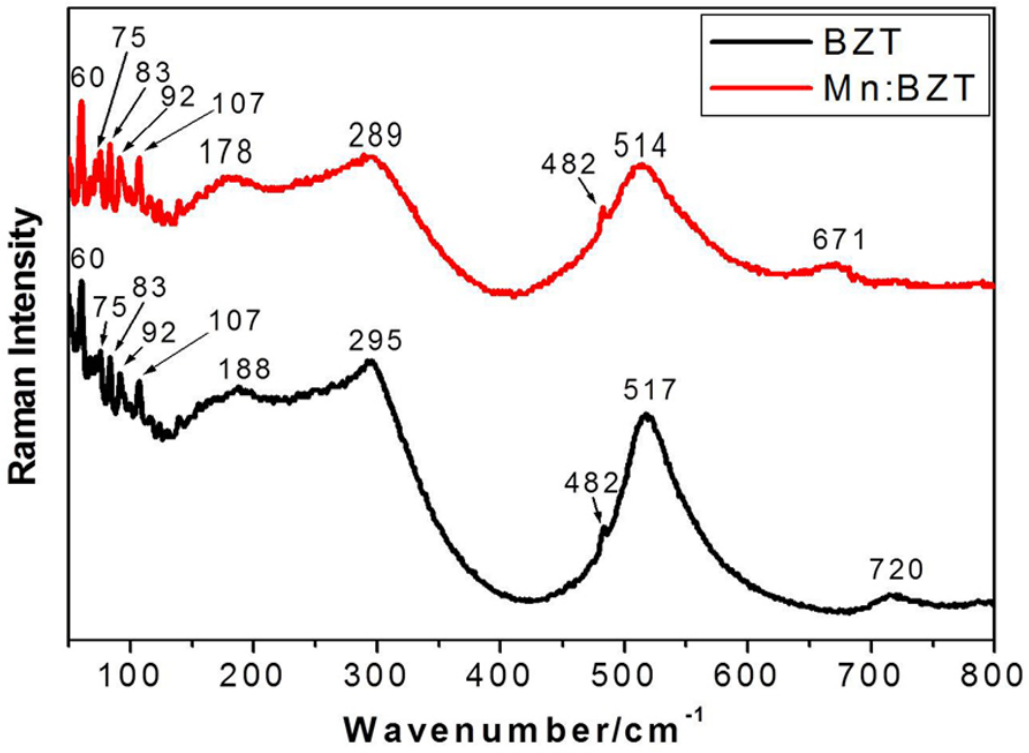

Figure 6.22 Raman spectra of an as-grown BZT (top) and Mn:BZT (bottom) films on MgO (001) substrate.

Figure 6.23 shows typical nano-indentation load-displacement curves for Mn:BZT and BZT films. The average hardness and modulus values were determined by performing 4×4 array indents with 3 μm ×3 μm distance and at the same displacement of 75 nm for each film. The mean hardness for Mn:BZT and BZT film is 10.89 and 7.23 GPa, respectively. The mean modulus for Mn:BZT and BZT film is 203.58 and 192.57 GPa, respectively. Comparing the load-displacement curves of Mn:BZT and BZT films, a large difference of the maximum load at maximum displacement of 75 nm and residual penetration at zero load in the unloading segment depths were clearly observed. The higher hardness and modulus of the Mn:BZT film is considered to be attributed to its smaller nanopillars size and larger number of twin domain boundaries located at close to film top surface compared to BZT film.

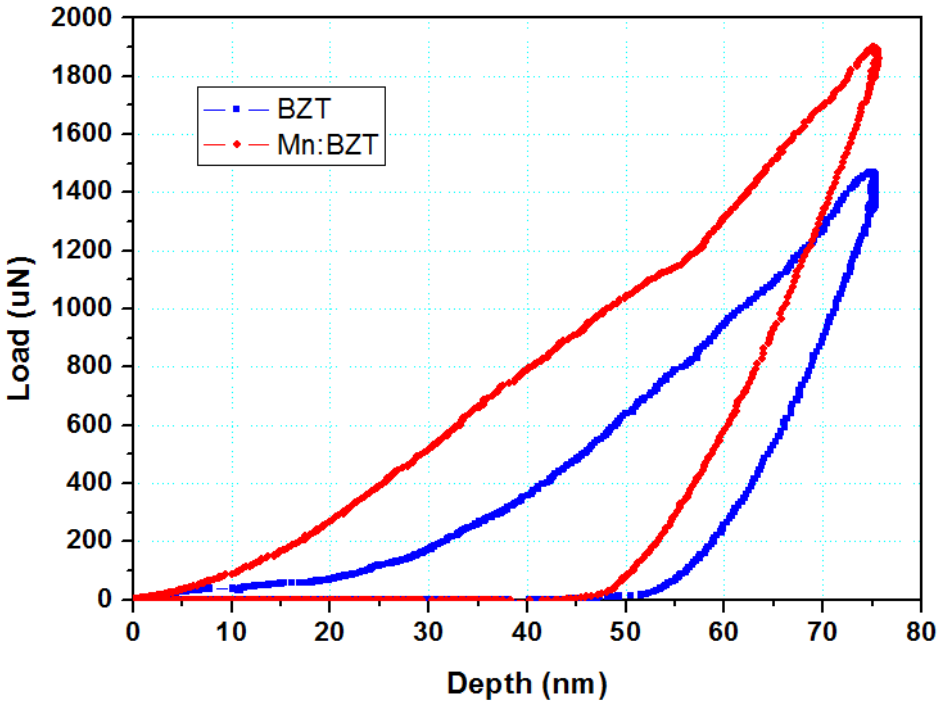

Figure 6.23 Load-displacement curves of nanoindentation measurement for Mn:BZT (red) and BZT (blue) films with the same 75 nm displacement.

From the aforementioned results, it can be seen that the epitaxial BZT and Mn:BZT thin films break into epitaxial twin-associated nanopillars by introducing twin boundaries at a certain thickness. The twin boundaries were introduced on the {111} or {110} planes, i.e., the epitaxial grains and their associated twin-coupled domains share the {111} or 110} planes as the common twin planes. The boundaries between the nanopillars were formed by either alternative introducing $(\bar{1}11)$ and $(1\bar{1}1)$ plane segments along the growth direction, or alternative introducing $(\bar{1}11)$ (or $(1\bar{1}1)$) and (110) (or $(1\bar{1}0)$) plane segments along the growth direction, of which the latter one plays an significant role in reducing the lateral size of the epitaxial grain (increasing the size of the twin-coupled grains) as the film grows. During the film growth, continuous epitaxial layer initially grows on the substrate and as the film grows, the effect of the substrate on the film microstructure gradually fades away and the twin-coupled domains and boundaries are then introduced. At a certain thickness, the epitaxial grains completely turn into

the twin-coupled domains. In the BZT and Mn doped BZT films, it is possible that the Zr and Mn atoms occupy certain positions to form Zr or Mn- rich (110) and (111) planes. Since the Zr^{4+} and Mn^{2+} ions have a larger ionic size than Ti^{4+}, the Zr and Mn- rich (110) and (111) planes are expected to expand, which are energetically favorable for forming twin boundaries. In the Mn:BZT films, Mn doping will make additional contribution to the expansion of the (110) and (111) planes and accordingly increases the strain. More twin boundaries and therefore smaller twin-coupled nanopillars in the Mn:BZT films are expected to be generated in order to accommodate the extra strain caused by the Mn doping. Furthermore, the increasing of the strain resulting from the Mn doping leads to the smaller commensurate domain at the film/substrate interface in order to relax the extra strain. On the other hand, atomic structure or atomic arrangement on the twin boundary layer, especially for the {110} plane twin boundaries, is different from that of the {111} twin domains. The BO_6 octahedral geometry at the twin boundaries is broken and does not exist anymore. The corresponding Raman spectra resulting from these twin boundaries might be different from that the single crystal structure. The smaller size of the twin-coupled nanopillars in Mn-BZT films indicates a larger number of the twin boundaries existed in the film compared with the BZT films, which can greatly enhance the nano-mechanical properties (modulus and hardness) of Mn:BZT films. The extra portion of the twin boundaries is speculated to contribute to the peak shifting of the Raman spectra to the lower wavenumbers in Mn:BZT films. The influence of such twin boundaries on the Raman Spectrum need to be further investigated.

6.5 Summary

6.5.1 Formation of Multi-oriented Twin Domain Structures in BZT Thin Films

BZT thin films consisting of (i) an epitaxial layer of pseudo-cubic perovskite structure and (ii) multi-oriented twin domain structures were fabricated on (001) MgO substrate using PLD. Four types of twin domain structures were formed by coherently joining their {111} planes with respect to the epilayer and aligning their <110> directions parallel to the <110> axes of the

epilayer. The EDPs of such a complex structure composed of an epilayer and twin domains with specific crystallographic orientation relationship to the substrate show characteristics/features similar to those of the single crystal diffraction patterns. Preliminary results show that the BZT thin films possessing such complex structure exhibit a non-uniform polarization switching behavior.

6.5.2 Structure Transition in Mn:BZT Thin Films driving by {110} Twin Boundaries

Mn:BZT thin films grown on (001) MgO substrate fabricated using PLD have a pseudo-cubic perovskite structure and are composed of an epitaxial layer (~150 nm) at the bottom of the film near the interface and multi-oriented twin-coupled nanopillars at the top of the film. The twin-coupled structures including epitaxial grain and twin domains coexist by sharing, in addition to the {111}, the {110} planes as the common twin boundary plane. The joining of the twin-coupled domains on the {110} twin boundary plane is accommodated by forming a two-dimensional super cell structure (a = 7.02 Å and b = 9.92 Å) on the twin boundary plane. Evolution from the epitaxial layer to the nanopillar structures is accomplished by introducing twin boundaries on {111} and {110} planes. In the Mn:BZT, the larger Zr^{4+} and Mn^{2+} atoms could possibly occupy certain positions to form Zr or Mn-rich expanded (110) and (111) planes which are energetically favorable for forming twin boundaries. Alternatively formation of the twin boundaries on {111} and {110} planes along the growth direction results in the lateral size reduction of the epitaxial grains and eventually leads the epitaxial grains to be completely transformed into twin-coupled nanopillars.

6.5.3 Formation and Growth Mechanism of {111} and {110} Twin Domain Structures in Both BZT and Mn:BZT Thin Films

Epitaxial BZT and Mn:BZT thin films grown on (001) MgO substrate were fabricated using PLD. Both films are composed of a two-layered structure: an epitaxial layer near the interface and twin-coupled nanopillars at the top of the film. The average lateral size of the nanopillars in BZT films is ~130 nm, four times larger than that in the Mn:BZT films (~35 nm). The twin-coupled structures including epitaxial grain and twin domains are connected by

sharing their {111} and/or {110} planes as the common plane. Development from the epitaxial layer to the nano-pillar structures is accomplished by alternatively introducing twin boundaries on {111} and {110} planes along the growth direction. The formation of the twin boundaries in BZT is possibly due to the occurrence of the larger Zr^{4+} ions on certain positions to form Zr^{4+} rich expanded (110) and (111) planes which are energetically favorable for forming twin boundaries. Mn doping in BZT films makes additional contribution to the expansion of the (110) and (111) planes to form more twin boundaries and smaller twin-coupled nanopillars and results in the shifting of the peak in Raman spectrum to the lower wavenumbers and improved dielectric properties, and therefore possess higher modulus and hardness compared to BZT film.

CHAPTER 7

MICROSTRURE AND INTERFACE STUDY OF [Mn:BZT//Mn:BST]$_N$ MULTILAYER FILMS

7.1 Introduction

In Chapter 5 and Chapter 6, (Ba,Sr)TiO_3 (BST), Ba(Zr,Ti)O_3 (BZT) and 2%Mn doped Ba(Zr,Ti)O_3 (Mn:BZT) have been intensively studied. The doped barium titanate films with different dopant (Sr^{2+} and Zr^{4+}) have been fabricated by PLD and used to study the film growth and interface effects. The BST epitaxial films grown on miscut (001) MgO substrate with 1^o, 3^o, 5^o angles provided the opportunity to study substrate surface morphology effects on the film microstructure and dielectric property. The BZT and Mn:BZT films grown on (001) MgO substrate revealed the formation of {111} and {110} twin coupled domain structures on the epilayer structure. In this Chapter, more efforts were made to investigate the microstructure and interfaces of 2% Mn doped BZT and 2% Mn doped BST (Mn:BZT//Mn:BST) multilayer films.

The selection of Mn doped BZT and BST as the single layer in multilayer films is due to the consideration of optimization of dielectric properties, since many reports have been proved that the dielectric properties, such as dielectric loss, tunability and resistivity, of BST and BZT thin films can be significantly improved by introducing small amount of acceptor dopants, e.g. Mg, Mn, Ce, Yb.[165, 166, 256, 257, 260-262]. Besides, other efforts have been dedicated to exploit the perovskite oxide multilayer/superlattices thin films composed of alternating sublayers, which have shown great advantageous in scaling down for highly dense electronic devices in new generation with a perfect combination of multiferroic properties. These multilayer films can possess enhanced or completely distinct properties and phenomena, such as simultaneous ferroelectric, ferromagnetic properties, enhanced remnant polarization, giant dielectric response and high dielectric tunability, compared to the single layer films or bulk materials [263-266]. In the heteroepitaxial multilayer films, stress is commonly generated from

the lattice mismatch at the interfaces between hetero-sublayers. Although the reason has not been highly confirmed, the internal stresses resulted from lattice distortion was speculated to be the origin of the larger tunability [267].

Some studies have shown that the growth of BZT//BST multilayer films can optimize the properties of each BZT or BST single layer by reducing dielectric tangent while retaining relatively high dielectric tunability and some permittivity [268-270]. However, very limited information can be found regarding the microstructure and growth mechanism of BZT//BST multilayered films. In this Chapter, the study is focused on (1) the microstructure of four-layered films consisting of 2% Mn doped BST (Mn:BST) and 2% Mn doped BZT (Mn:BZT) thin layers ($[Mn:BZT//Mn:BST]_2$) fabricated using different deposition rates and its influence on the microstructure and mechanical properties of the films; (2) the microstructure, interfaces and their influences on nanomechanical properties of epitaxial multilayer films ($[Mn:BZT//Mn:BST]_N$) consisting of Mn:BST and Mn:BZT thin layers with a series layer numbers fabricated PLD.

7.2 Influence of Deposition Rate on Microstructure and Mechanical Property of $[Mn:BZT//Mn:BST]_2$ Multilayer Films

Two four-layered $[Mn:BZT//Mn:BST]_2$ films were deposited on (001) MgO substrates with different deposition rates of (1) ~ 2.4 Å/second (noted by ***FL-S***) and (2) ~ 6 Å/second (noted by ***FL-F***) using puled laser deposition. The first deposition layer next to MgO substrate is Mn:BZT layer. The influence of deposition rates on the formation and growth of $[Mn:BZT//Mn:BST]_2$ films are investigated in detail as follows.

Figure 7.1(a) is a θ-2θ scan XRD of an as-deposited ***FL-S*** film on MgO (001) substrate. In addition to the (002) diffraction peak of MgO, (00*l*) diffraction peaks (*l*=1, 2 and 3) for both Mn:BZT and Mn:BST are observed. The lattice constant along the film growth direction is about 3.96 Å for Mn:BST and 4.03 Å for Mn:BZT layer. The out-of-plane lattice mismatch of the Mn:BST and Mn:BZT layer with respect to MgO substrate is about -5.94% and -4.27%, respectively, calculated using $(a_{film} - a_{MgO}) / a_{MgO}$ with a_{MgO}=4.212 Å.

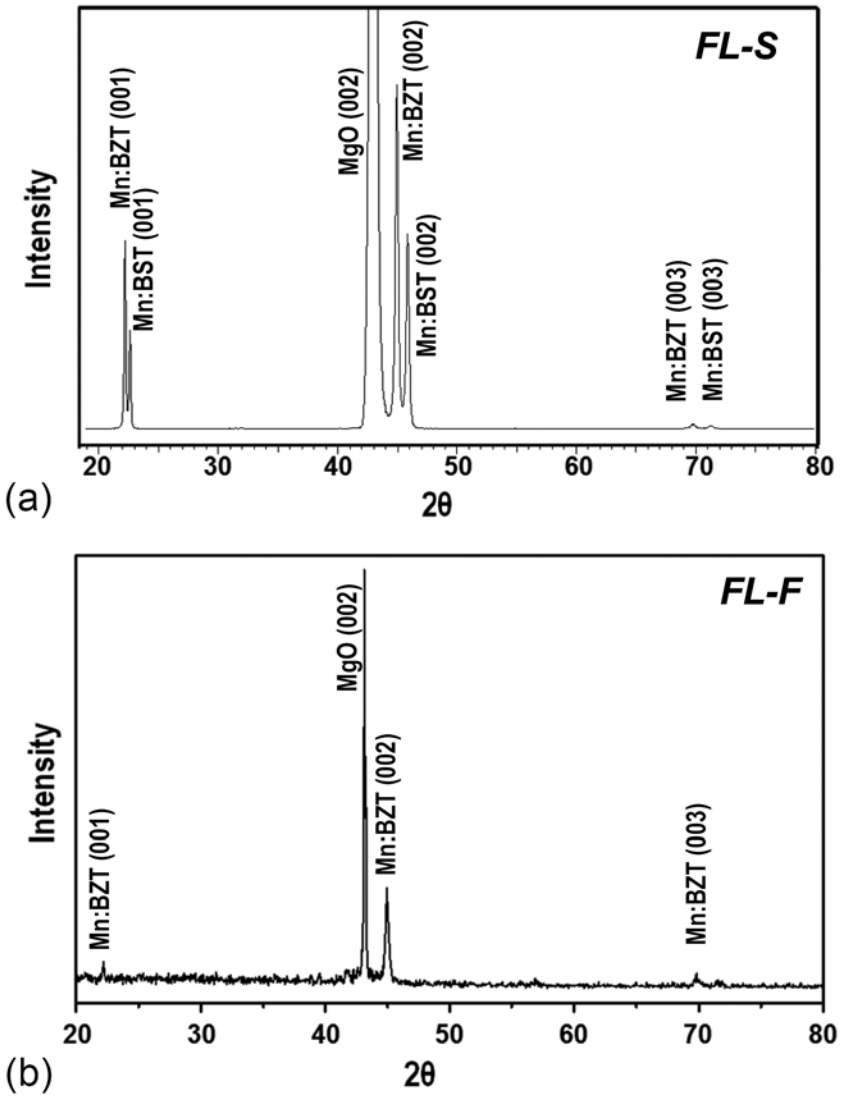

Figure 7.1 θ-2θ XRD pattern of as-deposited four-layered films (a) ***FL-S*** and (b) ***FL-F***.

Figure 7.1(b) is a θ-2θ scan XRD of an as-deposited FL-F film on MgO (001) substrate. Besides the (002) diffraction peak of MgO, only the (00l) diffraction peaks (l=1, 2 and 3) that belong to Mn:BZT are observed. Peaks that belong to Mn:BST are not observed. The lattice constant of Mn:BZT along the growth direction is 4.04 Å. The out-of-plane lattice mismatch between the Mn:BZT and MgO is -4.04%.

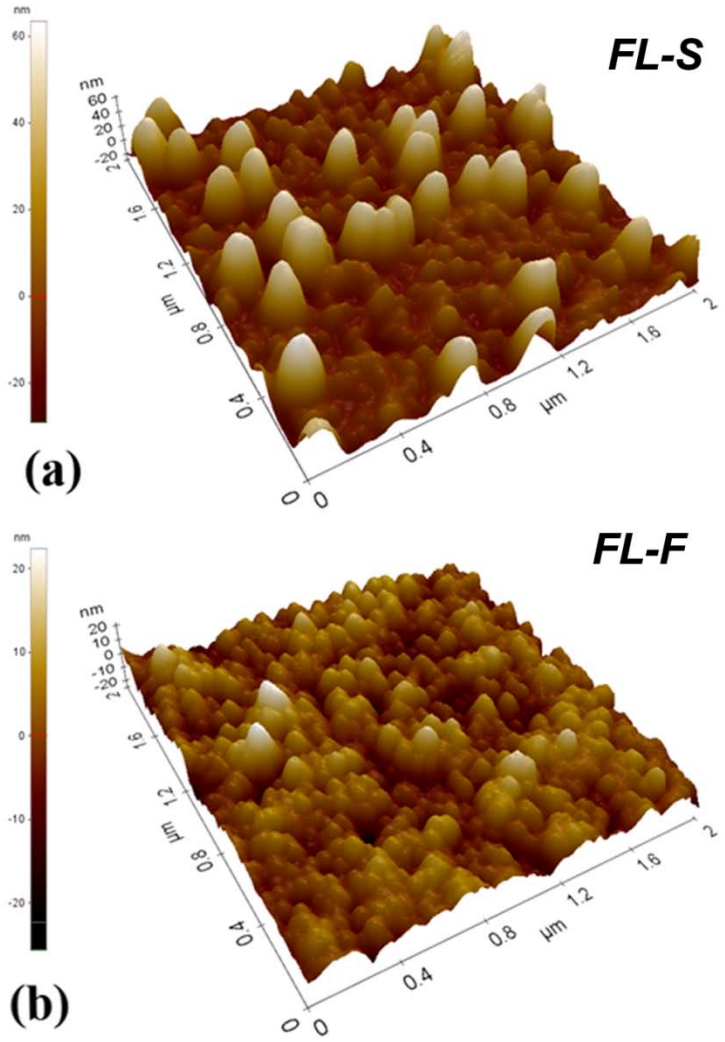

Figure 7.2 Non-contact AFM 3D images of as-deposited four-layered Mn:BZT//Mn:BST films (a) ***FL-S*** and (b) ***FL-F***.

The surface morphology and roughness of both four-layered films were investigated using AFM in the non-contact mode with a scanning size of 2×2 μm^2. Figure 7.2 (a) is a 3D AFM image of a ***FL-S*** film exhibiting a coarser granular structure with a larger number of extrusive columnar structures compared to that of ***FL-F*** film. The small granular structures have a size varying from 20 nm to 100 nm, while the coarse columnar structures have a uniform size of around 160-170 nm. The average roughness of the ***FL-S*** film is ~14.75 nm. Figure 7.2 (b) is a 3D AFM image of a ***FL-F*** film showing a granular structure with a relatively fine size of 60-80

nm. The average roughness of the film is ~4.17 nm indicating a flatter surface compared to the ***FL-S*** film.

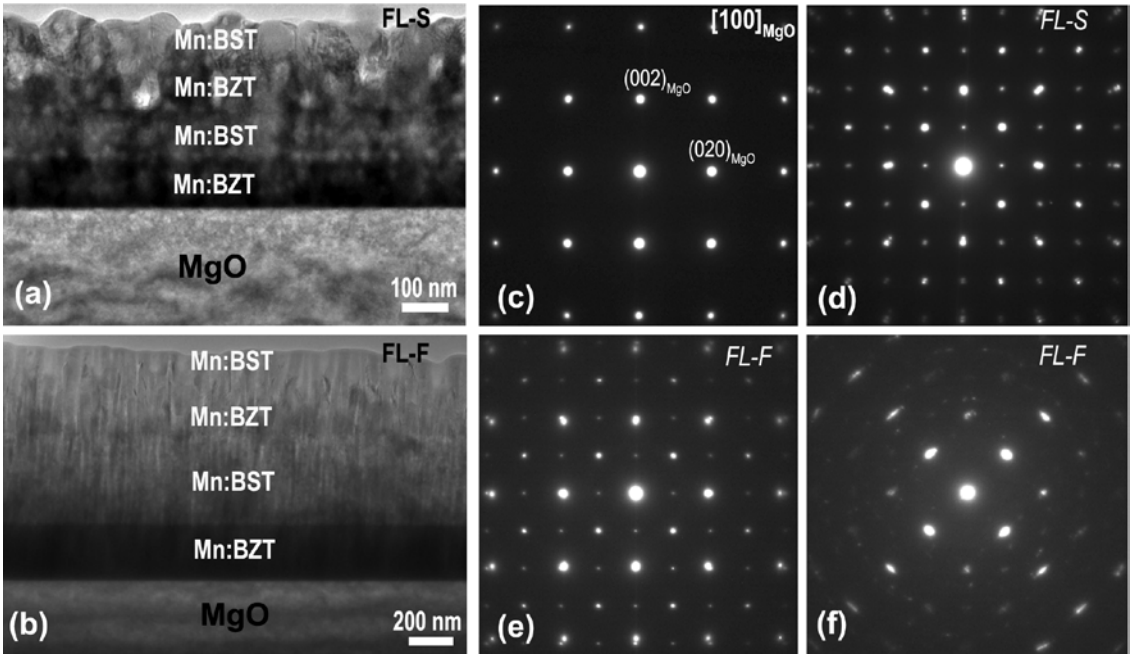

Figure 7.3 Cross-section TEM images of film (a) ***FL-S*** and (b) ***FL-F*** and SAED pattern of (c) MgO substrate; (d) the four layers and MgO substrate of ***FL-S*** sample; (e) interface region covering the first Mn:BZT layer and MgO substrate in ***FL-F*** sample; and (f) the second Mn:BST layer in ***FL-F*** sample.

Figure 7.3(a) and (b) are cross-section TEM images of ***FL-S*** and ***FL-F*** films obtained by having the electron beam parallel to the $[100]_{MgO}$. The ***FL-S*** and ***FL-F*** films have a thickness of 425 and 1060 nm, respectively. Contrast of four layers can be seen in both images. Figure 7.3(a) shows a continuous layer structure for the first two layers next to the substrate and a columnar structure for the top two layers. The size of the columns on the top layer varies from 50 nm to 150 nm, which is consistent with the results from the AFM measurements. Figure 7.3(b) shows a nanopillar structure over the entire ***FL-F*** film. It can be seen from the cross-section TEM that the ***FL-S*** film possesses a rougher surface compared to the ***FL-F*** film.

Figure 7.3(c) is a SAED pattern of the MgO substrate taken with the electron beam parallel to its [100] direction. Figure 7.3 (d) shows a SAED pattern of the entire film of the four layers and MgO substrate of the ***FL-S*** sample taken with the electron beam parallel to MgO

[100] axis. In Figure 7.3(d), three discrete subspots are observed on the higher order of the diffraction spots. This indicates that Figure 7.3 (d) is superposition of EDPs from [100] zone axis of MgO, Mn:BZT and Mn:BST layer. Figure 7.3(d) exhibits a very clean pattern of single crystal diffraction indicating that the four layers in ***FL-S*** film are epitaxially grown on the substrate. The in-plane and out-of-plane lattice parameter is 4.04 Å and 4.03 Å for the Mn:BZT layer, 3.97 Å and 3.96 Å for the Mn:BST layer, respectively. The first Mn:BZT layer has an in-plane lattice mismatch of about -3.70% with respect to the MgO substrate and about 1.76% with respect to the second Mn:BST layer.

Figure 7.3(e) is an SAED taken from an interface region covering the first Mn:BZT layer and MgO substrate of the ***FL-F*** film. It shows a superposition of EDPs from the MgO [100] zone and the first Mn:BZT layer. It can be seen from Figure 7.3(e) that the first Mn:BZT layer is epitaxially growing on the MgO substrate. The in-plane and out-of-plane lattice parameter of the first Mn:BZT layer is about 4.07 Å and 4.06 Å, which produces an in-plane and out-of-plane lattice mismatch of -3.34% and -3.56% with respect to the substrate, respectively. Figure 7.3(f) is a SAED pattern of the Mn:BST layer located on the top of the first Mn:BZT layer in the ***FL-F*** film. Figure 7.3(f) shows a clean pattern presenting only the $(0hh)$ and $(0h\bar{h})$ (*h* = ···-2, -1, 1, 2,···) diffraction spots. The pattern indicates that this Mn:BST layer in the ***FL-F*** film mainly consists of twin-coupled domain structures induced by sharing their {111} and {110} planes with epitaxially layers, as observed in BZT and Mn:BZT thin films. Further studies showed that the third and fourth layers of the ***FL-F*** film have a polycrystalline structure.

Figures 7.4(a) and (b) are the cross-section TEM images of the ***FL-S*** and ***FL-F*** films, respectively, viewed along the MgO [110] direction. It can be seen from Figure 7.4(a) that in the ***FL-S*** film, the two layers close to the substrate have continuous layer structure whereas the top two layers close to the surface have a columnar structure. The interfaces between the continuous layers and the columnar structures are clearly seen in this direction. The lateral size of the columnar structure in ***FL-S*** film is ~ 50- 60 nm. In the cross-section TEM image of the ***FL-***

F film (Figure 7.4(b)), a completely different microstructure from that of the ***FL-S*** film is clearly seen. The ***FL-F*** film has needle like nanopillar structures with a uniform column width of 30-40 nm. These nanopillars are aligned along the growth direction of the film and run through the entire film. The nanopillars observed from the MgO [110] direction are discrete and more obvious compared to the observation along the MgO [100] direction (Figure 7.3(b)).

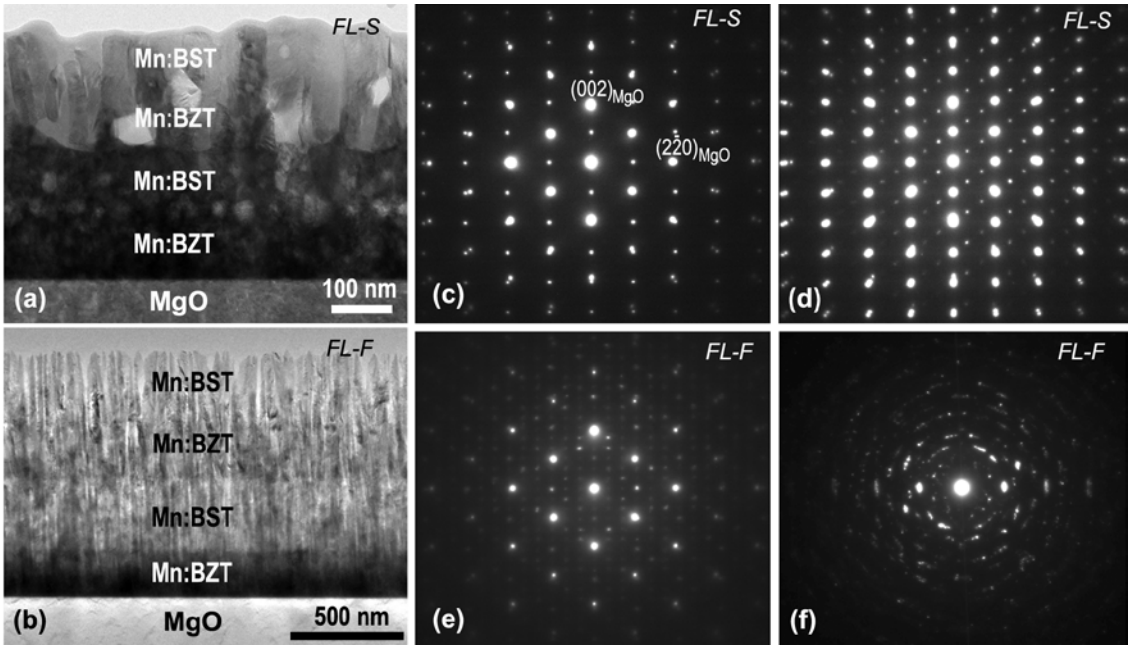

Figure 7.4 Cross-section TEM images of (a) ***FL-S*** and (b) ***FL-F*** film viewed along MgO [110] direction; SAED patterns taken with the electron beam parallel to MgO [110]: (c) from MgO/first Mn:BZT layer interface; (d) from area covering MgO, first Mn:BZT and second Mn:BST layer in the ***FL-S*** film; (e) from MgO/first Mn:BZT layer interface and (f) from the second Mn:BST layer in the ***FL-F*** film.

Figure 7.4 (c) is a SAED pattern taken from the interface between the first Mn:BZT layer and the MgO substrate in ***FL-S*** film. It shows a superposition of the MgO [110] zone EDP and one Mn:BZT [110] zone EDP. No diffraction spots associated with the formation of twin-induced domains were observed indicating that the first Mn:BZT layer is epitaxially grown on the MgO substrate. Figure 7.4 (d) is a SAED pattern taken from an area covering the MgO substrate, first Mn:BZT layer and second Mn:BST layer in ***FL-S*** film. In addition to the diffraction spots observed in Figure 7.4 (c), additional weak diffraction spots associated with the formation of the

twin-induced domains are observed. Figure 7.4(d) shows that only one of the four types of twin-induced domains were formed within the selected area in the second Mn:BST layer in ***FL-S*** film.

Figure 7.4 (e) is a SAED pattern taken from the interface between the first Mn:BZT layer and the MgO substrate in the ***FL-F*** film with the electron beam parallel to the MgO [110] axis. This diffraction pattern is a superposition of the EDPs of MgO [110] and Mn:BZT [110] zone. The regularly distributed extra weak diffraction spots are from twin-induced domains in the Mn:BZT layer. Figure 7.4(e) shows that all of four types of the {111} and {110} induced twin-coupled domains were formed within the selected area in the first layer of the Mn:BZT in FL-F film. The details about the formation and growth mechanism of the twin structures in BZT and Mn:BZT have been previously discussed. Figure 7.4 (f) is a SAED pattern taken from the second Mn:BST layer in the ***FL-F*** film showing a textured structure formed in this layer.

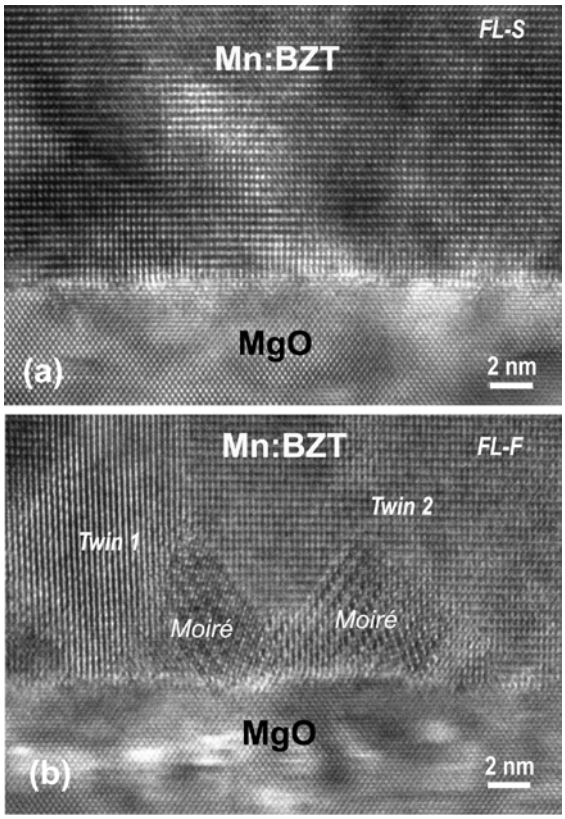

Figure 7.5 Cross-section HRTEM image of the interface between the first Mn:BZT layer and the MgO substrate taken with the electron beam parallel to the $[110]_{MgO}$ direction: (a) ***FL-S*** film; (b) ***FL-F*** film

Figure 7.5 (a) is a cross-section HRTEM image of the interface between the first Mn:BZT layer and the MgO substrate in the ***FL-S*** film, taken with the electron beam parallel to the MgO [110] direction. A single oriented crystal structure of Mn:BZT and an atomically sharp and clean film/substrate interface can be clearly seen. Figure 7.5 (b) is a cross-section HRTEM image of the interface between the first Mn:BZT layer and the MgO substrate in the ***FL-F*** film, taken along the MgO [110] direction. Instead of a single oriented structure, twin-induced domains with different crystallographic orientations (***Twin 1*** and ***Twin 2***) are observed in the Mn:BZT layer. Meanwhile, Moiré patterns due to the overlap of the twin domains are also frequently observed near the interface.

Figure 7.6 (a) is a plan-view TEM image taken from the top surface layer of the ***FL-S*** film showing grainy structures with an average grain size of ~70 nm. The grains in this film are tightly attached to their adjacent grains and leaving no gaps or pores. Figure 7.6 (d) is a SAED pattern of the surface layer of the ***FL-S*** film in a plan-view TEM foil. This diffraction pattern shows a mixture of the [001] zone single crystal and polycrystalline diffraction pattern indicating that the surface layer of the ***FL-S*** film has, in addition to the epitaxial single crystal structure, some polycrystalline structures.

Figure 7.6 (b) is a plan-view TEM image taken from top surface layer of ***FL-F*** film. It shows that the cross-sections of the nanopillars in the surface layer are not round but elongated along MgO [110] or $[1\bar{1}0]$ direction. The average length of the long axis of the cross-section of the nanopillars is about 60-70nm, which is close to the result obtained from the AFM measurements. The boundaries between nanopillars in which gaps and/or pores were observed are nearly parallel to the MgO [110] or $[1\bar{1}0]$ direction. This is the reason the nanopillars can be observed more clearly in the cross-section TEM image viewed along MgO [110] direction.

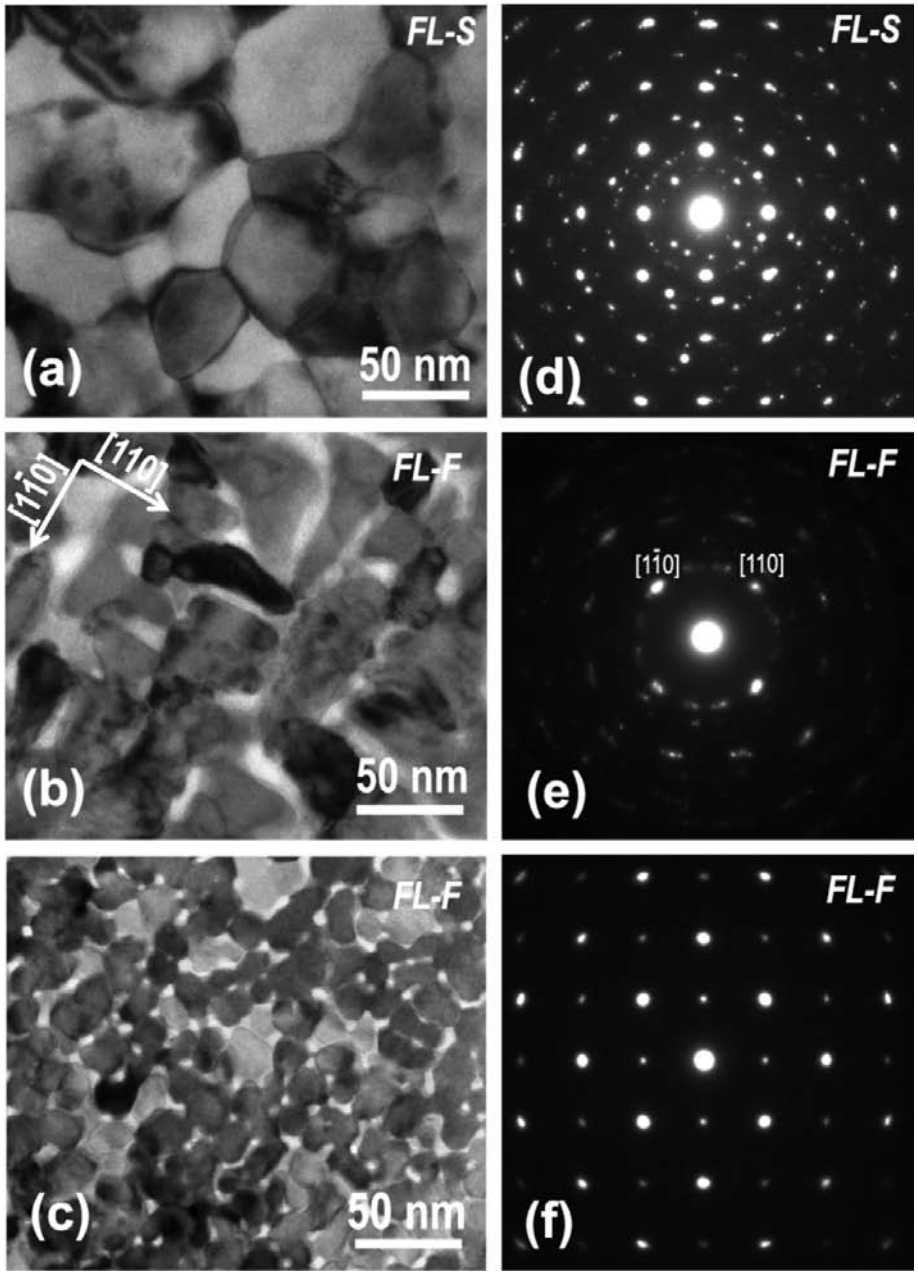

Figure 7.6 (a) Plan-view TEM image and (d) SAED pattern of the surface layer of ***FL-S*** film; (b) and (c) plan-view TEM images; (e) and (f) SAED patterns of the surface and bottom layer of ***FL-F*** film, respectively.

Figure 7.6 (e) is a SAED pattern from the top surface layer of the ***FL-F*** film. The diffraction pattern shows that the surface layer of the ***FL-F*** has a texture structure with a preferred orientation along MgO [110] and $[1\,\bar{1}0]$ direction. This indicates that the {111} twin

domains are dominant in the top layer of the ***FL-F*** film and no epitaxial grains remained. Figure 7.6 (c) is a plan-view image taken from bottom layer of the ***FL-F*** film, and Figure 7.6(f) is its corresponding SAED. The plan-view TEM specimen of the bottom layer (close to the substrate) was obtained by gradually Ar milling the specimen in Figure 7.6 (b). Figure 7.6 (c) shows smaller grain structures compared to Figure 7.6 (b). The average grain size in Figure 7.6 (c) is about 15 nm. Figure 7.6 (f) is similar to a single crystal diffraction pattern of the Mn:BZT [001] zone but with intensity variation for some diffraction spots. This indicates that the epitaxial structure dominates the bottom layer close to the substrate.

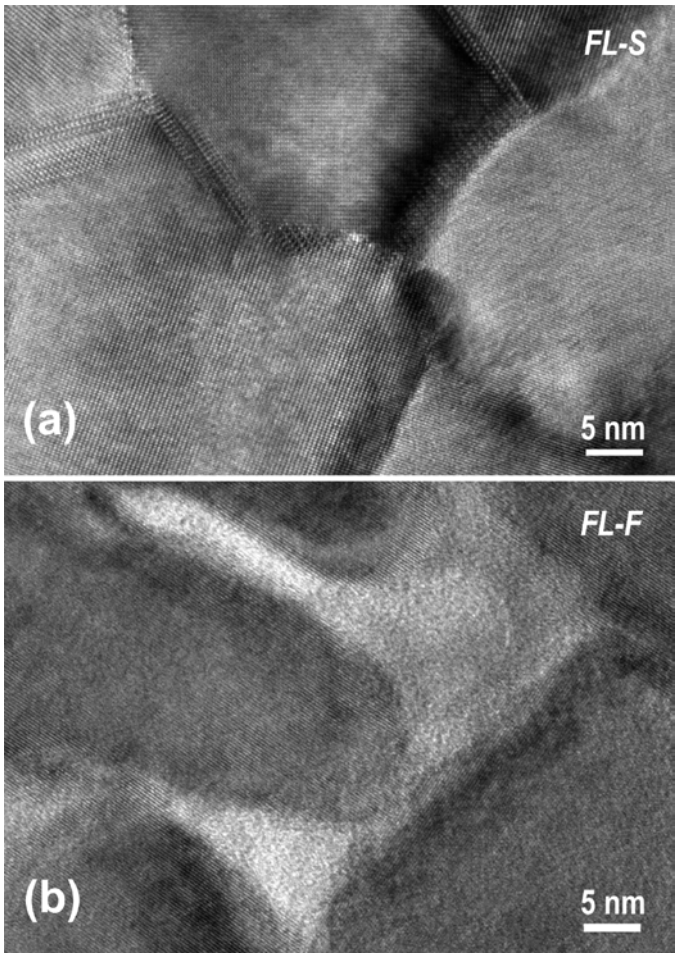

Figure 7.7 Plan-view HRTEM images of the top layer in the film: (a) ***FL-S*** and (b) ***FL-F***.

Figure 7.7 (a) is a plan-view HRTEM image taken from the same foil shown in Figure 7.6 (a) showing the atomic structure of the boundaries between the grains. It is evident that that

there is no porous at the grain boundaries even at the atomic scale. Figure 7.7 (b) is a plan-view HRTEM image taken from the same foil shown in Figure 7.6 (b). An amorphous structure was observed at the grain boundaries. Such observations indicate that the boundaries have lower density or are defect-rich regions in which the long range ordering of the crystal is not maintained.

The aforementioned results show that during the deposition of the Mn:BST//Mn:BZT four-layered films, the deposition rate exercises a critical influence on the epitaxial quality of the film. Deposition with a small rate can produce better epitaxial quality of the entire film, while deposition with a larger rate results in twin-coupled domain structures and accordingly less the epitaxial structure of the film.

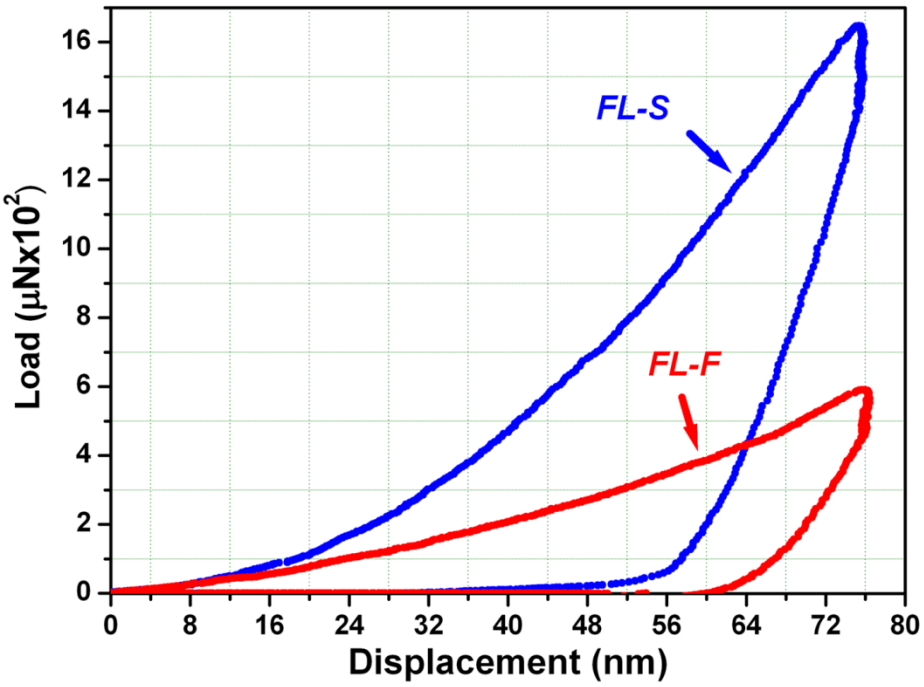

Figure 7.8 Load-displacement curves of nanoindentation measurement for ***FL-F*** (red) and ***FL-S*** (blue) films with the same 75nm displacement.

Figure 7.8 shows typical nano-indentation load-displacement curves for ***FL-S*** and ***FL-F*** films. The average hardness and modulus values were determined by performing 4×4 array indents with 3μm×3μm distance and at the same displacement of 75 nm for each film. The

mean hardness for ***FL-S*** and ***FL-F*** film is 6.70 and 2.25 GPa, respectively. The mean modulus for ***FL-S*** and ***FL-F*** film is 193.37 and 104.58 GPa, respectively. Comparing the load-displacement curves of ***FL-S*** and ***FL-F***, a large difference of the maximum load at maximum displacement of 75 nm and residual penetration at zero load in the unloading segment depths were clearly observed. The higher hardness and modulus of the ***FL-S*** film is attributed to its epitaxial quality and higher density compared to ***FL-F*** film.

7.3 Microstructure and Interfaces of $[Mn:BZT//Mn:BST]_N$ Multilayer Films With Various Deposition Periods

Two series $[Mn:BZT//Mn:BST]_N$ multilayer films with the deposition sequence of $[(Mn:BZT)_3:(Mn:BST)_1]_N$ (denoted as ***ZL*** multilayer films) and $[(Mn:BZT)_1:(Mn:BST)_3]_N$ (denoted as ***SL*** multilayer films) deposited on MgO (001) substrates were used to study the effect of layer numbers and the ratio of deposition time between each Mn:BZT and Mn:BST layer on the formation and microstructure of multilayer films. N represents the number of deposition periods, and the (3:1) or (1:3) represents the ratio of deposition time for each Mn:BZT or Mn:BST single layer at one period.

Figure 7.9 is a schematic illustration of the multilayer construction of $[(Mn:BZT)_3:(Mn:BST)_1]_N$ (***ZL***) and $[(Mn:BZT)_1:(Mn:BST)_3]_N$ (***SL***) films. The deposition period N was selected to be 4, 8, 16 for both ***ZL*** and ***SL*** series multilayer films (denoted as ***ZL-4***, ***ZL-8***, ***ZL-16*** and ***SL-4***, ***SL-8***, ***SL-16***, respectively), when considering Mn:BZT and Mn:BST layers as one deposition group. Therefore, the total layers number for each multilayer film is 2N when referring Mn:BZT and Mn:BST as an individual layer. The first deposited layer is Mn:BZT layer for all the multilayer films. Since the deposition rate for Mn;BZT and Mn:BST single layer is different, the total film thickness for each multilayered film ***ZL*** and ***SL*** films is slightly varied. Since Mn:BZT ($a_{Mn:BZT}$=4.04 Å [165,166]) has a larger lattice parameter than Mn:BST ($a_{Mn:BST}$=3.96 Å [23,132]). At close layer interface, Mn:BZT side is compressed, while Mn:BST side is expanded at the interface between Mn:BZT and Mn:BST layers.

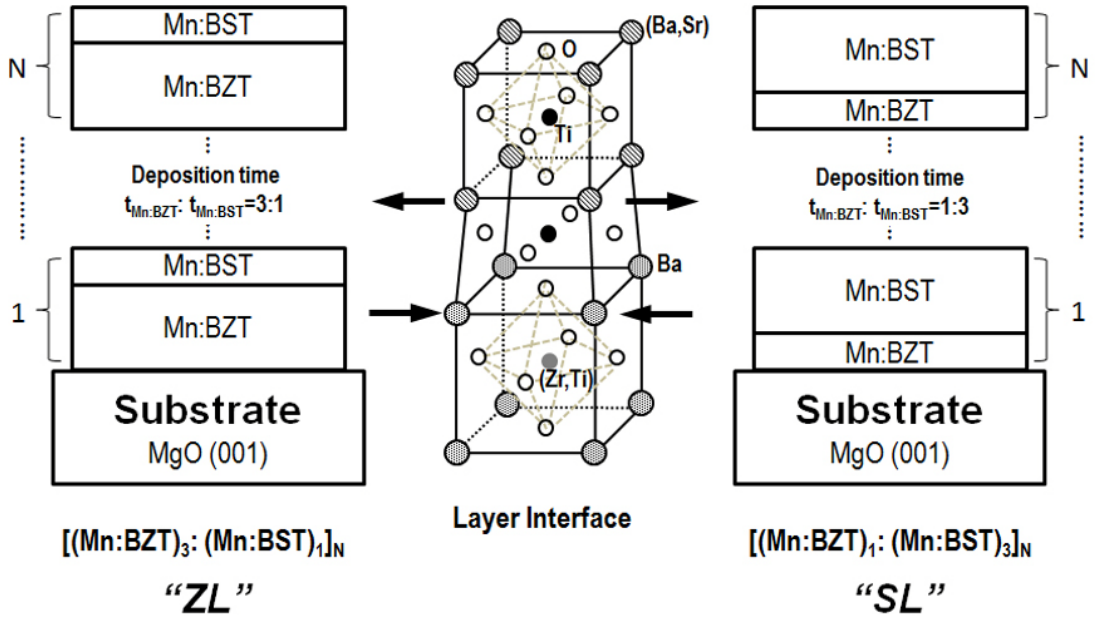

Figure 7.9 A schematic image of the fabrication of $[(Mn:BZT)_3:(Mn:BST)_1]_N$ (***ZL***) and $[(Mn:BZT)_1:(Mn:BST)_3]_N$ (***SL***) multilayer films by pulsed laser deposition and a model showing Mn:BZT and Mn:BST layer interface.

Figure 7.10 shows the typical XRD θ-2θ scans of $[Mn:BZT//Mn:BST]_N$ multilayer films: (a) ***ZL-4***; (b) ***ZL-8***; (c) ***ZL-16***; (d) ***SL-4***; (e) ***SL-8***; (f) ***SL-16***. The insets on the right top corner for each film are the rocking curves of Mn:BZT (002) and/or Mn:BST (002) reflections. For ***ZL-4*** and ***SL-4*** multilayer films, as shown in Figure 7.10 (a) and (d), two sets of (00*l*) peaks (*l*=1, 2, 3) can be clearly observed for Mn:BZT and Mn:BST layer respectively, in addition to MgO (002) reflection. The diffraction intensity for Mn:BZT layer is relatively higher than Mn:BST layer in ***ZL-4*** film, however lower than Mn:BST layer in ***SL-4*** film since different deposition time for each Mn:BZT and Mn:BST layer in ***ZL-4*** and ***SL-4*** films. The lattice constant along the film growth direction for Mn:BZT and Mn:BST layers are 4.035 Å and 3.966 Å in ***ZL-4*** film, and 4.033 Å and 3.958 Å in ***SL-4*** film, respectively. The out-of-plane lattice mismatch of the Mn:BZT and Mn:BST layer with respect to MgO substrate is about -4.08% and -5.73% in ***ZL-4*** film, and -4.15% and -5.93% in ***SL-4*** film, respectively, calculated using $(a_{film} - a_{MgO}) / a_{MgO}$ with a_{MgO}=4.212 Å. The out-of-plane lattice mismatch between Mn:BZT and Mn:BST layers at the layer interface is

about 1.74% in ***ZL-4*** film and 1.89% in ***SL-4*** film for Mn:BZT layer with respect to Mn:BST using the formula of $(a_{Mn:BZT} - a_{Mn:BST}) / a_{Mn:BST}$. The full width at half maximum (FWHM) from the rocking curves of Mn:BZT (002) and Mn:BST (002) in ***ZL-4*** film is about 0.94^{o} and 1.08^{o}, and those in ***SL-4*** film is about 1.13^{o} and 1.00^{o}, respectively, which indicate that both Mn:BZT and Mn:BST layers in ***ZL-4*** and ***SL-4*** films exhibit good single crystal structure and epitaxial quality, especially for multilayer films.

For ***ZL-8*** film, only (00*l*) (*l*=1, 2, 3) peaks with relatively lower intensity from Mn:BZT layer than that in ***ZL-4*** film, are shown in Figure 7.10 (b). Apart from MgO (002) reflection, no diffraction peaks from Mn:BST layer can be observed, revealing that the ***ZL-8*** film is epitaxial single crystal film with certain structure relationship not always agree with [100]film//[100]substrate and (100)film//(100)substrate. All the Mn:BST layers and most of Mn:BZT layers in ***ZL-8*** is not epitaxially grown along [001] direction of MgO. The lattice constant along [001]MgO for partial epitaxial Mn;BZT layer (Epi-Mn:BZT) is 4.039 Å, and lattice mismatch for Epi-Mn:BZT with respect to MgO substrate is about -4.03% in ***ZL-8*** film. In Figure 2(e), only Mn:BZT (002) peak along with all (00*l*) (*l*=1, 2, 3) peaks from Mn:BST layer of ***SL-8*** film is shown, which indicates that Mn;BZT layers are partially epitaxial grown along the growth direction (out of plane direction). The lattice constant for Epi-Mn:BZT and epitaxial Mn:BST (Epi-Mn:BST) in ***SL-8*** film is about 4.035 Å and 3.962 Å with the out-of-plane lattice mismatch of -4.11% and -5.85%, respectively. The lattice mismatch between Epi-Mn:BZT and Epi-Mn:BST layers along growth direction is calculated to be 1.84% for Epi-Mn:BZT with respect to Epi-Mn:BST in ***SL-8*** film. The FWHM of rocking curves for Mn:BZT (002) reflection in ***ZL-8*** and Mn:BST (002) reflection in ***SL-8*** is about 2.10^{o} and 1.43^{o}, respectively, which are relatively larger than the values measured from ***ZL-4*** and ***SL-4*** films, also indicating a less epitaxial quality along out-of-plane direction.

Figure 7.10 (c) and (f) are the X-ray diffractions for ***ZL-16*** and ***SL-16*** films. Only one set of (00*l*) reflections can be observed in both films in addition to the diffraction from MgO

substrate. Both Mn:BZT (002) peak in ***ZL-16*** and Mn:BST (002) peak in ***SL-16*** can be identified with broad reflection at peak bottom part and gradually shifting peak position to the angle corresponding to Mn:BZT (002) in ***ZL-16*** and Mn:BST (002) in ***SL-16***. It indicates that the angles of Mn:BZT (002) and Mn:BST (002) reflections are very close to each other and therefore merge two peaks together without showing separated individual Mn:BZT (002) and Mn:BST (002) peak in both ***ZL-16*** and ***SL-16*** films. The lattice constant along the film growth direction for Mn:BZT layer in ***ZL-16*** film is 4.057 Å, and the out-of-plane lattice mismatch with respect to MgO substrate is about -3.63%, which is smaller than that of ***ZL-8*** and ***ZL-16*** films. The lattice constant along the film growth direction for Mn:BST layer in ***SL-16*** film is 3.979 Å with the out-of-plane lattice mismatch to MgO substrate of -5.44%, which is also smaller than that of ***SL-8*** and ***SL-16*** films. The rocking curve FWHM for Mn:BZT (002) reflection in ***ZL-16*** and Mn:BST (002) reflection in ***SL-16*** is about 1.08^{o} and 1.34^{o}, respectively, which reveals that both films keep relatively good epitaxial quality through the entire films with total 32 hetero-layers.

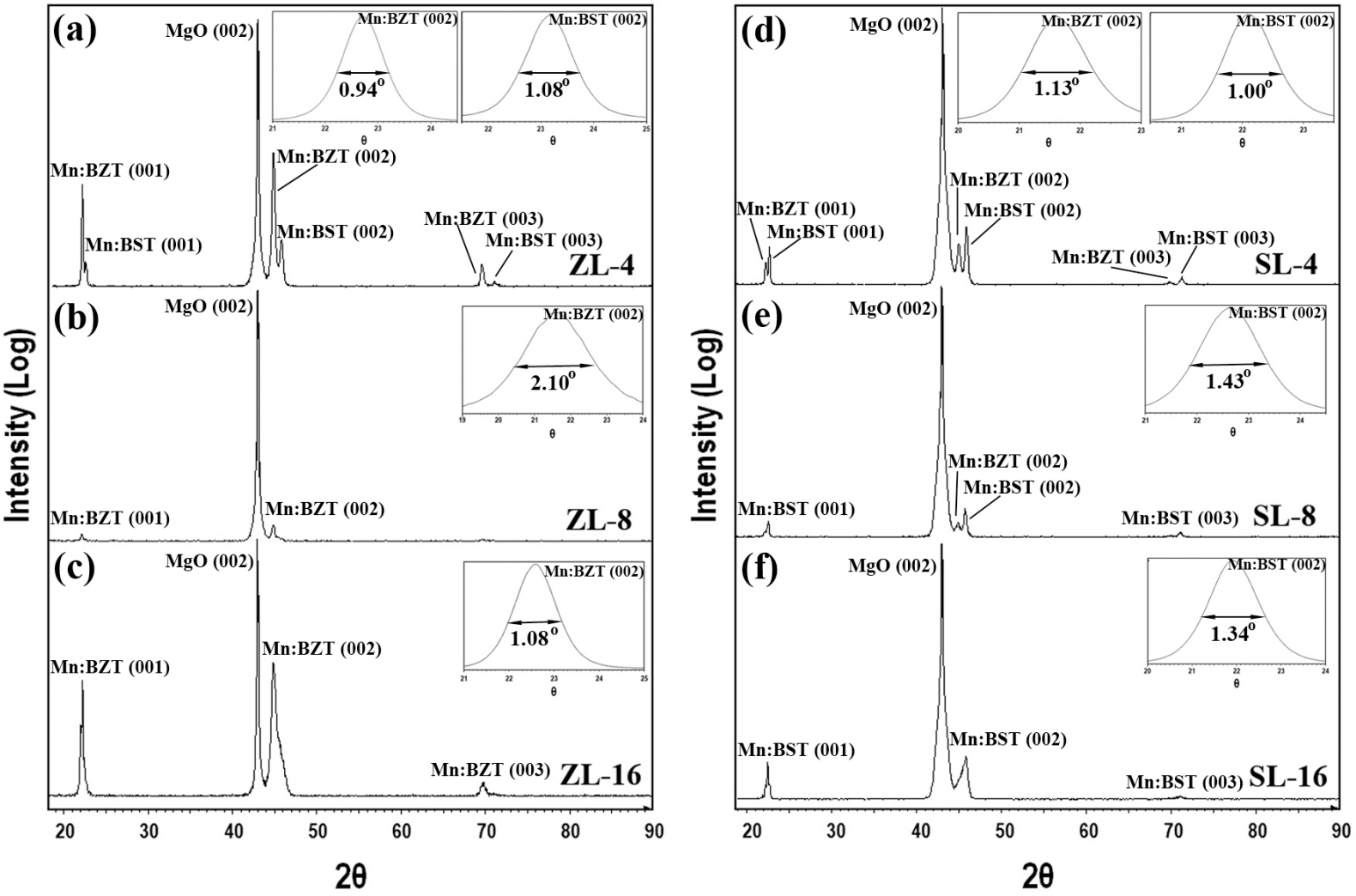

Figure 7.10 X-ray diffraction pattern of θ-2θ scans with Mn:BZT (002) and/or Mn:BST (002) rocking curves (top right insets) for as-deposited multilayer films (a) ***ZL-4***; (b) ***ZL-8***; (c) ***ZL-16***; (d) ***SL-4***; (e) ***SL-8***; (f) ***SL-16***.

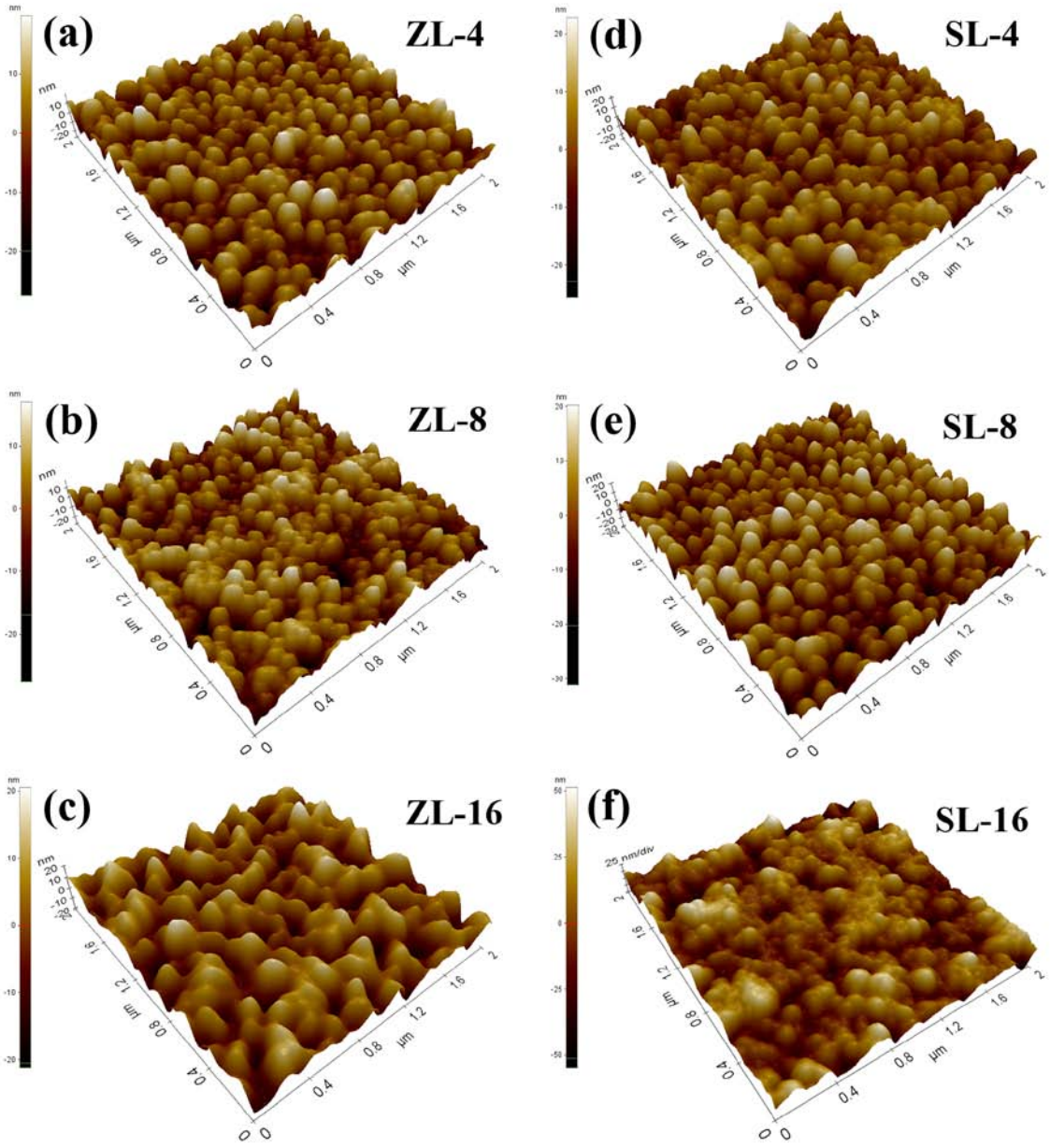

Figure 7.11 Non-contact AFM 3D images of as-deposited multilayer films (a) ***ZL-4***; (b) ***ZL-8***; (c) ***ZL-16***; (d) ***SL-4***; (e) ***SL-8***; (f) ***SL-16***.

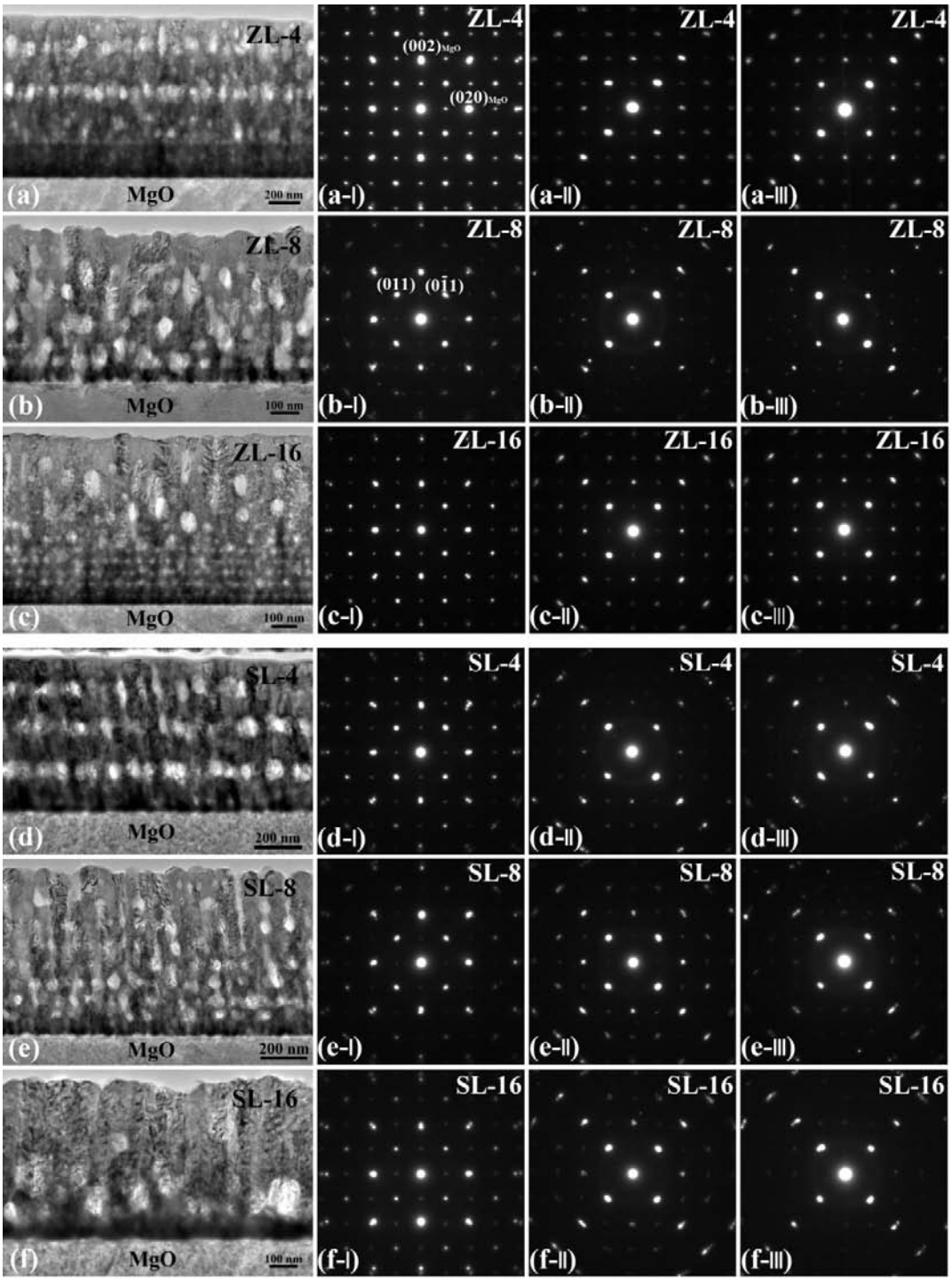

Figure 7.12 (a)-(f) Cross-section TEM images of multilayer films with electron beam parallel to MgO [100] direction; (a-I)-(f-I) SAED patterns from the interface covering first Mn:BZT//Mn:BST period layer and MgO substrate; (a-II)-(f-II) SAED patterns from intermediate area and (a-III)-(f-III) SAED patterns from top surface area for ***ZL-4***; ***ZL-8***; ***ZL-16***; ***SL-4***; ***SL-8***; ***SL-16***, respectively.

The surface roughness and morphology of all six multilayer films (***ZL-4***, ***ZL-8***, ***Zl-16*** and ***SL-4***, ***Sl-8***, ***SL-16***) were investigated using non-contact AFM with a scanning size of $2 \times 2 \mu m^2$, as shown in Figure 7.11. All six multilayer films exhibit a granular structure, however more uniform grain size and better distinguished grain boundaries can be observed in ***ZL-4***, ***ZL-8*** and ***SL-4***, ***SL-8*** films, comparing with ***ZL-16*** and ***SL-16*** films, which shows disordered granular size and granular clusters crowded together. Figure 7.11 (a)-(c) show that the ***ZL-4*** and ***ZL-16*** films have a larger granular structure with a size varying from 80 nm to 200nm, while ***ZL-8*** film has a smaller size of about 90 nm granular structure. Besides, Figure 7.11 (d)-(f) show that the ***SL-4*** and ***SL-8*** films have a similar granular size of around 100 nm, while ***SL-16*** film exhibits a uniform granular structure with the size range from 60 nm to 200 nm. The average roughness for ***ZL-4***, ***ZL-8*** and ***ZL-16*** is 5.186 nm, 4.987 nm, 5.405 nm, respectively. And the average roughness for ***SL-4***, ***SL-8*** and ***SL-16*** is 4.985 nm, 5.594 nm, and 12.496 nm, respectively, indicating ***SL-16*** has a much rougher surface compared to other multilayer films.

Figures 7.12 (a)-(f) are cross-section TEM (XTEM) images of ***ZL-4***, ***ZL-8***, ***ZL-16***, and ***SL-4***, ***SL-8***, ***SL-16*** multilayer films obtained with the electron beam parallel to the [100]MgO. Figures 7.12 (a-I)-(f-I) are selected area electron diffraction (SAED) patterns from the interface between MgO substrate and the first period layers (Mn:BZT//Mn:BST) close to interface. Figures 7.12 (a-II)-(f-II) are SAED patterns taken from the middle area (covering area around 300 nm in diameter) of the multilayer films, and the SAED patterns taken from the region covering the top surface area of each film are presented in Figures 7.12 (a-III) and (f-III). The contrast of four deposition periods, eight periods with a columnar structure through the entire film from the first layer close to substrate to the top surface, can be clearly seen in ***ZL-4*** and ***SL-4***; ***ZL-8*** and ***SL-8***, respectively, in Figures 7.12 (a), (b), (d) and (e). The film thickness of ***ZL-4*** and ***SL-4*** is 1028 nm and 650 nm, respectively, and that of ***ZL-8*** and ***SL-8*** is measured to be 544 nm and 687 nm. The lateral size of the columns at the top surface layers varies from 50 nm to 150 nm in ***ZL-4*** and 30 nm to 100 nm in ***SL-4***, ***ZL-8*** and ***SL-8*** films, which is consistent with

the results measured from AFM. Figure 7.12 (c) shows that ***ZL-16*** has a combination structure of a continuous layer structure for the first five or six deposition periods next to the substrate, and followed by a columnar structure formed on the top surface. However, ***SL-16*** shows a columnar structure through entire film with larger pores concentrated at the bottom area in Figure 7.12 (f). The thickness of ***ZL-16*** and ***SL-16*** is 660 nm and 565 nm. The lateral size of the columns at the top surface layers in ***ZL-16*** and ***SL-16*** is varying from 30 to 100 nm. The SAEDs taken from substrate and film interface in Figures 7.12 (a-I)-(f-I) show a superposition of EDP of the [100] zone MgO and EDP from the first Mn:BZT//Mn:BST period layers in ***ZL*** and ***SL*** films. Only two discrete subspots can be observed on the higher order of the diffraction spots, indicating that the diffractions mainly come from the MgO substrate and the layer with longer deposition time, e.g. Mn:BZT layer in ***ZL*** films or Mn:BST layer in ***SL*** films.

Figures 7.12 (a-I) and (c-I) present a clean EDP of Mn:BZT [100] zone with very few diffractions from Mn:BST layer since relatively shorter deposition time. It indicates that the first Mn:BZT layer is epiatxially grown from MgO substrate with a psedo-cubic structure in ***ZL-4*** and ***ZL-16*** films. However, Figure 7.12 (b-I) exhibits a preferred orientation along [011] and $[0\,\bar{1}1]$, which indicates the formation of twin structures starting from the initial growth of ***ZL-8*** film by sharing {111} planes. From our previous studies, BZT and Mn:BZT films have been reported to easily form twin-coupled structure by sharing their {111} and {110} planes along epitaxial layers [14-16]. The in-plane lattice mismatch between Mn:BZT layer and MgO substrate for ***ZL*** films is about -3.70% (***ZL-4***), -3.57% (***ZL-8***), -3.98% (***ZL-16***), which indicates that the formation of twin structures lower the in-plane lattice mismatch by sharing their {111} and {110} planes with respect to MgO substrate. The out-of-plane lattice mismatch between Mn:BZT layer and MgO substrate for ***ZL*** films is about -3.98% (***ZL-4***), -3.85% (***ZL-8***), -3.67% (***ZL-16***), which is decreasing with the increase of deposition periods since the shorter deposition period, the less deposition layers within the same total film thickness, and thicker for each Mn:BZT and Mn:BST layer, and therefore the lattice strain is easier to release in ***ZL-4*** film and lead to a larger out-of-

plane lattice mismatch. Similarly, since the triple deposition time of Mn:BST layer compared to Mn:BZT layer in ***SL*** films, SAEDs in Figures 7.12 (d-I) to (f-I) mainly show a superposition of EDPs from the MgO [100] zone and Mn:BST [100], which also suggests that the first Mn:BST layer has a pseudo-cubic structure and epitaxially grown with respect to MgO substrate. The in-plane and out-of-plane lattice mismatch between the Mn:BST layer and MgO substrate is about -5.49% and -5.07% for SL-4, -5.26% and -5.41% for SL-8, -5.22% and -5.41% for ***SL-16***, respectively. It shows that the in-plane lattice mismatch is decreased with the increasing of deposition periods; however ***SL-4*** has a lower out-of-plane lattice mismatch at close interface compared with ***SL-8*** and ***SL-16*** films. The summary for the lattice mismatches between Mn:BZT, Mn:BST and MgO substrate is listed in Table 7.1

Table 7.1 Lattice matches between Mn:BZT, Mn:BST and MgO substrate obtained from XRD and TEM results.

Films	XRD			TEM			
	δ% (Out-of-plane)			δ% (Out-of-plane)		δ% (Out-of-plane)	
	Mn:BZT /MgO	Mn:BST /MgO	Mn:BST /Mn:BZT	Mn:BZT /MgO	Mn:BST /MgO	Mn:BZT /MgO	Mn:BST /MgO
ZL-4	-4.08	-5.73	-1.71	-3.7	-	-3.98	-
ZL-8	-4.03	-	-	-3.57	-	-3.85	-
ZL-16	-3.63	-4.52	-0.92	-3.98	-	-3.67	-
SL-4	-4.15	-5.93	-1.85	-	-5.49	-	-5.07
SL-8	-4.11	-5.85	-1.81	-	-5.26	-	-5.41
SL-16	-4.43	-5.44	-1.05	-	-5.22	-	-5.41

The SAEDs in Figures 7.12 (a-II)-(c-II) and (a-III)-(c-III) give the information of the ***ZL*** films structure and orientation from the middle area to the top surface during the films growth. It shows a very clean pattern of single crystal diffraction, indicating that the ***ZL-4*** and ***ZL-16*** films have a pseudo-cubic structure and keep very good epitaxial relationship as [100]film//[100]MgO and (001)film//(001)MgO through the entire films. A little stronger diffraction spots along [011] and $[0\bar{1}1]$ indicates a preferred orientation and the formation of {111} and {110} twin structure

along epitaxial structure starting from the middle area of the film. The epitaxial structure and twin structure are co-existed in ***ZL-4*** and ***ZL-16*** films. However, the SAEDs in Figures 7.12 (bII) and (bIII) show a texture structure along [011] and $[0\bar{1}1]$, which suggests the {111} and {110} twin dominated structure formed in ***ZL-8***. Similarly, the SAEDs in Figures 7.12 (dII)-(fII) and (dIII)-(fIII) show the clean patterns presenting stronger $(0hh)$ and $(0h\bar{h})$ (h = ···-2, -1, 1, 2,···) diffraction spots, indicating that all SL films mainly consists of four types twin-coupled domain structure introduced by sharing their {111} and {110} planes with epitaxial layers, and dominated at the top surface area, as previous studies in BZT and Mn:BZT thin films [14-16]. Although Mn:BST films does not have preference to form twin structure during the film deposition or phase transition, BZT and Mn:BZT films have been found to easily form twin-coupled structure by sharing their {111} and {110} planes with epitaxially layers in chapter 6. The first deposition Mn:BZT layer next to MgO substrate has a critical influence on the growth of following Mn:BST layer.

Figures 7.13 (a)-(f) are the cross-section TEM (XTEM) images of ***ZL*** and ***SL*** films with the electron beam parallel to MgO [110] direction. The deposition periods of 4 and 8 Mn:BZT//Mn:BST layers can be clearly seen by contrast in ***ZL-4***, ***SL-4***, ***ZL-8*** and ***SL-8*** films in Figures 7.13 (a), (b), (d) and (e), respectively. A columnar structure also can be observed in ***ZL-4***; ***SL-4***; ***ZL-8*** and ***SL-8*** films with a columnar width varying from 50 nm to 150 nm in ***ZL-4*** and 30 nm to 100 nm in ***SL-4***, ***ZL-8*** and ***SL-8*** films, which is consistent with the results measured from XTEM images along MgO [100] direction in Figures 7.12 (a), (b), (d) and (e). These columns are aligned along the growth direction of the film and formed through the entire film. Figure 7.13 (c) shows that the ***ZL-16*** film is composed with two structures of a continuous layer structure formed in the initial six Mn:BZT//Mn:BST layers close to the MgO substrate, and a columnar structure grown in the next ten period layers at close to top surface, which is very similar as observed in Figure 7.12 (c). The transition from continuous layer to columnar structure is gradually changed without clear interface observed. However, ***SL-16*** film shows a

columnar structure through the entire film with 16 very thin Mn:BZT//Mn:BST repeated layers. The layer boundaries and column boundaries ***SL-16*** are not as obvious as shown in ***ZL-4***; ***SL-4***; ***ZL-8*** and ***SL-8*** films. The lateral size of the columnar structure in ***ZL-16*** and ***SL-16*** film has a range from 20 nm to 150 nm, which indicates a relatively rougher surface. The morphology observed from MgO [110] direction for ZL and SL films further confirm the observations along the MgO [100] direction.

Figures 7.13 (a-I)-(f-I) are SAED patterns taken from the interface between MgO substrate and the first period Mn:BZT//Mn:BST layer with electron beam parallel to MgO [110] direction. It shows a superposition of four EDPs from $[110]_{MgO}$, [110] zone of epitaixial structure ($[110]_{Epi}$) and two [110] zones of twin-related domain structure ($[110]_{T1}$ and $[110]_{T2}$). It indicates that the four kinds of twin-coupled structures were initially introduced in first Mn:BZT//Mn:BST period layer by sharing their $(1\bar{1}1)$, $(\bar{1}11)$, $(1\bar{1}\bar{1})$ and $(\bar{1}1\bar{1})$ planes with respect to the epitaxial structure in ***ZL*** and ***SL*** films, respectively. However, the much stronger diffraction spots from $[110]_{Epi}$ and $[110]_{MgO}$ compared with the weak diffraction spots from $[110]_{T1}$ and $[110]_{T2}$ suggest that the epitaxial structure are dominant in the first Mn:BZT//Mn:BST layer near the interface. Two discrete subspots can be observed on the higher order of the diffraction spots in ***ZL-4***, ***ZL-8***, ***ZL-16***, ***SL-8*** and ***SL-16*** films, while three separated subspots can be found in ***SL-4*** film. The extra diffraction spots shown on higher order in Figure 7.13 (d-I) are resulted from the Mn:BZT epitaxial structure formed close to interface.

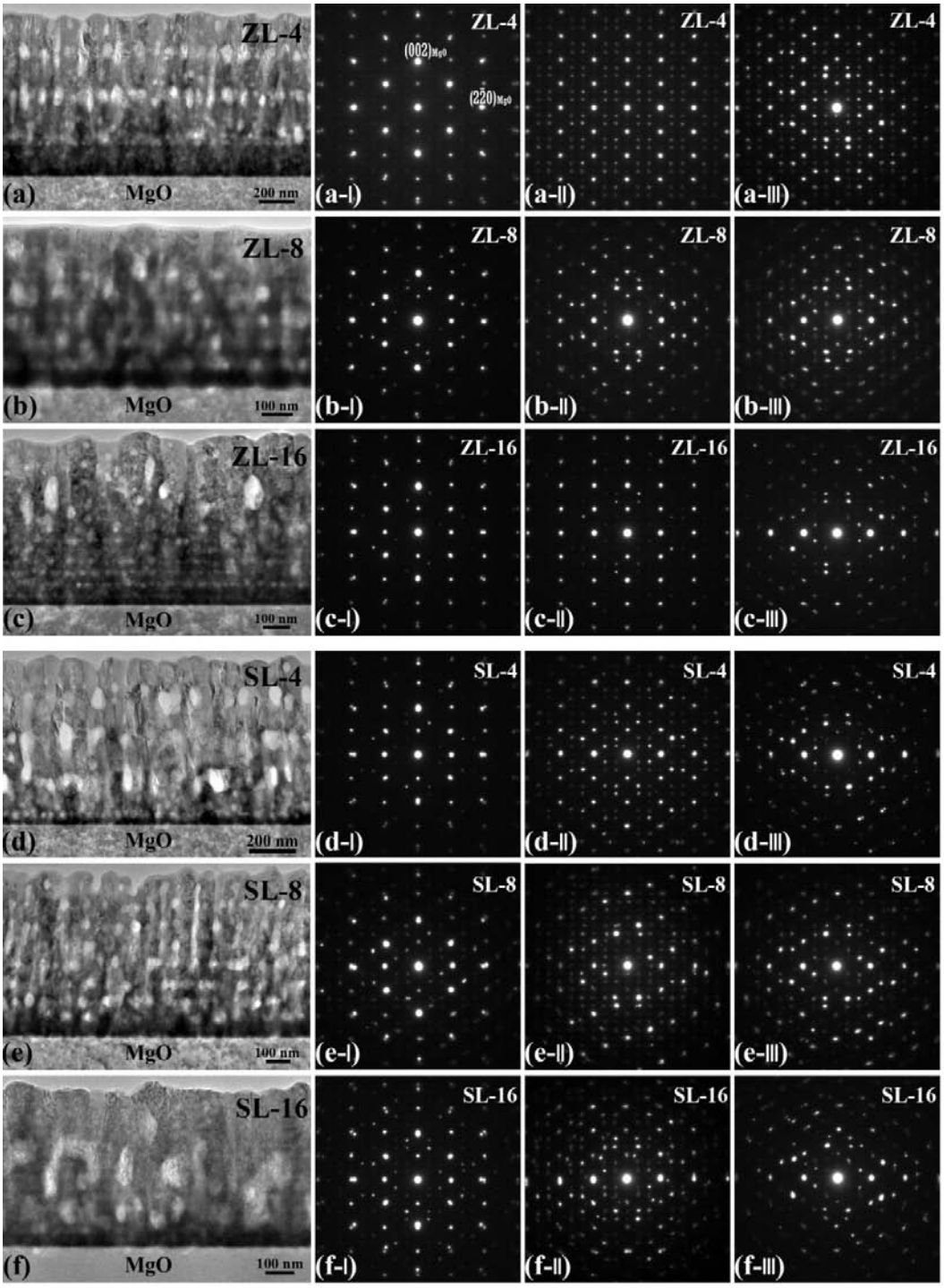

Figure 7.13 (a)-(f) Cross-section TEM images of multilayer films with electron beam parallel to MgO [110] direction; (a-I)-(f-I) SAED patterns from the interface covering first Mn:BZT//Mn:BST period layer and MgO substrate; (a-II)-(f-II) SAED patterns from intermediate area and (a-III)-(f-III) SAED patterns from top surface area for ***ZL-4***; ***ZL-8***; ***ZL-16***; ***SL-4***; ***SL-8***; ***SL-16***, respectively.

Figures 7.13 (a-II)-(f-II) are SAEDs taken from the region covering the middle area of each multilayer film with a size of around 300 nm diameter, viewed along MgO [110] direction. The diffraction patterns are superposed with three EDPs of $[110]_{Epi}$ and two [110] zones from {111} twin structures ($[110]_{T1}$ and $[110]_{T2}$). The diffraction spots intensities from $[110]_{Epi}$ zone of epitaxial structure remain stronger than those from $[110]_{T1}$ and $[110]_{T2}$ zones of twin domains in Figures 7.13 (a-II), (c-II) and (d-II). However, the diffractions from twin domains become more significant than those from epitaxial structure in Figures 7.13 (b-II), (e-II) and (f-II). It indicates that the epitaxial structure of Mn:BZT//Mn:BST layers is the dominant structure in the intermediate area of ***ZL-4***, ***ZL-16*** ad ***SL-4*** films, while the twin-coupled domain structure have become majority in the middle area of ***ZL-8***, ***SL-8*** and ***SL-16*** films. Figures 7.13 (a-III)-(f-III) give the SAED patterns obtained from top surface area with electron beam along $[110]_{MgO}$ direction. The EDPs are mainly composed of $[110]_{T1}$ and $[110]_{T2}$ zones of four types twin-coupled domain structure with very weak/no diffractions from epitaxial structure, indicating the twin domains are dominated at the top surface of all ***ZL*** and ***SL*** multilayer films (very few epitaxial structure if there is any).

Figures 7.14 (a) and (b) are cross-section HRTEM images of the interface between first Mn:BZT deposition layer and MgO substrate with the electron beam along MgO [110] direction for ***ZL-4*** film and ***SL-4*** film, respectively. Figure 7.14 (a) shows a clean and relatively flat film/substrate interface with an epitaxial structure of Mn:BZT for ***ZL-4*** film. The existing Moiré fringes due to the overlap of twin domains indicate the formation of multi-oriented twin domains (***Twin 1*** and ***Twin 2***) at close to interface. Similar interface feature has been found in ***SL-4***, ***ZL-16*** and ***SL-16*** films showing a sharp and atomically flat interface with some twin-coupled domains formed directly from interface or near to interface.

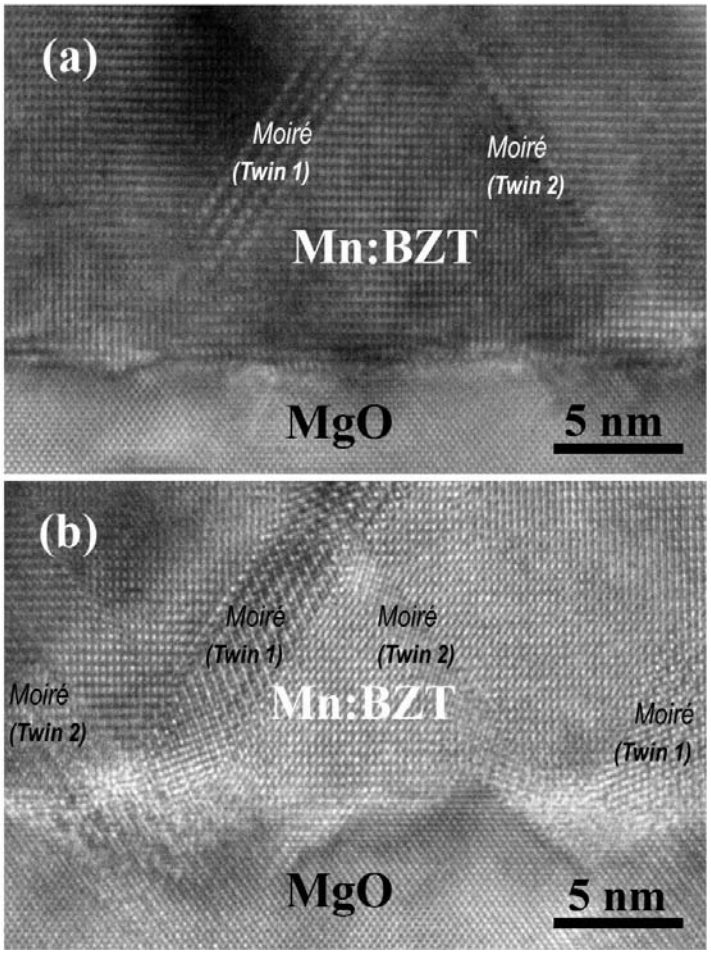

Figure 7.14 Cross-section HRTEM image of the interface between the first Mn:BZT layer and MgO substrate taken with the electron beam parallel to the MgO [110] direction: (a) ***ZL-4*** film; (b) ***ZL-8*** film.

In Figure 7.14 (b), the surface of MgO substrate in ***ZL-8*** film is much rougher than that of ***ZL-4*** film and therefore results in a large amount propagation of twin-induced domains with different crystallographic orientations (***Twin 1*** and ***Twin 2***). Thus, the density of multi-oriented twin domains grown from interface is much higher than that in Figure 7.14 (a), and the initial growth of twin domains are also frequently observed at near the interface region. The similar interface phenomenon was also observed in ***SL-4*** film. The morphology (including steps, kinks, terraces) of MgO substrate has a significantly influence on the growth of epitaxial films [23, 131, 225]. Therefore, the surface feature of MgO substrate at atomic scale is one of the key factors

for the generation of twin-coupled domain structures in the first Mn:BZT deposition layer of Mn:BZT//Mn:BST multilayer films. The investigations at film/substrate interface using HRTEM are consistent with the observations in SAEDs taken from the interface of Figures 7.13 (a-I)-(f-I), and also well explained the lower (00*l*) (*l*=1,2,3) reflection intensities from Mn:BZT and Mn:BST layers of ***ZL-8*** and ***SL-8*** films in X-ray θ-2θ scans showing in Figure 7.10 (b) and (e).

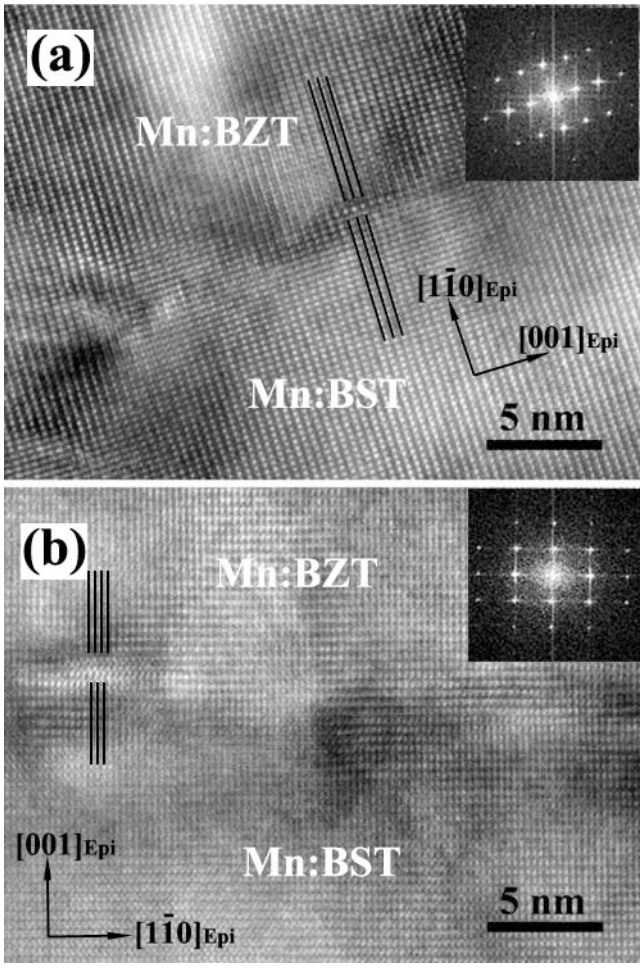

Figure 7.15 HRTEM images of Mn:BZT//Mn:BST layer interfaces viewed along [110] direction of MgO substrate: (a) a clear boundary in a {111} twin domain structure; (b) an interface region in epitaxial structure.

Figures 7.15 (a) and (b) show HRTEM images taken from the cross-section TEM foil with the electron beam parallel to the [110] direction of MgO substrate exhibiting several

different Mn:BZT//Mn:BST layer interface existing in ***ZL*** and ***SL*** multilayer films. Figure 7.15 (a) shows the layer interface in the {111} twin domain structure of multilayer films, which exhibits a clear atomic straight boundary between two layers. The lattice parameters measured from the inset FFT is 3.95 Å and 2.82 Å for top layer, and 3.90 Å and 2.81 Å at [110] zone axis for bottom layer, respectively. Thus, the top layer is referred to Mn:BZT layer and bottom layer is corresponding to Mn:BST layer. Similarly, the two layers are joined together at $\{1\bar{1}0\}_{Epi}$ planes with the lattice misfit calculated to be 1.28% of Mn:BZT with respect to Mn:BST along $[001]_{Epi}$ direction. The lattice misfit strain is released along $[001]_{Epi}$ direction with slightly shift and deformation at the boundary, as shown in Figure 7.15 (b).

Figure 7.15 (b) presents the layer interface between Mn:BZT and Mn:BST layers in the epitaxial structure. The lattice parameters estimated from inset FFT are 4.00 Å and 2.796 Å for top layer, and 3.957 Å and 2.758 Å for bottom layer, respectively. Therefore, the top layer is considered as Mn:BZT layer, and the bottom layer should be Mn:BST layer. The two layers are connected together at $\{001\}_{Epi}$ planes with the interface shown is Figure 7.15 (b) is not similar as observed in Figure 7.15 (a), showing a 2-4 nm length of strain area along growth direction to gradually release the lattice strain generated from the lattice constant difference within the two layers. The lattice mismatch along $[1\bar{1}0]_{Epi}$ direction calculated using FFT is 1.37% of Mn:BZT with respect to Mn:BST. The interfacial strain is finally released by shifting the $\{1\bar{1}0\}_{Epi}$ planes along $[1\bar{1}0]_{Epi}$ with half lattice spacing.

Figures 7.16 (a)-(f) are plan-view TEM images of ***ZL*** and ***SL*** films showing the microstructure of the top surface nanopillars. Grainy structures and nano pores were observed. Figure 7.16 (a) shows a larger grain size at the surface of ***ZL-4*** film with the size varying from 30 nm to 115 nm, compared to other ***ZL*** and ***SL*** films. The average grain size of ***SL-4*** film in Figure 7.16 (d) is around 50 nm, and the grain boundaries is more straight and well defined than

other films. The surface of ***SL-8*** film exhibits a grainy structure with more nanopores, while ***ZL-8***, ***ZL-16*** and ***SL-16*** films presents a more continuous layer with grains joining together leaving no/less gaps or pores. The average grain size of ***ZL-8***, ***SL-8***, ***ZL-16*** and ***SL-16*** is similar as ~ 60-70 nm.

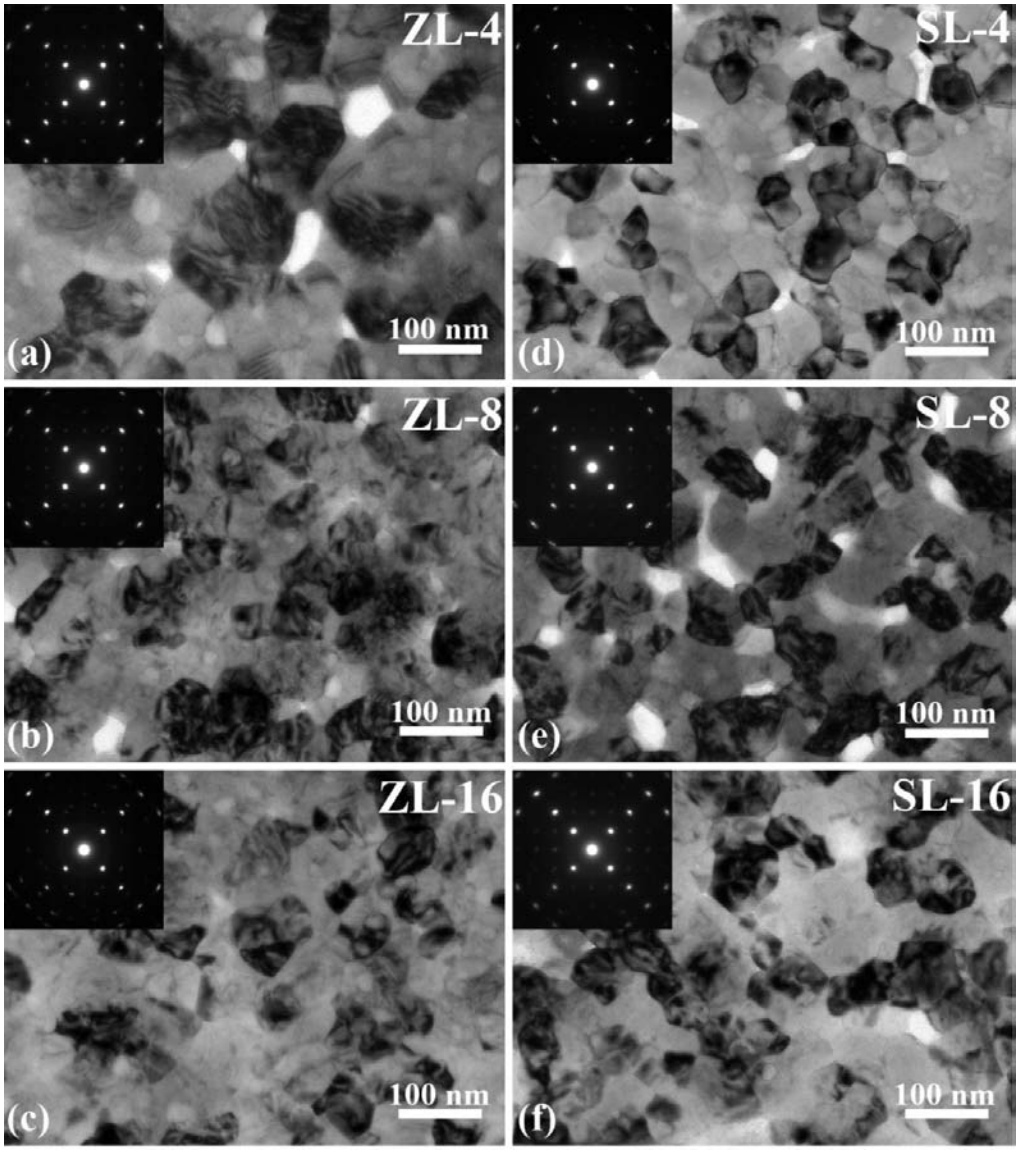

Figure 7.16 Plan-view TEM image from the surface layer of (a) ***ZL-4***; (b) ***ZL-8***; (c) ***ZL-16***; (d) ***SL-4***; (e) ***SL-8***; (f) ***SL-16***; and SAED patterns taken from the surface area covering many grains presenting in the inset of each corresponding image.

The inset SAEDs in Figures 7.16 (a)-(f) were taken from a surface area covering many grains. A similar clean single crystal electron diffraction pattern with preferred orientation can be observed regardless of the multi-grain structures in all ***ZL*** and ***SL*** films. The intensities of $(hh0)$ and $(h\bar{h}0)$ (h = ···-2, -1, 1, 2,···) diffraction spots are significantly stronger than that of the rest diffraction spots scattered from the epitaxial structure. It further proves that the top surface area of the ***ZL*** and ***SL*** multilayer films is mainly consisted of twin domain structures with very few epitaxial structures.

Figure 7.17 shows the mean modulus and hardness values for ***ZL***, ***SL*** multilayer films and Mn:BZT, Mn:BST single layer films using nano-indentation measurements. Figure 7.17 (a) and (b) show typical nano-indentation load-displacement curves for ***ZL*** and ***SL*** multilayer films, compared with Mn:BZT and Mn:BST single layer films, respectively. The differences in maximum load at 75 nm displacement, the slope of tangent line to the unloading section at the maximum loading point, and the residual penetration depth at zero load after unloading between each film exhibit different mechanical properties of hardness and elastic modulus for ***ZL*** and ***SL*** multilayer films. The average modulus and hardness value for ***ZL***, ***SL*** multilayer films and Mn:BZT, Mn:BST films are determined by applying corresponding loads with same 75 nm displacement/depth in total sixteen indentation tests of 4 × 4 array indents with 3μm× 3μm distance for each film, and shown in the histogram of Figure 7.17 (c).

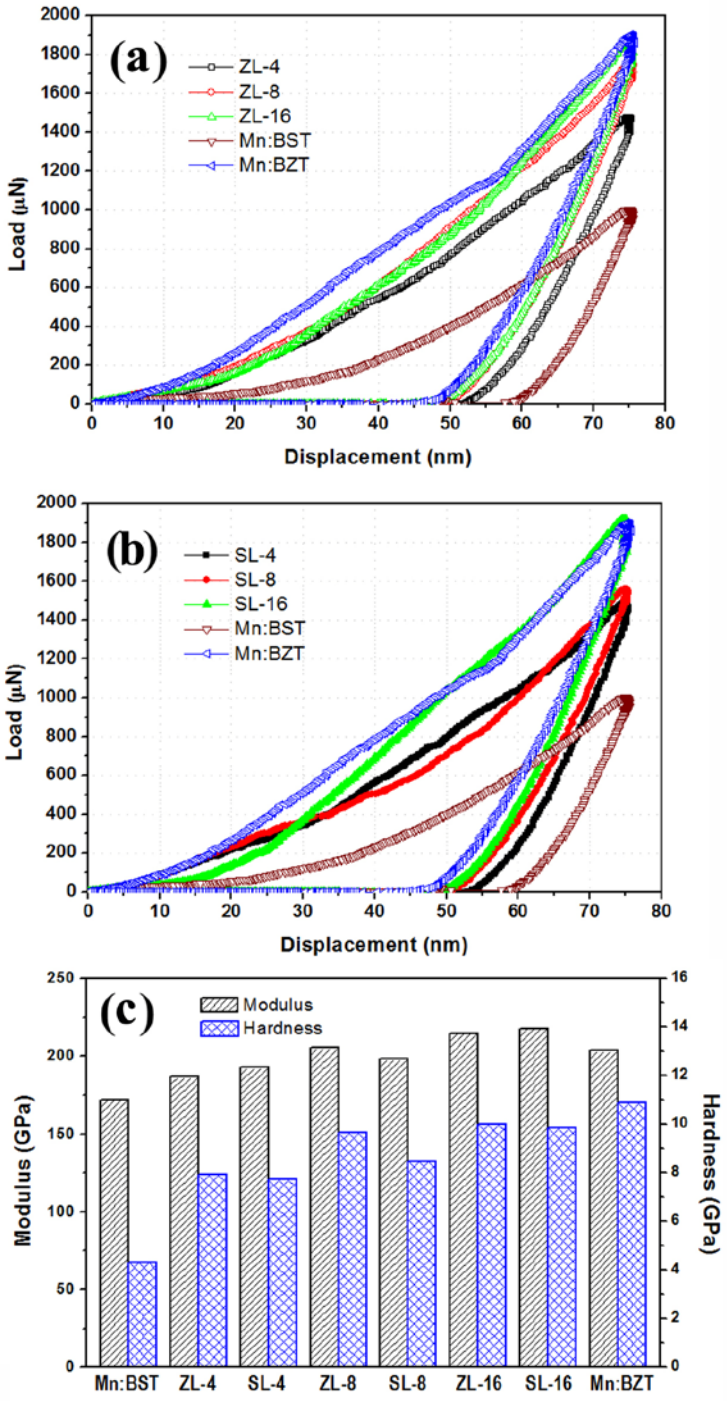

Figure 7.17 Nano-indentation measurements with the same 75 nm displacement, showing (a) typical load-displacement curves of ***ZL-4*** (black), ***ZL-8*** (red), ***ZL-16*** (green) multilayer films and (b) load-displacement curves of ***SL-4*** (black), ***SL-8*** (red), ***SL-16*** (green) multilayer films with Mn:BZT (blue) and Mn:BST (brown) films; (c) mean modulus and hardness histogram for ***ZL*** and ***SL*** multilayer film, comparing with Mn:BZT and Mn:BST single layer film.

Thus, Figures 7.17 (a)-(c) present that the Mn:BST film has the lowest modulus and hardness value of 172.23 GPa and 4.33 GPa, however Mn:BZT has the highest hardness of 10.89 GPa, and a mean modulus of 203.58 GPa. The possible determinant for higher hardness and modulus of Mn:BZT film, compared to Mn:BST is the formation of {111} and {110} multi-oriented twin domains nanopillar structure [14-16]. Since the similar twin-couple domain structures were observed in all multilayer films in TEM studies of Figure 7.12; Figure 7.13; and Figure 7.16, the modulus and hardness of the multilayer films are enhanced to a certain extent, comparing with epitaxial Mn:BST film. In ***ZL*** multilayer films, the modulus and hardness value is gradually increased with the increasing of deposition period number N, and therefore ***ZL-16*** film showing the highest modulus of 215.29 GPa and hardness of 9.91 GPa than ***ZL-4*** and ***ZL-8***. The mean modulus for ***ZL-4*** and ***ZL-8*** film is 187.19 GPa and 208.15 GPa, respectively. The mean hardness for ***ZL-4*** and ***ZL-8*** film is 7.86 GPa and 9.79 GPa, respectively. Similarly, the modulus and hardness is increased along with larger N in ***SL*** multilayer films, ***SL-16*** presenting the highest modulus of 219.21 GPa and hardness of 9.81 GPa than ***SL-4*** and ***SL-8***. The mean modulus for ***SL-4*** and ***SL-8*** film is 200.75 GPa and 187.45 GPa, respectively. The mean hardness for ***SL-4*** and ***SL-8*** film is 7.55 GPa and 8.67 GPa, respectively. Since all ***ZL*** and ***SL*** multilayer films exhibit epitaxial twin domain dominating structures, porous or gaps between nanopillars, similar nanopillar width and surface roughness, the slightly increase of modulus and hardness in ***ZL-8*** and ***SL-8*** is possible resulted from the higher density of twin domains due to the directly numerous growth from MgO substrate compared to ***ZL-4*** and ***SL-4*** films, in which the epitaxial structure maintain the majority until middle area, as shown in Figure 7.13 (a-I); (a-II); (b-I) and (b-II). The possible influence leading to higher hardness and Young's modulus in ***ZL-16*** and ***SL-16*** is considered to be contributed from the residual interface strains of total 31 Mn:BZT-Mn:BST or Mn:BST-Mn:BZT layer interfaces, which is much more than that of ***ZL-4***, ***SL-4***, ***ZL-8*** and ***SL-8*** films.

7.4 Summary

In this Chapter, $[Mn:BZT//Mn:BST]_N$ multilayer films with various deposition rates, deposition period numbers N, and deposition time ratios of single Mn:BZT and Mn:BST layer were investigated. Their impact on the growth, interfaces and microstructure of the multilayer films were intensively studied.

In summary, it can be concluded that:

(1) Both four-layered $[Mn:BZT//Mn:BST]_2$ films with different deposition rates were successfully grown on (001) MgO substrate using PLD. The ***FL-S*** film has a rougher surface than the ***FL-F***. The first two layers next to substrate in the ***FL-S*** film have a continuous layer structure that is basically epitaxially grown on the substrate. The first Mn:BZT layer has a single oriented crystal structure, an in-plane lattice mismatch of ~ -3.70%, and an atomically sharp interface with respect to the substrate. Twin-induced domains started to be formed in the second Mn:BST layer. The top two layers have a columnar structure with an average size of ~ 70 nm and consist of epitaxial single crystal structure and some polycrystalline structures. The columnar structures in these two layers are tightly attached to their adjacent ones without leaving any gaps or porosity. The ***FL-F*** film has a discrete needle-like nanopillar structure running through the entire film. The nanopillars are separated by an amorphous structure, have a uniform width of 30-40 nm and are aligned along the growth direction of the film. The first Mn:BZT layer consists of both epitaxial and twin-coupled domain structures induced by sharing their {111} and {110} planes. The epitaxial Mn:BZT first layer has an in-plane lattice mismatch of -3.34% with respect to MgO. The second, third and fourth layers of the ***FL-F*** have textured structures of {111} twin domains. The ***FL-S*** film exhibits a hardness of 6.70 GPa and a modulus of 193.37 GPa, larger than those of ***FL-F*** film (2.25 GPa and 104.58 GPa, respectively).

(2) Two series $[Mn:BZT//Mn:BST]_N$ multilayer films with the formula of $[(Mn:BZT)_3:(Mn:BST)_1]_N$ (N=4, 8, 16) and $[(Mn:BZT)_1:(Mn:BST)_3]_N$ (N=4, 8, 16) were successfully fabricated on (001) MgO substrate using PLD. ***ZL-4***, ***SL-4***, ***ZL-8***, ***SL-8*** and ***SL-16***

films show a columnar structure through the entire film from the first layer close to substrate to the top surface, with a column lateral size varied from 30-150 nm. ***ZL-16*** is composed with two structures of a continuous layer structure formed from interface up to the five or six deposition periods, and followed by a columnar structure formed until the top surface. The ***SL-16*** film has a rougher surface with average roughness of 12.496 nm compared to other multilayer film. Twin-induced domain structure was initially formed from the first Mn:BZT layer next to MgO substrate in all ***ZL*** and ***SL*** films. ***ZL-8*** and ***SL-8*** films show higher proportion of twin domains at close to substrate area than ***ZL-4***, ***ZL-16***, ***SL-4*** and ***SL-16*** films since the rougher film/substrate interfaces in ***ZL-8*** and ***SL-8*** films provide more opportunities to grow {111} twin structure. However, the clean and flat film/substrate interfaces in ***ZL-4***, ***ZL-16***, ***SL-4*** and ***SL-16*** films significantly help the epitaxial growth and keep the epitaxial structure dominated even to the intermediate area of the entire film. During the growth of ***ZL*** and ***SL*** films, {111} and {110} twin-coupled domains were expanded, while the epitaxial structure was reduced. And finally, the twin domains structure dominated the top surface area were observed in all ***ZL*** and ***SL*** multilayer films. Measured from the electron beam parallel to $[100]_{MgO}$, the in-plane lattice mismatch between Mn:BZT layer and MgO substrate for ***ZL*** films is about -3.70% (***ZL-4***), -3.57% (***ZL-8***), -3.98% (***ZL-16***), and the in-plane lattice mismatch of Mn:BST layer with respect to MgO substrate is about -5.49% for ***SL-4***, -5.26% for ***SL-8***, -5.22% for ***SL-16***, respectively. ***ZL-16*** and ***SL-16*** show higher average modulus of 216.29 GPa and 219.21 GPa, and hardness of 9.91 GPa and 9.81 GPa, respectively, compared with other ***ZL*** and ***SL*** films which is considered to be contributed from the residual layer-to-layer interface strains.

CHAPTER 8

CONCLUSIONS AND FUTURE WORK

8.1 Conclusions

Barium titanate is a good ferroelectric perovskite material which is widely used in practical applications. The Barium titanate thin films have great potential in microelectronic devices, memories, capacitors, and microwave device applications. In the barium titanate system, different doping position will tremendously change the properties of the whole system. Besides, in the barium titanate based films, the interfaces generated between film/substrate during film growth, sublayers and domains strongly effect on the properties of the films. Thus, this work was motivated and focused on the growth mechanism, microstructures and interface structures of barium titanate based thin films using the study system of perovskite barium titanate thin film. $BaTiO_3$ were successfully fabricated using RF magnetron sputtering. The epitaxial growth and nanodomain structure have been investigated in detailed. The doped barium titanate films (BST and BZT) with different dopant (Sr^{2+} and Zr^{4+}) have been systematically studied in terms of microstructures, doping effect, interface effect, and growth mechanisms. The BST epitaxial films grown on miscut MgO substrate with 1^o, 3^o, 5^o angles provided the opportunity to study substrate surface morphology effects on the film microstructure and dielectric property. The BZT and 2% Mn doped BZT grown on MgO substrate presented the formation of {111} and {110} twin coupled domain structures induced from epilayer. Consequently, epitaxial structure, layer interfaces and mechanical properties of the multilayer films composed with Mn doped BZT and Mn doped BST layers were discussed at different deposition rates and deposition periods.

This work developed a fundamental understanding of microstructure, interfaces and growth mechanism of perovskite barium titanate based thin films. The primary conclusions of this work are as follows:

8.1.1 Epitaxial Growth and Microstructure of BTO Thin Films Deposited on MgO Substrate Using RF Magnetron Sputtering

Epitaxial $BaTiO_3$ (BTO) thin films have been successfully fabricated on (001) MgO substrate using a home-made RF magnetron sputtering system. The as-deposited BTO thin film was ~200 nm thick and shows a smooth surface and rough film/substrate interface. The BTO thin film exhibits a tetragonal structure with a_{BTO} = 4.02Å, c_{BTO} = 4.11 Å and highly epitaxial quality with respect to MgO substrate as an orientation relationship of $(001)_{BTO}//(001)_{MgO}$ and $<100>_{BTO}//<100>_{MgO}$.

Nanodomain structures with a domain size varying from 3 to 20 nm have been investigated in epitaxial BTO films. Cross-section TEM and 2-D interface studies present a smaller lattice misfit near film/substrate interface region than the region away from interface. Such lattice misfit differences in different regions of BTO film, and the formation of the nano domains are due to the relatively rougher surface composed with steps, terraces and kinks of MgO substrate generated by surface plasma cleaning process.

8.1.2 Discovery of Two New $BaTiO_3$ Induced Phases Fabricated Using RF Magnetron Sputtering

Two new phases of Γ_γ ($Ba_{10}Ti_8O_{26}$) and H_β ($Ba_8Ti_8O_{24}$) were formed on MgO substrate using RF magnetron sputtering. Both phases exhibit ferroelectric properties and the polarization vector of the Γ_γ phase is more easily switched over under an external electrical field that of H_β phase. The atomic structures of the two new phases were determined and examined using electron diffraction pattern analysis, HRTEM images and corresponding calculated results. The Γ_γ phase ($Ba_{10}Ti_8O_{26}$ or $(Ba_5Ti_4O_{13})_2$) has a monoclinic structure with a space group of ***Cm*** (No. 8, *c*-unique axis) and lattice parameters of a=16.49 Å, b=8.94 Å, c=3.94 Å and γ=77°. The H_β

phase ($Ba_8Ti_8O_{24}$ or $(BaTiO_3)_8$) has a monoclinic structure with a space group of ***Cm*** (No. 8, *c*-unique axis) and lattice parameters of a = 17.88Å, b = 7.21Å, c = 3.94 Å and γ = 82°. In the as-deposited films, eight domains with four different oriented Γ_γ domains and four different oriented H_β domains are coexisted. The four domains of each phase are related to each other by either a 90° rotation operation around the [001] axis or a mirror plane operation. Both new structures are epitaxially grown on the MgO substrate with the following primary orientation relationship:

(1) $(001)_{\Gamma_\gamma}$ // $(001)_{MgO}$, $(820)_{\Gamma_\gamma}$ // $[100]_{MgO}$ and $[2\bar{4}0]_{\Gamma_\gamma}$ // $[010]_{MgO}$, for Γ_γ.

(2) $(001)_{H_\beta}$ // $(001)_{MgO}$, $[820]_{H_\beta}$ // $[100]_{MgO}$ and $[\bar{4}30]_{H_\beta}$ // $[010]_{MgO}$, for H_β.

8.1.3 The Effect of Substrate Surface Miscut on Interface Structure of BST Thin Films

Cross-section and plan-view TEM have been carried out to investigate the microstructure and two dimensional (2-D) interface structure of BST film grown on miscut MgO substrates with different miscut angles. The BST films grown on the substrate with an actual miscut angle of 1.2º, 3.5º, and 5.3º have a lattice mismatch of -5.4%, -5.7% and -5.5% with respect to MgO substrate, respectively, observed in on dimensional (1-D) interface space (Cross-section TEM).

Plan-view TEM studies of the BST film/MgO interface exhibit significant structural difference in the two dimensional (2-D) interface space: (i) the BST films grown on the substrate with a miscut angle of 1.2º, 3.5º, and 5.3º have a lattice mismatch of -5.6%, -6.0% and -5.7% with respect to MgO substrate, respectively, larger than the value from cross-section TEM; (ii) the size of the commensurate domains at the interface is about 30 to 40 nm for the films grown on the 1.2º and 5.3º miscut substrates, larger than that for the film grown on the 3.5º miscut, which is about 10 to 20 nm.

The BST films grown on 1.2º and 5.3º miscut substrates show about 30% higher dielectric constant and dielectric tunability than those for the film grown on 3.5º miscut

substrate. But, the BST film grown on 3.5º miscut substrate possesses higher average modulus and hardness value than those of the films grown on 1.2º and 5.3º miscut substrates. The differences on the interface domain structure, dielectric properties and mechanical properties in BST films grown on miscut MgO substrate can be resulted from the differences in steps, terraces and kinks on substrate surface, which are induced by various miscut angles. Those steps, terraces and kinks produce different commensuration domain structures at the 2-D interface plane, and therefore greatly modified the microstructure and properties of the BST films. Thus, substrate miscut can serve as a nanofabrication tool to locally modify the epitaxial at atomic level.

8.1.4 Formation and Growth Mechanism of Twin Domain Structures in BZT and Mn:BZT Thin Films

BZT and Mn:BZT thin films grown on (001) MgO substrate fabricated using PLD, is composed with two structure layers: (i) a epitaxial layer of pseudo-cubic perovskite structure at near to interface and followed by (ii) multi-oriented twin-coupled nanopillars dominated at the top surface of the film. The average lateral size of the nanopillars in BZT films is ~130 nm, four times larger than that in the Mn:BZT films (~35 nm).

Four types of twin domain structures were formed by coherently joining their {111} planes with respect to the epilayer and aligning their <110> directions parallel to the <110> axes of the epilayer. In addition to the {111}, the twin-coupled structures including epitaxial grain and twin domains can also coexist by sharing their {110} planes as the common plane. The joining of the twin-coupled domains on the {110} twin boundary plane is accommodated by forming a two-dimensional super cell structure (a = 7.02 Å and b = 9.92 Å) on the twin boundary plane. Structure evolution from the epitaxial layer to the nanopillar structures is accomplished by alternatively introducing twin boundaries on {111} and {110} planes along the growth direction.

The formation of the twin boundaries in BZT is possibly due to the occurrence of the larger Zr^{4+} ions on certain positions to form Zr^{4+} rich expanded (110) and (111) planes which are energetically favorable for forming twin boundaries. Mn doping in BZT films makes additional

contribution to the expansion of the (110) and (111) planes due to the larger Zr^{4+} and Mn^{2+} atoms to form more twin boundaries and smaller twin-coupled nanopillars and results in the shifting of the peak in Raman spectrum to the lower wavenumbers and improved dielectric properties, and therefore possess higher modulus and hardness compared to BZT film.

Alternatively formation of the twin boundaries on {111} and {110} planes along the growth direction results in the lateral size reduction of the epitaxial grains and eventually leads the epitaxial grains to be completely transformed into twin-coupled nanopillars.

8.1.5 Microstructure and Interfaces of [Mn:BZT//Mn:BST]$_N$ Multilayer Films

Four-layered [Mn:BZT//Mn:BST]$_2$ films with different deposition rates (***FL-S*** and ***FL-F***) were successfully grown on (001) MgO substrate using PLD. The ***FL-S*** film has rougher surface than the ***FL-F***. The first deposition layer is Mn:BZT layer for both films. The ***FL-S*** film exhibits a hardness of 6.70 GPa and a modulus of 193.37 GPa, larger than those of ***FL-F*** film (2.25 GPa and 104.58 GPa, respectively). The first two layers next to substrate in the ***FL-S*** film have a continuous layer structure and epitaxially grown on the substrate. The first Mn:BZT layer has a single oriented crystal structure, an in-plane lattice mismatch of ~-3.70%, and an atomically sharp interface with respect to the substrate. Twin-induced domains started to be formed in the second Mn:BST layer. The top two layers have a columnar structure with an average size of ~ 70 nm and consist of epitaxial single crystal structure and some polycrystalline structures. The columnar structures in top two layers are tightly attached without gaps or porosity. The ***FL-F*** film shows a needle shape nanopillar structure through the entire film. The nanopillars with a uniform width of 30-40 nm are separated by an amorphous structure and aligned along the growth direction of the film. The first Mn:BZT layer consists of both epitaxial and {111}/{110} twin-coupled domain structures. The epitaxial Mn:BZT first layer has an in-plane lattice mismatch of -3.34% with respect to substrate. The second, third and fourth layers of the ***FL-F*** have textured structures of {111} twin domains.

Two series $[Mn:BZT//Mn:BST]_N$ multilayer films with the formula of $[(Mn:BZT)_{7.5}:(Mn:BST)_{2.5}]_N$ (N=4, 8, 16) and $[(Mn:BZT)_{2.5}:(Mn:BST)_{7.5}]_N$ (N=4, 8, 16) on (001) MgO substrate have been investigate in terms of microstructures, layer interfaces as well as mechanical properties. ***ZL-4***, ***SL-4***, ***ZL-8***, ***SL-8*** and ***SL-16*** films show a columnar structure through the entire film with a column lateral size varied from 30-150 nm, while ***ZL-16*** is composed with two structures of a continuous layer structure at close to interface and followed by a columnar structure at close to surface. Twin-induced domain structure formed from the first Mn:BZT layer next to MgO substrate have been observed in all ***ZL*** and ***SL*** films. ***ZL-8*** and ***SL-8*** films show higher proportion of twin domain structures at close to interface region than ***ZL-4***, ***ZL-16***, ***SL-4*** and ***SL-16*** films since the rougher film/substrate interfaces in ***ZL-8*** and ***SL-8*** films provide more opportunities to grow {111} twin structure. During the growth of ***ZL*** and ***SL*** films, {111} and {110} twin-coupled domains were expanded, while the epitaxial structure was reduced. Thus, the twin domains structure dominated the top surface area were observed in all ***ZL*** and ***SL*** multilayer films. ***ZL-16*** and ***SL-16*** exhibit higher average modulus of 216.29 GPa and 219.21 GPa, and hardness of 9.91 GPa and 9.81 GPa, respectively, compared with other ***ZL*** and ***SL*** films due to the larger residual layer-to-layer interface strains.

8.2 Future Work

The perovskite epitaxial oxide thin films possess various novel properties and are considered as one of the most important material families to meet challenges in advanced material research and nanotechnology. Since the great potential of perovskite oxides in semiconductor and microelectronic devices industry, more work related this field can be focused on:

(1) Magetron sputtering is a low-cost but very effective depositon method to deposite oxide thin films over a large deposition area. During the deposition, the vacumm level, pressures, especially oxygen partial pressure, deposition temperature, Ar gas flow rate, target/substrate distance and/or angles can tremendously change the morphology, composition,

microstructure and the structure of as-deposited films. Thus, more interesting materials with functional properties can be produced by controlling the deposition parameters and deposition conditions in magnetron sputtering system. For example, the as-deposited films composed with two new BTO induced phases have been successfully fabricated on MgO substrate using our home-made magnetron sputtering system by sputtering a $BaTiO_3$ target. The atomic structures for the two new phases have been determined and examined. The initial study shows very interesting electric property which is rarely seen in perovskite $BaTiO_3$ films. Although the mechanisms for growing such complicated sturcutes and their novel electric property is needed to further explore, magnetron sputtering provides a method to fabricate more novel materials with designed functional properties.

(2) The interface effect study on the microstructure and properties of barium titanate based thin films in this study, provides a fundamental knowledge of the relationship between film preparation-microstructure-property. The interface stucture generated between film/substrate during the film growth can dramatically determine the microstructure and properties of thin films. The introduction of interface engineering can control and design the structure and properties in thin films, especially in multilayer and superlattice systems, to meet the as-expected requirements. More epitaxial multifunctional oxide films or compositional/structural gradient films can be achieved by carefully controlling and modifying the film/substrate interface and/or layer interfaces. Besides the BST, BZT and $[Mn:BZT//Mn:BST]_N$ epitaxial films introduced in this work, the attemptions for producing epitaxial heterostructure films with multiferroic properties can be achieved using interface engineering in the future.

APPENDIX A

LIST OF JOURNAL PUBLICATIONS

1. Discovery of Two New Superstructures in Epitaxial Barium Titanate Thin Films, ***J. He***, J.C. Jiang, E.I. Meletis, Manuscript.

2. Microstructure and Nano-mechanical Properties of Mn-doped $(Ba,Sr)TiO_3$//$Ba(Zr,Ti)O_3$ Layered Films on MgO, ***J. He***, J.C. Jiang, E.I. Meletis, Integrated Ferroelectrics, submitted.

3. Nanodomain and Interface Structure in Epitaxial $BaTiO_3$ Thin Films on MgO Deposited by Magnetron Sputtering, ***J. He***, H.Q. Jiang, J.C. Jiang, E.I. Meletis, Journal of Materials Science 47 (2012) 2763-2769.

4. Self-patterned Nano Structures in Structurally Gradient Epitaxial $La_{0.5}Ba_{0.5}CoO_3$ Films, ***J. He***, J.C. Jiang, J. Liu, M. Liu, G. Collins, C.R. Ma, C.L. Chen, E. I. Meletis, Thin Solid Films 519 (2011) 4371-4376.

5. Evolution of Nano-fingers in Epitaxial Mn-doped $Ba(Zr,Ti)O_3$ Thin Films Driven by {110} Twin Boundaries, ***J. He***, J.C. Jiang, E.I. Meletis, M. Liu, J. Liu, G. Collins, C.R. Ma, C.L. Chen, A. Bhalla, Philosophical Magazine Letters 91 (2011) 361-374.

6. Refining of Nanopillars Induced by Mn-doping in Epitaxial $Ba(Zr,Ti)O_3$ Thin Films, ***J. He***, J.C. Jiang, E. I. Meletis, M. Liu, G. Collins, C. R. Ma, C. L. Chen, A. Bhalla, Integrated Ferroelectrics 131 (2011) 72-81.

7. Interface Engineered Ferroelectric $BaTiO_3$//$SrTiO_3$ Heterostructures with Anomalous Clamped Polarization on Si (100), M. Liu, G. Collin, E. Silva, C.R. Ma, J. Liu, C.L. Chen, ***J. He***, J.C. Jiang, E.I. Meletis, S.W. Qu, Q.Y. Zhang, A. Bhalla, Integrated Ferroelectrics 131 (2011) 89-94.

8. Growth Microstructure and Properties of Epitaxial $La_{1-x}Sr_xMnO_3$ Thin Films on Various Substrates Using RF Magnetron Sputtering, Y. Fang, V.R. Sakhalkar, ***J. He***, H.Q. Jiang, J.C. Jiang, E.I. Meletis, Journal of Nano Research 14 (2011) 83-93.

9. Microwave Dielectric Properties with Optimized Mn-doped $Ba_{0.6}Sr_{0.4}TiO_3$ Highly Epitaxial Thin films, M. Liu, C. Ma, G. Collins, J. Liu, C.L. Chen, L. Shui, H. Wang, C. Dai, Y. Lin, ***J. He***, J.C. Jiang, E.I. Meletis, Q.Y. Zhang, Crystal Growth and Design 10 (2010) 4221-4223.

10. Photoluminescence and Extinction Enhancement from ZnO Films Embedded with Ag nanoparticles, M. Liu, S.W. Qu, W.W. Yu, S.Y. Bao, C.Y. Ma, Q.Y. Zhang, ***J. He***, J.C. Jiang, E.I. Meletis, C.L. Chen, Applied Physics Letters 97 (2010) 231906.

11. Epitaxial Nature and Transport Properties in $LaBaCo_2O_{5.5+\delta}$ Thin Films, J. Liu, M. Liu, G. Collins, C.L. Chen, X.N. Jiang, W.Q. Gong, A.J. Jacobson, ***J. He***, J.C. Jiang, E.I. Meletis, Chemistry of Materials 22 (2010) 799-802. [Cover page of Special Issue: Materials of Energy Research]

12. Magnetic and Transport Properties of Epitaxial $(LaBa)CoO_{5.5+\delta}$ Thin Films on (001) $SrTiO_3$, M. Liu, J. Liu, G. Collins, C.R. Ma, C.L. Chen, ***J. He***, J.C. Jiang, E.I. Meletis, A.J. Jacobson, Q.Y. Zhang, Applied Physics Letters 96 (2010) 132106.

13. Ferroelectric $BaTiO_3$ Thin Films on Ti Substrate Fabricated Using Pulsed-laser Deposition, ***J. He***, J. C. Jiang, E. I. Meletis, J. Liu, G. Collins, C. L. Chen, B. Lin, V. Giurgiutiu, R.Y. Guo and A. Bhalla, Journal of Nanoscience and Nanoengineering 10 (2010) 1-6.

14. Two-dimensional Interface Structures of Epitaxial (Ba,Sr)TiO_3 film on Miscut (001) MgO, J.C. Jiang, ***J. He***, E.I. Meletis, C. L. Chen, Y. Lin, J. Horwitz, and A. J. Jacobson, Thin Solid Films 518 (2009) 147-153.

15. Twin-coupled Domain Structures in Epitaxial Relaxor Ferroelectric Ba(Zr,Ti)O_3 Thin Films on (001) MgO Substrate, ***J. He***, J. C. Jiang, E.I. Meletis, J. Liu, G. Collins, C. L. Chen, and A. Bhalla, Philosophical Magazine Letters 89 (2009) 493-503.

16. Integration of Ferroelectric $BaTiO_3$ Thin Films Directly on Ni and Ti Metallic Tapes for Structural Health Monitoring Systems and Energy Harvest Applications, J. Weaver, Z. Yuan, J. Liu, G. Collins, C.L. Chen, J.C. Jiang, ***J. He***, E.I. Meletis, R.Y. Guo, A. Bhalla, B. Lin, V. Giurgiutiu and M.W. Cole, Integrated Ferroelectrics 100 (2008) 61-71 (invited).

17. Two-dimensional Modulated Interfacial Structures of Highly Epitaxial Ferromagnetic (La,Ca)MnO_3 and Ferroelectric (Pb,Sr)TiO_3 Thin Films on (001) MgO, J. C. Jiang, ***J. He***, E.I. Meletis, J. Liu, Z. Yuan, and C. L. Chen, Journal of Nano Research 3 (2008) 59-66.

18. Reinforcing Copper Matrix Composites Through Molecular-level Mixing of Functionalized Nanodiamond by Co-deposition Route, ***J. He***, N.Q. Zhao, C.S. Shi, X.W. Du, J.J. Li, P. Nash, Materials Science and Engineering A 490 (2008) 293-299.

APPENDIX B

CONFERENCE PUBLICATIONS AND PRESENTATIONS

1. Growth Mechanism of Multi-oriented Twin Domain Structure in Epitaxial $Ba(Zr,Ti)O_3$ Thin Films, ***J. He***, J.C. Jiang, E.I. Meletis, J. Liu, G. Collins, C.L. Chen, A. Bhalla, ASM 2nd North Texas Inter-University Student Symposium, Oral Presentation, April 13, 2011, University of Texas at Arlington, Texas, USA.

2. Growth Mechanism of Epitaxial Perovskite-type Oxide Thin Films, ***J. He***, J.C. Jiang, E.I. Meletis, J. Liu, G. Collins, C.L. Chen, A. Bhalla, The Annual Celebration of Excellence by Students (ACES) Symposium, Oral Presentation, March 24, 2011, University of Texas at Arlington, Texas, USA.

3. Self-patterned Nano Structures in Structurally Gradient Epitaxial $La_{0.5}Ba_{0.5}CoO_3$ Films, ***J. He***, J.C. Jiang, E.I. Meletis, J. Liu, M. Liu, G. Collins, C.R. Ma and C.L. Chen, Materials Science and Technology (MS&T) 2010 Conference and Exhibition, Oral Presentation, October 17-21, 2010, Houston, Texas, USA.

4. Growth, Microstructure and Properties of Epitaxial $La_{1-x}Sr_xMnO_3$ Thin Films on Various Substrates Using RF Magnetron Sputtering, Y. Fang, V.R. Sakhalkar, ***J. He***, H.Q. Jiang, J.C. Jiang and E.I. Meletis, Materials Science and Technology (MS&T) 2010 Conference and Exhibition, Poster Paper, October 17-21, 2010, Houston, Texas, USA.

5. Interfacial Structures of Perovskite Epitaxial Films, J.C. Jiang, ***J. He***, C.L. Chen, E.I. Meletis, XVIII International Materials Research Congress 2009, Symposium: Ferroelectricity and Piezoelectricity: Materials, Devices, and Applications, Cancun, Mexico, 16 - 21 August 2009. (invited)

6. Graded Structures In Epitaxial Relaxor Ferroelectric $Ba(Zr,Ti)O_3$ Films, ***J. He***, J. C. Jiang, J. Liu, G. Collins, C. L. Chen, A. Bhalla, E.I. Meletis, XVIII International Materials Research Congress 2009, Symposium: Nanostructured Materials and Nanotechnology, Cancun, Mexico, 16 - 21 August 2009.

7. Effects of Substrate Miscut on the Two-Dimensional Interface Structure of Epitaxial $(Ba,Sr)TiO_3/MgO$, J. Jiang, ***J. He***, E. Meletis, and C. Chen, Materials Science and Technology (MS&T) 2009 Conference and Exhibitor, Ceramic and Glass Materials: Multifunctional Oxide: Interface in Epitaxial Oxide Thin Films. October 25-29, 2009, Pittsburgh, Pennsylvania, USA, pp.87.

8. Multi-Oriented Twin-Coupled Domain Structures in Epitaxial $Ba(Zr,Ti)O_3$ Films, ***J. He***, J.C. Jiang, E.I. Meletis, J. Liu, G. Collins, C.L. Chen, A. Bhalla, Materials Science and Technology (MS&T) 2009 Conference and Exhibitor, Ceramic and Glass Materials: Multifunctional Oxide: Microstructure and Multilayer. October 25-29, 2009, Pittsburgh, Pennsylvania, USA, pp.126.

9. Composite-like Structure in the Epitaxial Relaxor Ferroelectric $Ba(Zr,Ti)O_3$ Thin Films on (001) MgO Substrate, ***J. He***, J.C. Jiang, E.I. Meletis, C.L. Chen and A. Bhalla, Materials Science and Technology (MS&T) 2008 Conference and Exhibitor, Electronic and magnetic properties: Fabrication, Microstructures and Interfacial Properties of Multifunctional Oxide Thin Films: Microstructure and Dielectric Properties of Oxide Films. October 5-9, 2008, Pittsburgh, Pennsylvania, USA, pp.261.

10. Fabrication and microstructure of the $BaTiO_3$ thin films on Ti substrate, J.C. Jiang, ***J. He***, E.I. Meletis, Z. Yuan, J. Liu, J. Weaver, C.L. Chen, B. Lin, V. Giurgiutiu, R. Guo, A. Bhalla, Materials Science and Technology (MS&T) 2008 Conference and Exhibitor, Electronic and magnetic properties: Fabrication, Microstructures and Interfacial Properties of

Multifunctional Oxide Thin Films: Preparation and Properties of Oxide Films. October 5-9, 2008, Pittsburgh, Pennsylvania, USA, pp.200.

11. Interfacial Structures of Epitaxial Perovskite Oxide Thin Films on (001) MgO Substrate, J.C. Jiang, ***J. He***, E.I. Meletis, J. Liu, Z. Yuan, and C.L. Chen, Materials Science and Technology (MS&T) 2008 Conference and Exhibitor, Electronic and magnetic properties: Fabrication, Microstructures and Interfacial Properties of Multifunctional Oxide Thin Films: Microstructures, Defects, and Interfaces. October 5-9, 2008, Pittsburgh, Pennsylvania, USA, pp. 227.

12. Microstructure of Ferroelectric $BaTiO_3$ Thin Films on Ti Substrate, ***J. He***, J.C. Jiang, E.I. Meletis, Z. Yuan, J. Liu, J. Weaver, C.L. Chen, B. Lin, V. Giurgiutiu, R.Y. Guo and A. Bhalla, Proceedings of Microscopy and Microanalysis, Microscopy Society of America, Vol. 14, Supplement 2, pp.346-347, Albuquerque, New Mexico, August 3-7, 2008.

13. Plan-view TEM Study on Interfacial Structure of (La,Ca)MnO_3/MgO, J.C. Jiang, ***J. He***, E.I. Meletis, Z. Yuan and C.L. Chen, Proceedings of Microscopy and Microanalysis, Microscopy Society of America, Vol. 14, Supplement 2, pp.232-233, Albuquerque, New Mexico, August 3-7, 2008.

14. Two-dimensional Interfacial Structures of Epitaxial Perovskite Structure Thin Films on MgO, J.C. Jiang, ***J. He***, E.I. Meletis and C.L. Chen, International Conference from Nanoparticles & Nanomaterials to Nanodevices & Nanosystems, June 16-18, 2008, Halkidiki, Greece.

REFERENCES

1. Landolt-Bornstein (1981), in Numerical Data and Functional Relationships in Science and Technology, Vol. 16, K.-H. Hellwege and A.M. Hellwege (Eds.), Springer, Berlin.

2. K. H. Hellwege and A. M. Hellwege, (1981), “Ferroelectrics and Related Substances”, subvolume a: Oxides, in Landolt-Bornstern Numerical Data and Functional Relationships in Science and Technology, Vol. 16. K.-H. Hellwege (Ed.), Springer, Berlin.

3. M.E. Lines and A.M. Glass, (1977), “Macroscopic and Phenomenology”, in Principles and Applications of Ferroelectrics and Related Materials, Clarendon, Oxford, pp. 59-86.

4. F. Jona and G. Shirane, Ferroelectric Crystals. Pergamon Press, New York, (1962).

5. H.D. Megaw, Ferroelectricity in Crystals. Methuen London, (1957).

6. C.Z. Cao, “Functional Thin Films and Functional Materials” Chapter 3: Ferroelectric Thin Films and Applications, D.L. Shi (Ed.), Springer, Berlin, (2003)

7. R.C. Buchanan (Ed.), Ceramic Materials for Electronics: Processing, Properties, and Applications, 2nd. Edition, (Marcel Dekker, New York, 1991)

8. R.E. Cohen, Nature, 358,136 (1992)

9. B. Jaffe, W.R. Cook and H. Jaffee, Piezoelectric Ceramics. Academic Press, New York, (1971)

10. M.E. Lines and A.M. Glass, Principles and Applications of Ferroelectrics and Related Materials, Clarendon press, Oxford, (1977).

11. R. Ramesh (Ed.), Thin Film Ferroelectric materials and Devices, Kluwer, Norwell, MA, (1998).

12. B.A. Strukov and A.P. Levanyuk, Ferroelectric Phenomena in Crystals: Physical Foundations, Springer, Heidelberg, (1998).

13. R.E. Treece, R.E. Jones, C.M. Foster, S.B. Desu, I.K. Yoo (Ed.), Ferroelectric Thin Films VI. Mater. Res. Soc. Symp. Proc. 493, (1998).

14. K. Iijima, T. Terashima, K. Yamamoto, K. Hirata, and Y. Bando, Appl. Phys. Lett. 56, 527 (1990).

15. D. Roy and S.B. Krupanidhi, Appl. Phys. Lett. 61, 2057 (1992).

16. K. Nashimoto, D.K. Fork, F.A. Ponce, and J.C. Tramontana, Jpn. J. Appl. Phys. 32, 4099 (1992).

17. H.A. Lu, L.A. Wills, and B.W. Wessels, Appl. Phys. Lett. 64, 2973 (1994).

18. T.M. Shaw, S. Trolier-McKinstry, and P.C. McIntyre, Annu. Rev. Mater. Sci. 30, 263 (2000).

19. D.L. Polla and L.F. Francis, Annu. Rev. Mater. Sci. 28, 563 (1998).

20. L.R. Dalton, Nature 359, 269 (1992)

21. P. Muralt, J. Micromech. Microeng. 10, 136 (2000).

22. C.L. Chen, J. Shen, S.Y. Chen, G.P. Luo, C.W. Chu, F.A. Miranda, F.W. Van Keuls, J.C. Jiang, E.I. Meletis, H. Chang, Appl. Phys. Lett. 78, 652 (2001)

23. J.C. Jiang, Y. Lin, C.L. Chen, C.W. Chu, E.I. Meletis, J. Appl. Phys. 91, 3188 (2002).

24. T. Maiti, R. Guo, A.S. Bhalla, Appl. Phys. Lett. 89, 122909 (2006).

25. T. Maiti, R. Guo, A.S. Bhalla, Appl. Phys. Lett. 90, 182901 (2007).

26. J. He, J.C. Jiang, E.I. Meletis, J. Liu, G. Collins, C.L. Chen, B. Lin, V. Giurgiutiu, R.Y. Guo, and A. Bhalla, J. Nanosci. Nanotechnol. 10, 1 (2010).

27. J.C. Jiang, X.Q. Pan, C.L. Chen, Appl. Phys. Lett. 72, 909 (1998).

28. J.C. Jiang, W. Tian, X.Q. Pan, Q. Gan, C.B. Eom, Appl. Phys. Lett. 72, 2963 (1998).

29. J.C. Jiang, X.Q. Pan, J. Appl. Phys. 89, 6365 (2001)

30. I. Bozovic, G. Logvenov, I. Belca, B. Narimbetov, I. Sveklo, Phys. Rev. Lett. 89, 107001 (2002).

31. D.T. Margulies, F.T. Parker, A.E. Berkowitz, J. Appl. Phys. 75, 6097 (1994).

32. M. Itoh, R. Wang, Y. Inaguma, T. Yamaguchi, Y.J. Shan, T. Nakamura, Phys. Rev. Lett. 82, 3540 (1999)

33. A.S. Bhalla, R. Guo and R. Roy, The perovskite structure-a review of its role in ceramic science and technology, Mat. Res. Innvat. 4. 3-26 (2000) and references therein.

34. Y.M. Chiang, D.P. Birnie, W.D. Kingery, Physical Ceramics: Principles for Ceramic Science and Engineering, John Wiley & Sons, Inc. (1997) ISBN: 0471598739.

35. W.D. Kingery, H.W. Bowen, and D.R. Uhlmann. Introduction to Ceramics, 2nd edn. Wiley, New York, (1976)

36. K.C. Kao, Dielectric phenomena in solids, Elsevier Academic Press, San Diego, (2004)

37. M. Johnsson, P. Lemmens, Crystallography and Chemistry of Perovskites, Handbook of Magnetism and Advanced Magnetic Materials, John Wiley & Sons, Ltd (2007)

38. A.F. Wells, Structural Inorganic Chemistry, Oxford Science publications, (1995)

39. U. Müller, Inorganic Structural Chemistry, Wiley & Sons Ltd, (1993)

40. Inorganic Crystallographic structure database (ICSD), FIZ Karlsruhe, Germany, (2005)

41. G.A. Smolenskii, V.A. Isupov, Dokl. Akad. Nauk SSSR, 96, 53 (1954)

42. T.N. Verbitskaya, E.I. Gindin, G.S. Prokhvatilov, Y.N. Venevtsev, S.P. Solov'ev, Kristallografiya, 3, 186 (1958)

43. H. Jahn and E. Teller, "Stability of Polyatomic Molecules in Degenerate Electronic States. I. Orbital Degeneracy", Proceedings of the Royal Society of London, Series A, Mathematical and Physical Sciences (1934-1990), 161 (905): 220-235, (1937)

44. S.H. Wemple, J.M. DiDomenico and I. Camlibel, "Dielectric and Optical Properties of Melt-Grown $BaTiO_3$", J. Phys. Chem. Solids, 29, 1797 (1968)

45. F. Jona and G. Shirane, "Barium Titanate", Ferroelectric Crystals, Dover Publications, New York, 108-215, (1993)

46. B.C. Frazer, H.R. Danner, and R. Pepinsky, "Single-Crystal Neutron Analysis of Tetragonal $BaTiO_3$", Phys. Rev., 100, 745 (1955)

47. H.F. Kay, P. Vousden, “Symmetry Changes in Barium Titanate at Low Temperatures and their Relation to its Ferroelectric Properties”, Phil. Mag., 40, 1019 (1949)

48. B. Jaffe, W.R. Cook, H.L. Jaffe, Piezoelectric Ceramics, Academic Press Ltd., New York, (1971)

49. H.D. Megaw, Ferroelectricity in Crystals, Methuen & Co. Ltd., London, (1957)

50. J. Valasek, Piezo-electric and Allied Phenomena in Rochelle Salt, Physical Review, 17, 475 (1921)

51. G. Busch, P. Scherrer, A New Seignettoelectric Substance, Naturwissenschaften, 23, 737 (1935)

52. B.M. Vul, I.M. Goldman, Dielectric Constant of Barium Titanate as a Function of Strength of an Alternating Field, Doklady Akademii Nauk SSSR, Seriya A 49, 177 (1945)

53. S. Miyake, R. Ueda, Journal of the Physical Society of Japan, 1, 32 (1946)

54. H. Thurnauer, J. Deaderick, Insulating Material, U.S.P. 2, Editor (1941)

55. E. Wainer, Transactions of the Electrochemical Society, 89, 331 (1946)

56. P.R. Coursey, K.G. Brand, Nature, 157, 297 (1946)

57. R.B. Gray, U.S.P. 2, Editor. (1946)

58. F. Jona, G. Shirane, Ferroelectric crystals, Oxford, New York: Pegamon Press, (1962)

59. L.L. Hench, J.K. West, Principles of Electronic Ceramics. Wiley, New York, (1990)

60. A.J. Moulson, J.M. Herbert, Electroceramics: Materials, Properties, Applications, Chapman & Hall, London (1990)

61. J.C. Burfoot, G.W. Taylor, Polar dielectrics and their applications, Berkeley: University of California Press. Viii, (1979)

62. D. Damjanovic, Ferroelectric, dielectric and piezoelectric properties of ferroelectric thin films and ceramics, Reports on Progress in Physics, 61, 1267, (1998)

63. G.H. Haertling, Ferroelectric ceramics: History and technology. Journal of the American Ceramic Society, 82, 797, (1999)

64. D. Damjanovic, Ferroelectric, dielectric and piezoelectric properties of ferroelectric thin films and ceramics, Reports on Progress in Physics, 61, 1267, (1998)

65. W.J. Merz, “Double Hysteresis Loop of BaTiO3 at the Curie Point”, Phys. Rev., 91, 513, (1953)

66. R.J. Zednik, Stress effects in ferroelectric perovskite thin-films, dissertation, pp17, (2008)

67. J.M. Herbert, Ferroelectric transducers and sensors, New York: Gordon and Breach, (1982)

68. S.M. Aygun, Processing Science of Barium Titanate, Dissertation, North Carolina State University, pp26, (2009)

69. A.K. Tagantsev, V.O. Sherman, K.F. Astafiev, J. Venkatech, N. Setter, Ferroelectric materials for tunable applications, Journal of Electroceramics, 11, 5, (2003)

70. S. Gevorgian, IEEE Transactions on Microwave Theory and Techniques, 49, 2117, (2001).

71. O. Auciello, S. Saha, D.Y. Kaufman, S.K. Streiffer, W. Fan, B. Kabius, J. Im, P. Baumann, Journal of Electroceramics, 12, 119, (2004)

72. D. Dimos, C.H. Mueller, Perovskite thin films for high-frequency capacitor applications, Annual Review of Materials Science, 28, 397, (1998)

73. J.F. Ihlefeld, Synthesis and Properties of Barium Titanate Solid Solution Thin Films Deposited On Copper Substrates, pp 16, (2006)

74. J.O. Gentner, P. Gerthsen, N.A. Schmidt, R.E. Send, Dielectric Losses in Ferroelectric Ceramics Produced by Domain-Wall Motion, Journal of Applied Physics, 49, 4485, (1978)

75. K. Carl, K.H. Hardtl, Electrical Aftereffects in $Pb(Ti,Zr)O_3$ Ceramics, Ferroelectrics, 17, 473, (1978)

76. R.E. Hummel, Electronic Properties of Materials, Springer-Verlag, Berlin; New York, (1992)

77. A.K. Tagantsev, V.O. Sherman, K.F. Astafiev, J. Venkatesh, N. Setter, Elearooerarnks, 11, 5-66 (2003)

78. O.G. Vendik, LJVL Platonova, Sou Phys. Solid State, 13, 1354 (1971)

79. V.L. Gurevich, A.K. Tagantsev, Intrinsic Dielectric Loss in Crystals, Advances in Physics, 40, 719, (1991)

80. V.L. Gurevich, A.K. Tagantsev, Dielectric Losses in Ferroelectrics of Displacive Type as Compared to the Losses in Ordinary Dielectrics, Ferroelectrics, 64, 423, (1985)

81. A. K. Jonscher, Dielectric Relaxation in Solids, London: Chelsea Dielectrics Press (1983)

82. O. Auciello, R. Waser, Science and Technology of Electmmirnk Thin Film, Dordrecht: Kluwer (1994)

83. J. Jameson, W. Harrison, P. B. Griffin, J. D. Plummer, Appl. Phys. Lett. 84, 3489, (2004)

84. J. Jameson, W. Harrison, P. B. Griffin, J. D. Plummer, Y. Nishi, Appl. Phys. Lett., 100, 124104, (2006)

85. M. Schumacher, G. W. Dietz, K Waser, Integr. Ferroelectr., 10, 231 (1995)

86. W.J. Merz, The Electric and Optical Behavior of $BaTiO_3$ Single-Domain Crystals, Physical Review, 76, 1221, (1949)

87. A.R. Von Hippel, Ferroelectricity, Domain Structure, and Phase Transitions of Barium Titanate, Reviews of Modern Physics, 22, 221, (1950)

88. M.S. Ugorek, Patterned Solid State Growth of $BaTiO_3$ Crystals, Dissertation, The Pennsylvania State University, pp20, (2009)

89. X.H. Du, Q.M. Wang, U. Belegundu, A. Bhalla, K. Uchino, Crystal Orientation Dependence of Piezoelectric Properties of Single Crystal Barium Titanate, Mater. Let., 40, 109, (1999)

90. S. Wada, K. Yako, H. Kakemoto, T. Tsurumi, T. Kiguchi, Enhanced Piezoelectric Properties of Barium titanate Single Crystals with Different Engineered-Domain Sizes, J. Appl. Phys. 98: 014109, 1-7 (2005)

91. P. Muralt, J. Micromech. Microeng., 10, 136 (2000)

92. B.M. Wul, I.M. Goldman, Dielectric Constants of Titanates of Metals of the Second Group, C. R. Acad. Sci. URSS, 46, 139-42 (1945)

93. A. Von Hippel, Ferroelectricity, Domain Structure, and Phase Transitions of $BaTiO_3$, Rev. Mod. Phys., 22, 221-37, (1950)

94. W.O. Statton, Phase diagram of the BaO-TiO_2 system, J. Chem. Phys., 19, 33-40 (1951)

95. D.E. Rase, R. Roy, Phase Equilibria in the system BaO-TiO_2, J. Am. Ceram. Soc., 38, 102-13 (1955)

96. H.M. O'Bryan Jr., J. Thomson Jr., Phase Equilibria in the TiO_2-Rich Region of the System BaO-TiO2, J. Am. Ceram. Soc., 57, 522-526, (1974)

97. T. Negas, R.S. Roth, H.S. Parker, D. Minor, Subsolidus Phase Relations in the $BaTiO_3$-TiO_2 System, J. Solid State Chem., 9, 297 (1974)

98. J.J. Ritter, R.S. Roth, J.E. Blendell, Alkoxide Precursor Synthesis and Characterization of Phases in the Barium-Titanium Oxide System, J. Am. Ceram. Soc., 69, 155-62 (1986)

99. K.W. Kirby, B.A. Wechsler, Phase Relations in Barium Titanate-Titanium Oxide System, J. Am. Ceram. Soc., 74, 1841-7 (1991)

100. X. Lu, Z. Jin, Thermodynamic Assessment of the BaO-TiO_2 Quasibinary System,

101. S. Lee, C.A. Randall, Z.K. Liu, Modified Phase Diagram for the Barium Oxide-Titanium Dioxide System for the Ferroelectric Barium Titanate, J. Am. Ceram. Soc., 90, 2589 (2007)

102. H.M. O'Bryan Jr., J. Thomson Jr., J.K. Plourde, New BaO-TiO_2 compound with Temperature Stable High Permittivity and Low Microwave Loss, J. Am. Ceram. Soc., 57, 450, (1974)

103. D.J. Masse, R.A. Pucel, D.W. Readey, E.A. Maguire, C.P. Hartwig, A New Low-Loss High-K Temperature-Compensated Dielectric for Microwave Applications, Proc. IEEE, 59, 1628-9 (1971)

104. Y. Akinshige, K. Fukano, H. Shigematsu, Crystal Growth and Dielectric Properties of New Ferroelectric Barium Titanate: $BaTi_2O_5$, J. Electroceram., 13, 561-5, (2004)

105. U. Waghmare, M.H.F. Sluiter, T. Kimura, T. Goto, Y. Kawazoe, A Lead-Free High-TC Ferroelectric $BaTi_2O_5$: A First-Principles Study, Appl. Phys. Lett., 84, 4917-9, (2004)

106. A.J. Moulson, J.M. Herbert, Electroceramics, Materials, Properties, Applications, Second ed., Wiley, Chichester, (2003)

107. W. Van Gool, Principles of Defect Chemistry of Crystalline Solids, Academic Press, New York and London, (1966)

108. Y. Torii, K. Tato, A. Tsuzuki, H.J. Hwang, S.K. Dey, J. Mater. Sci. Lett., 17, 827 (1998)

109. V.A. Bokov, I.E. Myl'nikov, Soviet Phys.-Solid State (Engl. Transl.), 3, 613 (1961)

110. J.C. Burfoot, R. Clarke, Ferroelectrics, 8, 505, (1974)

111. L.E. Cross, S.J. Jang, R.E. Newnham, K. Uchino, S. Nomura, Ferroelectrics, 23, 187 (1980)

112. S.J. Jang, L.E. Cross, K. Uchino, J. Am. Ceram. Soc., 64, 209 (1981)

113. T. Takeda, A. Watanabe, Journal of the Physical Society of Japan, 19, 1742, (1964)

114. G. Goodman, J. Am. Ceram. Soc., 46, 48-54 (1963)

115. B.A. Rotenber, Y.L. Danilyuk, E.I. Gindin, V.G. Prokhvat, Soviet Physics Solid State, USSR 7, 2465 (1966)

116. Y. Tsur, T.D. Dunbar, C.A. Randall, Journal of Electroceramics 7, 25-34 (2001)

117. W. Jackson, W. Reddish, High Permittivity Crystalline Aggregates, Nature, 156, 717, (1945)

118. J.F. Ihlefeld, Synthesis and Properties of Barium Titanate Solid Solution Thin Films Deposited on Copper Substrates, North Carolina State University, Dissertation, pp42, (2006)

119. P.C. Joshi, M.W. Cole, Appl. Phys. Lett., 77, 289, (2000)

120. C.L. Chen, H.H. Feng, Z. Zhang, A. Brazdeikis, F.A. Miranda, F.W. Van Kewls, R.R. Romanofsky, Z.J. Huang, Y. Liou, W.K. Chu, C.W. Chu, Appl. Phys. Lett. 75, 412 (1999)

121. W.J. Kim, W. Chang, S.B. Qadri, J.M. Pond, S.W. Kirchoefer, D.B. Chrisey, J.S. Horwitz, Appl. Phys. Lett., 76, 1185 (2000)

122. J.S. Scott, Ferroelectr. Rev., 1, 1 (1998)

123. A.T. Findikoglu, Q.X. Jia, D.W. Reagor, IEEE Trans. Appl. Supercond., 7, 2925 (1997)

124. Q.X. Jia, J.R. Groves, P. Arendt, Y. Fan, A.T. Findikoglu, S.R. Foltyn. H. Jiang, F.A. Miranda, Appl. Phys. Lett., 74, 1564 (1999)

125. C.L. Chen, Z. Zhang, H. Feng, G.P. Luo, S.Y. Chen, A. Heilman, W.K. Chu, C.W. Chu, H.J. Gao, B. Rafferty, S.J. Pennycook, Y. Liou, F.A. Miranda, F. Van Keuls, J. Integrated Ferroelectrics, 28, 237 (2000)

126. C.L. Chen, J. Shen, S.Y. Chen, G.P. Luo, C.W. Chu, F.A. Miranda, F.W. Van Keuls, J.C. Jiang, E.I. Meletis, H.Y. Chang, Appl. Phys. Lett., 78, 652 (2001)

127.T.M. Shaw, Z. Suo, M. Huang, E. Liniger, R.B. Laibowwitz, J.D. Baniecki, Appl. Phys. Lett., 75, 3044 (1999)

128. B.T. Lee, C.S. Hwang, Appl. Phys. Lett., 77, 124 (2000)

129. S. Hoffmann, R. Waser, Control of the Morphology of CSD-Prepared (Ba,Sr)TiO_3 Thin Films, Journal of the European Ceramic Society, 19, 1339-43 (1999)

130. C. Basceri, S.K. Streiffer, A.I. Kingon, R. Waser, The Dielectric Response as a Function of Temperature and Film Thickness of Fiber-Textured (Ba,Sr)TiO_3 Thin Films Grown by Chemical Vapor Deposition, J. Appl. Phys., 82, 2497-2504 (1997)

131. J.C. Jiang, J. He, E.I. Meletis, C.L. Chen, Y. Lin, J. Horwitz, A.J. Jacobson, Two-dimensional Interface Structures of Epitaxial (Ba,Sr)TiO_3 film on Miscut (001) MgO, Thin Solid Films, 518, 147-153 (2009).

132. M. Liu, C. Ma, G. Collins, J. Liu, C.L. Chen, L. Shui, H. Wang, C. Dai, Y. Lin, J. He, J.C. Jiang, E.I. Meletis, Q.Y. Zhang, Microwave Dielectric Properties with Optimized Mn-doped $Ba_{0.6}Sr_{0.4}TiO_3$ Highly Epitaxial Thin films, Crystal Growth and Design, 10, 4221-4223 (2010).

133. T.R. Taylor, P.J. Hansen, N. Pervez, B. Acikel, R.A. York, J.S. Speck, Influence of Stoichiometry on the Dielectric Properties of Sputtered Strontium Titanate Thin Films, J. Appl. Phys., 94, 3390 (2003)

134. B. Laughlin, J. Ihlefeld, J.P. Maria, Preparation of Sputtered (Ba_xSr_{1-x})TiO_3 Thin Films Directly on Copper, J. Am. Ceram. Soc., 88, 2652-4 (2005)

135. J. Zhai, X. Yao, L. Zhang, B. Shen, Appl. Phys. Lett., 84, 3136 (2004)

136. R. Farhi, M.EI Marssi, A. Simon, J. Ravez, Eur. Phys. J., B9, 599 (1999)

137. F.M. Pontes, M.T. Escote, C.C. Escudeiro, E.R. Leite, E. Longo, A.J. Chiquito, P.S. Pizani, J.A. Varela, J. Appl. Phys., 96, 4386 (2004)

138. T. Maiti, R. Guo, A.S. Bhalla, Structure-Property Phase Diagram of $BaZr_xTi_{1-x}O_3$ system, J. Am. Ceram. Soc., 91, 1769 (2008)

139. S. Wada, H. Adachi, H. Kakemoto, H. Chazono, Y. Mizuno, H. Kishi, T. Tsurumi, Phase Transition Behaviors of $BaTiO_3$-$BaZrO_3$ Solid Solutions Under High Direct Current Bias Fields, Journal of Materials Research, 17, 456 (2002)

140. T.N. Verbitskaia, G.S. Zhdanov, I.N. Venevtsev, S.P. Soloviev, Electrical and X-ray Diffraction Studies of the $BaTiO_3$-$BaZrO_3$ system, Soviet Physics Crystallography, 3, 182-192 (1958)

141. D. Hennings, A. Schnell, G. Simon, Diffuse Ferroelectric Phase-Transitions In $Ba(Ti_{1-y}Zr_y)O_3$ Ceramics, J. Am. Ceram. Soc., 65, 539-44, (1982)

142. J. Ravez, A. Simon, Temperature and Frequency Dielectric Response of Ferroelectric Ceramics with Composition $Ba(Ti_{1-x}Zr_x)O_3$, European Journal of Solid State and Inorganic Chemistry, 34, 1199-1209 (1997)

143. G.A. Smolensky, Physical Phenomena in Ferroelectrics with Diffused Phase Transitions, Journal of the Physical Society of Japan, 28, Supplement, 26-37 (1970).

144. A. Dixit, S. B. Majumder, R. S. Katiyar, A. S. Bhalla, Studies on the Relaxor Behavior of Sol – Gel Derived $Ba(Zr_xTi_{1-x})O_3$ ($0.30<x<0.70$) Thin Films, J. Mater. Sci., 41, 87 – 96 (2006).

145. Y. Zhi, A. Chen, R. Guo, A. S. Bhalla, Piezoelectric and Strain Properties of $Ba(Ti_{1-x}Zr_x)O_3$ Ceramics, J. Appl. Phys., 92, 1489 – 93 (2002).

146. A. Dixit, S. B.Majumder, P. S. Dobal, R. S. Katiyar, A. S. Bhalla, Phase Transition Studies of Sol – Gel Deposited Barium Zirconate Titanate Thin Films, Thin Solid Films, 447, 284 – 8 (2004).

147. Z. Yu, R. Guo, A. S. Bhalla, Dielectric Polarization and Strain Behavior of $Ba(Ti_{0.92}Zr_{0.08})O_3$ Single Crystals, Mater. Lett., 57, 349 – 54 (2002).

148. Y. Zhi, A. Chen, R. Guo, A. S. Bhalla, Ferroelectric-Relaxor Behavior of $Ba(Ti_{0.7}Zr_{0.3})O_3$ Ceramics, J. Appl. Phys., 92, 2655 – 7 (2002).

149. C. M. Wu, T. B. Wu, and M. L. Chen, Highly Insulative Barium Zirconate-Titanate Thin Films Prepared by Rf Magnetron Sputtering for Dynamic Random Access Memory Applications, Appl. Phys. Lett., 69, 2659 – 61 (1996).

150. X. G. Tang, J.Wang, X. X. Wang, H. L. W. Chan, Effects of Grain size on the Dielectric Properties and Tunabilities of Sol – Gel Derived $Ba(Zr_{0.2}Ti_{0.8})O_3$ Ceramics, Solid State Commun., 131, 163 – 8 (2004).

151. X. P. Jiang, M. Zeng, H. L. W. Chan, and C. L. Choy, Relaxor Behaviors and Tunability in $Ba(Zr_{0.35}Ti_{0.65})O_3$ Ceramics, Mater. Sci. Eng. A, 438, 198 – 201 (2006).

152. T. Maiti, R Guo, and A. S. Bhalla, Electric Field Dependent Dielectric Properties and High Tunability of $BaZr_xTi_{1-x}O_3$ Relaxor Ferroelectrics, Appl. Phys. Lett., 89, 122909 – 1 – 3, (2006)

153. T. Maiti, R. Guo, and A. S. Bhalla, Enhanced Electric Field Tunable Dielectric Properties of $BaZr_xTi_{1-x}O_3$ Relaxor Ferroelectrics, Appl. Phys. Lett., 90, 182901 – 1 – 3 (2007).

154. J. Zhai, X. Yao, L. Zhang, and B. Shen, Dielectric Nonlinear Characteristics of $Ba.Zr_{0.35}Ti_{0.65}O_3$ Thin Films Grown by A Sol – Gel Process, Appl. Phys. Lett., 84, 3136 – 8 (2004).

155. H. Shizuno, S. Kusumi, H. Saito, H. Kishi, Properties of Y5V Multilayer Ceramic Capacitors with Nickel Electrodes, Jpn. J. Appl. Phys., 32, 4380-4383 (1993).

156. Y. Mizuno, K. Morita, T. Hagiwara, H. Kishi, K. Ohnuma, H. Ohsato, Relationship Between Microstructural Evolution and Electrical Properties in $Ba(Ti, Zr)O_3$-Based Materials for Ni-MLCC, Jpn. J. Appl. Phys., 43, 6640-6644 (2004).

157. T. Tsurumi, Y. Yamamoto, H. Kakemoto, S. Wada, H. Chazono, H. Kishi, Dielectric Properties of $BaTiO_3$-$BaZrO_3$ Ceramics Under a High Electric Field. Journal of Materials Research 17, 755-759 (2002).

158. S. Hoffmann, R.M. Waser, Dielectric Properties, Leakage Behaviour and Resistance Degradation of Thin Films of the Solid Solution Series $Ba(Ti_{1-y}Zr_y)O_3$, Integrated Ferroelectrics, 17, 141-152 (1997).

159. C. Hofer, M. Hoffmann, U. Boettger, R. Waser, Relaxors as High ε Materials for Multilayer and Thin Film Capacitors. Ferroelectrics 270, 179-184 (2002).

160. C. Hofer, U. Ellerkamnn, S. Halder, R. Meyer, R. Waser, Scaling Effect on the Dielectric Constant in $Ba(Ti_xZr_{1-x})O_3$ Thin Films, Journal of Electroceramics, 13, 101- 104 (2004).

161. R. Ganster, S. Hoffmann-Eifert, R. Waser, Characterization of $BaTiO_3$ - $BaZrO_3$ Solid Solution Thin Films Prepared by MOCVD. Integrated Ferroelectrics, 55, 795-805 (2003)

162. T. Tohma, H. Masumoto, T. Goto, Dielectric Properties of $Ba(Ti_{0.85}\ Zr_{0.15})O_3$ Film Prepared by Metalorganic Chemical Vapor Deposition, Jpn. J. Appl. Phys., 42, 6969-6972 (2003).

163. X.G. Tang, D.Y. Wang, J. Wang, H.L.W. Chan, Nonlinear Dielectric Properties of $(Ba,Sr)TiO_3$ and $Ba(Zr,Ti)O_3$ Thin Films for Tunable Microwave Device Applications. Integrated Ferroelectrics, 77, 151-156 (2005)

164. J. He, J. C. Jiang, E.I. Meletis, J. Liu, G. Collins, C. L. Chen, and A. Bhalla, Twin-coupled Domain Structures in Epitaxial Relaxor Ferroelectric $Ba(Zr,Ti)O_3$ Thin Films on (001) MgO Substrate, Philosophical Magazine Letters, 89, 493-503 (2009)

165. J. He, J.C. Jiang, E.I. Meletis, M. Liu, J. Liu, G. Collins, C.R. Ma, C.L. Chen, A. Bhalla, Evolution of Nano-fingers in Epitaxial Mn-doped $Ba(Zr,Ti)O_3$ Thin Films Driven by {110} Twin Boundaries, Philosophical Magazine Letters 91, 361-374, (2011).

166. J. He, J.C. Jiang, E. I. Meletis, M. Liu, G. Collins, C. R. Ma, C. L. Chen, A. Bhalla, Refining of Nanopillars Induced by Mn-doping in Epitaxial $Ba(Zr,Ti)O_3$ Thin Films, Integrated Ferroelectrics, 131, 72-81, (2011).

167. T.M. Shaw, Z. Suo, M. Huang, E. Linger, K.B. Laibowitz, App. Phys. Lett, 75, 2129, (1999)

168. Z.G. Ban, S.P. Alpay, J. Appl. Phys. 91, 11, (1992)

169. N.A. Pertsev, A.G. Zembilgotov, A.K. Tagantsev, Phys. Rev. Lett., 80, 1988-91, (1998)

170. R. Waser, J. Am. Ceram, Soc., 71, 58, (1988)

171. N.H. Chan, D.M. Smyth, J. Electrochem. Soc., 123, 1584, (1976)

172. C.L. Chen, J.S. Horwitz, Ferroelectric Thin Films for Microwave Device Applications, Pulsed Laser Deposition of Thin Films, R. Eason (ed.),John Wiley & Sons, Inc. pp 550, (2007)

172. Robert Eason (editor), Pulsed Laser Deposition of Thin Films, John Wiley & Sons, Inc. (2007)

173. M. Ohring, Materials Science of Thin Films: Deposition and Structure, San Diego, Academic Press (2002)

174. D.J. Gennardo, Design, Construction, and Optimization of a Magnetron Sputtering System for Urania depsotion, University of Illinois at Urbana-Champaign, Thesis, pp8-38, (2010).

175. S. Kirkpatrick, Anomalous Current and Voltage Fluctuations in High Power Impulse Magnetron Sputtering, University of Nebraska, Dissertation, pp9-19, (2009).

176. J.G. Li, Electrical and Optical Properties of Silver Films Deposited by High Power Impulse Magnetron Sputtering, University of Nebraska, Dissertation, pp12-14, (2008).

177. J.R. Piascik, Evaluation of Structure and Material Properties of RF Magnetron Sputter-Deposited Yttria-Stabilized Zirconia Thin Films, University of North Carolina at Chapel Hill, Dissertation, pp7-14, (2007).

178. J.W. Cho, Pulsed DC reactive magnetron sputtering of aluminum nitride thin films, North Carolina State University, Dissertation, pp5-15, (2002).

179. J. Jung, The effect of the sputtering parameters on the ITO films deposited by RF magnetron sputtering, The University of Texas at San Antonio Thesis, pp9-19, (2011).

180. D. Mattox, Handbook of Physical Vapor Deposition (PVD) Processing: Film Formation, Adhesion, Surface Preparation and Contamination Control. Park Ridge, New Jersey: Noyes Publications, (1998).

181. J.A. Thornton. Influence of substrate temperature and deposition rate on structure of thick sputtered Cu coatings. Journal of Vacuum Science and Technology, 12, 830, (1975).

182. J.A. Thorton, The Microstructure of Sputter-deposited Coatings, Journal of Vacuum Science Technology, A4(6), 3059-3065, (1986).

183. J.A. Thorton, Influence of apparatus geometry and deposition conditions on the structure and topography of thick sputtered coatings, J. Vac. Sci. Technol., 11(4), 666-670, (1974).

184. J.A. Thorton, Magnetron sputtering: basic physics and application to cylindrical magnetrons, J. Vac. Sci. Technol. 15, 171, (1978).

185. O. Auciello, C.M. Foster, R. Ramesh, Sputtering deposition is a very popular technique in film deposition and has been extensively studied for ferroelectric thin film growth, Annu Rev Mater. Sci., 28, 501-531, (1998).

186. X.Y. Zhou, Dielectric properties of barium strontium titanate (BST) thin films and phase shifters based on BST thin films, The Hong Kong Polytechnic University, dissertation, pp22-24, (2007).

187. Z. Yuan, Nanostructure and strain effects in active thin films for novel electronic device applications, The University of Texas at San Antonio, Dissertation, pp17-24, (2007).

188. H. Du, Processing, microstructure, and microwave dielectric properties of tunable (Ba,Sr)TiO_3 thin films, Carnegie Mellon University, Dissertation, pp90-100 (2009).

189. R.D.D. Martínez, Synthesis of $CuAlO_2$ thin films by pulsed laser deposition, University ogf Puerto Rico, Thesis, pp19-28 (2009).

190. S.H. Yoon, Growth and Characterization of low stress amorphous carbon films by pulsed laser deposition process, University of Florida, dissertation, pp15-20 (2004).

191. G.R. Collins, Interface engineered multifunctional oxide thin films with optimized properties, The University of Texas at San Antonio, Dissertation, pp23-33 (2010).

192. A. Erlacher, Pulsed-laser deposition and characterization of hetero-paired thin-film gallium arsenide, Bowling Green State University, Dissertation, pp4-17 (2005).

193. H.M. Smith, A.F. Turner, Vacuum deposited thin films using a ruby laser, Appl. Opt. 4, 147, (1965).

194. D. Dijkamp, T. Venkatesan, X.D. Wu, S.A. Shaheen, N. Jisrawi, Y.H. Min-Lee, W.L. Mclean, M. Croft, Preparation of Y-Ba-Cu oxide superconductor thin films using pulsed laser evaporation from high TC bulk material, Appl. Phys. Lett. 51, 619, (1987).

195. J.A. Venables, G.D.T. Spiller, M. Hanbucken, Nucleation and growth of thin films, Rep. Prog. Phys. 47, 399, (1984).

196. J.E. Green, O. Auciello, J. Engemann (Eds), Multicomponent and multilayered thin films for advanced microtechnologies, NATO/ASI Series E 234, 39, Kluwer Academic Publishers, The Netherlands, (1993).

197. I. Markov, and R. Kaischew, Influence of supersaturation on the mode of crystallization on crystalline substrate, Thin Solid Films 32, 163, (1976)

198. K. Reichelt, Nucleation and growth of thin films, Vacuum 38, 1083, (1988).

199. L. B. Freund, Thin film materials: stress, defect formation, and surface evolution, Cambridge University Press, New York (2003).

200. D. L. Smith, Thin-film deposition: principles and practice, McGraw-Hill, New York (1995).

201. C.J. Lu, L. A. Bendersky, K. Chang, I. Takeuchi, Journal of Applied Physics 93,512-521, (2003).

202. M. H. Grabow, G. H. Gillmer, Semiconductor-based heterostructures: interfacial structure and stability, Metallurgical Soc., Warrendale, PA (1986).

203. M.H. Francombe, Thin Solid Films 13, 413, (1973).

204. L. Beckers, J. Schubert, W. Zander, J. Ziesmann, A. Eckau,D. Leinenbach, Ch. Buchal, J. Appl. Phys. 83, 3305, (1998).

205. H.B. Sharma, H.N.K. Sarma, A. Mansingh, J. Mater. Sci. 34,1385, (1999).

206. R.A. Mckee, F.J. Walker, E.D. Specht, K.B. Alexander, Mater. Res. Soc. Symp. Proc. 341, 309, (1994).

207. B. Bihari, J. Kumar, G.T. Stauf, P.C. Van Buskirk, C.S. Hwang, J. Appl. Phys. 76 (1994) 1169.

208. L.A. Wills, B.W. Wessels, D.S. Richeson, T.J. Marks, Appl. Phys. Lett. 60 (1992) 41.

209. Y. Yoneda, T. Okabe, K. Sakaue, H. Terauchi, Surface Science, 410 (1998) 62.

210. K. Iijima, T. Terashima, K. Yamamoto, K. Hirata, Y. Bando, Appl. Phys. Lett. 56 (1990) 527

211. M. Matsuoka, K. Hoshino, K. Ono, J. Appl. Phys. 76 (1994) 1768

212. W.J. Lin, T.Y. Tseng, H.B. Lu, S.L. Tu, S.J. Yang, I.N. Lin, J. Appl. Phys. 77 (1995) 6466

213. J.H. Kim, S. Hishita, J. Mater. Sci. 30 (1995) 4645

214. Y. Yoneda, T. Okabe, K. Sakaue, H. Terauchi, H. Kasatani, K. Deguchi, J. Appl. Phys. 83 (1998) 2458.

215. H.Z. Guo, L. F. Liu, Z.H. Chen, S. Ding, H.B. Lu, K.J. Jin, Y.L. Zhou, B.L. Cheng, Europhys. Lett., 73 (2006) 110.

216. C.L. Li, D.F. Cui, Y.L. Zhou, H.B. Lu, Z.H. Chen, D.F. Zhang, F. Wu, Appl. Surf. Sci. 136 (1998) 173.

217. S. Hontsu, J. Ishii, H. Tabata, T. Kawai, Appl. Phys. Lett 67 (1995) 554.

218. C.L. Li, Z.H. Chen, Y.L. Zhou, D.F. Cui, J. Phys.:Condens. Matter 13 (2001) 5261.

219. L.D. Rotter, D.L. Kaiser, M.D. Vaudin, Appl. Phys. Lett. 68 (1996) 310.

220. H. Funakubo, D. Nagano, A. Saiki, Y. Inagaki, K. Shinozaki, N. Mizutani, Japan. J. Appl. Phys. 36 (1997) 5879.

221. W.C. Shih, M.H. Chiang, J. Mater. Sci: Mater Electron, 21 (2010) 844.

222. S.S. Kim, J.H. Je, J. Mater. Res., 14 (1999) 3734.

223. S. Kim, S. Hishita, Y.M. Kang, S. Baikb, J. Appl. Phys. 78 (1995) 5604.

224. S. Kim, Y. Park, Y. Kang, W. Park, S. Baik, A. Gruverman, Thin Solid Films, 312 (1998) 249.

225. A. Lotnyk, A. Graff, S. Senz, N.D. Zakharov, D. Hesse, Topotaxial formation of titanium-rich barium titanates during solid state reactions on (110) TiO2 (rutile) and (001) $BaTiO_3$ single crystals, Solid State Sciences, 10 (2008) 702-708.

226. E. Tillmanns, Acta Crystallogr. B, Refinement of barium dititanate, 30 (1974) 2894-2896.

227. V. Kraševec, D. Kolar, J. Am. Ceram. Soc., Existence of the $Ba_2Ti_5O_{12}$ Phase in Ca-Doped TiO_2-Rich $BaTiO_3$, 71 (1988) C426-C427.

228. E. Tillmanns, W.H. Baur, Acta Crystallogr. B, Crystal Structure of Hexabarium Heptadecatitanate, 26 (1970) 1645-54.

229. E. Tillmanns, Inorg. Nucl. Chem. Lett., Crystal Structure of Tetrabarium Tridecatitanate, 7 (1971) 1169-71.

230. K. Lukaszewicz, Rocz. Chem., Crystal Structure of Barium Tetratitanate, $BaO\text{-}4TiO_2$, 31 (1957) 1111-22.

231. E. Tillmanns, W. Hofmeister, W.H. Baur, J. Am. Ceram. Soc., Crystal Structure of the Microwave Dielectric Resonator $Ba_2Ti_9O_{20}$, 66 (1983) 268-271.

232. E. Tillmanns, Acta Crystallogr. B, Crystal Structure of Barium Titanium Oxide ($BaTi_5O_{11}$), 25 (1969) 1444-52.

233. E. Tillmanns, Cryst. Struct. Commun., Barium Hexatitanate, $BaTi_6O_{13}$, 1 (1972) 1-4.

234. J.A. Bland, Acta Cryst., The crystal structure of barium orthotitanate, Ba_2TiO_4, 14 (1961) 875-881.

235. J. Akimoto, Y. Gotoh, M. Sohma, K. Kawaguchi, Y. Oosawa, Journal of Solid State Chemistry, Synthesis and Crystal Structure of $Ba_2Ti_{13}O_{22}$: A Reduced Form of $BaTi_5O_{11}$ by the Titanium Insertion, 113 (1994) 384-392.

236. J.C. Jiang, E.I. Meletis, Z. Yuan, C.L. Chen, Appl. Phys. Lett., 90 (2007) 051904.

237. J. C. Jiang, J. He, E.I. Meletis, J. Liu, Z. Yuan, and C. L. Chen, Journal of Nano Research, 3 (2008) 59-66.

238. C. L. Chen, Z. Zhang, H. Feng, G. P. Luo, S. Y. Chen, A. Heilman, W. K. Chu, C. W. Chu, H. J. Gao, B. Rafferty, S. J. Pennycook, Y. Liou, F. A. Miranda, and F. Van Keuls, J. Integrated Ferroelectrics 28, 237 (2000).

239. P. C. Joshi and M. W. Cole, Appl. Phys. Lett. 77, 289 (2000).

240. B. T. Lee and C. S. Hwang, Appl. Phys. Lett. 77, 124 (2000).

241. L. E. Shilkrot, D. J. Srolovitz, and J. Tersoff, Appl. Phys. Lett. 77, 304 (2000).

242. P. A. Stadelmann, Ultramicroscopy 21, 131 (1987).

243. I. Bozovic, G. Logvenov, I. Belca, B. Narimbetov, I. Sveklo, Phys. Rev. Lett. 89 (2002) 107001.

244. D.T. Margulies, F.T. Parker, F.E. Spada, R.S. Goldman, J. Li, R. Sinclair, A.E. Berkowitz, Phys. Rev., B 53 (1996) 9175.

245. D.T. Margulies, F.T. Parker, A.E. Berkowitz, J. Appl. Phys. 75 (1994) 6097.

246. M. Itoh, R.Wang, Y. Inaguma, T. Yamaguchi, Y.J. Shan, T. Nakamura, Phys. Rev. Lett. 82 (1999) 3540.

247. Q. Meng, R. Moerman, A.H. Sonnenberg, G.J. Gerritsma, Appl. Phys. A 68 (1999) 239.

248. U. Weber, G. Greuel, U. Boettger, S. Weber, D. Hennings, R. Waster, R., J. Am. Ceram. Soc., 84, 759, (2001).

249. J.W. Zhai, X. Yao, L.Y. Zhang, B. Shen, Appl. Phys. Lett., 84, 3136, (2004).

250. T. Maiti, R. Guo, A.S. Bhalla, Appl. Phys. Lett. , 89, 122909, (2006).

251. A. Dixit, S.B. Majumder, R.S. Katiyar, A.S. Bhalla, Appl. Phys. Lett., 82, 2679, (2003).

252. X.H. Zhu, J. Li, D.N. Zheng, Appl. Phys. Lett., 90, 142913, (2007).

253. J.W. Zhai, X. Yao, J. Shen, L.Y. Zhang, H. Chen, Structural and dielectric properties of $Ba(Zr_xTi_{1-x})O_3$ thin films prepared by the sol-gel process. J. Phys. D: Appl. Phys, 37, 748-752, (2004).

254. C.S. Hsi, C.Y. Chen, N.C. Wu, M.C. Wang, Dielectric properties of $Ba(Zr_xTi_{1-x})O_3$ thin films prepared using radio frequency magnetron sputtering. J. Appl. Phys. 2003; 94: 598-604.

255. X.G. Tang, H.Y. Tian, J. Wang, K.H. Wang, H.L.W. Chan, Effect of $CaRuO_3$ interlayer on the dielectric properties of $Ba(Zr,Ti)O_3$ thin films prepared by pulsed laser deposition. Appl Phys Lett. 2006; 89: 142911.

256. W.S. Choi, J.S. Yi, B.Y. Hong, The effect of cerium doping in barium zirconate titanate thin films deposited by rf magnetron sputtering system. Mater Sci Eng B. 2004; 109: 146-151.

257. W.J. Jie, J. Zhu, W.F. Qin, X.H. Wei, J. Xiong, Y. Zhang, A. Bhalla, Y.R. Li, Enhanced dielectric characteristics of preferential (111)-oriented BZT thin films by manganese doping. J Phys D: Appl Phys. 2007; 40: 2854-2857.

258. D. Hennings, A. Schnell, G. Simon, J. Am. Ceram. Soc., 65, 539, (1982).

259. P.S. Dobal, A. Dixit, R.S. Katiyar, Z. Yu, R. Guo, A.S. Bhalla, J. Appl. Phys., 89, 8085, (2001).

260. Z.Yuan, Y. Lin, J. Weaver, X. Chen, C.L. Chen, G. Subramanyam, J.C. Jiang, E.I. Meletis, Large dielectric tunability and microwave properties of Mn-doped (Ba,Sr)TiO_3 thin films. Appl Phys Lett. 2005; 87: 152901-152903.

261. M.W. Cole, W.D. Nothwang, C. Hubbard, E. Ngo, M. Eryin, Low dielectric loss and enhanced tunability of $Ba_{0.6}Sr_{0.4}TiO_3$ based thin films via material compositional design and optimized film processing methods. J Appl Phys. 2003; 93: 9218-9225.

262. Y.L. Wang, L.T. Li, J.Q. Qi, Z.L. Gui, Ferroelectric characteristics of ytterbium-doped barium zirconium titanate ceramics. Ceram Int. 2002; 28: 657-661.

263 A. Ohtomo, H.Y. Hwang, Nature 427(6973), 423 (2004).

264. H.W. Jang, D.A. Felker, C.W. Bark, Y. Wang, M.K. Niranjan, C.T. Nelson, Y. Zhang, D. Su, C.M. Folkman, S.H. Baek, S. Lee, K. Janicka, Y. Zhu, X.Q. Pan, D.D. Fong, E.Y. Tsymbal, M.S. Rzchowski, C.B. Eom, Science, 331 (6019), 886 (2011).

265. J.C. Jiang, X.Q. Pan, W. Tian, C.D. Theis, D.G Schlom, Appl. Phys. Lett., 74, 2851 (1999).

266. M. Liu, G. Collins, E. Silva, C.R. Ma, J. Liu, C.L. Chen, J. He, J.C. Jiang, E.I. Meletis, S.W. Qu, Q.Y. Zhang, A. Bhalla, Integrated Ferroelectrics, 131, 89 (2011).

267. L. Kim, J. Kim, D. Jung, J. Lee, U.V. Waghmare, Appl. Phys. Lett., 87, 052903 (2005).

268. W.F. Qin, J. Xiong, J. Zhu, J.L. Tang, W.J. Jie, Y. Zhang, Y.R. Li, Enhanced electrical properties of multilayer $Ba(Zr_{0.2}Ti_{0.8})O_3$/$Ba_{0.6}Ti_{0.4}TiO_3$/ $Ba(Zr_{0.2}Ti_{0.8})O_3$ thin films for tunable microwave applications, J Mater Sci. 2008; 43: 409-412.

269. N.Y. Chan, G.Y. Gao, Y. Wang, H.L.W. Chan, Preparation and characterizations of $Ba(Zr,Ti)O_3/(Ba,Sr)TiO_3$ heterostructures grown on $(LaAlO_3)_{0.3}(Sr_2AlTaO_6)_{0.35}$ single crystal substrates by pulsed laser deposition. Thin Solid Films. 2010; 518: e82–e84.

270. W.F. Qin, J. Xiong, Y.R. Li, Structure and Properties of BST/BZT/BST Multilayer Film. Journal of Inorganic Material. 2010; 25: 247-250.

BIOGRAPHICAL INFORMATION

Jie He was born in Tianjin, China. She reveived her bachelor degree in Materials Science and Engineering from Tianjin University in 2005. After that, she continued and received her master degree in Materials Science and Engineering from Tianjin University in 2007. In 2012, she received her Ph.D degree in Materials Science and Engineering from University of Texas at Arlington. During her graduate study in Tianjin University, she focused on the preparation of Cu-based composites reinforced with nano diamond particles using chemistry co-precipitation and chemical plating, and the physical and mechanical performance of as-prepared composites. During her study in University of Texas at Arlington, her studies focused on understanding the growth mechanism of epitaxial, perovskite-type oxide thin films via microstructure analysis at the atomic/nano scale. Her dissertation is a fundamental study regarding the processing-microstructure-property relationship in oxide thin films using X-ray diffraction, transmission electron microscopy (TEM), high-resolution TEM, electron diffraction and other major materials characterization techniques. More than 30 refereed journal papers and conference presentations have been published from her work, which attest to the importance of her study and her research abilities. The strong specialization on analytical TEM, high-resolution TEM, *in-situ* high temperature TEM, electron diffraction analysis, cross-section and plan-view TEM sample preparation, image processing, modeling and simulation, provide her the opportunity to achieve a high quality research level and address challenging issues in material science.